DISS. ETH NO. 22484

Growth, Interaction and Packing of Thin Objects

A thesis submitted to attain the degree of
DOCTOR OF SCIENCES OF ETH ZÜRICH
(DR. SC. ETH ZÜRICH)

presented by
ROMAN VETTER

MSc ETH CSE, ETH Zürich

born on 04.08.1985

citizen of Affeltrangen TG, Switzerland

accepted on the recommendation of
Prof. Dr. HANS J. HERRMANN
Prof. Dr. MARTINE BEN AMAR

2015

Preface

The doctoral thesis at hand is the result of my work as a scientific assistant at the group of Computational Physics for Engineering Materials (comphys) at the Institute for Building Materials (IfB) at ETH Zürich, Switzerland. During this time, I have profited from the knowledge, collaboration and advice of many friends and colleagues, without whom this project could not have been realized. In particular, I would like to express my sincere gratitude to

- Prof. Hans J. Herrmann from ETH Zürich, whose far-sighted, strategic and deep grasp of an amazingly wide range of physics has guided me through my scientific career to this day, and whose enthusiasm for science and teaching has been truly inspiring,
- Dr. Falk K. Wittel from ETH Zürich for sharing his broad experience in material modeling with me, for his commitment and verve in preparing and carrying out experimental work, and for his invaluable guidance in scientific writing and presentation, all of which has had a considerable stake at the successful outcome of my work,
- Dr. Norbert B. Stoop from the Massachusetts Institute of Technology, who always willingly took the time to share his deep knowledge, and whose outstanding work on morphogenesis in rigid confinement paved the way for the present project,
- Kornél Kovács from ETH Zürich, whose great expertise and restless efforts (even in numerous night shifts) as a Linux and cluster administrator have been invaluable for my everyday work,
- Gautam Munglani and Alessandro Leonardi from ETH Zürich for their fruitful collaboration and discussions on thin shell mechanics,
- Frédéric Ablitzer from l'Université du Maine, my discussions with whom were of great avail for the accurate implementation of large beam rotations, and
- Prof. Martine Ben Amar from l'École normale supérieure, for kindly agreeing to co-examine me.

Special thanks go to the developers of the marvelous C++ finite element library `libMesh`, with the aid of which the numerical simulations presented in this doctoral thesis were implemented. Dr. ROY H. STOGNER from the University of Texas at Austin, Dr. BENJAMIN S. KIRK from the Lyndon B. Johnson Space Center, Dr. JOHN W. PETERSON and DEREK R. GASTON from the Idaho National Laboratory and Dr. DAVID J. KNEZEVIC from Harvard University were kindly providing technical support in usage and extension of the library.

This work was financially supported by the ETH Independent Investigators' Research Award Grant "Packing of Slender Objects in Deformable Confinements" (ETH-IRA Grant No. ETH-03 10-3) and the European Research Council Advanced Grant "Fluid Flow in Complex and Curved Spaces" (ERC Adv. Grant No. FP7-319968 FFLOWCCS).

Roman Vetter
Zürich, March 2015

Zusammenfassung

Wer ein langes Kabel oder eine Schnur platzsparend verstauen will, wird diese in der Regel zu einer Rolle aufwickeln, im Wissen, dass dies eine effiziente Lösung darstellt, die anschliessend auch das erneute Abrollen ohne starkes Verheddern ermöglicht. Gleichzeitig kennt jeder das Phänomen, dass sich Ohrhörerkabel in der Hosentasche verblüffend schnell ineinander verfangen, obschon man sie nicht absichtlich verknotet hat, besonders wenn sie eine reibungsbehaftete Oberfläche besitzen. Diese alltäglichen Beispiele zeigen eine Klasse von komplexen Problemstellungen auf, die auch in der Natur weit verbreitet sind: Die Packung langer und dünner, verformbarer Objekte in einer beschränkten Räumlichkeit, und die damit einhergehende Tendenz sich spontan zu bündeln, falten, winden und zerknüllen. So etwa spulen Viren die DNS-Stränge ihres Genoms unter Ausübung erheblicher Kräfte eng in Kapsiden auf, Aktinfilament-Netzwerke reorganisieren sich plötzlich zu ringförmigen Bündeln wenn die flexiblen Vesikel, in denen sie eingeschlossen sind, an Ausdehnung verlieren, und die Darmkanäle im Körperhohlraum vieler Wirbeltiere formieren sich im Wachstumsstadium aufgrund unterschiedlicher Wachstumsraten zu verworrenen Schlaufen. Solche Formfindungsprozesse treten auf einer grossen Bandbreite von Längenskalen auf und unterliegen oft universellen Verhaltensmustern, die sich rein mechanisch erklären lassen.

Bislang wurden Wachstum, Packung und Formbildung dünner Körper in beschränkten räumlichen Verhältnissen fast ausschliesslich unter dem Gesichtspunkt unverformbarer Behälter systematisch untersucht. Diese idealisierte Betrachtungsweise vernachlässigt aber Effekte gegenseitiger mechanischer Interaktionen des gepackten Materials mit seiner Hülle, wie sie in diversen biologischen, medizinischen und materialwissenschaftlichen Anwendungen beobachtet werden können. Die vorliegende Doktorarbeit nimmt sich genau dieser grundlegenden Problematik an. Die zentrale Fragestellung ist die nach der deterministischen Morphogenese dünner, stark verformbarer Schalen und Filamente unter verschiedenen geometrischen und materiellen Gegebenheiten wie anisotropes volumetrisches Wachstum, Selbstkontakt, Kontakt zwischen verschiedenen flexiblen Strukturen und makroskopischen Materialkennwerten. Spezielles Augenmerk wird dabei gelegt auf die Verallgemeinerung der bis dato untersuchten starren kugelförmigen Kavität hin zu einer flexiblen dünnen Schale, und die dadurch auftretenden neuartigen Packungsverhal-

ten darin eingeschlossener dünner Stränge. Weil dabei eine Vielzahl komplizierter Vorgänge zusammenspielen, werden primär numerische Simulationen entwickelt und eingesetzt. Dies erlaubt eine präzise Kontrolle der Systemparameter sowie eine systematische Durchforstung der morphologischen Phasenräume innert nützlicher Frist. Die Methode der Finiten Elemente stellt für viele kontinuumsmechanische Probleme mit starker Anisotropie oder Effekten höherer Ordnung das mächtigste und flexibelste numerische Werkzeug dar und kommt daher hier zur Anwendung.

Die hierin gewonnenen Erkenntnisse beginnen bei der Identifikation derjenigen dimensionslosen Kontrollparameter, die unter verschiedenen Randbedingungen den Wachstums- oder Packungsprozess bestimmen. Überraschenderweise ändert die Schalenflexibilität nicht nur die geometrische Struktur zu der sich darin eingeführte lange Filamente aufwinden, sondern auch die Rolle, die die Reibung dabei einnimmt. Während Reibungskräfte in starren Kugelbehältern nur untergeordneten Einfluss auswirken, bestimmen sie die Morphologie in flexiblen Kugelschalen massgebend. Entscheidend sind aber nicht alleine die Verhältnisse der interagierenden intrinsischen Materialkennzahlen, sondern auch die konkurrierenden Längenskalen, die ebenfalls identifiziert werden. Ein quantitatives Bild des morphologischen Phasenraumes zeigt im Folgenden präzise auf, wie geometrische und materielle Grössen zusammenspielen bei der Gestaltbildung wachsender Ringfilamente in verformbaren Membranen. Dadurch ergibt sich eine universelle Vorhersehbarkeit der Form. Schliesslich gewährt die Messung der mit den Phasenübergängen verbundenen Ordnungsparametern einen offenbarenden Einblick in dabei auftretende Symmetriebrechungen und Instabilitäten, welche die spontane Aufwicklung, Bündelung und Faltung verschiedener Filamente in biologischen und verwandten Systemen mit mechanischen Prinzipien erklären.

Abstract

When a long cable or string is to be stowed away in a space-saving manner, it is typically rolled up into an ordered coil, which provides an efficient solution that allows it to be uncoiled again later without getting tangled up much. On the other hand, the astounding phenomenon that earphone cords tend to entangle without much further action in a pocket, even though one likewise carefully coiled them up beforehand, is known to everyone from painful daily experience, especially if they possess a rough or sticky surface. These everyday examples illustrate a class of complex problems that are widely spread also in Nature: The packing of long and thin deformable objects in spatial confinement, which is accompanied by their tendency to spontaneously bundle, fold, coil and crumple under different conditions. Viruses, for instance, apply significant molecular forces to tightly wind up their DNA strands in capsids. Actin filament networks spontaneously restructure to ring-like bundles upon sufficient shrinkage of the giant vesicles they are enclosed by, and the gut tubes of various vertebrates develop a distinct loop pattern in the body cavity as a result of differential growth during early growth stages. Such kinds of shape transformations occur on a large range of length scales and can oftentimes be explained by pure mechanics, which hints at universal underlying principles.

To this date, the systematic studies of packing and morphogenesis of thin bodies in limited spatial circumstances have almost entirely been restricted to the special case of rigid containers. Under this idealized viewpoint, however, effects are neglected that result from the mechanical interaction between the packed structure and its hull, as it can be observed in various biological and medical applications as well as in materials engineering. The dissertation at hand is concerned with precisely this fundamental problem statement. The central question addressed is the one regarding deterministic morphogenesis of thin shells and filaments undergoing large deformation, subject to various geometrical and material conditions such as anisotropic volumetric growth, self-contact, contact between different flexible structures, and macroscopic material properties. Special attention is paid to generalizing the rigid spherical cavity of packing studies preceding the present work toward a flexible thin shell, and to the emerging novel packing processes of injected or enclosed thin strands. Since so many complicated mechanisms mutually interfere in this, numerical simulations are developed and employed primarily, allowing for a precise control

of the system parameters as well as to systematically sift through the morphological phase spaces in a timely manner. The powerful finite element method is utilized here as it offers the best flexibility for many problems in continuum mechanics, in particular with strong anisotropy and effects of higher order.

The herein gained novel insights set in at the identification of those dimensionless control parameters that govern growth and packing processes under given boundary conditions. Surprisingly, a finite shell flexibility does not merely alter the geometric structure and coiling of an injected long filament; it also affects the role friction takes in the game. While frictional forces have only minor influence in rigid containers, they turn into a key factor governing morphogenesis in flexible shells. The decisive parameters are thus found to be ratios of interacting intrinsic material properties, but also the involved competing length scales, which are identified too. A quantitative image of the morphological phase space subsequently reveals how exactly geometric and material properties interplay when elastic ring filaments grow in deformable membranes, yielding the power to predict the emergence of shapes universally. Finally, a set of order parameters that quantitatively characterize the phase transitions are proposed and measured, shedding light on instabilities and symmetries that are spontaneously broken. Various instances of filament coiling, bundling and folding occurring in biological and related systems are thereby explained by mechanical principles.

List of publications

A large part of the arguments and results presented in this thesis, as well as applications of the developed methodologies, have been published in international peer-reviewed journals and conference proceedings as listed below in chronological order of appearance. Some of them contain additional supporting information on the respective topic that is left out in the present work for the sake of conciseness.

R. Vetter, F. K. Wittel, N. Stoop, and H. J. Herrmann. Finite element simulation of dense wire packings. *Eur. J. Mech. A* **37** (2013), 160–171.

R. Vetter, N. Stoop, T. Jenni, F. K. Wittel, and H. J. Herrmann. Subdivision shell elements with anisotropic growth. *Int. J. Numer. Meth. Eng.* **95** (2013), 791–810.

R. Vetter, N. Stoop, F. K. Wittel, and H. J. Herrmann. Simulating Thin Sheets: Buckling, Wrinkling, Folding and Growth. *J. Phys.: Conf. Ser.* **487** (2014), 012012.

R. Vetter, F. K. Wittel, and H. J. Herrmann. Morphogenesis of filaments growing in flexible confinements. *Nat. Commun.* **5** (2014), 4437.

A. Leonardi, F. K. Wittel, M. Mendoza, R. Vetter, and H. J. Herrmann. Particle-fluid-structure interaction for debris flow impact on flexible barriers. *Computer-aided Civ. Inf. Eng.* (2015). Submitted.

G. Munglani, R. Vetter, F. K. Wittel, and H. J. Herrmann. Orthotropic rotation-free thin shell elements. *Comput. Mech.* (2015). Submitted.

R. Vetter, F. K. Wittel, and H. J. Herrmann. Packing of elastic wires in flexible shells. *Phys. Rev. Applied* (2015). Submitted.

Contents

List of Figures

List of Tables

Nomenclature

The following is a list of the most prevalent symbols and abbreviations in this work. More are defined within different contexts in the main text, possibly with differing meanings for the same variable. The page on which each symbol is introduced is given at the end of the corresponding entry in the list. Generally, the following face types are used for easy identification of different classes of quantities:

x, X	Scalars
$\boldsymbol{x}$, $\mathbf{x}$	Vectors
$\mathbf{X}$	Matrix
$\boldsymbol{X}$	Tensor

Roman symbols

A	Area of the circular filament cross section	19
a	Spacing of the beam mesh (length of one element)	35
$\mathbf{a}_1$, $\mathbf{a}_2$, $\mathbf{a}_3$	Parameterization derivatives in direction of θ^1, θ^2, θ^3	12
$\mathbf{A}$	Trihedron of filament directors	17
$\boldsymbol{C}$	Elasticity tensor	14
$\mathbf{D}$	Viscous damping matrix	50
D	Bending rigidity of the shell	15
E	YOUNG's modulus	15
$\boldsymbol{E}$	GREEN–LAGRANGE strain tensor	13
$\boldsymbol{F}$	Geometric deformation gradient	13
f	Confinement flexibility, or conversely, the relative filament rigidity	86
$\boldsymbol{F}_\mathrm{g}$	Growth tensor	13
$\mathbf{f}$	Generalized forces	25
G	Shear modulus	15
h	Shell thickness	11
I	Area moment of inertia	19
$\mathbf{I}$	Identity matrix	38
J	Polar moment of inertia	19
K	Membrane stiffness of the shell	15
$\mathbf{K}$	Stiffness matrix	33
L	Filament length	79
l	Normalized filament length	84
$\mathbf{M}$	Mass matrix	50

Greek symbols

Subscripts and superscripts

Operators

Abbreviations

Chapter 1

Introduction

It behoves us always to remember that in physics it has taken great men to discover simple things. [...] It is but the slightest adumbration of a dynamical morphology that we can hope to have until the physicist and the mathematician shall have made these problems of ours their own.

– D'Arcy Wentworth Thompson, *On Growth and Form* (1917)

1.1 Overview and motivation

A century ago—quite a step ahead of his time—a mathematical biologist postulated that a good share of the wealth of patterns, shapes and forms found in Nature may be described and understood as an inevitable consequence of mechanical growth. D'Arcy Thompson's famous 1917 landmark monograph *On Growth and Form* [227] inspired and motivated many natural scientists in the decades to follow to tackle the mysteries of morphogenesis in a rigorous way from first principles, revolutionizing the way we nowadays see the variety of shapes in Nature and in our everyday environment. His thesis that growth and mechanical response of soft tissue (rather than design or pure evolution) lies at the core of many shape transformations observed in biology has been confirmed theoretically and experimentally in countless occasions. Thompson realized that a key player in the game of morphogenesis is a certain degree of non-uniformity underlying a plethora of growth scenarios. From a modern perspective, this very broad notion can be divided into two types: anisotropic growth and differential growth. The former accounts for a variation in the *directions* of growth, whereas the latter introduces a growth *gradient* or different growth *rates* along one of said directions. It is the combination of these complementary concepts with ideas from elasticity that has let the study of pattern and shape formation blossom over recent decades.

D'Arcy Thompson also acknowledged the inherent need for a quantitative description of growth phenomena—the language and approach of a mathematician or physicist—to be able to comprehend forms and structures that biologists and chemists had previously struggled to explain in their entirety. Along with this different viewpoint comes an additional level of abstraction: The mathematical description of growth requires cause and effect to be decoupled. What gives rise to growth—be it a chemical catalyst, a biological morphogen, genetic programming or a material response to temperature or moisture changes—becomes irrelevant for the physicist who seeks to explore the space of assumable shapes of a growing body and to identify universal behavior and fundamental principles. Such a decoupling treats growth and its induced morphogenesis as a dead process, disregarding active regulations or control by a living organism. Although it should not be mistaken for the sole answer to the question of shape development in the biological context, this approach has been widely and successfully applied to dead and living matter alike.

A morphologist necessarily employs a geometrician's tools to characterize certain shapes. Perhaps the most intriguing patterns and structures emerge when thin objects undergo very large deformations. A body is considered thin if, locally, its geometrical extent in at least one of the spatial dimensions is much smaller than in another one. This local definition can be extended to the global scale by requiring that the body be locally thin at all points constituting its volume. In Euclidean space, two classes of slender objects are known to everyone from daily life: shells or sheets, and filaments or wires. Examples are so numerous that any feasible attempt at listing them will be incomplete. They span virtually all observable length scales—from graphene sheets to plant leaves and the crust of Earth, from molecular chains to hair and intercontinental gas pipelines. Thin bodies have relatively little rigidity to oppose to transverse forces, enabling a large variety of complex three-dimensional deformations induced by external loading, spatial constraints or volumetric growth.

No study on pattern formation is complete without knowledge about the circumstances under which they occur. Large deformations of soft thin tissue such as insect wings, cell membranes or flowers are often on account of growth [43, 221], inevitably leading to the development of residual stresses [90, 204]. The *kind* of growth—its anisotropy and spatial variation—is thus one of these circumstances. External forcing and volumetric exclusion are further important ones. A whole class of parameters arises from the geometrical conditions involved: Characteristic length scales and size ratios governing the transformations of thin objects need to be identified. Finally, macroscopic material properties that characterize elastic or inelastic behavior and contact friction can be key to grasping the unparalleled variety of shapes Nature is furnished with. Only if the role of each of these constituents is well understood one can hope to make the big leap from observation to prediction; to be able to answer the question which form will be assumed under given conditions, and to eventually utilize this knowledge for the design and optimization of technological or medical devices. In the field of bionics or material engineering, for instance, smart or self-actuating materials are indeed craft based on this principle (e.g., [102, 103]).

1.2 State of research

A particular subclass of large deformation processes occurs when thin objects are spatially confined to a degree that requires them to spontaneously rearrange and self-organize in order to adapt to the altered spatial circumstances. Many living organisms dynamically pack their polymer chains, filaments or membranes inside of rigid or deformable cavities like vesicles, cell walls, chorions, and buds. Various numerical simulations—predominantly employing the discrete element method (DEM)— of folded and crumpled elastic [112, 222, 235, 236] and elasto-plastic [124, 223] sheets and membranes in shrinking containers have been carried out over the last two decades. The main finding is that thin sheets tightly crumpled into balls, although consisting mostly of air, develop a very large bulk stiffness resulting from a network of ridges and vertices of high magnitudes of mean curvature [17]. A very large portion of the bending energy is condensed into this network [15, 127].

A well-known natural instance of filament packing is the injection and subsequent coiling of long DNA strands in bacteriophage capsids and globules (e.g., [75, 104, 159, 166, 186, 205]). A similar technique called *endovascular coiling* has been harnessed by neurosurgeons to revolutionize the minimally invasive treatment of saccular cerebral aneurysms: Detachable platinum wires are fed through a microcatheter into the aneurysm to inhibit blood circulation and to initiate occlusion of the vessel [84, 85] (Fig. 1.1). High packing densities have been reported to favor a better long-term stability of the embolization [224]. Extremely dense fiber packing can also be observed for instance in hagfish, who manufacture and coil protein threads within specialized gland thread cells [61]. Albeit their morphology has recently been unraveled [239] (Fig. 1.2), the understanding of *morphogenesis*—that is, the process of shape transformation and development—remains vague.

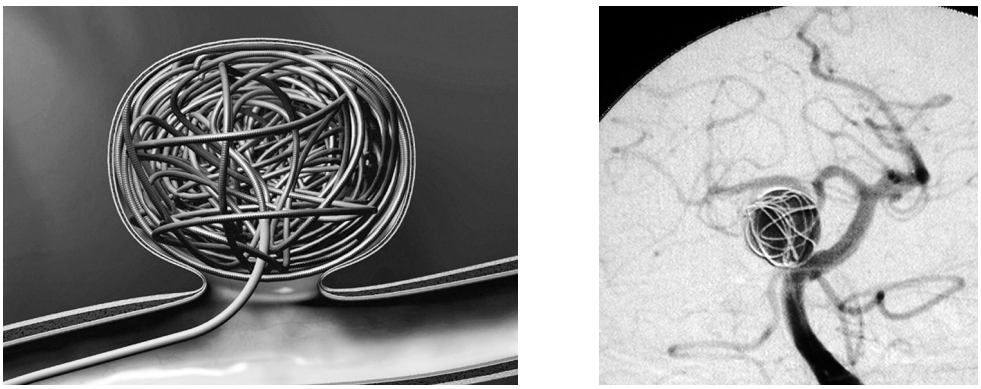

Figure 1.1: **Minimally invasive surgical treatment of saccular aneurysms.** Left: Computer animation reproduced from ref. [65] with permission of Wissenschaftsverlag der Universität Duisburg-Essen. Right: Angiogram showing an embolized aneurysm, copyright by Operation Backbone (`http://www.operationbackbone.com`).

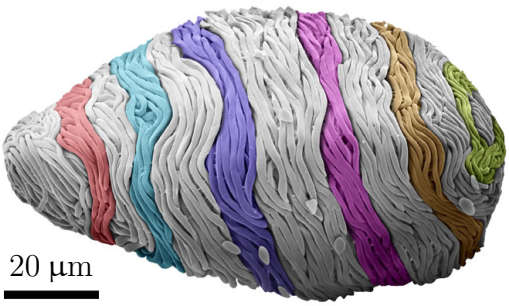

Figure 1.2: **Hagfish slime thread densely packed in a gland thread cell.** Focused ion beam scanning electron microscopy image reproduced from ref. [239] and adapted with permission of Nature Publishing Group.

Significant progress has recently been made in the understanding of two-dimensional packings of long elastic and elasto-plastic wires inside of rigid circular containers. Several experimental studies [47–50, 73] revealed how they form loop patterns and alignment between contacting segments, depending on how exactly they are injected. Subsequent numerical simulations [213] explored the corresponding morphological phase space with friction and plastic yield point as control parameters, emphasizing on the strong impact the material properties can have on the packing process. It wasn't until very recently that wire packing experiments were extended to three dimensions. Numerical and experimental studies [152, 206, 214] of the three-dimensional elastic case have unveiled two wire morphologies mainly dependent on boundary conditions and internal twist rather than the stiffness or amount of friction of the filament. Figure 1.3 shows an example of these experiments. The packing of inelastic wires on the other hand, albeit briefly occurring once [72], apparently has been widely disregarded in the literature.

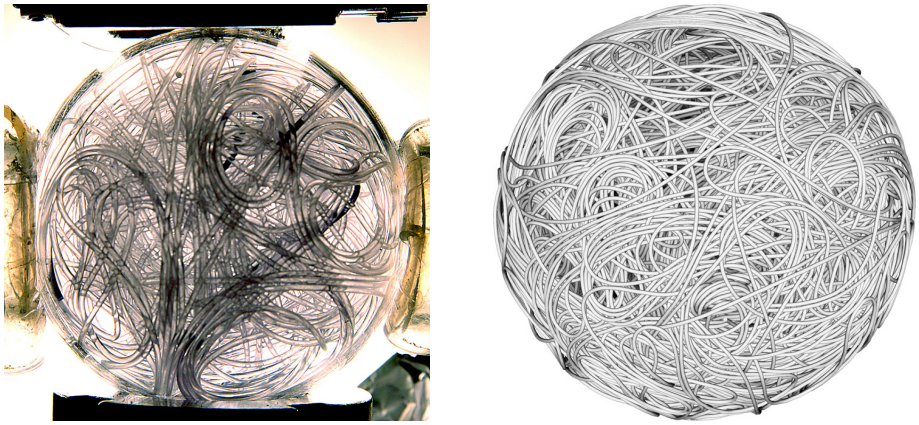

Figure 1.3: **State-of-the-art experiment of wire packing in rigid spherical cavities**, carried out by N. B. Stoop and F. K. Wittel. Left: Photography of a nylon cord fed through a small hole into a sphere held tight by four clamps. Right: X-ray computer tomography scan of a large, densely packed sphere.

A particular restriction shared by these studies is the perfect rigidity of the cavities—a constraint rarely met in Nature or biomedical applications. Detachable platinum coils used for aneurysm embolization, for example, are many orders of magnitude stiffer than the arterial walls they are fed into [209]. Microtubules confined in lipid bilayer membranes [57, 114] and erythrocytes [39, 155] as well as actin/filamin networks in vesicles [91, 123] are able to deform their weak confinements significantly. In turn, such cavities force the contained filaments to buckle, bundle and reorder if their persistence length grows large enough. A noteworthy reported observation is that lipid bilayers can drive the emergence of bundled actin filament protrusions through elastic interaction [125]. Recent experiments on coiled elastic nanowires and nanotubes encapsulated in swelling polymer shells and emulsion droplets have demonstrated how mechanical work can be stored and deployed through deformable spatial confinement [32, 33, 242]. Furthermore, Monte Carlo (MC) molecular dynamics simulations at finite temperature have shown that long fluctuating polymer chains tend to align and coil when spatially enclosed by soft vesicles [66, 139], and that the latter thus assume an obloid conformation.

Surprisingly little is known about morphogenesis due to growth or packing in flexible confinements—perhaps owing to the daunting complexity lying in the nonlinear feedback between two different deformable thin shapes when they come in contact with one another. None of the aforementioned studies provide a complete view on the space of possible shapes and configurations of such systems, even though they have clearly demonstrated how widely they are spread across the fields of natural sciences and engineering.

1.3 Purpose and objectives

The nonlinear interplay between large thin-body deformations, anisotropic or differential growth, self-contact, contact between different flexible shapes, spatial constraints or strong external forces can be too complex to handle analytically, while large-scale experiments oftentimes are time-consuming or suffer from numerous uncertainties. In such cases, one resorts to numerical methods, which additionally offer the most direct access to quantitative measurements, especially in very dense or entangled packings. Parameter studies are most conveniently carried out in computer simulations. At the core of the present thesis lies the assumption that all relevant macroscopic length scales—including the ones in in the thinness directions—are far larger than the microscopic building blocks of the considered materials, making continuum mechanics the theory to base these numerical methods on. In line with this is the additional assumption that effects of thermal fluctuations are negligible. Both of them bound the scope of application from below to the super-atomic scale.

The objective of this work is thus twofold. First, a highly efficient and robust numerical tool is developed, inherently featuring geometrically nonlinear deformations of thin shells and wires, the capability to let them grow according to arbitrary prescribed growth fields, as well as exchange of normal and tangential contact forces. The finite element method (FEM) has proven to be among the most flexible and efficient frameworks for a large number of such problems, in particular where complicated geometries, strong material nonlinearities, or anisotropy come into play. It is hence the method of choice here.

With such a powerful and versatile tool at hand, the second purpose is to explore the growth, interaction and packing of thin bodies in a quantitative manner. Starting from the recent results on sheet crumpling and filament morphogenesis in rigid spherical cavities, several open questions are addressed and answered: What are the similarities between a thin foil crumpled by hand and a blossom growing in a closed bud? How do periodic undulations and wrinkles emerge in leaves and flowers, and what controls how many of them occur? How does confinement shape influence the packing and coiling of an injected thin filament? What if the enclosing shell is flexible enough to conform to the inserted thread, and how does that alter the packing process? What are the resulting morphologies, and how can they be quantitatively characterized? Which geometrical and material parameters govern morphogenesis of slender filaments in deformable confinements?

1.4 Structure and organization

The main body of this thesis follows a structure that is divided into three parts spread over six chapters. The technical part consists of Chapters 2 and 3 and covers the theoretical foundation and efficient numerical simulation of thin elastic objects undergoing large deformation, growth and contact. In the second part that spans Chapters 4 and 5, these models are applied to a series of problems with both theoretical and practical relevance to study buckling and wrinkling in anisotropic differential growth, large growth in limited room and the packing of long filaments in deformable confinement. Special attention is paid to the interaction of thin elastic bodies on the example of filament packing in a flexible shell in Chapter 5: how they bundle, coil, fold, twist, and break symmetries. Finally, in the third part (Chapters 6 and 7), various extensions of the present work are discussed, with a focus on elasto-plastic materials and their computationally efficient implementation. In summary, the basic outline follows the path of modeling–implementation–verification–application–extension.

In Chapter 5, which is the main chapter in terms of morphological analysis, the rigid spatial constraints of previous filament packing studies are gradually relaxed from radial insertion into perfect spheres to ellipsoidal shapes and, finally, very flexible shells. A change of topology from an open elastic thread to a closed growing ring brings about a completely new set of morphologies. Along this way, a recurring phenomenon is filament alignment at low to moderate frictional forces—a type of spontaneous order that grants access to simple geometrical models approximating the observed structures and coils. Where possible, the results on morphology and energetics obtained numerically are hence compared to analytical expressions, the complete derivation of which is also given in the respective sections of Chapter 5. Moreover, the thread morphologies in elastic shells presented in this thesis are simple enough for everyone to reconstruct in table-top experiments, which is likewise shown in the same chapter.

A note on terminology is in order here for clarity. Growth as a general concept of change of volume, area or length, may also be negative, under which circumstances it is typically referred to as *shrinkage*. Here, the term *growth* is used to represent both these mutually inverse processes, including shrinkage. Furthermore, depending on the material and context, a long thin thread is sometimes termed wire, fiber, filament, string or similar, whereas a thin sheet may also be called a shell, membrane or foil. In accordance with the level of abstraction introduced in Section 1.1, these expressions are henceforth used interchangeably.

Chapter 2

Continuum description of thin elastic objects

> *[The zoologist] is deeply reluctant to compare the living with the dead, or to explain by geometry or by mechanics the things which have their part in the mystery of life.*
>
> – D'Arcy Wentworth Thompson, *On Growth and Form* (1917)

This chapter covers the quantitative description of large deformations and anisotropic growth of thin elastic bodies in the framework of classical continuum mechanics, in a way that is amenable to efficient numerical implementation in Chapter 3 for the study of growth, morphogenesis and dense packing problems. The main goals are to establish a theoretical basis for the considerations to follow in the subsequent chapters, and to introduce the various quantities and terms used throughout. At the core of the abstract continuum approach below lie the following assumptions:

- All relevant length scales of the theory are so large that the discrete building blocks of matter and natural tissue—atoms, grains, cells etc.—can be disregarded. There is thus a separation of length scales between microscopic and macroscopic, of which the former is considered absent, such that the material can be perpetually subdivided into infinitesimal pieces with conserved intrinsic properties, completely filling a closed portion of Euclidean space.
- There are no effects from thermal fluctuations (i.e., temperature is identically zero), quantum mechanics or relativity.
- All body transformations are continuous in spacetime, and thus there are no discontinuous effects due to fracture, dislocations, or other types of damage.
- All materials are considered to be free of any texture at any scale, i.e., they are homogeneous, without imperfections and micro- or mesostructure.

- Any control or active regulation by a living organism can be decoupled from the geometrical and mechanical description of the material and growth; it is dead in THOMPSON's spirit.

The result is a uniform field description of the averaged interaction between the microscopic constituents. In Chapter 3, these fields will be discretized for numerical implementation, introducing a mesoscopic length scale, the size of a finite element. The governing equations are chosen to be those of linear elasticity, as that reduces the parametric complexity to a minimum, allowing for a quantitative interpretation of thin body interaction mechanisms as they result from the most basic principles. It is assumed in the following that the reader is familiar with the fundamental concepts of continuum mechanics, linear elasticity and tensor calculus.

Compared to solving the full three-dimensional elasticity problem on a narrow volumetric domain, the slenderness of long elastic sheets and filaments offers a well-established way to save a considerable amount of computational expenses, at the cost of somewhat increased technical complexity. In *shell* and *beam theories*, the 3D elastic bulk equations are expanded in the direction(s) of small thickness, and the series is truncated at low order to yield a set of governing equations operating on two- or one-dimensional domains, termed *middle surface* and *centerline*, respectively. Under certain kinematic restrictions imposed to the material deformation in the expanded direction(s), the stresses can then be integrated over the small thickness to yield *stress resultants*, and the continuum theory is reformulated in this reduced set of variables. The KIRCHHOFF kinematic assumptions [106], which premise that straight material lines that point in a thickness direction

1. remain straight,
2. keep their length, and
3. remain perpendicular to the middle surface or centerline

under deformation, lead to a truncation at first order. When imposed in *one* thickness direction, they result in the widely used KIRCHHOFF–LOVE shell theory [106, 131], which will be employed to describe thin sheet mechanics in Section 2.1. Higher order theories such as the second-order MINDLIN–REISSNER theory [145, 181], which includes a linear transverse shear profile, are less restrictive and thus apply also to thicker shells. When imposed in both transverse directions of beams, the KIRCHHOFF assumptions induce the well-known EULER–BERNOULLI beam theory, as outlined in Section 2.2. The second-order counterpart with linear transverse shear is due to TIMOSHENKO [228, 229], and a third-order approach that accounts for the actual quadratic shear profile will be revisited in Section 3.2 for its convenient algorithmic implementation. The idea of dimensional reduction can in principle be carried on to expanding all three directions in order to express all types of thin and thick deformable bodies in one unified model that works with "elastons" [141]. This approach, however, requires high spatial resolution in discretized form and is not well suited for thin filaments with circular cross section.

2.1 Thin sheets

The adopted continuum model for thin sheets is based on the geometrically exact, nonlinear KIRCHHOFF–LOVE shell theory, expressed in the common total Lagrangian stress resultant formulation. As is standard in reduced-dimensionality solid mechanics, a purely kinematic description of deformation states is given in a first step, independent of the material considered. The kinematics are then extend by a large-strain continuum growth model that supports anisotropic differential in-plane growth fields. In the second step, a constitutive relationship between strains and stresses establishes the connection between geometry and physics.

The volumetric growth model employed here is based on the ideas of RODRIGUEZ et al. [184], which have been put on rigorous foundation [45, 133]. The basic premise is that body deformations can be due to both a growth-induced change of mass or volume, and an elastic response [92, 204], which results in a multiplicative decomposition of the deformation gradient. Since the continuum mechanical model presented in the following is a joint effort with STOOP, it has been covered in full elaboration in ref. [215], and is recapitulated here only in a condensed form for conciseness.

2.1.1 KIRCHHOFF–LOVE kinematic theory with anisotropic growth

Let $\overline{\Omega} \subset \mathbb{R}^3$ be the compact, two-dimensional, stress-free, undeformed ("reference") middle surface of a sheet with small uniform thickness h, embedded in Euclidean space. Under the action of growth or external forces, the sheet deforms into a new ("deformed") configuration with middle surface $\Omega \subset \mathbb{R}^3$. In the following, let Greek indices $\alpha, \beta, \gamma, \delta$ take values in $\{1, 2\}$, and Roman indices i, j in $\{1, 2, 3\}$. EINSTEIN's summation convention applies to repeated indices, and lower (upper) indices denote covariant (contravariant) tensorial components. Barred symbols henceforth always refer to the reference state. Moreover, let $\{\theta^1, \theta^2, \theta^3\}$ be a curvilinear coordinate system, and let $\overline{\mathbf{x}}(\theta^1, \theta^2) \in \overline{\Omega}$ and $\mathbf{x}(\theta^1, \theta^2) = \overline{\mathbf{x}}(\theta^1, \theta^2) + \mathbf{u}(\theta^1, \theta^2) \in \Omega$ be parameterizations of the respective middle surfaces, as shown in Fig. 2.1, where $\mathbf{u} = \mathbf{x} - \overline{\mathbf{x}}$ is the displacement field. The positions $\overline{\mathbf{r}} \in \mathbb{R}^3$ and $\mathbf{r} = \chi(\overline{\mathbf{r}}) \in \mathbb{R}^3$ of material points in the reference and deformed shell may be parameterized as

$$\overline{\mathbf{r}}(\theta^1, \theta^2, \theta^3) = \overline{\mathbf{x}}(\theta^1, \theta^2) + \theta^3 \overline{\mathbf{a}}_3(\theta^1, \theta^2), \tag{2.1a}$$

$$\mathbf{r}(\theta^1, \theta^2, \theta^3) = \mathbf{x}(\theta^1, \theta^2) + \theta^3 \mathbf{a}_3(\theta^1, \theta^2), \tag{2.1b}$$

where $\theta^3 \in [-h/2, h/2]$ is the through-the-thickness coordinate. χ is a diffeomorphism that maps from the reference to the deformed material positions. The local tangent space of the middle surface is spanned by the vectors

$$\overline{\mathbf{a}}_\alpha(\theta^1, \theta^2) = \overline{\mathbf{x}}_{,\alpha} := \frac{\partial \overline{\mathbf{x}}}{\partial \theta^\alpha}, \qquad \mathbf{a}_\alpha(\theta^1, \theta^2) = \mathbf{x}_{,\alpha} := \frac{\partial \mathbf{x}}{\partial \theta^\alpha}, \tag{2.2}$$

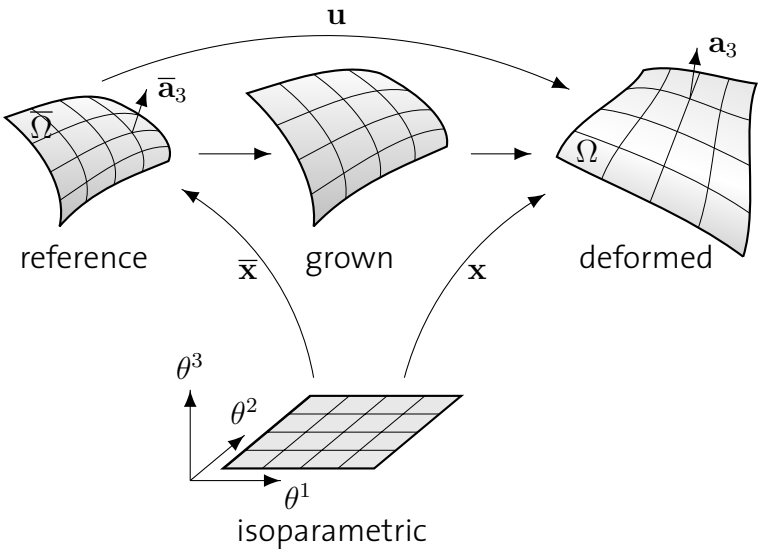

Figure 2.1: **Reference, grown and deformed configurations of the shell.** The middle surface is shown with parameterizations $\overline{\mathbf{x}}(\theta^1, \theta^2)$ for the stress-free reference state and $\mathbf{x}(\theta^1, \theta^2)$ for the deformed state, respectively.

and by virtue of the three KIRCHHOFF kinematic assumptions, the material orientation in the thickness direction of the shell is determined by the unit surface normal vectors

$$\overline{\mathbf{a}}_3 = \frac{\overline{\mathbf{a}}_1 \times \overline{\mathbf{a}}_2}{\|\overline{\mathbf{a}}_1 \times \overline{\mathbf{a}}_2\|}, \qquad \mathbf{a}_3 = \frac{\mathbf{a}_1 \times \mathbf{a}_2}{\|\mathbf{a}_1 \times \mathbf{a}_2\|}, \tag{2.3}$$

which are commonly called *shell directors*. Through the relationships $\overline{\mathbf{a}}_i \cdot \overline{\mathbf{a}}^j = \delta_i^j$ and $\mathbf{a}_i \cdot \mathbf{a}^j = \delta_i^j$, the contravariant vectors are defined. The infinitesimal reference area element can be expressed as $\mathrm{d}\overline{\Omega} = \overline{j}\ \mathrm{d}\theta^1\, \mathrm{d}\theta^2$, where $\overline{j} = \|\overline{\mathbf{a}}_1 \times \overline{\mathbf{a}}_2\|$ is the Jacobian determinant of the reference configuration. The components of the surface metric tensor, or first fundamental form, are given by

$$\overline{a}_{\alpha\beta} = \overline{\mathbf{a}}_\alpha \cdot \overline{\mathbf{a}}_\beta, \qquad a_{\alpha\beta} = \mathbf{a}_\alpha \cdot \mathbf{a}_\beta, \tag{2.4}$$

and those of the shape tensors, or second fundamental forms, by

$$\overline{b}_{\alpha\beta} = -\overline{\mathbf{a}}_{3,\alpha} \cdot \overline{\mathbf{a}}_\beta = \overline{\mathbf{a}}_3 \cdot \overline{\mathbf{a}}_{\alpha,\beta}, \qquad b_{\alpha\beta} = -\mathbf{a}_{3,\alpha} \cdot \mathbf{a}_\beta = \mathbf{a}_3 \cdot \mathbf{a}_{\alpha,\beta}. \tag{2.5}$$

The covariant basis vectors for a generic point within the shell follow as

$$\overline{\mathbf{g}}_\alpha = \frac{\partial \overline{\mathbf{r}}}{\partial \theta^\alpha} = \overline{\mathbf{a}}_\alpha + \theta^3 \overline{\mathbf{a}}_{3,\alpha}, \qquad \overline{\mathbf{g}}_3 = \frac{\partial \overline{\mathbf{r}}}{\partial \theta^3} = \overline{\mathbf{a}}_3, \tag{2.6a}$$

$$\mathbf{g}_\alpha = \frac{\partial \mathbf{r}}{\partial \theta^\alpha} = \mathbf{a}_\alpha + \theta^3 \mathbf{a}_{3,\alpha}, \qquad \mathbf{g}_3 = \frac{\partial \mathbf{r}}{\partial \theta^3} = \mathbf{a}_3, \tag{2.6b}$$

and their duals are defined by $\overline{\mathbf{g}}_i \cdot \overline{\mathbf{g}}^j = \delta_i^j$ and $\mathbf{g}_i \cdot \mathbf{g}^j = \delta_i^j$. This allows the definition of the shell metric tensors in curvilinear coordinates,

$$\overline{\boldsymbol{G}} = \overline{\mathbf{g}}_i \otimes \overline{\mathbf{g}}^j = \overline{G}_{ij}\, \overline{\mathbf{g}}^i \otimes \overline{\mathbf{g}}^j, \qquad \boldsymbol{G} = \mathbf{g}_i \otimes \mathbf{g}^j = G_{ij}\, \mathbf{g}^i \otimes \mathbf{g}^j \tag{2.7}$$

where $\overline{G}_{ij} = \overline{\mathbf{g}}_i \cdot \overline{\mathbf{g}}_j$ and $G_{ij} = \mathbf{g}_i \cdot \mathbf{g}_j$. Owing to the KIRCHHOFF constraint, equation (2.3), $\overline{G}_{33} = G_{33} = 1$ and $\overline{G}_{\alpha 3} = \overline{G}_{3\alpha} = G_{\alpha 3} = G_{3\alpha} = 0$. The geometric deformation gradient $\boldsymbol{F}$, which maps between deformed and reference metric according to $\boldsymbol{F}\overline{\mathbf{g}}_i = \mathbf{g}_i$, follows as

$$\boldsymbol{F} = \nabla\chi = \frac{\partial \mathbf{r}}{\partial \overline{\mathbf{r}}} = \frac{\partial \mathbf{r}}{\partial \theta^i}\left[\frac{\partial \overline{\mathbf{r}}}{\partial \theta^i}\right]^{-1} = \mathbf{g}_i \otimes \overline{\mathbf{g}}^i \tag{2.8}$$

In the growth model proposed by RODRIGUEZ et al. [184], the deformation gradient is multiplicatively decomposed into a growth tensor $\boldsymbol{F}_{\mathrm{g}}$, which accounts for a permanent change of volume, and a purely elastic response $\boldsymbol{F}_{\mathrm{e}}$, that ensures compatibility and continuity of the body, according to

$$\boldsymbol{F} = \boldsymbol{F}_{\mathrm{e}}\,\boldsymbol{F}_{\mathrm{g}} \tag{2.9}$$

analogous to LEE's multiplicative decomposition in elasto-plastic modeling [116]. This introduces an intermediate "grown" configuration as depicted in Fig. 2.1, with respect to which the elastic strains of the deformed state are expressed. In order not to violate the KIRCHHOFF constraints (equation (2.3)), growth is restricted to the tangent plane, such that the growth tensor can be written in matrix form as

$$\boldsymbol{F}_{\mathrm{g}} = [(F_{\mathrm{g}})_{ij}] = \begin{bmatrix} [(F_{\mathrm{g}})_{\alpha\beta}] & \mathbf{0} \\ \mathbf{0}^{\mathsf{T}} & 1 \end{bmatrix} \tag{2.10}$$

with respect to the reference basis $\{\overline{\mathbf{g}}_i\}_{i=1,2,3}$. If one requires that $\boldsymbol{F}_{\mathrm{g}}$ be independent of the deformed configuration, the GREEN–LAGRANGE strain tensor in curvilinear coordinates reads

$$\begin{aligned} \boldsymbol{E} &= \frac{1}{2}\big(\boldsymbol{F}_{\mathrm{e}}^{\mathsf{T}}\boldsymbol{F}_{\mathrm{e}} - \overline{\boldsymbol{G}}\big) \\ &= \frac{1}{2}\big(\boldsymbol{F}_{\mathrm{g}}^{-\mathsf{T}}\boldsymbol{F}^{\mathsf{T}}\boldsymbol{F}\boldsymbol{F}_{\mathrm{g}}^{-1} - \overline{\boldsymbol{G}}\big) \\ &= E_{ij}\,\overline{\mathbf{g}}^i \otimes \overline{\mathbf{g}}^j \end{aligned} \tag{2.11}$$

where the non-zero strain components are expanded in the thickness coordinate θ^3 to

$$E_{\alpha\beta} = \alpha_{\alpha\beta} + \theta^3\beta_{\alpha\beta} + \mathcal{O}((\theta^3)^2). \tag{2.12}$$

Second and higher-order terms $\mathcal{O}((\theta^3)^2)$ are neglected conforming to the definition of the shell directors in equation (2.3), making the KIRCHHOFF–LOVE theory a first order shell theory which is valid for small thickness h. The leading-order terms $\alpha_{\alpha\beta}$ and $\beta_{\alpha\beta}$ are the *membrane strains* and *bending strains* in curvilinear coordinates, which, after some tensor algebra, read

$$\alpha_{\alpha\beta} = \frac{1}{2}(\widetilde{a}_{\alpha\beta} - \overline{a}_{\alpha\beta}), \tag{2.13a}$$

$$\beta_{\alpha\beta} = \overline{b}_{\alpha\beta} - \widetilde{b}_{\alpha\beta}. \tag{2.13b}$$

where the growth-corrected first and second fundamental forms in matrix notation are given by

$$[\widetilde{a}_{\alpha\beta}] = [(F_{\mathrm{g}})_{\alpha\beta}]^{-\mathsf{T}}\,[a_{\alpha\beta}]\,[(F_{\mathrm{g}})_{\alpha\beta}]^{-1}, \tag{2.14a}$$

$$[\widetilde{b}_{\alpha\beta}] = [(F_{\mathrm{g}})_{\alpha\beta}]^{-\mathsf{T}}\,[b_{\alpha\beta}]\,[(F_{\mathrm{g}})_{\alpha\beta}]^{-1}. \tag{2.14b}$$

The strain expressions in equation (2.13) are formally identical to the strains of a KIRCHHOFF–LOVE shell without growth. Growth enters the final form only through the transformations in equation (2.14). Note also that the three in-plane growth parameters $(F_{\mathrm{g}})_{11} > 0$, $(F_{\mathrm{g}})_{22} > 0$, $(F_{\mathrm{g}})_{12} = (F_{\mathrm{g}})_{21}$, which in general may be functions of various external or internal variables such as time, space, stress etc. [3, 149], are expressed with respect to the reference tangent basis $\{\overline{\mathbf{a}}_1, \overline{\mathbf{a}}_2\}$ in the above formalism. In practice, it is thus necessary to perform a change of basis when they are to be given with respect to a specific coordinate system. Likewise, it is convenient for a number of reasons (in particular for the formulation of constitutive models, see Section 2.1.2 and Section 3.1.2), to express also the GREEN strains in an orthonormal basis of the tangent plane of the of the middle surface, rather than the curvilinear coordinate system. Denote by $\{\mathbf{e}_1, \mathbf{e}_2\}$ any such orthonormal basis. The curvilinear membrane and bending strains can then be transformed to the classical shell stretches $\varepsilon_{\alpha\beta}$ and curvatures $\kappa_{\alpha\beta}$ in the orthonormal coordinates through

$$\varepsilon_{\gamma\delta} = t_{\alpha\gamma}\,\alpha_{\alpha\beta}\,t_{\beta\delta}, \tag{2.15a}$$

$$\kappa_{\gamma\delta} = t_{\alpha\gamma}\,\beta_{\alpha\beta}\,t_{\beta\delta}, \tag{2.15b}$$

where $t_{\alpha\beta} = \overline{\mathbf{a}}^{\alpha} \cdot \mathbf{e}_{\beta}$ [52], and the in-plane growth tensor components $(F_{\mathrm{g}})_{\alpha\beta}$ are transformed accordingly.

2.1.2 Nonlinear KOITER energy functional

Assuming that the thin shell obeys the geometrically nonlinear, linearly elastic ST. VENANT–KIRCHHOFF law, the connection between its kinematics and energetics is provided by KOITER's elastic potential energy per unit surface area of the reference configuration [34, 109]

$$\begin{aligned} W &= \frac{1}{2}\int_{-h/2}^{h/2} \lambda\,\mathrm{tr}^2(\boldsymbol{E}) + 2G\,\mathrm{tr}\big(\boldsymbol{E}^2\big)\;\mathrm{d}\theta^3 \\ &= \frac{h}{2}\varepsilon_{\alpha\beta}C^{\alpha\beta\gamma\delta}\varepsilon_{\gamma\delta} + \frac{h^3}{24}\kappa_{\alpha\beta}C^{\alpha\beta\gamma\delta}\kappa_{\gamma\delta} \end{aligned} \tag{2.16}$$

where $C^{\alpha\beta\gamma\delta}$ denotes the components of the fourth-order elasticity tensor, given by

$$C^{\alpha\beta\gamma\delta} = \lambda\delta_{\alpha}^{\beta}\delta_{\gamma}^{\delta} + G\big(\delta_{\alpha}^{\gamma}\delta_{\beta}^{\delta} + \delta_{\alpha}^{\delta}\delta_{\beta}^{\gamma}\big), \tag{2.17}$$

with LAMÉ parameters

$$\lambda = \frac{E\nu}{(1+\nu)(1-2\nu)}, \qquad G = \frac{E}{2(1+\nu)}. \tag{2.18}$$

Here, E represents YOUNG's modulus and ν POISSON's ratio of the sheet. Equation (2.16) is typically transformed into the curvilinear coordinate system by writing

$$W = \frac{1}{2} K \alpha_{\alpha\beta} H^{\alpha\beta\gamma\delta} \alpha_{\gamma\delta} + \frac{1}{2} D \beta_{\alpha\beta} H^{\alpha\beta\gamma\delta} \beta_{\gamma\delta} \tag{2.19}$$

with membrane stiffness K and bending rigidity D, given by

$$K = \frac{Eh}{1-\nu^2}, \qquad D = \frac{Eh^3}{12(1-\nu^2)}. \tag{2.20}$$

$H^{\alpha\beta\gamma\delta}$ are the stripped-down components of the isotropic plane-stress elasticity tensor in curvilinear coordinates, which read

$$H^{\alpha\beta\gamma\delta} = \nu \overline{a}^{\alpha\beta} \overline{a}^{\gamma\delta} + \frac{1-\nu}{2} (\overline{a}^{\alpha\gamma} \overline{a}^{\beta\delta} + \overline{a}^{\alpha\delta} \overline{a}^{\beta\gamma}), \tag{2.21}$$

where the contravariant components of the reference surface metric tensor, $\overline{a}^{\alpha\beta}$, derive from equation (2.4) through the usual relation $\overline{a}_{\alpha\gamma} \overline{a}^{\gamma\beta} = \delta^{\beta}_{\alpha}$. The curvilinear resultant membrane stresses $n^{\alpha\beta}$ and bending stresses $m^{\alpha\beta}$ follow by the principle of work conjugacy:

$$n^{\alpha\beta} = \frac{\partial W}{\partial \alpha_{\alpha\beta}} = K H^{\alpha\beta\gamma\delta} \alpha_{\gamma\delta}, \qquad m^{\alpha\beta} = \frac{\partial W}{\partial \beta_{\alpha\beta}} = D H^{\alpha\beta\gamma\delta} \beta_{\gamma\delta}. \tag{2.22}$$

The total elastic energy U_{s} of the shell is obtained by integrating the energy density in equation (2.19) over the reference middle surface:

$$U_{\mathrm{s}} = U_{\mathrm{m}} + U_{\mathrm{b}} = \int_{\overline{\Omega}} W \, \mathrm{d}\overline{\Omega}, \tag{2.23}$$

in which U_{m} and U_{b} are the *membrane energy* and *bending energy*, respectively, given by

$$U_{\mathrm{m}} = \frac{1}{2} \int_{\overline{\Omega}} \alpha_{\alpha\beta} \, n^{\alpha\beta} \, \mathrm{d}\overline{\Omega}, \qquad U_{\mathrm{b}} = \frac{1}{2} \int_{\overline{\Omega}} \beta_{\alpha\beta} \, m^{\alpha\beta} \, \mathrm{d}\overline{\Omega}. \tag{2.24}$$

Notice that the energy density in the above form coincides with the non-Euclidean plate approach derived in ref. [56]. To complete the material characterization of the thin sheet, its total mass M_{s} is determined from its homogeneous mass density ρ as

$$M_{\mathrm{s}} = \int_{\overline{\Omega}} h\rho \, \mathrm{d}\overline{\Omega}. \tag{2.25}$$

2.2 Thin filaments

In 1859, KIRCHHOFF was the first to introduce a theory for the three-dimensional deformation modes of a thin rod [105]. His equations were justified later by LOVE [132], who showed how KIRCHHOFF's assumptions can be rationalized by a series expansion of the three-dimensional equations of elasticity in the directions of an invariant cross section. It wasn't until the COSSERAT brothers introduced the more convenient parameterization using point orientations [40], however, that the development of thin elastic filaments began to follow a more modern representation suitable for numerical implementation (see ref. [46] for a comprehensive historical review). These difficulties arose from the observation that—unlike the middle surface of thin shells—a parametric space curve alone is insufficient to describe the elastic state of a thin filament. An angle of rotation is needed to describe the orientational evolution of the cross section along the centerline. The use of a convected set of *director vectors* to describe this material point orientation is commonly attributed to the COSSERATS.

The contemporary treatment of first-order thin elastic filaments in 3D therefore consists of imposing the KIRCHHOFF kinematic assumptions on the COSSERAT brothers' director parameterization of an elastic rod. The kinematic description can be outlined in a manner that starts off analogously to KIRCHHOFF-LOVE shells, but then takes a somewhat different turn to account for the additional twisting angle, just to return to the constitutive description known from thin shells in terms of stress resultants again. While the KIRCHHOFF shell required six internal variables (three strain components for both stretching and bending), the analogous description of thin KIRCHHOFF wires needs only four degrees of freedom: uniaxial stretch, two bending curvature components, and the new variable, axial twist.

2.2.1 COSSERAT–KIRCHHOFF kinematic theory with axial growth

Let $\overline{\Gamma} \subset \mathbb{R}^3$ be the compact, one-dimensional, stress-free, undeformed ("reference") centerline of the filament, whose cross section is a circle with small uniform radius r. Under the action of growth or external forces, the filament deforms into a new ("deformed") configuration with centerline $\Gamma \subset \mathbb{R}^3$. Moreover, let $\overline{\mathbf{x}}(\theta^1) \in \overline{\Gamma}$ and $\mathbf{x}(\theta^1) = \overline{\mathbf{x}}(\theta^1) + \mathbf{u}(\theta^1) \in \Gamma$ be parameterizations of the respective centerlines, where $\mathbf{u} = \mathbf{x} - \overline{\mathbf{x}}$ denotes the displacement field. The positions $\overline{\mathbf{r}} \in \mathbb{R}^3$ and $\mathbf{r} = \chi(\overline{\mathbf{r}}) \in \mathbb{R}^3$ of material points in the reference and deformed filament may be parameterized as

$$\overline{\mathbf{r}}(\theta^1, \theta^2, \theta^3) = \overline{\mathbf{x}}(\theta^1) + \theta^2 \overline{\mathbf{a}}_2(\theta^1) + \theta^3 \overline{\mathbf{a}}_3(\theta^1), \tag{2.26a}$$

$$\mathbf{r}(\theta^1, \theta^2, \theta^3) = \mathbf{x}(\theta^1) + \theta^2 \mathbf{a}_2(\theta^1) + \theta^3 \mathbf{a}_3(\theta^1), \tag{2.26b}$$

where θ^2 and θ^3 are the through-the-thickness coordinates, subject to the constraint $(\theta^2)^2 + (\theta^3)^2 \leq r^2$. Evidently, in strong contrast to thin shells, the directors $\mathbf{a}_2$

and $\mathbf{a}_3$, which span the circular cross section, cannot be defined through the one-dimensional tangent space alone, which is in line with the intuitive notion of an additional degree of freedom that thin filaments offer: axial twist. The kinematic description is not fully established by the centerline only. In addition, an angle of rotation about the centerline is required to describe the evolution of the cross section along the space curve. The KIRCHHOFF kinematic assumptions are manifest in thin COSSERAT rods through the restriction that the three COSSERAT vectors $\{\mathbf{a}_1, \mathbf{a}_2, \mathbf{a}_3\}$, that define the material orientation, form an orthonormal basis of $\mathbb{R}^3$ and remain orthonormal under any deformation [46]. The first one is thus given by the unit tangent

$$\overline{\mathbf{a}}_1(\theta^1) = \frac{\overline{\mathbf{x}}_{,1}}{\|\overline{\mathbf{x}}_{,1}\|} = \frac{\partial \overline{\mathbf{x}}}{\partial \theta^1} \Big/ \left\| \frac{\partial \overline{\mathbf{x}}}{\partial \theta^1} \right\|, \qquad \mathbf{a}_1(\theta^1) = \frac{\mathbf{x}_{,1}}{\|\mathbf{x}_{,1}\|} = \frac{\partial \mathbf{x}}{\partial \theta^1} \Big/ \left\| \frac{\partial \mathbf{x}}{\partial \theta^1} \right\|, \tag{2.27}$$

and the third one can be chosen according to

$$\overline{\mathbf{a}}_3 = \overline{\mathbf{a}}_1 \times \overline{\mathbf{a}}_2, \qquad \mathbf{a}_3 = \mathbf{a}_1 \times \mathbf{a}_2, \tag{2.28}$$

so that $\mathbf{A} = [\mathbf{a}_1, \mathbf{a}_2, \mathbf{a}_3]$ defines a right-handed trihedron. This implicitly defines the angle of twist through the unconstrained direction of the director $\mathbf{a}_2$, with $\|\mathbf{a}_2\| = 1$. The infinitesimal reference line element can be expressed as $\mathrm{d}\overline{s} = \overline{j}\, \mathrm{d}\theta^1$, where $\overline{j} = \|\overline{\mathbf{x}}_{,1}\|$ is the Jacobian determinant of the reference configuration, and s denotes the centerline arclength. By virtue of the FRENET–SERRET formulas, there exists a vector $\mathbf{k}$ which is uniquely defined by

$$\frac{\partial \overline{\mathbf{a}}_i}{\partial \overline{s}} = \overline{\mathbf{k}} \times \overline{\mathbf{a}}_i, \qquad \frac{\partial \mathbf{a}_i}{\partial s} = \mathbf{k} \times \overline{\mathbf{a}}_i, \qquad i = 1, 2, 3, \tag{2.29}$$

for the reference and deformed configurations; it is usually referred to as the DARBOUX vector. Notice that $\mathbf{k}$ in equation (2.29) relates the derivatives $\partial \mathbf{a}_i / \partial s$ to the basis of the *reference* configuration, $\overline{\mathbf{a}}_i$, so that rigid body transformations as well as axial extension are eliminated from the difference between $\mathbf{k}$ and $\overline{\mathbf{k}}$. For notational convenience, it is useful to relate the director basis $\{\mathbf{a}_1, \mathbf{a}_2, \mathbf{a}_3\}$ to the FRENET frame consisting of the tangent vector $\mathbf{t}$, the normal vector $\mathbf{n}$ and the binormal vector $\mathbf{b}$ (see Fig. 2.2) through [143]

$$\mathbf{t} = \mathbf{a}_1, \qquad \frac{\partial \mathbf{t}}{\partial s} = \kappa \mathbf{n}, \qquad \mathbf{b} = \mathbf{t} \times \mathbf{n}, \qquad \frac{\partial \mathbf{b}}{\partial s} = -\tau \mathbf{n}, \tag{2.30}$$

where κ is the FRENET curvature along the centerline and τ is its torsion. This allows to write the DARBOUX vector explicitly in terms of the angle φ between the cross section director $\overline{\mathbf{a}}_2$ and the normal vector $\mathbf{n}$:

$$\mathbf{k} = \begin{bmatrix} k_1 \\ k_2 \\ k_3 \end{bmatrix} = \begin{bmatrix} \tau + \partial \varphi / \partial s \\ \kappa \sin \varphi \\ \kappa \cos \varphi \end{bmatrix}. \tag{2.31}$$

k_1 represents the change of twist per unit arclength, and k_2 and k_3 are the two curvature components along the centerline satisfying $\kappa^2 = k_2^2 + k_3^2$.

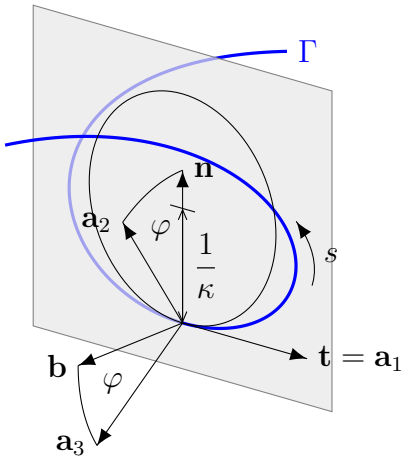

Figure 2.2: **Relationship between the COSSERAT directors and the FRENET frame.** The material orientation of a thin KIRCHHOFF filament is defined by a parametric centerline Γ (blue) and a twist angle φ, which locally represents the relative orientation of the cross section with respect to the FRENET frame of the space curve. The local FRENET curvature κ defines a touching circle with radius $1/\kappa$ that lies in the plane spanned by the tangent vector $\mathbf{t}$ and the normal vector $\mathbf{n}$ (gray).

As a direct consequence of how the directors were defined, the convected CAUCHY strain tensor components ε_{22}, ε_{33}, γ_{23} vanish identically, i.e., there is no cross-sectional deformation (stretching or shear) in the KIRCHHOFF filament. The three remaining non-zero components are found by substituting equation (2.29) in equation (2.26):

$$\begin{aligned}
[\varepsilon_{11},\, \gamma_{12},\, \gamma_{13}]^{\mathsf{T}} &= \frac{\partial \mathbf{u}}{\partial \overline{s}} + \theta^2\left(\frac{\partial \mathbf{a}_2}{\partial s} - \frac{\partial \overline{\mathbf{a}}_2}{\partial \overline{s}}\right) + \theta^3\left(\frac{\partial \mathbf{a}_3}{\partial s} - \frac{\partial \overline{\mathbf{a}}_3}{\partial \overline{s}}\right) \\
&= \frac{\partial(\mathbf{x} - \overline{\mathbf{x}})}{\partial \overline{s}} + \theta^2(\mathbf{k} \times \overline{\mathbf{a}}_2 - \overline{\mathbf{k}} \times \overline{\mathbf{a}}_2) + \theta^3(\mathbf{k} \times \overline{\mathbf{a}}_3 - \overline{\mathbf{k}} \times \overline{\mathbf{a}}_3) \\
&= \frac{\partial \mathbf{x}}{\partial \overline{s}} - \frac{\partial \overline{\mathbf{x}}}{\partial \overline{s}} + \theta^2 \boldsymbol{\vartheta} \times \overline{\mathbf{a}}_2 + \theta^3 \boldsymbol{\vartheta} \times \overline{\mathbf{a}}_3 \\
&= \begin{bmatrix} \zeta - \theta^2\vartheta_3 + \theta^3\vartheta_2 \\ -\theta^3\vartheta_1 \\ \theta^2\vartheta_1 \end{bmatrix},
\end{aligned} \tag{2.32}$$

where the short-hand notation

$$\boldsymbol{\vartheta} = \begin{bmatrix} \vartheta_1 \\ \vartheta_2 \\ \vartheta_3 \end{bmatrix} = \begin{bmatrix} k_1 - \overline{k}_1 \\ k_2 - \overline{k}_2 \\ k_3 - \overline{k}_3 \end{bmatrix} = \mathbf{k} - \overline{\mathbf{k}} \tag{2.33}$$

was used to express the change of curvatures and twist of the filament between the reference and deformed configurations, and

$$\zeta = \left\| \frac{\partial \mathbf{x}}{\partial \overline{s}} \right\| - 1 \tag{2.34}$$

denotes the axial strain due to compression or tension. In this framework, volumetric growth is trivial to incorporate. All that is needed is to redefine ζ to

$$\zeta = (F_{\mathrm{g}})_{11}^{-1} \left\| \frac{\partial \mathbf{x}}{\partial \overline{s}} \right\| - 1 \tag{2.35}$$

where $(F_{\mathrm{g}})_{11} > 0$ is the axial growth tensor component analogous to equation (2.10).

2.2.2 Three-dimensional EULER–BERNOULLI beam theory

Like the thin shell, it is assumed here that the filament obeys HOOKE's law and is characterized by an isotropic, homogeneous YOUNG's modulus E, POISSON's ratio ν, and a shear modulus of $G = E/2(1+\nu)$. The non-zero convected CAUCHY stress components hence directly follow from equation (2.32) as [245]

$$\begin{bmatrix} \sigma_{11} \\ \sigma_{12} \\ \sigma_{13} \end{bmatrix} = \begin{bmatrix} E & 0 & 0 \\ 0 & G & 0 \\ 0 & 0 & G \end{bmatrix} \begin{bmatrix} \varepsilon_{11} \\ \gamma_{12} \\ \gamma_{13} \end{bmatrix} = \begin{bmatrix} E(\zeta - \theta^2\vartheta_3 + \theta^3\vartheta_2) \\ -G\theta^3\vartheta_1 \\ G\theta^2\vartheta_1 \end{bmatrix}. \tag{2.36}$$

The stress resultants are then obtained by integrating the corresponding stress components over the cross section, yielding

$$N = \int_A \sigma_{11} \, \mathrm{d}A \qquad = EA\zeta, \tag{2.37a}$$

$$M_1 = \int_A (\theta^2\sigma_{13} - \theta^3\sigma_{12}) \, \mathrm{d}A = GJ\vartheta_1, \tag{2.37b}$$

$$M_2 = \int_A \theta^3\sigma_{11} \, \mathrm{d}A \qquad = EI\vartheta_2, \tag{2.37c}$$

$$M_3 = \int_A -\theta^2\sigma_{11} \, \mathrm{d}A \qquad = EI\vartheta_3, \tag{2.37d}$$

N is the axial force due to extension or compression along the tangent, and M_i represents the torque ($i = 1$) or bending moments ($i = 2, 3$) about the i-th basis vector. The sign convention is chosen such that positive angles induce positive moments for simplicity. For a circular cross section with radius r, the cross section area is $A = \pi r^2$, the area moment of inertia $I = \pi r^4/4$ and the polar moment of inertia $J = 2I = \pi r^4/2$. The elastic strain energy of the filament can finally be compactly expressed by

$$U_{\mathrm{f}} = U_{\mathrm{x}} + U_{\mathrm{t}} + U_{\mathrm{b}} \tag{2.38}$$

in which U_x, U_t and U_b are the *stretching energy*, *torsion energy* and *bending energy*, respectively, given by

$$U_\mathrm{x} = \frac{1}{2}\int_{\overline{\Gamma}} \zeta N \,\mathrm{d}\overline{s} \qquad = \frac{1}{2}\int_{\overline{\Gamma}} EA\zeta^2 \,\mathrm{d}\overline{s}, \tag{2.39a}$$

$$U_\mathrm{t} = \frac{1}{2}\int_{\overline{\Gamma}} \vartheta_1 M_1 \,\mathrm{d}\overline{s} \qquad = \frac{1}{2}\int_{\overline{\Gamma}} GJ\vartheta_1^2 \,\mathrm{d}\overline{s}, \tag{2.39b}$$

$$U_\mathrm{b} = \frac{1}{2}\int_{\overline{\Gamma}} \vartheta_2 M_2 + \vartheta_3 M_3 \,\mathrm{d}\overline{s} = \frac{1}{2}\int_{\overline{\Gamma}} EI\left(\vartheta_2^2 + \vartheta_3^2\right) \,\mathrm{d}\overline{s}. \tag{2.39c}$$

Notice that by setting $\vartheta_1 = \vartheta_2 = 0$, no else than the classical strain energy of an EULER–BERNOULLI beam in large uniaxial bending and compression/tension is retrieved. Analogous to the thin sheet, the material characterization is completed by noting that the filament carries a homogeneous mass density ρ, which gives rise to a total mass of

$$M_\mathrm{f} = \int_{\overline{\Gamma}} A\rho \,\mathrm{d}\overline{s}. \tag{2.40}$$

With these definitions, the theoretical foundation for the present work has been laid. In Chapter 3, a detailed description will be given of how the elastic energies of thin shells and wires can be minimized efficiently by means of the finite element method. The deformation variables and energies established in this chapter will also be referred to again in Chapters 4 to 7, where the configuration of thin bodies is to be quantified in terms of their individual degrees of freedom or energies in various growth and packing problems.

Chapter 3

Numerical implementation

> *Dreams apart, numerical precision is the very soul of science, and its attainment affords the best, perhaps the only criterion of the truth of theories and the correctness of experiments.*
>
> – D'Arcy Wentworth Thompson, *On Growth and Form* (1917)

The large deformation response of thin bodies to external loading or internal growth, be it for whatever physical cause or technical purpose, is often too complex to admit complete analytical treatment. This holds in particular when contact gives rise to completely new shapes through spatial rearrangements. Dense three-dimensional packing problems entail the additional difficulty that the inner structure is difficult to access quantitatively, which hampers experimental approaches, calling for an efficient and robust numerical tool to be applied instead. When it comes to thin shells, not many common numerical discretization techniques are fit for anisotropic growth. The DEM, or beam networks, for instance, are not well suited, as their only degree of freedom capable of accounting for in-plane growth is the edge length connecting the mesh vertices, which may not be aligned with the desired growth direction. To the FEM, on the other hand, anisotropic behavior poses no problem, since the mesh faces are numerically integrated over, regardless of their orientation. Additional advantages of the FEM include its well-known convergence properties and ability to cope with arbitrarily complicated geometries. To study the growth and packing of thin elastic sheets and filaments, as they were defined in Chapter 2, the FEM is therefore employed as the main tool here.

In this chapter, a compact account is given of how to efficiently minimize the elastic energies of said thin bodies. As their kinematic descriptions departed from one another in the previous chapter as a result of the different deformation modes they allow, also their numerical discretization follows separate pathways. Kirchhoff–Love shells are fully determined by their middle surface, such that the displacement

field $\mathbf{u} = \mathbf{x} - \overline{\mathbf{x}}$ is the only unknown to solve for. The orientation of the cross-sectional trihedron in COSSERAT–KIRCHHOFF wires, on the other hand, requires an approach that includes rotations on top of the purely translational displacement of the centerline. A unified contact model is then presented in Section 3.3 that takes volumetric exclusion as well as frictional forces into account. The latter will turn out to be pivotal in the interaction problem of flexible slender objects in Chapter 5. To trace the evolution of deformations over time, NEWTON's equations of motion are discretized in Section 3.4. In the final section of this chapter, a series of numerical test problems is worked through to verify and benchmark the numerical simulations.

It is assumed in the following that the reader is sufficiently familiar with the fundamental FEM concepts. The implementation of the finite element program has been realized with the aid of the `libMesh` C++ library [107], which provides common basic FEM functionality such as degree-of-freedom (DOF) mapping, matrix and vector assembly, numeric quadrature etc. The present work has lead to various extensions of the library. Most notably, subdivision surface shape functions were added for the representation of thin shells in version 0.9.4. The program has been parallelized with the OpenMP application programming interface [161].

3.1 Shell finite element model

Even though the KIRCHHOFF–LOVE theory provides a straightforward kinematic parameterization, numerically sound finite element implementations of thin shells have turned out to be difficult and cumbersome in the past. The KOITER energy functional in equation (2.19) represents the integral form of partial differential equations of fourth order, as it integrates the squared curvature over the shell's middle surface. For boundedness of the bending energy, this inevitably calls for twice differentiable shape functions with continuous first derivatives (C^1 continuity) across element boundaries, i.e., functions that belong to the SOBOLEV space $H^2(\overline{\Omega}, \mathbb{R})$. This requirement has posed a tough challenge in the history of shell finite elements. Higher order theories such as the MINDLIN–REISSNER shells decouple the shell director from the middle surface, thus reducing the continuity requirements, but typically suffer from numerical deficiencies such as the parasitic *shear locking*, which in turn requires explicit counter-measures to be taken. As a starting point of the extremely extensive literature on this issue, see e.g. ref. [246].

To recapitulate ref. [215], many of the developed elements introduce interpolation coefficients for higher derivatives of the displacement field, leading to a significant increase in the number of unknowns to compute. PARISCH [165] has proposed quadrilateral shell elements with only displacement variables at lateral surface nodes and an auxiliary degree of freedom on the middle surface. An entire class of quadrilateral C^1 elements is obtained from tensor products of HERMITE polynomials, see

e.g. ref. [245]. However, while simple to construct, they are restricted to regular rectangular meshes. Non-uniform rational B-splines (NURBS) were recently popularized as shape functions for use with KIRCHHOFF–LOVE shells [101], but are likewise topologically limited. The family of HSIEH–CLOUGH–TOCHER triangles have shown success in plate bending and other biharmonic problems [210], but are tedious to set up and add many additional DOFs.

These problems can be successfully overcome since CIRAK et al. have ported the subdivision surface paradigm to the FEM in 2000 [36, 38]. LOOP subdivision surfaces, being C^1-continuous everywhere and even C^2-continuous except at a finite set of extraordinary ("irregular") vertices, fully meet the continuity requirement of KIRCHHOFF–LOVE shells. However, as will be detailed in Section 3.1.3, they substantially deviate from traditional shell elements in the following respects:

- They don't *interpolate* the mesh vertices, instead they *approximate* them. That is to say, the vertices of the computational mesh don't lie in $\overline{\Omega}$.
- They gain C^1-continuity at the expense of a larger local support of the individual shape functions. The solution on a given element is determined not only by the displacements of its own nodes, but also by the displacements of the vertices of all directly neighboring elements.
- The number of shape functions required to represent an element, and consequently the surface evaluation procedure, varies with the mesh connectivity.

LOOP subdivision surface shape functions provide many advantages over traditional C^0 elements and other C^1 shape functions:

- They meet the continuity requirement imposed by the KIRCHHOFF–LOVE theory and thus permit a shell finite element description in the classical RAYLEIGH–RITZ formalism with all its amenities like straightforward implementation and optimal convergence.
- They operate on triangular elements and can thus handle arbitrary mesh topologies, even those homeomorphic to a sphere, which is difficult to impossible to achieve with alternative C^1 finite elements. This feature is of particular importance here because a closed spherical thin shell will be used to model a flexible hull for filament packing problems in Chapter 5.
- They require only three DOFs per vertex, nine per element. No rotational or auxiliary variables are needed. The computational efficiency of the subdivision shell elements is outstanding, which will be demonstrated in Section 3.5.
- One GAUSS point per element is generally sufficient for KIRCHHOFF–LOVE shells (see however Section 3.5.1).

Despite their clear superiority to C^0 elements in this regard, subdivision shell elements are accompanied by new challenges:

- The extended local support of subdivision shape functions requires new con-

cepts for boundary conditions, adaptive mesh refinement and fracture modeling [37, 79, 80, 113], which are more intricate than conventional techniques applicable to C^0 finite elements or discrete elements (e.g., [241]). The only points that is relevant for the present work is the treatment of domain boundaries, which will be addressed in Section 3.1.3.
- Contact detection on the smooth physical surface is a nonlinear optimization problem (see Section 3.3).

Details on the LOOP subdivision surface shape functions, which are employed in the following, will be given in Section 3.1.3. For the moment being, it is sufficient to bear in mind that they enable a finite element discretization in which the only unknowns are the three translational components of the displacement field $\mathbf{u} = [u,\, v,\, w]^\mathsf{T}$. The procedure outlined below has been compiled in collaboration with the author of ref. [215].

3.1.1 Finite element discretization

The total mechanical energy Π of the KIRCHHOFF–LOVE shell with total Lagrangian displacement of the middle surface, $\mathbf{u} = \mathbf{x} - \overline{\mathbf{x}}$, subject to applied distributed loads $\mathbf{q}(\theta^1, \theta^2)$ per unit surface area, takes the form

$$\Pi[\mathbf{u}] = \int_{\overline{\Omega}} h\rho\dot{\mathbf{u}} \cdot \dot{\mathbf{u}} \, \mathrm{d}\overline{\Omega} + \int_{\overline{\Omega}} W[\mathbf{u}] \, \mathrm{d}\overline{\Omega} - \int_{\overline{\Omega}} \mathbf{q} \cdot \mathbf{u} \, \mathrm{d}\overline{\Omega}. \tag{3.1}$$

where $\dot{\mathbf{u}} = \partial\mathbf{u}/\partial t$ denotes the velocity field, and W is the KOITER energy density functional of equation (2.19). Minimizing equation (3.1) is equivalent to finding a displacement field $\mathbf{u}$ satisfying the variational problem

$$\begin{aligned} 0 &= \delta\Pi[\mathbf{u}] \\ &= \int_{\overline{\Omega}} h\rho \, \delta\dot{\mathbf{u}} \cdot \dot{\mathbf{u}} \, \mathrm{d}\overline{\Omega} + \int_{\overline{\Omega}} \left(\delta\alpha_{\alpha\beta} n^{\alpha\beta} + \delta\beta_{\alpha\beta} m^{\alpha\beta}\right) \, \mathrm{d}\overline{\Omega} - \int_{\overline{\Omega}} \mathbf{q} \cdot \delta\mathbf{u} \, \mathrm{d}\overline{\Omega}. \end{aligned} \tag{3.2}$$

If the growth tensor is assumed not to depend on the displacement field, the variations of the membrane and bending strains are easily calculated by resorting to equations (2.13) and (2.14):

$$[\delta\alpha_{\alpha\beta}] = [(F_\mathrm{g})_{\alpha\beta}]^{-\mathsf{T}} \, [\delta a_{\alpha\beta}/2] \, [(F_\mathrm{g})_{\alpha\beta}]^{-1}, \tag{3.3a}$$

$$[\delta\beta_{\alpha\beta}] = [(F_\mathrm{g})_{\alpha\beta}]^{-\mathsf{T}} \, [-\delta b_{\alpha\beta}] \, [(F_\mathrm{g})_{\alpha\beta}]^{-1}. \tag{3.3b}$$

$\delta a_{\alpha\beta}/2$ and $-\delta b_{\alpha\beta}$ are the usual first strain variations for thin shells without growth, see e.g. refs. [199, 201]. Since NEWTON's equations of motion induced by equation (3.1) will be integrated explicitly in time (see Section 3.4), no second variations are needed at this point. Note, however, that the derivation of the second variations straightforwardly follows the usual formalism (e.g., [77, 201]) without complications for the growth-modified strains.

The finite element discretization is then carried out in the usual way. First, the exact minimization problem is replaced by an approximate minimization over a finite-dimensional subspace $V \subset H^2(\overline{\Omega}, \mathbb{R}^3)$ of admissible displacements:

$$\inf\{\Pi[\mathbf{u}] \mid \mathbf{u} \in H^2(\overline{\Omega}, \mathbb{R}^3)\} \quad \longrightarrow \quad \min\{\Pi[\mathbf{u}] \mid \mathbf{u} \in V\}. \tag{3.4}$$

Second, the computational domain $\overline{\Omega}$ is divided into $\mathcal{N}^{\mathrm{e}}$ finite elements indexed by $e \in \{1, \ldots, \mathcal{N}_{\mathrm{e}}\}$, and an affine finite element map

$$\Theta\colon (\theta^1, \theta^2) \mapsto (e, \xi, \eta) \tag{3.5}$$

is defined that assigns each point in the parametric domain its corresponding element e and barycentric element coordinates ξ, η. On each element e, the trial space V is spanned by a finite set of shape functions

$$\{N_I(\xi, \eta) \mid I = 1, \ldots, \mathcal{N}_e^{\mathrm{f}}\} \tag{3.6}$$

with compact local support (to be specified in Section 3.1.3), where $\mathcal{N}_e^{\mathrm{f}}$ is the number of shape functions contributing to the solution associated with element e. This setup allows the displacement field and its spatial and temporal derivatives to be written as a linear combination of the local trial space shape functions N_I:

$$\mathbf{u}(\theta^1, \theta^2) = \sum_{I=1}^{\mathcal{N}_e^{\mathrm{f}}} \mathbf{u}_I N_I(\xi, \eta), \qquad \delta\mathbf{u}(\theta^1, \theta^2) = \sum_{I=1}^{\mathcal{N}_e^{\mathrm{f}}} \delta\mathbf{u}_I N_I(\xi, \eta). \tag{3.7}$$

with $(e, \xi, \eta) = \Theta(\theta^1, \theta^2)$. By substituting the above interpolation into the weak form (equation (3.2)), and using the arbitrariness of the trial field, the variational statement is recast into an algebraic minimization problem for the nodal displacements $\mathbf{u}_I$, which are driven by nodal forces $\mathbf{f}_I$:

$$\sum_J M_{IJ}\ddot{\mathbf{u}}_J + \mathbf{f}_I^{\mathrm{int}} = \mathbf{f}_I^{\mathrm{ext}} \tag{3.8}$$

where M_{IJ} are the entries of the mass matrix, given by

$$M_{IJ} = \int_{\overline{\Omega}} h\rho N_I N_J \, \mathrm{d}\overline{\Omega}, \tag{3.9}$$

and the generalized internal and external forces read

$$\mathbf{f}_I^{\mathrm{int}} = \int_{\overline{\Omega}} \left(\frac{\partial \alpha_{\alpha\beta}}{\partial \mathbf{u}_I} n^{\alpha\beta} + \frac{\partial \beta_{\alpha\beta}}{\partial \mathbf{u}_I} m^{\alpha\beta} \right) \mathrm{d}\overline{\Omega}, \tag{3.10a}$$

$$\mathbf{f}_I^{\mathrm{ext}} = \int_{\overline{\Omega}} \mathbf{q} N_I \, \mathrm{d}\overline{\Omega}. \tag{3.10b}$$

As usual in finite element analysis, the integrals in equation (3.10)) are numerically evaluated on each element e using a quadrature rule with $\mathcal{N}_e^{\mathrm{p}}$ integration points

$$\{q_p = (\xi_p, \eta_p) \mid p = 1, \ldots, \mathcal{N}_e^{\mathrm{p}}\} \tag{3.11}$$

and corresponding weights

$$\{w_p \mid p = 1, \ldots, \mathcal{N}_e^{\mathrm{p}}\}, \tag{3.12}$$

taking advantage of the local support of the shape functions. A single element's contribution to the masses and generalized forces thus becomes

$$M_{IJ,e} = \sum_{p=1}^{\mathcal{N}_e^{\mathrm{p}}} w_p \big\{ h\rho N_I N_J \bar{j} \big\}_{e,q_p}, \tag{3.13a}$$

$$\mathbf{f}_{I,e}^{\mathrm{int}} = \sum_{p=1}^{\mathcal{N}_e^{\mathrm{p}}} w_p \left\{ \left(\frac{\partial \alpha_{\alpha\beta}}{\partial \mathbf{u}_I} n^{\alpha\beta} + \frac{\partial \beta_{\alpha\beta}}{\partial \mathbf{u}_I} m^{\alpha\beta} \right) \bar{j} \right\}_{e,q_p}, \tag{3.13b}$$

$$\mathbf{f}_{I,e}^{\mathrm{ext}} = \sum_{p=1}^{\mathcal{N}_e^{\mathrm{p}}} w_p \big\{ \mathbf{q} N_I \bar{j} \big\}_{e,q_p}. \tag{3.13c}$$

where $\{\cdot\}_{e,q_p}$ denotes evaluation of the integrand at the quadrature point q_p on element e. Explicitly, if the nodal displacement vector is written as $\mathbf{u}_I = [u_{I1},\, u_{I2},\, u_{I3}]^{\mathsf{T}}$, and $\mathbf{e}_k$ denotes the k-th canonical unit vector, the k-th components of the growth-corrected strain gradients $\partial(\cdot)/\partial \mathbf{u}_I$ in equation (3.13b), are given in terms of the shape functions by

$$\left[\frac{\partial \alpha_{\alpha\beta}}{\partial u_{Ik}} \right] = [(F_{\mathrm{g}})_{\alpha\beta}]^{-\mathsf{T}} \left[A_{\alpha\beta}^{Ik} \right] [(F_{\mathrm{g}})_{\alpha\beta}]^{-1}, \tag{3.14a}$$

$$\left[\frac{\partial \beta_{\alpha\beta}}{\partial u_{Ik}} \right] = [(F_{\mathrm{g}})_{\alpha\beta}]^{-\mathsf{T}} \left[B_{\alpha\beta}^{Ik} \right] [(F_{\mathrm{g}})_{\alpha\beta}]^{-1}. \tag{3.14b}$$

in matrix form due to equation (3.3), where [38, 77, 215]

$$A_{\alpha\beta}^{Ik} = \frac{1}{2} (N_{I,\alpha} \mathbf{a}_\beta + N_{I,\beta} \mathbf{a}_\alpha) \cdot \mathbf{e}_k, \tag{3.15a}$$

$$B_{\alpha\beta}^{Ik} = \left(\frac{1}{j} (\mathbf{a}_{\alpha,\beta} - b_{\alpha\beta}\, \mathbf{a}_3) \times (N_{I,1} \mathbf{a}_2 - N_{I,2} \mathbf{a}_1) - N_{I,\alpha\beta} \mathbf{a}_3 \right) \cdot \mathbf{e}_k, \tag{3.15b}$$

in which $j = \|\mathbf{a}_1 \times \mathbf{a}_2\|$ is the Jacobian determinant of the deformed surface. Finally, the global mass matrix and force vectors are assembled by summing over all elements and shape functions in the usual way.

The above finite element description accounts for the change of reference curvature when the surface grows. This is a noteworthy difference to numerical approaches with tethered mass-spring models, that were employed recently to simulate prescribed non-Euclidean target metrics [6, 108, 136, 138], which missed this feature.

3.1.2 Efficient VOIGT formulation

KIRCHHOFF–LOVE shells are commonly formulated and implemented using VOIGT's vector notation for convenience and efficiency, exploiting the symmetry of the involved tensors [38, 200]. The first and second fundamental forms of the reference and deformed middle surfaces from equations (2.4) and (2.5) are rewritten in vector form as

$$\overline{\boldsymbol{a}} = \begin{bmatrix} \overline{a}_{11} \\ \overline{a}_{22} \\ 2\overline{a}_{12} \end{bmatrix}, \qquad \boldsymbol{a} = \begin{bmatrix} a_{11} \\ a_{22} \\ 2a_{12} \end{bmatrix}, \qquad \overline{\boldsymbol{b}} = \begin{bmatrix} \overline{b}_{11} \\ \overline{b}_{22} \\ 2\overline{b}_{12} \end{bmatrix}, \qquad \boldsymbol{b} = \begin{bmatrix} b_{11} \\ b_{22} \\ 2b_{12} \end{bmatrix}. \tag{3.16}$$

Since the thin shell is always in a state of locally plane stress, the curvilinear strain tensors in equation (2.13) can be compactly expressed as

$$\boldsymbol{\alpha} = \begin{bmatrix} \alpha_{11} \\ \alpha_{22} \\ 2\alpha_{12} \end{bmatrix} = \frac{1}{2}\Big(\widetilde{\mathbf{G}}\boldsymbol{a} - \overline{\boldsymbol{a}}\Big), \qquad \boldsymbol{\beta} = \begin{bmatrix} \beta_{11} \\ \beta_{22} \\ 2\beta_{12} \end{bmatrix} = \overline{\boldsymbol{b}} - \widetilde{\mathbf{G}}\boldsymbol{b}. \tag{3.17}$$

where

$$\widetilde{\mathbf{G}} = \begin{bmatrix} \widetilde{g}_{11}^2 & \widetilde{g}_{21}^2 & \widetilde{g}_{11}\widetilde{g}_{21} \\ \widetilde{g}_{12}^2 & \widetilde{g}_{22}^2 & \widetilde{g}_{12}\widetilde{g}_{22} \\ 2\widetilde{g}_{11}\widetilde{g}_{12} & 2\widetilde{g}_{21}\widetilde{g}_{22} & \widetilde{g}_{11}\widetilde{g}_{22} + \widetilde{g}_{12}\widetilde{g}_{21} \end{bmatrix}, \qquad [\widetilde{g}_{\alpha\beta}] = [(F_{\mathrm{g}})_{\alpha\beta}]^{-1}, \tag{3.18}$$

is the matrix form of the inverse growth transformation in equation (2.14). The corresponding local transformation of the strains into an orthonormal basis of the tangent space $\{\mathbf{e}_1, \mathbf{e}_2\}$ (equation (2.15)) then reads

$$\boldsymbol{\varepsilon} = \begin{bmatrix} \varepsilon_{11} \\ \varepsilon_{22} \\ 2\varepsilon_{12} \end{bmatrix} = \mathbf{T}\boldsymbol{\alpha}, \qquad \boldsymbol{\kappa} = \begin{bmatrix} \kappa_{11} \\ \kappa_{22} \\ 2\kappa_{12} \end{bmatrix} = \mathbf{T}\boldsymbol{\beta} \tag{3.19}$$

with the asymmetric transformation matrix

$$\mathbf{T} = \begin{bmatrix} t_{11}^2 & t_{21}^2 & t_{11}t_{21} \\ t_{12}^2 & t_{22}^2 & t_{12}t_{22} \\ 2t_{11}t_{12} & 2t_{21}t_{22} & t_{11}t_{22} + t_{12}t_{21} \end{bmatrix}, \qquad t_{\alpha\beta} = \overline{\mathbf{a}}^{\alpha} \cdot \mathbf{e}_{\beta}, \tag{3.20}$$

analogous to equation (3.18). In this reduced representation, KOITER's energy density (equation (2.16)) is simply given by

$$\begin{aligned} W &= \frac{1}{2}\left(h\boldsymbol{\varepsilon}^{\mathsf{T}}\mathbf{C}\boldsymbol{\varepsilon} + \frac{h^3}{12}\boldsymbol{\kappa}^{\mathsf{T}}\mathbf{C}\boldsymbol{\kappa}\right) \\ &= \frac{1}{2}\big(K\boldsymbol{\alpha}^{\mathsf{T}}\mathbf{H}\boldsymbol{\alpha} + D\boldsymbol{\beta}^{\mathsf{T}}\mathbf{H}\boldsymbol{\beta}\big) \\ &= \frac{1}{2}\big(\boldsymbol{\alpha}^{\mathsf{T}}\mathbf{n} + \boldsymbol{\beta}^{\mathsf{T}}\mathbf{m}\big) \end{aligned} \tag{3.21}$$

with the rigidities K and D from equation (2.20). Here,

$$\mathbf{H} = \frac{1-\nu^2}{E}\mathbf{T}^{\mathsf{T}}\mathbf{C}\mathbf{T} \tag{3.22}$$

is the symmetric, stripped-down plane-stress constitutive matrix in curvilinear coordinates of equation (2.21) in VOIGT notation, calculated through a change of coordinates from the common form

$$\mathbf{C} = \frac{E}{1-\nu^2}\begin{bmatrix} 1 & \nu & 0 \\ \nu & 1 & 0 \\ 0 & 0 & (1-\nu)/2 \end{bmatrix}. \tag{3.23}$$

The curvilinear stress resultants in VOIGT's vector notation are defined through equation (3.21) as

$$\mathbf{n} = \begin{bmatrix} n^{11} \\ n^{22} \\ n^{12} \end{bmatrix} = K\mathbf{H}\boldsymbol{\alpha}, \qquad \mathbf{m} = \begin{bmatrix} m^{11} \\ m^{22} \\ m^{12} \end{bmatrix} = D\mathbf{H}\boldsymbol{\beta}. \tag{3.24}$$

Consequently, the contribution of element e to the generalized internal force vector (equation (3.13b)) can be rewritten and implemented in the very convenient form

$$\mathbf{f}_{I,e}^{\text{int}} = \sum_{p=1}^{\mathcal{N}_e^{\text{p}}} w_p \Big\{ \Big((\widetilde{\mathbf{G}}\mathbf{A}_I)^{\mathsf{T}}\mathbf{n} + (\widetilde{\mathbf{G}}\mathbf{B}_I)^{\mathsf{T}}\mathbf{m} \Big) \bar{j} \Big\}_{e,q_p}, \tag{3.25}$$

where the membrane and bending strain matrices $\mathbf{A}_I$ and $\mathbf{B}_I$ are given by [38]

$$\mathbf{A}_I = \begin{bmatrix} A_{11}^{I1} & A_{11}^{I2} & A_{11}^{I3} \\ A_{22}^{I1} & A_{22}^{I2} & A_{22}^{I3} \\ 2A_{12}^{I1} & 2A_{12}^{I2} & 2A_{12}^{I3} \end{bmatrix}, \qquad \mathbf{B}_I = \begin{bmatrix} B_{11}^{I1} & B_{11}^{I2} & B_{11}^{I3} \\ B_{22}^{I1} & B_{22}^{I2} & B_{22}^{I3} \\ 2B_{12}^{I1} & 2B_{12}^{I2} & 2B_{12}^{I3} \end{bmatrix}, \tag{3.26}$$

with entries from equation (3.15). Notice that ref. [38] is missing the factor 2 in the third row of $\mathbf{B}_I$.

3.1.3 LOOP subdivision surfaces

All that remains to be specified to complete the implementation are the shape functions $N_I \in H^2(\overline{\Omega}, \mathbb{R})$. LOOP subdivision surface box splines are used in this work, as they are currently the only two-dimensional, topologically unconstrained, C^1-continuous finite elements available. Subdivision surfaces were developed simultaneously by CATMULL and CLARK [26] in the context of computer graphics in 1978 as a method of representing smooth surfaces by a coarse polygonal mesh, termed the *control mesh*. CIRAK et al. have ported them to the finite element analysis of thin and thick shells [36, 38, 129]. The methodology is based on STAM's eigenanalysis [208]

of LOOP's recursive refinement rule [130] for triangulated surfaces with arbitrary topology, which gave access to a set of 12 quartic box splines, that exactly interpolate the infinitely refined surface (the *limit surface*) at all parametric points except on elements connected to mesh vertices that have a valence other than six (*irregular vertices*). Recursive subdivision of these *irregular elements* allows one to evaluate the surface and its derivatives arbitrarily close to *irregular vertices* using the same 12 basis functions (see ref. [38] for details on the algorithm). In a compact notation, they read

$$N_1(\xi,\eta) = N_4(\xi,\eta) + 2\xi^2(1-\xi) + \xi(\xi^3+\eta^3+\zeta^3)/2 + \xi\eta\zeta(5-3\xi)/2 \tag{3.27a}$$
$$N_2(\xi,\eta) = N_5(\xi,\eta) + 2\eta^2(1-\eta) + \eta(\xi^3+\eta^3+\zeta^3)/2 + \xi\eta\zeta(5-3\eta)/2 \tag{3.27b}$$
$$N_3(\xi,\eta) = N_6(\xi,\eta) + 2\zeta^2(1-\zeta) + \zeta(\xi^3+\eta^3+\zeta^3)/2 + \xi\eta\zeta(5-3\zeta)/2 \tag{3.27c}$$
$$N_4(\xi,\eta) = N_8(\xi,\eta) + N_{12}(\xi,\eta) + \eta\zeta(1-\xi)/2 \tag{3.27d}$$
$$N_5(\xi,\eta) = N_9(\xi,\eta) + N_{10}(\xi,\eta) + \xi\zeta(1-\eta)/2 \tag{3.27e}$$
$$N_6(\xi,\eta) = N_7(\xi,\eta) + N_{11}(\xi,\eta) + \xi\eta(1-\zeta)/2 \tag{3.27f}$$
$$N_7(\xi,\eta) = \xi^3(\xi+2\zeta)/12 \tag{3.27g}$$
$$N_8(\xi,\eta) = \eta^3(\eta+2\xi)/12 \tag{3.27h}$$
$$N_9(\xi,\eta) = \zeta^3(\zeta+2\eta)/12 \tag{3.27i}$$
$$N_{10}(\xi,\eta) = \xi^3(\xi+2\eta)/12 \tag{3.27j}$$
$$N_{11}(\xi,\eta) = \eta^3(\eta+2\zeta)/12 \tag{3.27k}$$
$$N_{12}(\xi,\eta) = \zeta^3(\zeta+2\xi)/12 \tag{3.27l}$$

where $\xi \geq 0$ and $\eta \geq 0$ are the natural coordinates of the standard triangle, subject to $\zeta = 1-\xi-\eta \geq 0$. They are visualized to scale in Fig. 3.1.

In fundamental difference to traditional finite elements (but much like with NURBS), the the middle surface in general locally *approximates* the mesh nodes rather than *interpolating* them ($\overline{\mathbf{x}}_I \notin \overline{\Omega}$ and $\mathbf{x}_I \notin \Omega$), as depicted in Fig. 3.2, according to

$$\overline{\mathbf{x}}(\theta^1,\theta^2) = \sum_{I=1}^{12} \overline{\mathbf{x}}_I N_I(\xi,\eta), \qquad \mathbf{x}(\theta^1,\theta^2) = \sum_{I=1}^{12} \mathbf{x}_I N_I(\xi,\eta), \tag{3.28}$$

where the finite element map notation of equation (3.5) is implied. Subdivision surfaces gain H^2 integrability at the expense of a larger local support of the shape functions. The shape of an element is determined by the nodal coordinates of all vertices belonging to the element itself or one of its direct neighbors.

A single GAUSS point per element has been found sufficient for convergence and accuracy in previous geometrically linear [38] and nonlinear shell models [36]. This apparently stems from the enhanced support of the shape functions. While classical triangular elements with quartic polynomials require at least six integration points per triangle [217], each element is integrated using only its own points. The numerical integration over subdivision surface elements, on the other hand, includes

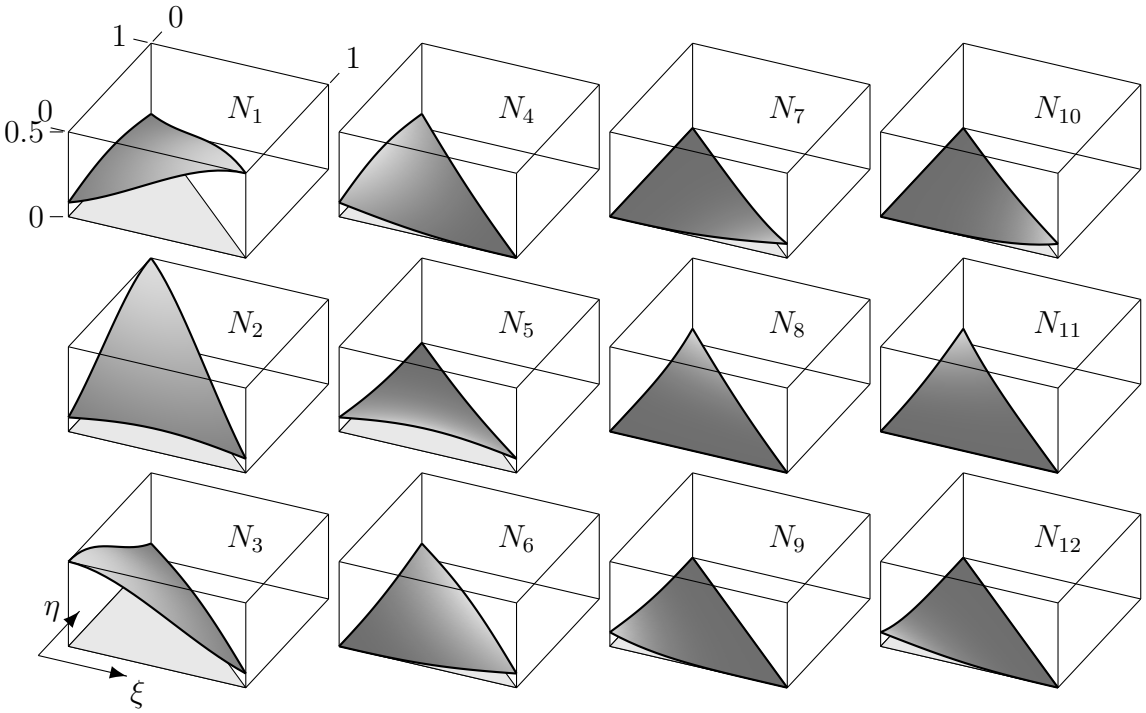

Figure 3.1: **The 12 quartic Loop subdivision surface shape functions** on the regular standard element. The numbering is identical to the node order in Fig. 3.2.

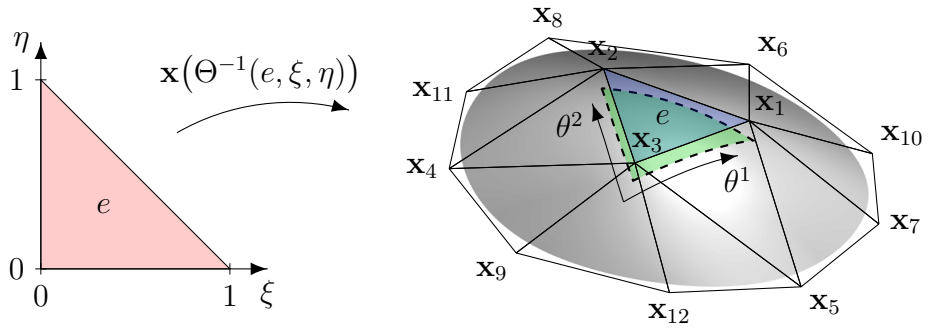

Figure 3.2: **Regular Loop subdivision patch.** The nodal coordinates map from the standard triangle (red) to the control mesh in real space (blue). The limit surface (green) of the triangular domain is obtained as a linear superposition of the 12 shape functions from equation (3.27) with the corresponding vertices $\mathbf{x}_I$ as weights, via equation (3.28).

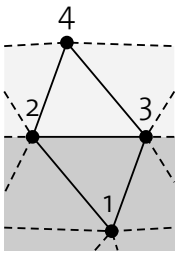

Ghost elements

Ghost node position:
$\overline{\mathbf{x}}_4 = \overline{\mathbf{x}}_2 + \overline{\mathbf{x}}_3 - \overline{\mathbf{x}}_1$

BC type	Imposed displacements
free	$\mathbf{u}_4 = \mathbf{u}_2 + \mathbf{u}_3 - \mathbf{u}_1$
pinned	$\mathbf{u}_2 = \mathbf{u}_3 = \mathbf{0}$, $\mathbf{u}_4 = -\mathbf{u}_1$
clamped	$\mathbf{u}_1 = \mathbf{u}_2 = \mathbf{u}_3 = \mathbf{u}_4 = \mathbf{0}$

Figure 3.3: **Boundary conditions of the SCHWEITZER–CIRAK type.**

all points from the element's 1-neighborhood (typically 12, except at irregular vertices), so a single point per triangle suffices to satisfy the theoretical lower bound. Indeed, no significant inaccuracies or spurious modes were found when using a one-point quadrature even in situations with extremely large deformation (see however Section 3.5.1). Of course, increasing the number of quadrature points can assist in resolving strong material inhomogeneities or differential growth.

Boundary Conditions

The treatment of domain boundaries is in general non-trivial for subdivision surface interpolation because elements along a shell boundary lack a complete 1-neighborhood and hence *per se* cannot be interpolated like elements in the interior of the domain. Three principal approaches have been proposed to solve this problem.

1. As pointed out by CIRAK et al. and BIERMANN et al. [16, 35, 38], a special subdivision rule may be applied to boundary elements, corresponding to one-dimensional subdivision on the boundary curve.
2. Alternatively, SCHWEITZER [194] suggested appending an additional row of "ghost" vertices and elements to the control mesh along its boundaries as shown in Fig. 3.3. If these ghost vertices are positioned and the displacement field is projected onto them component-wise according to CIRAK et al. [38], the usual boundary conditions can easily be imposed. This type of boundary will be referred to as the SCHWEITZER–CIRAK type in the following. However, as demonstrated by GREEN [77, 78], such boundary constraints are overly restrictive and lead to a reduction of the convergence with the number of elements from order two to one. In practice, this implies that rather fine meshes are required for high accuracy, undermining the otherwise high computational efficiency of subdivision finite elements.
3. The third approach was proposed by GREEN [77, 78] as a remedy to the limitations of the second. Instead of drastically constraining the ghost displacements according to Fig. 3.3, only the minimum set of necessary conditions is imposed directly on the limit surface. The resulting linear constraint equations can be solved using the penalty method, LAGRANGE multipliers, or any other solving

technique suitable for constrained minimization.

In summary, SCHWEITZER–CIRAK boundaries are the easiest to implement, but should be avoided in cases where high accuracy is needed with only few elements. The two alternatives are significantly more complex to implement in general, with the exception of free GREEN boundaries, where the ghost nodes are simply left unconstrained. In cases where the shell boundary is free, GREEN's convenient method is applied here. SCHWEITZER–CIRAK boundaries are used in all other situations for simplicity.

3.2 Beam finite element model

Unlike for thin surfaces, the C^1-continuity requirement imposed on the transverse displacements by the KIRCHHOFF kinematic restriction is easy to satisfy in the finite element interpolation of thin bent beams. Most naturally, this is achieved by using cubic HERMITE splines [245], and indeed, EULER–BERNOULLI beams are commonly implemented with these shape functions in finite element analysis. Pure torsion and axial extension or compression, on the other hand, are governed by second-order differential equations and hence require only piecewise linear shape functions (C^0 continuity). The computational challenge of large-deformation beams instead lies in handling the geometric nonlinearity, which exhibits considerable complexity arising from the superposition of axial twist and bidirectional bending.

Three prominent approaches have been developed, refined, mixed, and broadly applied over decades to incorporate geometric nonlinearity in beam finite elements. In the *total Lagrangian* (TL) formulation, the sought deformation fields are expressed with respect to the stress-free initial configuration, as was done in the implementation of thin shell mechanics in Section 3.1. The *updated Lagrangian* (UL) formulation, which can be shown to be effectively equivalent to the TL [195], deploys a series of intermediate states which are incrementally used as a reference. Finally, in the *corotational* (CR) formulation, a local reference frame is introduced for each element that continuously translates and rotates along with the element, within which the theory can be considered geometrically linear. The CR approach has been acclaimed for superiority over the TL and UL formulations in various regards such as accuracy, performance, simplicity and generality [13, 41, 142, 175, 225, 233], and it is utilized in the following.

3.2.1 Finite element discretization

A very convenient feature of the CR formulation is that it is sufficient to state the beam theory in its linear limit, which is addressed first here. Assuming small dis-

placements and rotations, an element's contribution to the generalized internal forces can be written in linear elasticity as the product of an element stiffness matrix $\mathbf{K}_e$ and a vector of generalized element coordinates $\mathbf{u}_e$,

$$\mathbf{f}_e^{\text{int}} = \mathbf{K}_e \mathbf{u}_e. \tag{3.29}$$

Most commonly, the global x-axis is taken as the beam reference centerline, and each mesh node n carries six degrees of freedom: three Cartesian displacements u_n, v_n, w_n in x-, y-, and z-direction, respectively, and three generalized angles φ_n, θ_n, ψ_n representing the nodal rotation about these respective axes in a way that depends on the order of the kinematic theory considered. In the first-order EULER–BERNOULLI beam theory (EBT), $\theta = -\,\mathrm{d}w/\mathrm{d}x$ and $\psi = \mathrm{d}v/\mathrm{d}x$ represent the slopes of the transverse displacements. The conventional element DOF ordering

$$\mathbf{u}_e = [\mathbf{u}_1^\mathsf{T},\, \mathbf{u}_2^\mathsf{T}] = [u_1,\, v_1,\, w_1,\, \varphi_1,\, \psi_1,\, \theta_1,\, u_2,\, v_2,\, w_2,\, \varphi_2,\, \psi_2,\, \theta_2]^\mathsf{T}, \tag{3.30}$$

is employed in the following, where the subscript $i = 1, 2$ locally refers to the element's i-th node. The six deformation fields are then interpolated across the element according to

$$v(\xi) = \sum_{I=1}^{2} v_I N_I(\xi) + \psi_I N_{I+2}(\xi), \qquad w(\xi) = \sum_{I=1}^{2} w_I N_I(\xi) + \theta_I N_{I+2}(\xi) \tag{3.31}$$

for the transverse deflections, and

$$u(\xi) = \sum_{I=1}^{2} u_I N_{I+4}(\xi), \qquad \varphi(\xi) = \sum_{I=1}^{2} \varphi_I N_{I+4}(\xi) \tag{3.32}$$

for axial displacement and torsion, where $\xi \in [0, 1]$ is the element's natural coordinate. As mentioned earlier, the four cubic HERMITE splines [245]

$$N_1(\xi) = \zeta^2(2\xi + 1) \tag{3.33a}$$
$$N_2(\xi) = \xi^2(2\zeta + 1) \tag{3.33b}$$
$$N_3(\xi) = -\xi\zeta^2 \tag{3.33c}$$
$$N_4(\xi) = \xi^2\zeta \tag{3.33d}$$

are usually used for bending, with $\zeta = 1 - \xi$. For the reader's convenience, they are plotted in Fig. 3.4. The axial variables are interpolated using the trivial C^0 basis functions

$$N_5(\xi) = \zeta, \qquad N_6(\xi) = \xi. \tag{3.34}$$

By substituting equations (3.31) and (3.32) in equations (2.37) to (2.39) with

$$\zeta = \frac{\mathrm{d}u}{\mathrm{d}x}, \qquad \vartheta_1 = \frac{\mathrm{d}\varphi}{\mathrm{d}x}, \qquad \vartheta_2 = \frac{\mathrm{d}^2 w}{\mathrm{d}x^2}, \qquad \vartheta_3 = \frac{\mathrm{d}^2 v}{\mathrm{d}x^2}, \tag{3.35}$$

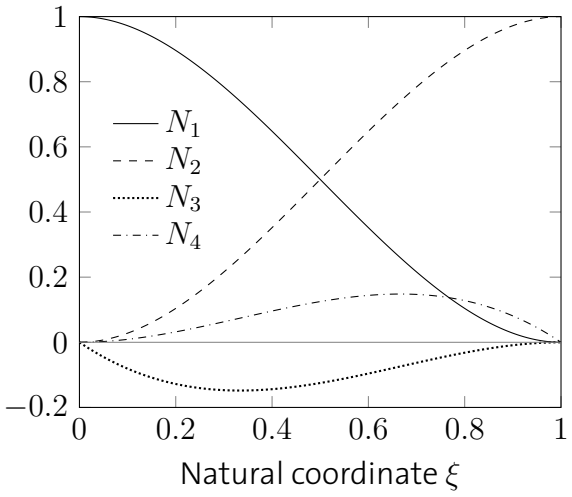

Figure 3.4: **The four cubic HERMITE shape functions** on the standard element.

carrying out the usual variation (omitted here for brevity, see e.g. ref. [245]), and integrating over the element analytically, the element stiffness matrix $\mathbf{K}_e$ can be calculated exactly.

Remarkably, in 1997 REDDY et al. [178, 180] showed that by cleverly simplifying the involved equilibrium equations of third-order beams, which include the true quadratic transverse shear profile in bending, a stiffness matrix can be derived that is technically identical to that of the first-order beams considered here so far. The governing equations of third-order beams are of sixth order in the displacement field, which they reduced to fourth order by neglecting higher-order terms. In this *simplified third-order beam theory* (henceforth termed RBT), the stiffness matrix resulting from integration over the HERMITE splines as usual accommodates those of EBT and even TIMOSHENKO beam theory [228, 229] as a special case, without suffering from shear locking [171, 226]. Adopting the DOF ordering introduced in equation (3.30), the linear three-dimensional RBT element stiffness matrix can be written as [178, 180]

$$\mathbf{K}_e = \begin{bmatrix} k_u & 0 & 0 & 0 & 0 & 0 & -k_u & 0 & 0 & 0 & 0 & 0 \\ & k_v & 0 & 0 & k_{v\psi} & 0 & 0 & -k_v & 0 & 0 & k_{v\psi} & 0 \\ & & k_w & 0 & 0 & -k_{w\theta} & 0 & 0 & -k_w & 0 & 0 & -k_{w\theta} \\ & & & k_\varphi & 0 & 0 & 0 & 0 & 0 & -k_\varphi & 0 & 0 \\ & & & & k_\psi & 0 & 0 & -k_{v\psi} & 0 & 0 & k_{\psi\psi} & 0 \\ & & & & & k_\theta & 0 & 0 & k_{w\theta} & 0 & 0 & k_{\theta\theta} \\ & & & & & & k_u & 0 & 0 & 0 & 0 & 0 \\ & & & & & & & k_v & 0 & 0 & -k_{v\psi} & 0 \\ & & \text{symm.} & & & & & & k_w & 0 & 0 & k_{w\theta} \\ & & & & & & & & & k_\varphi & 0 & 0 \\ & & & & & & & & & & k_\psi & 0 \\ & & & & & & & & & & & k_\theta \end{bmatrix} \tag{3.36}$$

with entries

$$k_w = \frac{12EI_{yy}}{\mu_{xz}a_e^3}, \qquad k_\theta = \frac{4EI_{yy}}{\mu_{xz}a_e}\lambda_{xz}, \qquad k_{w\theta} = \frac{6EI_{yy}}{\mu_{xz}a_e^2}, \qquad k_{\theta\theta} = \frac{2EI_{yy}}{\mu_{xz}a_e}\xi_{xz}, \quad (3.37)$$

$$k_v = \frac{12EI_{zz}}{\mu_{xy}a_e^3}, \qquad k_\psi = \frac{4EI_{zz}}{\mu_{xy}a_e}\lambda_{xy}, \qquad k_{v\psi} = \frac{6EI_{zz}}{\mu_{xy}a_e^2}, \qquad k_{\psi\psi} = \frac{2EI_{zz}}{\mu_{xy}a_e}\xi_{xy}, \quad (3.38)$$

$$\mu_{xz} = 1 + 12\Omega_{xz}, \qquad \lambda_{xz} = 1 + 3\Omega_{xz}, \qquad \xi_{xz} = 1 - 6\Omega_{xz}. \quad (3.39)$$

Here, $a_e = (F_\mathrm{g})_{11}\,\overline{a}_e = (F_\mathrm{g})_{11}\,\|\overline{\mathbf{x}}_2 - \overline{\mathbf{x}}_1\|$ denotes the (grown) mesh spacing, i.e., the current equilibrium length of element e. Notice that in equation (3.36) the generalized rotations in the two bending directions have opposite sign convention. Ω_{xz} is the parameter determining the order of the kinematic theory. The stiffness matrix of EBT is retrieved by setting $\Omega_{xz} = 0$, whereas in RBT,

$$\Omega_{xz} = \frac{E\Big(I_{yy}^{(2)} - 2I_{yy}^{(4)}/(3r_z^2) + I_{yy}^{(6)}/(9r_z^4)\Big)}{a_e^2 G\Big(I_{yy}^{(0)} - 2I_{yy}^{(2)}/r_z^2 + I_{yy}^{(4)}/r_z^4\Big)} \quad (3.40)$$

in which r_z is the half thickness of the beam in z direction. $I_{yy}^{(i)}$ is the i-th moment of inertia of the beam about the y-axis, calculated as

$$I_{yy}^{(i)} = \int_A z^i \,\mathrm{d}A. \quad (3.41)$$

Equations (3.39) to (3.41) hold analogously with the roles of y and z interchanged. The axial and torsional spring constants are given by

$$k_u = \frac{EA}{a_e}, \qquad k_\varphi = \frac{GJ}{a_e}, \quad (3.42)$$

where the polar moment of inertia reads $J = I_{yy} + I_{zz}$ by the perpendicular axis theorem. For a filament with circular cross-section and radius $r = r_y = r_z$, one can write $I^{(i)} = I_{yy}^{(i)} = I_{zz}^{(i)}$, which implies that

$$k_v = k_w, \quad k_\psi = k_\theta, \quad k_{v\psi} = k_{w\theta}, \quad k_{\theta\theta} = k_{\psi\psi}, \quad (3.43)$$

$$I^{(0)} = A = \pi r^2, \quad I^{(2)} = I = \frac{\pi}{4}r^4, \quad I^{(4)} = \frac{\pi}{8}r^6, \quad I^{(6)} = \frac{5\pi}{64}r^8, \quad J = 2I, \quad (3.44)$$

such that $\Omega_{xy} = \Omega_{xz} = \frac{101}{180}(1+\nu)(r/a_e)^2$ in RBT. Since this form of the element stiffness matrix offers improved physical accuracy over that of EBT without substantially altering implementation, it is used in this work.

3.2.2 Corotational quaternion formulation

The corotational formulation is rooted in in the works of WEMPNER [238], BELYTSCHKO and HSIEH [13], and ORAN [162, 163]. Its fundamental principle is based on the polar decomposition theorem, which states that any general motion can be expressed as the sum of a rigid body transformation and a pure shape deformation. Mathematically, this is reflected in a unique multiplicative decomposition of the deformation gradient into an orthogonal tensor with determinant 1 representing the change of orientation, and a symmetric positive-definite tensor to account for local straining [232]. Indeed, in Section 2.2.1, equations (2.29) and (2.32), this decomposition was implicitly carried out to derive the filament strains. The same is achieved in the CR formulation by corotating a dedicated coordinate frame with each beam element, exactly passing through its nodes, hence the name of the method. All strains are assumed to be small, allowing for the linear beam theory of Section 3.2.1 to be applied locally within the corotated coordinate system. It is for this reason that the CR approach is computationally highly competitive. The stiffness matrix in equation (3.36), which was derived by analytically integrating the shape functions over the element, holds in each corotated frame independent of rigid body motions. Therefore, no numerical quadrature is involved, and no shape function ever needs to be evaluated in a practical implementation.

In 1990, CRISFIELD [41] was the first to provide a beam-theory-independent, consistent, three-dimensional CR formulation for two-node elements with three translational and three rotational DOFs each. His method is employed here to compute the elastic forces and moments of beam elements undergoing arbitrarily large rotations. Before the CR transformation is specified further below, a few technicalities regarding the parameterization of orientation in space are in order.

Quaternion representation of the COSSERAT directors

To avoid the gimbal lock in parametric representations of large rotations using three angles, such as those of EULER, auxiliary nodal unit quaternions

$$\mathbf{q}_n = \begin{bmatrix} q_0 \\ \widetilde{\mathbf{q}} \end{bmatrix} = \begin{bmatrix} q_0 \\ q_1 \\ q_2 \\ q_3 \end{bmatrix} \in \mathbb{R}^4 \tag{3.45}$$

are used, with a scalar part q_0 and a vectorial part $\widetilde{\mathbf{q}} = [q_1,\, q_2,\, q_3]^\mathsf{T}$. Each of them defines the nodal unit trihedron $\mathbf{A}_n = [\mathbf{a}_1, \mathbf{a}_2, \mathbf{a}_3]$, which holds the COSSERAT directors

introduced in Section 2.2.1, through

$$\mathbf{A}_n = \begin{bmatrix} q_0^2+q_1^2-q_2^2-q_3^2 & 2(q_1q_2-q_0q_3) & 2(q_0q_2+q_1q_3) \\ 2(q_1q_2+q_0q_3) & q_0^2-q_1^2+q_2^2-q_3^2 & 2(q_2q_3-q_0q_1) \\ 2(q_1q_3-q_0q_2) & 2(q_0q_1+q_2q_3) & q_0^2-q_1^2-q_2^2+q_3^2 \end{bmatrix}, \tag{3.46}$$

thus specifying the nodal orientation in space. SPURRIER's algorithm [207] can be used to perform the inverse operation of equation (3.46), i.e., to convert a unit trihedron $\mathbf{A}_n = [A_{ij}]$ back to a normalized quaternion. Let

$$A_{\max} = \max\{\mathrm{tr}(\mathbf{A}_n), A_{11}, A_{22}, A_{33}\}. \tag{3.47}$$

If $A_{\max} = \mathrm{tr}(\mathbf{A}_n)$, then the quaternion components are

$$q_0 = \sqrt{1+A_{\max}}/2, \tag{3.48a}$$
$$q_i = (A_{kj}-A_{jk})/4q_0, \qquad i=1,2,3, \tag{3.48b}$$

where i,j,k are the cyclic permutation of $1,2,3$. If, on the other hand, $A_{\max} = A_{ii}$, then

$$q_i = \sqrt{A_{\max}/2+(1-\mathrm{tr}(\mathbf{A}_n))/4}, \tag{3.49a}$$
$$q_0 = (A_{kj}-A_{jk})/4q_i, \tag{3.49b}$$
$$q_l = (A_{li}+A_{il})/4q_i, \qquad l=j,k. \tag{3.49c}$$

To initialize the nodal quaternions from a set of mesh nodes $\{\overline{\mathbf{x}}_n\}$, the following procedure can be applied. For each element e, let $[d_x,\, d_y,\, d_z]^\mathsf{T} = \overline{\mathbf{x}}_2 - \overline{\mathbf{x}}_1$ denote the vector connecting its two nodes, and let $l_z = \sqrt{d_x^2+d_y^2}$. Assuming zero initial axial rotation, the direction cosine matrix

$$\overline{\mathbf{R}}_e = \begin{bmatrix} d_x/a_e & -d_y/l_z & -d_xd_z/l_za_e \\ d_y/a_e & d_x/l_z & -d_yd_z/l_za_e \\ d_z/a_e & 0 & l_z/a_e \end{bmatrix} \tag{3.50}$$

if $l_z/a_e > 0$, and

$$\overline{\mathbf{R}}_e = \begin{bmatrix} 0 & 0 & -\operatorname{sgn} d_z \\ 0 & 1 & 0 \\ \operatorname{sgn} d_z & 0 & 0 \end{bmatrix} \tag{3.51}$$

otherwise, specifies the element's orientation in space. The initial nodal trihedra $\{\overline{\mathbf{A}}_n\}$ are computed from $\{\overline{\mathbf{R}}_e\}$ in the following way. If e is the only element connected to node n (i.e., n is a boundary node), one can set $\overline{\mathbf{A}}_n = \overline{\mathbf{R}}_e$, which corresponds to zero momentum at free boundary nodes. If however two elements e_1 and e_2 meet at node n, it makes sense to use the "average" orientation of the elements as initial guess for the nodal orientation, $\overline{\mathbf{A}}_n = \widetilde{\mathbf{A}}(\overline{\mathbf{R}}_{e_2}, \overline{\mathbf{R}}_{e_2})$, as detailed below. In the simplest

case of a straight rod, all elements of the reference configuration are parallel to the global x-axis, which yields identity matrices $\overline{\mathbf{A}}_n = \mathbf{I}$ at all nodes.

The "average" orientation $\widetilde{\mathbf{A}}$ of two unit trihedra $\mathbf{A}_1$ and $\mathbf{A}_2$ can generally be approximated with the following efficient algorithm [41, 42], if the magnitude of the pseudo-vector between the two is smaller than π. Calculate the quaternion $\mathbf{q} = [q_0,\, \widetilde{\mathbf{q}}^{\mathsf{T}}]^{\mathsf{T}}$ corresponding to the differential trihedron $\mathbf{A}_2\mathbf{A}_1^{\mathsf{T}}$ using equations (3.47) to (3.49). Obtain the differential pseudo-vector

$$\boldsymbol{\omega} = [\omega_1,\, \omega_2,\, \omega_3]^{\mathsf{T}} = \frac{\widetilde{\mathbf{q}}}{q_0} \tag{3.52}$$

with magnitude $\omega = \|\boldsymbol{\omega}\|$. If $\omega < \epsilon$, where ϵ is a small numerical tolerance value, the two trihedra are identical and the procedure terminates with $\widetilde{\mathbf{A}} = \mathbf{A}_1$. Otherwise, proceed by defining the half tangent-scaled pseudo-vector

$$\widetilde{\boldsymbol{\omega}} = \tan\left[\frac{1}{2}\tan^{-1}(\omega)\right]\frac{\boldsymbol{\omega}}{\omega} \tag{3.53}$$

and rotate $\mathbf{A}_1$ by these half angles to obtain [4]

$$\widetilde{\mathbf{A}} = \mathbf{A}_1 + \frac{2}{1 + \widetilde{\boldsymbol{\omega}} \cdot \widetilde{\boldsymbol{\omega}}}\big[\mathbf{S}(\widetilde{\boldsymbol{\omega}}) + \mathbf{S}^2(\widetilde{\boldsymbol{\omega}})\big]\mathbf{A}_1, \tag{3.54}$$

where

$$\mathbf{S}(\boldsymbol{\omega}) = \begin{bmatrix} 0 & -\omega_3 & \omega_2 \\ \omega_3 & 0 & -\omega_1 \\ -\omega_2 & \omega_1 & 0 \end{bmatrix} \tag{3.55}$$

is the skew-symmetric cross product operator.

What remains to be specified is the update operation for the quaternions, to determine how the COSSERAT directors evolve as the beam deforms. From a small increment to the generalized nodal deformations in equation (3.30),

$$\boldsymbol{\Delta}\mathbf{u}_n = [\Delta u_n,\, \Delta v_n,\, \Delta w_n,\, \Delta\varphi_n,\, \Delta\psi_n,\, \Delta\theta_n]^{\mathsf{T}}, \tag{3.56}$$

the corresponding "incremental" unit quaternions

$$\boldsymbol{\Delta}\mathbf{q}_n = \begin{bmatrix}\Delta q_0 \\ \boldsymbol{\Delta}\widetilde{\mathbf{q}}\end{bmatrix} = \begin{bmatrix} \cos\frac{\Delta\varphi_n}{2}\cos\frac{\Delta\theta_n}{2}\cos\frac{\Delta\psi_n}{2} + \sin\frac{\Delta\varphi_n}{2}\sin\frac{\Delta\theta_n}{2}\sin\frac{\Delta\psi_n}{2} \\ \sin\frac{\Delta\varphi_n}{2}\cos\frac{\Delta\theta_n}{2}\cos\frac{\Delta\psi_n}{2} - \cos\frac{\Delta\varphi_n}{2}\sin\frac{\Delta\theta_n}{2}\sin\frac{\Delta\psi_n}{2} \\ \cos\frac{\Delta\varphi_n}{2}\sin\frac{\Delta\theta_n}{2}\cos\frac{\Delta\psi_n}{2} + \sin\frac{\Delta\varphi_n}{2}\cos\frac{\Delta\theta_n}{2}\sin\frac{\Delta\psi_n}{2} \\ \cos\frac{\Delta\varphi_n}{2}\cos\frac{\Delta\theta_n}{2}\sin\frac{\Delta\psi_n}{2} - \sin\frac{\Delta\varphi_n}{2}\sin\frac{\Delta\theta_n}{2}\cos\frac{\Delta\psi_n}{2} \end{bmatrix}. \tag{3.57}$$

are computed, and the quaternions are updated by applying the non-commutative HAMILTON product

$$\mathbf{q}_n \leftarrow \boldsymbol{\Delta}\mathbf{q}_n\, \mathbf{q}_n = \begin{bmatrix} \Delta q_0\, q_0 - \boldsymbol{\Delta}\widetilde{\mathbf{q}} \cdot \widetilde{\mathbf{q}} \\ \Delta q_0\, \widetilde{\mathbf{q}} + q_0\, \boldsymbol{\Delta}\widetilde{\mathbf{q}} + \boldsymbol{\Delta}\widetilde{\mathbf{q}} \times \widetilde{\mathbf{q}} \end{bmatrix}. \tag{3.58}$$

Finally, they are renormalized ($\mathbf{q}_n \leftarrow \mathbf{q}_n / \|\mathbf{q}_n\|$) after each update to avoid numerical drift away from unit length.

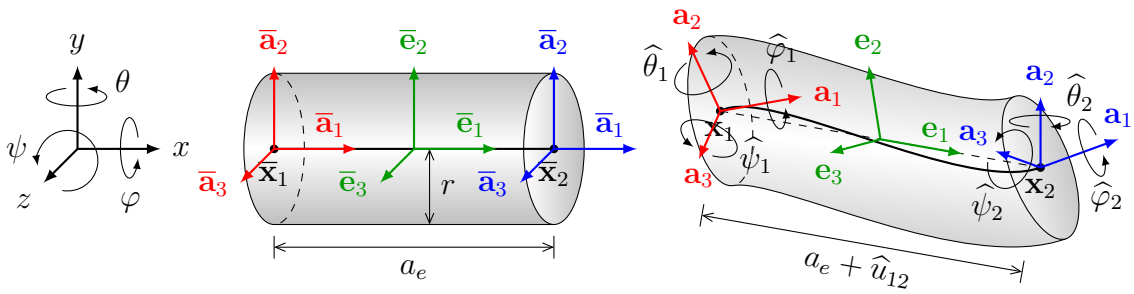

Figure 3.5: **Visualization of the corotated beam element.** In an initially straight configuration (left), each element carries canonical trihedra $\overline{\mathbf{E}}_e = \overline{\mathbf{A}}_1 = \overline{\mathbf{A}}_2 = \mathbf{I}$ (the identity matrix). After deformation (right), the seven local element DOFs (bearing a hat) are found with the help of the trihedra $\mathbf{A}_1$ (red) and $\mathbf{A}_2$ (blue) storing the nodal orientations, via the corotated element frame $\mathbf{E}_e$ (green) encoding the element orientation.

Internal force computation

With the prerequisites for large rotations established, CRISFIELD's arguments [41, 42] allow to uncouple the rigid body motion from the local, small deformation of each finite beam element e. Given the nodal unit trihedra $\mathbf{A}_1$ and $\mathbf{A}_2$ of the element's nodes, their average

$$\mathbf{R}_e = [\mathbf{r}_1,\, \mathbf{r}_2,\, \mathbf{r}_3] = \widetilde{\mathbf{A}}(\mathbf{A}_1, \mathbf{A}_2) \tag{3.59}$$

is estimated using equations (3.52) to (3.55) from the quaternion belonging to $\mathbf{A}_2\mathbf{A}_1^{\mathsf{T}}$. A *corotated frame* $\mathbf{E}_e = [\mathbf{e}_1, \mathbf{e}_2, \mathbf{e}_3]$ is then assigned to the element in the corotational formulation, in such a way that it represents its orientation in space. The first column is given by the vector connecting the two element nodes,

$$\mathbf{e}_1 = \frac{\mathbf{x}_2 - \mathbf{x}_1}{\|\mathbf{x}_2 - \mathbf{x}_1\|}. \tag{3.60}$$

The second and third vectors are obtained from rotating $\mathbf{r}_1$ onto $\mathbf{e}_1$, yielding

$$\mathbf{e}_i = \mathbf{r}_i - \frac{\mathbf{e}_1 \cdot \mathbf{r}_i}{1 + \mathbf{e}_1 \cdot \mathbf{r}_1}(\mathbf{e}_1 + \mathbf{r}_1), \qquad i = 2, 3. \tag{3.61}$$

The global element DOFs $\mathbf{u}_e$ from equation (3.30) are then expressed with respect to $\mathbf{E}_e$. In the following, all variables carrying a hat refer to this local element frame. Note that this renders the small error in $\mathbf{R}_e$, resulting from the approximation in equation (3.53) due to non-additivity of pseudo-vectors, irrelevant for physical correctness of the method. By construction of $\mathbf{e}_1$ in equation (3.60), the transverse deflections vanish identically:

$$\widehat{v}_1 = \widehat{v}_2 = \widehat{w}_1 = \widehat{w}_2 = 0. \tag{3.62}$$

Moreover, the displacement variables u_1, u_2 can be reduced to a single axial deflection $\widehat{u}_{12} = \|\mathbf{x}_2 - \mathbf{x}_1\| - a_e$. The remaining six local rotational DOFs with respect to $\mathbf{E}_e$ can

be computed as

$$\widehat{\varphi}_n = \sin^{-1}\left[\frac{1}{2}(\mathbf{a}_2 \cdot \mathbf{e}_3 - \mathbf{a}_3 \cdot \mathbf{e}_2)\right] - \widehat{\varphi}_n^{\text{int}}, \tag{3.63a}$$

$$\widehat{\psi}_n = \sin^{-1}\left[\frac{1}{2}(\mathbf{a}_1 \cdot \mathbf{e}_2 - \mathbf{a}_2 \cdot \mathbf{e}_1)\right] - \widehat{\psi}_n^{\text{int}}, \tag{3.63b}$$

$$\widehat{\theta}_n = \sin^{-1}\left[\frac{1}{2}(\mathbf{a}_1 \cdot \mathbf{e}_3 - \mathbf{a}_3 \cdot \mathbf{e}_1)\right] - \widehat{\theta}_n^{\text{int}}, \tag{3.63c}$$

for both nodes $n = 1, 2$ connected to element e, each using their respective trihedron $\mathbf{A}_n = [\mathbf{a}_1, \mathbf{a}_2, \mathbf{a}_3]$. The angles $\widehat{\varphi}^{\text{int}}$, $\widehat{\psi}^{\text{int}}$ and $\widehat{\theta}^{\text{int}}$ allow to furnish the filament with intrinsic twist or curvature, i.e., twist or curvature that remains in absence of external loads or moments. They are initialized to hold the $\sin^{-1}(\cdot)$ values of the undeformed configuration. Explicitly, local intrinsic twist of $\partial\varphi/\partial s$ and intrinsic curvature κ_y (κ_z) in the xz (xy) plane are achieved by setting

$$-\widehat{\varphi}_1^{\text{int}} = \widehat{\varphi}_2^{\text{int}} = \frac{a_e}{2}\frac{\partial\varphi}{\partial s}, \tag{3.64a}$$

$$-\widehat{\psi}_1^{\text{int}} = \widehat{\psi}_2^{\text{int}} = \frac{a_e}{2}\kappa_z, \tag{3.64b}$$

$$-\widehat{\theta}_1^{\text{int}} = \widehat{\theta}_2^{\text{int}} = \frac{a_e}{2}\kappa_y. \tag{3.64c}$$

This defines the seven local deformation DOFs

$$\widehat{\mathbf{u}}_e = [\widehat{\varphi}_1,\, \widehat{\psi}_1,\, \widehat{\theta}_1,\, \widehat{u}_{12},\, \widehat{\varphi}_2,\, \widehat{\psi}_2,\, \widehat{\theta}_2]^{\mathsf{T}} \tag{3.65}$$

from which the rigid body motion has been completely detached, and which are shown together with the trihedra in Fig. 3.5. The corresponding local element stiffness matrix $\widehat{\mathbf{K}}_e$ is easily devised from equation (3.36) using the definition of the corotated frame as

$$\widehat{\mathbf{K}}_e = \begin{bmatrix} k_\varphi & 0 & 0 & 0 & -k_\varphi & 0 & 0 \\ & k_\psi & 0 & 0 & 0 & k_{\psi\psi} & 0 \\ & & k_\theta & 0 & 0 & 0 & k_{\theta\theta} \\ & & & k_u & 0 & 0 & 0 \\ & & & & k_\varphi & 0 & 0 \\ & \text{symm.} & & & & k_\psi & 0 \\ & & & & & & k_\theta \end{bmatrix}, \tag{3.66}$$

which yields the corotated internal forces and moments through

$$\widehat{\mathbf{f}}_e^{\text{int}} = \widehat{\mathbf{K}}_e \widehat{\mathbf{u}}_e. \tag{3.67}$$

To complete the corotational formulation, an element transformation matrix $\mathbf{T}_e \in \mathbb{R}^{12\times 7}$ is required that maps the local forces and moments to the global coordinate system according to

$$\mathbf{f}_e^{\text{int}} = \mathbf{T}_e \widehat{\mathbf{f}}_e^{\text{int}} = \mathbf{T}_e \widehat{\mathbf{K}}_e \widehat{\mathbf{u}}_e. \tag{3.68}$$

In CRISFIELD's formalism, it takes the form [41, 42]

$$\mathbf{T}_e = [\mathbf{t}_1,\, \mathbf{t}_2,\, \mathbf{t}_3,\, \mathbf{t}_4,\, \mathbf{t}_5,\, \mathbf{t}_6,\, \mathbf{t}_7] \tag{3.69}$$

where

$$2\cos\widehat{\varphi}_1\mathbf{t}_1 = [\mathbf{0}^\mathsf{T},\, (\mathbf{a}_2\times\mathbf{e}_3 - \mathbf{a}_3\times\mathbf{e}_2)^\mathsf{T},\, \mathbf{0}^\mathsf{T},\, \mathbf{0}^\mathsf{T}]^\mathsf{T} + \mathbf{L}(\mathbf{r}_3)\mathbf{a}_2 - \mathbf{L}(\mathbf{r}_2)\mathbf{a}_3, \tag{3.70a}$$

$$2\cos\widehat{\psi}_1\mathbf{t}_2 = [(\mathbf{J}\mathbf{a}_2)^\mathsf{T},\, (\mathbf{a}_1\times\mathbf{e}_2 - \mathbf{a}_2\times\mathbf{e}_1)^\mathsf{T},\, -(\mathbf{J}\mathbf{a}_2)^\mathsf{T},\, \mathbf{0}^\mathsf{T}]^\mathsf{T} + \mathbf{L}(\mathbf{r}_2)\mathbf{a}_1, \tag{3.70b}$$

$$2\cos\widehat{\theta}_1\mathbf{t}_3 = [(\mathbf{J}\mathbf{a}_3)^\mathsf{T},\, (\mathbf{a}_1\times\mathbf{e}_3 - \mathbf{a}_3\times\mathbf{e}_1)^\mathsf{T},\, -(\mathbf{J}\mathbf{a}_3)^\mathsf{T},\, \mathbf{0}^\mathsf{T}]^\mathsf{T} + \mathbf{L}(\mathbf{r}_3)\mathbf{a}_1, \tag{3.70c}$$

$$\mathbf{t}_4 = [-\mathbf{e}_1^\mathsf{T},\, \mathbf{0}^\mathsf{T},\, \mathbf{e}_1^\mathsf{T},\, \mathbf{0}^\mathsf{T}]^\mathsf{T}, \tag{3.70d}$$

$$2\cos\widehat{\varphi}_2\mathbf{t}_5 = [\mathbf{0}^\mathsf{T},\, \mathbf{0}^\mathsf{T},\, \mathbf{0}^\mathsf{T},\, (\mathbf{a}_2\times\mathbf{e}_3 - \mathbf{a}_3\times\mathbf{e}_2)^\mathsf{T}]^\mathsf{T} + \mathbf{L}(\mathbf{r}_3)\mathbf{a}_2 - \mathbf{L}(\mathbf{r}_2)\mathbf{a}_3, \tag{3.70e}$$

$$2\cos\widehat{\psi}_2\mathbf{t}_6 = [(\mathbf{J}\mathbf{a}_2)^\mathsf{T},\, \mathbf{0}^\mathsf{T},\, -(\mathbf{J}\mathbf{a}_2)^\mathsf{T},\, (\mathbf{a}_2\times\mathbf{e}_3 - \mathbf{a}_3\times\mathbf{e}_2)^\mathsf{T}]^\mathsf{T} + \mathbf{L}(\mathbf{r}_2)\mathbf{a}_1, \tag{3.70f}$$

$$2\cos\widehat{\theta}_2\mathbf{t}_7 = [(\mathbf{J}\mathbf{a}_3)^\mathsf{T},\, \mathbf{0}^\mathsf{T},\, -(\mathbf{J}\mathbf{a}_3)^\mathsf{T},\, (\mathbf{a}_2\times\mathbf{e}_3 - \mathbf{a}_3\times\mathbf{e}_2)^\mathsf{T}]^\mathsf{T} + \mathbf{L}(\mathbf{r}_3)\mathbf{a}_1, \tag{3.70g}$$

with

$$\mathbf{L}^\mathsf{T} = \left[\mathbf{L}_1^\mathsf{T},\, \mathbf{L}_2^\mathsf{T},\, -\mathbf{L}_1^\mathsf{T},\, \mathbf{L}_2^\mathsf{T}\right], \tag{3.71a}$$

$$\mathbf{L}_1^\mathsf{T}(\mathbf{r}_i) = \frac{\mathbf{r}_i\cdot\mathbf{e}_1}{2}\mathbf{J} + \frac{1}{2}\mathbf{J}\mathbf{r}_i(\mathbf{e}_1+\mathbf{r}_1)^\mathsf{T}, \tag{3.71b}$$

$$\mathbf{L}_2^\mathsf{T}(\mathbf{r}_i) = \frac{1}{2}\mathbf{S}(\mathbf{r}_i) - \frac{\mathbf{r}_i\cdot\mathbf{e}_1}{4}\mathbf{S}(\mathbf{r}_1) - \frac{1}{4}\mathbf{S}(\mathbf{r}_i)\mathbf{e}_1(\mathbf{e}_1+\mathbf{r}_1)^\mathsf{T}, \tag{3.71c}$$

$$\mathbf{J} = \frac{1}{\|\mathbf{x}_2-\mathbf{x}_1\|}\left(\mathbf{I} - \mathbf{e}_1\mathbf{e}_1^\mathsf{T}\right). \tag{3.71d}$$

$\mathbf{I}$ denotes the three-dimensional identity matrix and $\mathbf{S}(\cdot)$ is the cross-product matrix defined in equation (3.55). In the transformation responsible for the first node (equations (3.70a) to (3.70c)), the first trihedron $\mathbf{A}_1 = [\mathbf{a}_1,\, \mathbf{a}_2,\, \mathbf{a}_3]$ is used, whereas equations (3.70e) to (3.70g) operate with $\mathbf{A}_2 = [\mathbf{a}_1,\, \mathbf{a}_2,\, \mathbf{a}_3]$.

The procedure outlined in equations (3.59) to (3.71) is repeated for each element, and the global internal force vector $\mathbf{f}^{\text{int}}$ is assembled from the elemental contributions in equation (3.68) as usual in the FEM. The discretization of beam masses will be covered in Section 3.4.

3.3 Contact model

A crucial feature of packing problems is mutual volumetric exclusion of the packed objects, as it geometrically constrains the room available for further deformations and rearrangements. The rigorous treatment of contact mechanics in a continuum setting dates back to the pioneering works of HERTZ published in 1882 [89]. When two non-adhesive frictionless elastic bodies come into contact, they exchange repulsive normal forces distributed over a common interface that result from a focused

stress distribution in the interior of the bodies. For the type of packing problems studied here, the local body deformations that yield this finite contact interface are of no more than subordinate importance and are hence neglected. HERTZ' considerations nevertheless allow for a consistent, physically sound treatment of elastic contacts by providing the net normal force resulting from an effective virtual depth by which the two bodies overlap.

The computational challenge lies in the efficient detection of contacting elements. It can be decomposed into two steps: First, pairs of spatially close elements need to be identified in a way that reduces the algorithmic complexity of the naive approach, $\mathcal{O}(N^2)$, where N stands for the total number of finite elements, to a bearable $\mathcal{O}(N)$. Second, the points of closest approach on the two shapes must be found to evaluate the gap function and eventually determine if their volumes indeed overlap. Since the number of element pairs in contact grows like the square of the packing density in the uncorrelated thin rod limit in 3D [167], an efficient treatment of these pairs is crucial for performance. These two purely geometrical problems are addressed in the next subsection in reverse order, subsequently followed by a description of the exchanged forces upon detected contact.

3.3.1 Contact detection

Finding the closest points of approach

Assume, for the moment being, that a valid pair of beam or shell finite elements has been identified, which potentially overlap. The remaining algorithmic challenge is to locate the points of closest approach on their respective disjunct parametric centerlines or middle surfaces, $\mathbf{c}_1 \neq \mathbf{c}_2$, from which the mutual indentation is determined by its depth

$$d = \begin{cases} h - \|\mathbf{c}_{12}\|, & \text{shell-shell contact} \\ 2r - \|\mathbf{c}_{12}\|, & \text{wire-wire contact} \\ r + h/2 - \|\mathbf{c}_{12}\|, & \text{wire-shell contact} \end{cases} \tag{3.72}$$

and direction $\mathbf{n} = \mathbf{c}_{12}/\|\mathbf{c}_{12}\|$, where $\mathbf{c}_{12} = \mathbf{c}_1 - \mathbf{c}_2$. If $d \geq 0$, the two body parts are in contact. Consider first the case where both of them are subdivision surface shell elements. $\mathbf{c}_i$, $i = 1, 2$, are found when their barycentric coordinates (ξ_i, η_i) are known, thanks to STAM who provided a direct way to evaluate the physical surface at any barycentric point on each triangle [208], even arbitrarily close to irregular nodes. On regular elements, the solution is just the shape function interpolant

$$\mathbf{c}_i(\xi_i, \eta_i) = \sum_{I=1}^{12} \mathbf{x}_I N_I(\xi_i, \eta_i), \qquad i = 1, 2 \tag{3.73}$$

with N_I from equation (3.27). Let $\boldsymbol{\xi} = [\xi_1, \eta_1, \xi_2, \eta_2]^\mathsf{T}$ for short-hand notation, and define the squared gap function

$$f(\boldsymbol{\xi}) = \|\mathbf{c}_2(\xi_2, \eta_2) - \mathbf{c}_1(\xi_1, \eta_1)\|^2. \tag{3.74}$$

The task is then to solve the following four-dimensional nonlinear optimization problem with linear inequality constraints. Find $\boldsymbol{\xi}^* = [\xi_1^*, \eta_1^*, \xi_2^*, \eta_2^*]^\mathsf{T}$ such that

$$f(\boldsymbol{\xi}^*) = \min\{f(\boldsymbol{\xi}) \mid \mathbf{A}\boldsymbol{\xi} \geq \mathbf{b}\}, \tag{3.75a}$$

$$\mathbf{A} = \begin{bmatrix} 1 & 0 & 0 & 0 \\ 0 & 1 & 0 & 0 \\ 0 & 0 & 1 & 0 \\ 0 & 0 & 0 & 1 \\ -1 & -1 & 0 & 0 \\ 0 & 0 & -1 & -1 \end{bmatrix}, \qquad \mathbf{b} = \begin{bmatrix} 0 \\ 0 \\ 0 \\ 0 \\ -1 \\ -1 \end{bmatrix}. \tag{3.75b}$$

The problem statement for wire-wire contacts follows the same lines: Let $\boldsymbol{\xi} = [\xi_1, \xi_2]^\mathsf{T}$ and

$$f(\boldsymbol{\xi}) = \|\mathbf{c}_2(\xi_2) - \mathbf{c}_1(\xi_1)\|^2. \tag{3.76}$$

To obtain the deformed element centerline in isoparametric form, the cubic HERMITE splines of equation (3.33) are stretched by the axial strain, twisted by the torsion angle, and affinely transformed to real space using the nodal positions $\mathbf{x}_1$, $\mathbf{x}_2$ and the mean element orientation $\mathbf{E}_e$ from equations (3.60) and (3.61), resulting in

$$\mathbf{c}_i(\xi_i) = \mathbf{x}_1 + \mathbf{E}_e\, \mathbf{R}_x\big([\xi_i - 1/2]\widehat{\varphi}_{12}\big) \begin{bmatrix} \xi_i \|\mathbf{x}_2 - \mathbf{x}_1\| \\ \sum_{I=1}^2 \widehat{\psi}_I N_{I+2}(\xi_i) \\ \sum_{I=1}^2 \widehat{\theta}_I N_{I+2}(\xi_i) \end{bmatrix}, \qquad i = 1, 2, \tag{3.77}$$

where $\widehat{\varphi}_{12} = \widehat{\varphi}_2 - \widehat{\varphi}_1$ denotes the change of twist angle over the element, and the twisting matrix is given by

$$\mathbf{R}_x(\varphi) = \begin{bmatrix} 1 & 0 & 0 \\ 0 & \cos\varphi & -\sin\varphi \\ 0 & \sin\varphi & \cos\varphi \end{bmatrix}. \tag{3.78}$$

The wire-wire contact problem is thus recast to finding $\boldsymbol{\xi}^* = [\xi_1^*, \xi_2^*]^\mathsf{T}$ such that

$$f(\boldsymbol{\xi}^*) = \min\{f(\boldsymbol{\xi}) \mid \mathbf{A}\boldsymbol{\xi} \geq \mathbf{b}\}, \tag{3.79a}$$

$$\mathbf{A} = \begin{bmatrix} 1 & 0 \\ 0 & 1 \\ -1 & 0 \\ 0 & -1 \end{bmatrix}, \qquad \mathbf{b} = \begin{bmatrix} 0 \\ 0 \\ -1 \\ -1 \end{bmatrix}. \tag{3.79b}$$

It is straightforward to combine equations (3.73) to (3.79) to formulate wire-shell contacts in analogous form as a nonlinear constrained optimization problem with three parameters $\boldsymbol{\xi} = [\xi_1, \xi_2, \eta_2]^\mathsf{T}$. Equations (3.75) and (3.79) can be solved with, e.g., ROSEN's projected gradient method [187], the NEWTON–RAPHSON method with penalized constraint violations [121, 122], or any other scheme dedicated to such problems. The projected gradient method has been implemented in the present work with ARMIJO inexact backtracking line search [158] for guaranteed global convergence [51], which is an important feature because the problem of locating the closest points of approach is non-convex and often discontinuous in time (see Fig. 3.6).

This solution procedure, however, proved to be too computationally costly in practice for the dense packings faced in Chapters 4 and 5. At large contact numbers, the computing time consumed for contact problems can easily take the upper hand over all other computations. A more economical approach is found by linearizing the centerlines and middle surfaces, i.e., applying collision detection on the faceted finite element meshes instead. This way, the contact points are just linearly interpolated between the element vertices according to

$$\mathbf{c}_i(\xi_i, \eta_i) = \mathbf{x}_1 + \xi_i(\mathbf{x}_2 - \mathbf{x}_1) + \eta_i(\mathbf{x}_3 - \mathbf{x}_1), \qquad i = 1, 2 \tag{3.80}$$

for thin shells and

$$\mathbf{c}_i(\xi_i) = \mathbf{x}_1 + \xi_i(\mathbf{x}_2 - \mathbf{x}_1), \qquad i = 1, 2 \tag{3.81}$$

for thin filaments. In the shell-shell case, the problem consequently boils down to evaluating the distance between all nine edge-edge pairs and six vertex-triangle pairs belonging to the two triangular shell elements in question [20]. In wire-wire contact, only a single edge-edge test is needed, whereas mixed contacts require three edge-edge checks and two vertex-triangle checks. The closest points on edge-edge pairs are calculated here using the quadric algorithm by SUNDAY [218], which provides an efficient implementation based on a note by EBERLY [54, 55], with the modification that the centerline segments are normalized to unit length to fix the faulty detection of short parallel segments in SUNDAY's algorithm. ERICSON's robust method [58] is used for the vertex-triangle pairs.

All possible types of inter-element contact are covered by this unified description, be it between parallel elements, or at any angle. It also inherently handles the cases where the contact points lie on boundary edges or nodes, in which case these boundaries are treated as rounded off like indicated in Fig. 3.7.

The linearization in equations (3.80) and (3.81) comes at the cost of artificial friction due to ratcheting [2]. Simulations have shown, however, that this discretization side effect can be reduced to a negligible amount by using reasonably fine computational meshes, while still being more computationally efficient than solving the original piecewise smooth problems in equations (3.75) and (3.79). As a compromise, one could consider to linearize the elements after adaptive local refinement of the smooth interpolated surfaces, like has been done in ref. [81].

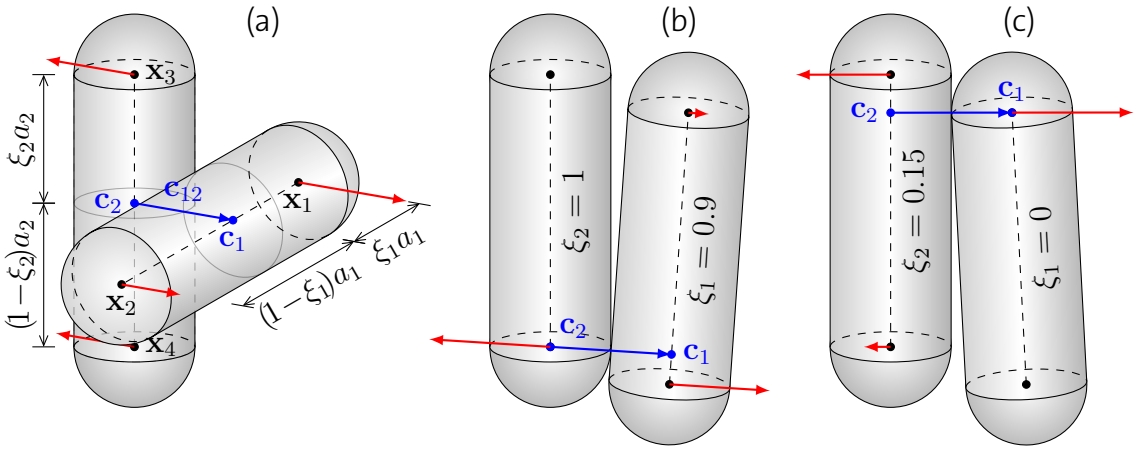

Figure 3.6: **Linearized filament-filament contact model.** All contact elements are effectively cylindrical in shape with hemispherical caps. (a) Closest points of approach (blue). The repulsion force (red) is distributed to the four involved nodes. (b,c) A small change of element displacements can cause the contact parameters ξ_1, ξ_2 to jump.

Identification of potentially contacting element pairs

A hierarchical spatial decomposition is used to identify nearby finite elements as contact pair candidates, similarly to ref. [81]. Since the procedure is essentially very akin to that utilized in the preceding work by STOOP [215], it is only briefly sketched here. The concept is based on linked cell lists, which have been a standard technique in many-body problems with short-range interactions since more than 40 years [173], for its power to reduce the computational complexity from squared to linear in the total number of elements.

On the coarsest level, all elements are placed into an array of cubic axis-aligned cells of size α, which span the whole spatial domain of interest, as follows, and as visually summarized in Fig. 3.7. Compute the axis-aligned boundary boxes (AABBs) of each element's middle surface or centerline. In each of its six Cartesian directions, extend it by the half structure thickness

$$\delta = \begin{cases} r & \text{for thin filaments} \\ h/2 & \text{for thin shells} \end{cases} \tag{3.82}$$

and additionally by a small margin $\epsilon > 0$. Store a reference to the element in each cell its AABB overlaps with. Each pair of elements sharing at least one cell and whose geodesic distance on the manifold is larger than 2δ (see ref. [215] for details) enters the mid-level check where their AABBs (without ϵ) are tested for overlap. If they do, the closest points of approach are finally computed on the finest level of the hierarchy as outlined earlier in this section. The purpose of the margin ϵ is to avoid the cost of rebuilding the linked cells after each time step. They need to be

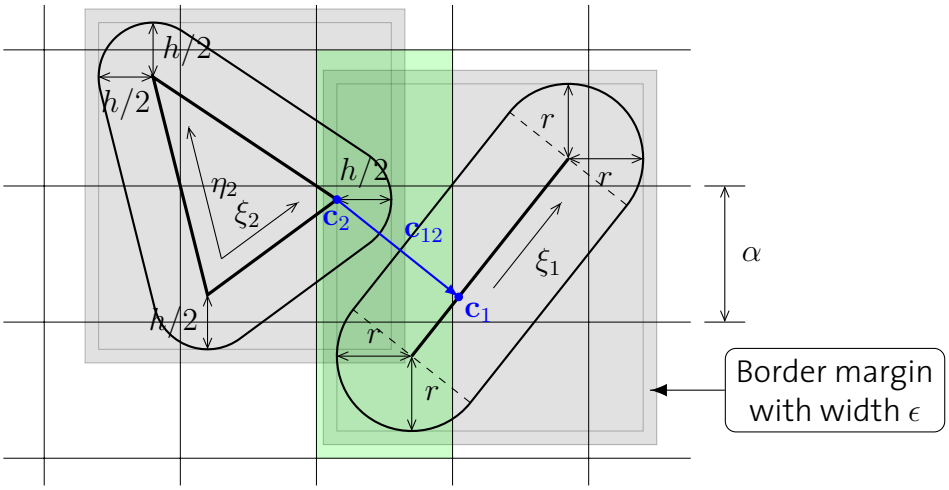

Figure 3.7: **Hierarchic contact detection** on the example of a shell and a wire element. Three cells (green) contain the extended AABBs (gray) of both elements. The AABBs are therefore tested for overlap, with positive result. In the third step, the primitive tests yield the barycentric coordinates $\xi_1^* = 0.3$, $\xi_2^* = 1$, $\eta_2^* = 0$ of the closest points of approach $\mathbf{c}_1$ and $\mathbf{c}_2$ (blue).

recomputed only when the contained objects have moved farther than ϵ. A good general choice turned out to be $\alpha = 3\overline{a}$, $\epsilon = 0.05\overline{a}$, where $\overline{a}$ represents the average edge length of the involved computational meshes.

Determining the element AABBs is easy and cheap for the linearized contact handling described above, but very non-trivial if the actual curved element shape is used. This holds in particular for irregular subdivision surface elements, where the limit surface can be evaluated only point-wise. A simple pragmatic remedy is to use the AABB of the faceted element nonetheless but extend it by an estimated maximum deformation length, at the cost of more fine-grained contact pair tests.

3.3.2 Volumetric exclusion

Once a pair of contacting elements has been found with positive indentation depth $d > 0$, normal direction $\mathbf{n}$ and the isoparametric locations $\boldsymbol{\xi}^*$ of the contact points on the respective middle surfaces or centerlines, volumetric exclusion of the two elastic bodies is weakly imposed by exchange of repulsive normals forces $f_\perp$ inspired by Hertzian theory. The exact kind of the applied force law turns out to be of negligible importance for the present packing model, in agreement with the findings in the closely related preceding project [215]. It is set to

$$f_\perp = E^* A_\mathrm{m} d/h \tag{3.83}$$

for contacts of the shell-shell type, where A_{m} is the surface area of the smaller element, and

$$f_{\perp} = E^* a_{\mathrm{m}} d\pi/4 \tag{3.84}$$

in case of wire-wire or wire-membrane contacts, in which a_{m} denotes the length of the shorter wire element. The force in Equation (3.84) is that of a Hertzian contact between two parallel cylinders [99]. E^* combines the elastic material parameters of the touching objects, (E_1, ν_1) and (E_2, ν_2), according to

$$\frac{1}{E^*} = \frac{1-\nu_1^2}{E_1} + \frac{1-\nu_2^2}{E_2}. \tag{3.85}$$

Since the normal force $f_{\perp}\mathbf{n}$ may act on any point on the element surfaces, it is linearly distributed to the involved nodal translational DOFs using the nodal weights naturally implied by the barycentric contact coordinates $\boldsymbol{\xi}^*$ (see the exemplary Fig. 3.6).

Rigid cavities

A first step in the gradual departure from previous thin object packing studies in rigid confinement with ideal spherical symmetry will be made in Chapter 5 by considering the effect of confinement asphericity. To this end, a simple model for the nodal contact between an elastic body element and the interior wall of a rigid aspherical cavity is outlined here. Although specifically carried through for general ellipsoidal containers, the basic idea applies straightforwardly for other shapes such as boxes, cylinders etc. with only minor modifications, and even easily translates to contacts with external obstacles by flipping the orientation of the rigid shape inside out.

The calculation of the shortest distance between an exact ellipsoid and a point in space is equivalent to the problem of finding the roots of a sixth order polynomial [88], for which no analytical solution is known. Thus, the exact indentation depth d can only be found numerically, which is very inconvenient. Instead, a closed-form approximation is developed here. Consider an ellipsoidal cavity, axis-aligned and centered at the spatial origin without loss of generality, defined by

$$\left(\frac{x}{R_x}\right)^2 + \left(\frac{y}{R_y}\right)^2 + \left(\frac{z}{R_z}\right)^2 = 1. \tag{3.86}$$

For reasonably shaped ellipsoids not too far away from a sphere, i.e., for $R_x \approx R_y \approx R_z \gg r, h$, a cavity contact is assumed if $\Delta \geq 0$ in the implicit formula of an *effective* ellipsoid

$$E_{\mathrm{eff}}(\mathbf{x}_n) = \left(\frac{x}{R_x-\delta}\right)^2 + \left(\frac{y}{R_y-\delta}\right)^2 + \left(\frac{z}{R_z-\delta}\right)^2 = 1+\Delta, \tag{3.87}$$

given the nodal position $\mathbf{x}_n = [x,\, y,\, z]^{\mathsf{T}} = \overline{\mathbf{x}}_n + \mathbf{u}_n$. δ is the half thickness of the thin object under consideration as defined in equation (3.82). Since the Hertzian

force outgrows the internal forces of the slender body even for small indentations d when compared to its length scales, the force *magnitude* is far less important than its *direction*. Therefore, d can legitimately be approximated using

$$(\widetilde{R} - \delta + d)^2 \approx x^2 + y^2 + z^2 \approx (\widetilde{R} - \delta)^2(1 + \Delta), \tag{3.88}$$

where $\widetilde{R} = (R_x + R_y + R_z)/3$ averages the ellipsoidal radii. Taking the square root yields the sought approximation for d as a function of the surface isovalue $1 + \Delta$:

$$d \approx (\widetilde{R} - \delta)\Big(\sqrt{1 + \Delta} - 1\Big). \tag{3.89}$$

A consistent approximation of the outer surface normal vector $\mathbf{n}$ assuming that $\Delta \ll 1$ is found by normalizing the gradient of the effective ellipsoid:

$$\mathbf{n} \approx \frac{\nabla E_{\text{eff}}(\mathbf{x}_n)}{\|\nabla E_{\text{eff}}(\mathbf{x}_n)\|} =: \frac{\widetilde{\mathbf{x}}_n}{\|\widetilde{\mathbf{x}}_n\|}. \tag{3.90}$$

The effective direction $\widetilde{\mathbf{x}}_n$ can be compactly written as $\widetilde{\mathbf{x}}_n = 2\,\mathbf{R}^{-2}\mathbf{x}_n$ with a 3×3 diagonal matrix

$$\mathbf{R} = \operatorname{diag}(R_x - \delta, R_y - \delta, R_z - \delta). \tag{3.91}$$

The impact of the approximations in equations (3.89) and (3.90) is twofold. First, the magnitude of the Hertzian contact force is subject to an error that grows with the disparity of R_x, R_y, R_z. Since the Hertzian contact model used here is itself only a crude approximation, this has no negative consequence in practice. The sole purpose is to keep the packed body inside the confining container. Second, the effective ellipsoid has slightly deformed aspect ratios compared to the desired cavity. This defect is also minor for $R_x \approx R_y \approx R_z$ and vanishes for arbitrary R_x, R_y, R_z in the slender body limit $\delta/\widetilde{R} \to 0$. All approximations above become exact under spherical symmetry ($R_x = R_y = R_z$).

In the event that the sphere with radius δ around a node n indents the cavity wall by a depth $d > 0$ in direction of $\mathbf{n}$ as computed above, the normal force $-f_\perp \mathbf{n}$ is applied to the three translational DOFs of the penetrating node. The force modulus $f_\perp$ is calculated from equations (3.83) and (3.84) with the modification that A_{m} stands for the mean surface area of all shell elements connected to node n, while a_{m} analogously denotes the mean adjacent wire edge length. For the calculation of E^* in equation (3.85), the elastic properties of the fixed wall are set to $(E_2, \nu_2) = (\infty, 0)$. Alternative models such as the Hertzian force between a sphere and a half-space, where the force is not linearly proportional to d, may be used instead if desired.

3.3.3 COULOMB friction

Many practical materials resist tangential sliding by exchange of frictional forces—even DNA does so [69, 110, 164]. To arrive at a simple macroscopic model of dry

friction that includes the stick-slip phenomenon but at the same time retains low parametric dimensionality, COULOMB's law is assumed between any two contacting surfaces, in accordance with a suggestion for condensed DNA [159]. Sophisticated computational models for the frictional contact between two wire segments and between a wire and a surface are available in the literature [156, 243]. They include the exchange of angular momentum resulting from the tangential contact force components, at the cost of enormous modeling complexity. Here, a simplified model is employed that reduces the action of tangential contact forces to the translational displacement field, neglecting bending moments and torques on the filament. This is justified by the fact that in dense packing problems, twist and bending angles are strongly constrained at both ends of contacting wire segments through their geometrical coupling with the translational DOFs, which in turn are highly confined by normal contact forces. Thus, if all simulations are carried out close to the static equilibrium, frictional forces will be mediated to the rotational filament variables indirectly via the translational ones with sufficient accuracy.

COULOMB's friction model bounds the tangential forces $f_\parallel$ proportionally to the normal ones according to $f_\parallel \leq \mu f_\perp$. For a broad class of materials, the isotropic friction coefficient $\mu \geq 0$ takes a marginally larger value when the contacting bodies are at relative rest than when they slide [62], giving rise to the stick-slip phenomenon. The coefficients of *static* and *dynamic* friction are henceforth denoted by μ_s and μ_d, respectively. The model is implemented for all types of contact mentioned earlier, following the efficient element-by-element approach proposed by MARGOLIS [140], which goes as follows. Given $f_\perp$ and $\mathbf{n}$ of a detected contact, as well as the velocity vector of the second element with respect to the Lagrangian frame of the first, $\mathbf{v}_{12} = \mathbf{v}_2 - \mathbf{v}_1$, compute the relative tangential velocity $\mathbf{v}_\mathrm{t} = \mathbf{v}_{12} - (\mathbf{v}_{12} \cdot \mathbf{n})\mathbf{n}$. If $\|\mathbf{v}_\mathrm{t}\| \geq v_\mathrm{s}$, where $v_\mathrm{s} > 0$ is a small predefined constant speed below which the bodies are considered to be at rest, dynamic friction is applied by adding the tangential force

$$\mathbf{f}_\mathrm{t} = -\mu_\mathrm{d} f_\perp \frac{\mathbf{v}_\mathrm{t}}{\|\mathbf{v}_\mathrm{t}\| + v_\epsilon}. \tag{3.92}$$

$v_\epsilon > 0$ is a small tolerance speed to avoid the singularity in the direction vector at rest, and is set to $v_\epsilon = 10^{-8} v_\mathrm{s}$ here. If $\|\mathbf{v}_\mathrm{t}\| < v_\mathrm{s}$ on the other hand, static friction is imposed by coupling the two bodies with an auxiliary viscoelastic spring made of a KELVIN–VOIGT material with stiffness k and dynamic viscosity η. A convenient choice for the spring parameters is $k = \delta E^*$, $\eta = \tau E^*$, where δ is the characteristic structural thickness from equation (3.82), and τ is a short viscous time scale to damp high-frequency oscillations. This then yields the tangential force

$$\mathbf{f}_\mathrm{t} = -k\mathbf{u}_\mathrm{s} - \tau k \mathbf{v}_\mathrm{t}. \tag{3.93}$$

For a smooth transition from the dynamic to the static case, the spring deflection vector $\mathbf{u}_\mathrm{s}$ is initialized such that equations (3.92) and (3.93) are balanced, resulting in

$$\mathbf{u}_\mathrm{s} = \left(\frac{\mu_\mathrm{d} f_\perp}{k(\|\mathbf{v}_\mathrm{t}\| + v_\epsilon)} - \tau \right) \mathbf{v}_\mathrm{t}. \tag{3.94}$$

As soon as the elastic spring force violates COULOMB's law, $f_{\parallel} = \|\mathbf{f}_{\mathrm{t}}\| > \mu_{\mathrm{s}} f_{\perp}$, the static spring is removed and dynamic friction is applied according to equation (3.92). Likewise, the spring is removed upon separation of the elements. To avoid accidental loss of the static friction spring when the indentation depth numerically oscillates about zero without actual separation of the two bodies, a tolerated separation is used below which the spring is maintained anyway. A tolerance of 0.1δ proved to work well in all simulated settings. Finally, all normal forces mentioned in Section 3.3.2 are augmented by the same viscous dashpot as the auxiliary spring so as to diminish high-frequency oscillations also in normal direction.

3.4 Time integration

NEWTON's hyperbolic nonlinear equations of motion

$$\mathbf{M}\ddot{\mathbf{u}}(t) + \mathbf{D}\dot{\mathbf{u}}(t) + \mathbf{f}^{\mathrm{int}}(\mathbf{u}(t)) = \mathbf{f}^{\mathrm{ext}}(\mathbf{u}(t), t) \tag{3.95}$$

are integrated in time to track the dynamic evolution of deformations, where $\mathbf{u}(t)$ is the displacement vector containing the nodal DOF coefficients $\mathbf{u}_I$ at time t, $\mathbf{M}$ is the mass matrix assembled from element contributions, and $\mathbf{D}$ is a viscous damping matrix for equilibration, to be specified at the end of this section. As usual, a superscribed dot denotes the derivative with respect to time. $\mathbf{f}^{\mathrm{int}}$ and $\mathbf{f}^{\mathrm{ext}}$ hold the internal elastic out-of-equilibrium forces (equations (3.13b) and (3.67)) and external loads and contact forces, respectively.

NEWMARK's family of integration methods [157] is one of a few schemes widely used in structural dynamics to solve equation (3.95) numerically [94, 179, 244]. Let $\mathbf{u}_t \approx \mathbf{u}(t)$, $\mathbf{v}_t \approx \dot{\mathbf{u}}(t)$ and $\mathbf{a}_t \approx \ddot{\mathbf{u}}(t)$ be the discretized approximations of the displacement vector and its time derivatives. For fixed NEWMARK scheme parameters β and γ, they are integrated according to

$$\mathbf{u}_{t+\Delta t} = \mathbf{u}_t + \Delta t\, \mathbf{v}_t + \frac{(\Delta t)^2}{2}\big[(1-2\beta)\mathbf{a}_t + 2\beta\, \mathbf{a}_{t+\Delta t}\big], \tag{3.96a}$$

$$\mathbf{v}_{t+\Delta t} = \mathbf{v}_t + \Delta t\big[(1-\gamma)\mathbf{a}_t + \gamma\, \mathbf{a}_{t+\Delta t}\big], \tag{3.96b}$$

where Δt denotes the finite time step, and the nodal accelerations at time t are given by

$$\mathbf{a}_t = \mathbf{M}^{-1}\big[\mathbf{f}^{\mathrm{ext}}(\mathbf{u}_t, t) - \mathbf{f}^{\mathrm{int}}(\mathbf{u}_t) - \mathbf{D}\mathbf{v}_t\big]. \tag{3.97}$$

Depending on the choice of parameters, the method becomes implicit or explicit. A general advantage of implicit integration in time over explicit schemes is the ability to cope with larger time steps without losing numerical stability. In many applications including the present large deformation model, however, this benefit is compromised by significantly more time-consuming computations per

time step. A preliminary computational analysis [234] revealed that the potential energy landscape of dense thin-body packing problems is too rough to be efficiently traversed with an implicit integrator. Further difficulties include the discontinuous nature of contacts sketched in Section 3.3, a significantly more involved numerical implementation as well as increased inter-process communication overhead in parallelization.

For the sum of these reasons, the unconditionally stable *constant average acceleration method*, that is obtained by setting $\beta = 1/4$ and $\gamma = 1/2$, is applied in this work in form of a single-step predictor-corrector scheme of second order. It is particularly well suited because very simple *a posteriori* local error estimators are available in publications by ZIENKIEWICZ and XIE [244, 247]. The prediction step is obtained from the explicit part of equation (3.96):

$$\widetilde{\mathbf{u}}_{t+\Delta t} = \mathbf{u}_t + \Delta t\, \mathbf{v}_t + \frac{(\Delta t)^2}{2}(1-2\beta)\mathbf{a}_t, \tag{3.98a}$$

$$\widetilde{\mathbf{v}}_{t+\Delta t} = \mathbf{v}_t + \Delta t\,(1-\gamma)\mathbf{a}_t, \tag{3.98b}$$

$$\widetilde{\mathbf{a}}_{t+\Delta t} = \mathbf{M}^{-1}\big[\mathbf{f}^{\mathrm{ext}}(\widetilde{\mathbf{u}}_{t+\Delta t}, t+\Delta t) - \mathbf{f}^{\mathrm{int}}(\widetilde{\mathbf{u}}_{t+\Delta t}) - \mathbf{D}\widetilde{\mathbf{v}}_{t+\Delta t}\big]. \tag{3.98c}$$

Based on the predicted accelerations $\widetilde{\mathbf{a}}_{t+\Delta t}$, the displacements and velocities are corrected by the previously omitted implicit part:

$$\mathbf{u}_{t+\Delta t} = \widetilde{\mathbf{u}}_{t+\Delta t} + (\Delta t)^2 \beta\, \widetilde{\mathbf{a}}_{t+\Delta t}, \tag{3.99a}$$

$$\mathbf{v}_{t+\Delta t} = \widetilde{\mathbf{v}}_{t+\Delta t} + \Delta t\, \gamma\, \widetilde{\mathbf{a}}_{t+\Delta t}. \tag{3.99b}$$

A simple estimator for the relative local error made by performing such a step is given by

$$\epsilon_{t+\Delta t} = \left|\beta - \frac{1}{6}\right| \frac{(\Delta t)^2}{u_{\mathrm{ref}}} \left\|\widetilde{\mathbf{a}}_{t+\Delta t} - \mathbf{a}_t\right\|_\infty, \qquad \beta \neq \frac{1}{6}, \tag{3.100}$$

where $\|\cdot\|_\infty$ denotes the maximum norm, which is chosen here to induce a conservative metric. u_{ref} is a characteristic reference length (or angle for rotational DOFs) for normalization, and is set to the structure semi-thickness δ from equation (3.82) for the translational variables and to $\pi/8$ for the beam rotations, which yielded the best balance between the different DOF types in typical simulations. Ideally, the tradeoff between large time step and small error is dealt with in such a way that the local error is approximately constant over time. ZIENKIEWICZ and XIE found that this can be efficiently achieved by applying the following adaptive time stepping rules, given a desired target value $\bar{\epsilon}$ for the relative local error, a maximum tolerance $\epsilon_{\max} > \bar{\epsilon}$, and a lower bound $\epsilon_{\min} < \bar{\epsilon}$ above which the time step is considered large enough:

- If $\epsilon_{t+\Delta t} \in [\epsilon_{\min}, \epsilon_{\max}]$, accept the time step without modifying Δt.
- If $\epsilon_{t+\Delta t} < \epsilon_{\min}$, accept the time step and continue with $\Delta t \leftarrow \left(\bar{\epsilon}/\epsilon_{t+\Delta t}\right)^{1/3} \Delta t$.
- If $\epsilon_{t+\Delta t} > \epsilon_{\max}$, reject the time step and repeat with $\Delta t \leftarrow \left(\bar{\epsilon}/\epsilon_{t+\Delta t}\right)^{1/3} \Delta t$.

A variety of simulation scenarios revealed that a good generic choice that maximizes computational efficiency while maintaining stability of the method is $\epsilon_{\min} = 5{\times}10^{-5}$,

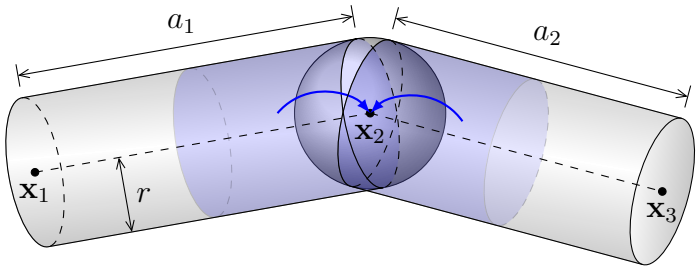

Figure 3.8: **Lumping of masses and moments of inertia.** Half of the mass and moment of inertia of each beam element is assigned to each node (blue). The masses are concentrated in points, while for the calculation of the nodal moment of inertia J, they are uniformly distributed in a sphere of radius r.

$\epsilon_{\max} = 10\epsilon_{\min}$ and a target error which is the geometric mean of the two bounds, $\overline{\epsilon} = \sqrt{\epsilon_{\min}\,\epsilon_{\max}}$.

In order to avoid the relatively expensive matrix inversion $\mathbf{M}^{-1}$ in equation (3.98c), all masses are lumped such that $\mathbf{M}$ becomes diagonal. Several mass lumping methods are in common use in finite element analysis [94]. A straightforward approach is *direct mass lumping* [231], which is employed here for the filament. $\mathbf{M}$ is assembled from nodal contributions

$$\mathbf{M}_n = \mathrm{diag}(m_n, m_n, m_n, J_n, J_n, J_n) \tag{3.101}$$

with nodal point masses $m_n = A\overline{a}_n\rho$, where $A = \pi r^2$ is the cross-section area of the tubular filament, ρ denotes its mass density, and $\overline{a}_n = (a_1 + a_2)/2$ averages the reference lengths of the elements connected to node n. For the nodal moments of inertia J_n, the masses m_n are uniformly distributed within balls of the same radius as the filament, resulting in $J_n = \frac{2}{5}m_n r^2$ (see Fig. 3.8). For the mass contributions of the thin shell, equation (3.8) lends itself to *row-sum lumping* [177], $M_I = \sum_I M_{IJ}$.

On a final note on dynamics, the damping matrix is likewise chosen in diagonal form according to $\mathbf{D} = \mathbf{M}/\tau$ with a viscous relaxation time τ that is set large enough for damping to be subcritical in all relevant modes, depending on the simulated time scales.

3.5 Verification and numerical benchmarks

A physical computer simulation is only as good as its correct functioning has been verified. In this final section of the technical part, a series of standard test problems are solved for verification and benchmarking purposes as well as to pinpoint model limitations, before the focus will be turned to the practical application to morphological studies in the next chapter.

A standard verification obstacle course for thin shell deformations in the geometrically linear regime with subdivision surface elements can be found in ref. [38]. Although the present implementation has been verified using such examples, the details are omitted here, as the focus is on large deformations with geometric nonlinearity. A few tests of nonlinear subdivision shells are available in refs. [35, 36] for different constitutive material models.

Verifying and benchmarking nonlinear beam implementations can be done by comparison to various published static examples (e.g. in ref. [9]). One of the most popular and significant ones is reiterated here to conclude the obstacle course. More benchmarks, including a comparison to exact bending solutions and a convergence assessment, can be found in the author's Master's thesis [234].

3.5.1 Patch test

Passing IRONS' *patch test* [60, 94] is a fundamental requirement for a finite element to correctly represent the local stress distribution on the element level. It assesses the element's *completeness* and should therefore be carried out to complement convergence tests. It also often serves as a simple tool to verify new finite element implementations.

In their original papers [36, 38], CIRAK et al. did not report on patch test performance of the triangular LOOP subdivision surface finite elements, which is why it is carried out here. Subdivision surfaces of the LOOP type are *affine covariant* (i.e., affine transformations of the limit surface are obtained by applying the same transformation to the control mesh), a property that is essential for passing patch tests [93]. Nevertheless, it is demonstrated here that they pass the test only for regular patches, i.e., patches exclusively consisting of ordinary nodes with valence 6. To illustrate this, consider a square shell in the xy plane experiencing a uniform uniaxial CAUCHY strain $\varepsilon_x = \partial u/\partial x \equiv 1$. When the corresponding displacement field $u \equiv x$ is imposed on the boundary nodes of a patch while leaving the interior DOFs unconstrained, the patch test is said to be passed only if the strains are likewise constant across the interior elements of the patch. From Fig. 3.9 it is evident that this is the case for a regular patch, but not otherwise. The error can be diminished by using a quadrature of higher order, but apparently not completely eliminated. LOOP subdivision surfaces cannot be exactly integrated on irregular elements using Gaussian quadrature, an observation that can be understood by recalling the special recursive limit surface evaluation needed for irregular elements [208]. Irregular patches thus fail the patch test when Gaussian quadrature is applied. Interestingly, IRONS et al. originally initiated the patch test by observing (albeit in the context of non-conforming elements instead of subdivision shape functions) that node connectivity can be decisive for correct element behavior [12, 95], as is the case here.

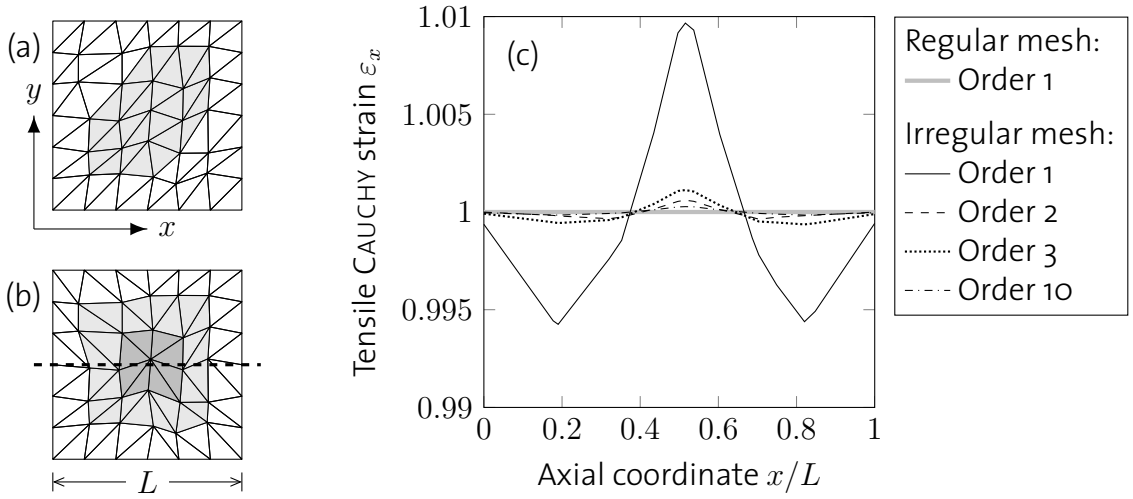

Figure 3.9: **Displacement patch test.** (a) Distorted triangular tiling of the square, consisting of regular elements only. The tested patch is marked in light gray. (b) Irregular mesh with one extraordinary node in the center (valence 8) and 8 irregular elements marked in dark gray. (c) Measured axial strain profile along the dashed line in (b), for both meshes and various GAUSS quadrature orders.

In conclusion, it should be kept in mind that meshes with extraordinary vertices should be avoided for high-precision measurements of stress distributions on the element level with LOOP subdivision elements. In this sense, it is desirable to use (distorted) triangular tilings of the surface domain, which consist of ordinary vertices only, where topologically possible, in particular for surfaces with a vanishing EULER characteristic. On irregular elements, a high-order numerical quadrature should be used.

3.5.2 Numerical locking

As the presented thin shell model is an extension of the KIRCHHOFF–LOVE shell with the displacement field as the only unknown, *shear locking* and POISSON *thickness locking* are pathologies that lie out of the model's scope and need not be addressed here. *Membrane locking* [211, 212], however, has been shown to occur in thin shells independently of the smoothness of the approximation space [30, 31], unless dedicated counter-measures are taken. This type of numerical locking occurs in situations where pure bending is not inhibited in the limit of vanishing structural thickness, i.e., where the geometric, loading and boundary conditions allow for a deformed state without stretching/compression. It is an over-stiff response of the finite element solution resulting from the fact that some pure bending deformations cannot be represented by piecewise polynomials on curved elements without additionally stretching/compressing the structure. When a thin shell finite element is imple-

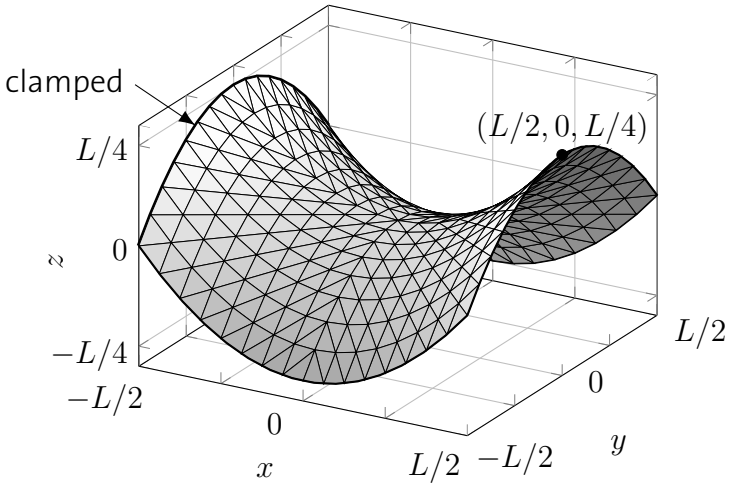

Figure 3.10: **Partly clamped hyperbolic paraboloid.** A 16×16 triangulation of the middle surface is shown.

Thickness h	Displacement w_{ref}	Elastic energy U_{ref}
10^{-2}	-9.3355×10^{-5}	1.6790×10^{-3}
10^{-3}	-6.3941×10^{-3}	1.1013×10^{-2}
10^{-4}	-5.2988×10^{-1}	8.9867×10^{-2}

Table 3.1: **Reference solution of the clamped hyperbolic paraboloid**, computed using 48×48 MITC shell elements in ref. [10].

mented for general purposes like in the present work, it is important to understand under which circumstances membrane locking must be expected. The following two touchstone problems are dedicated to this task.

Figure 3.10 shows the "partly clamped hyperbolic paraboloid" benchmark, which has been advocated as a sophisticated test for membrane locking [30]. The parametric middle surface is defined by

$$z = x^2 - y^2, \qquad x, y \in [-L/2, L/2]. \tag{3.102}$$

The shell is clamped along its boundary at $x = -L/2$ and it is loaded by self-weight. The material properties are set to approximately mimic steel: $E = 2\times10^{11}$, $\nu = 0.3$ and $\rho = 8{,}000$. A unit gravitational acceleration is applied, and $L = 1$. This choice of parameters is motivated by comparability to a reference solution computed numerically with elements of the mixed interpolation of tensorial components (MITC) type [10]. Table 3.1 lists the reference vertical displacement w_{ref} at $(x, y, z) = (L/2, 0, L/4)$ and the reference total strain energy U_{ref}, which are used in Fig. 3.11 to normalize the results obtained here with subdivision elements. Considerable membrane locking is observed below a relative shell thickness of $h/L \approx 10^{-3}$.

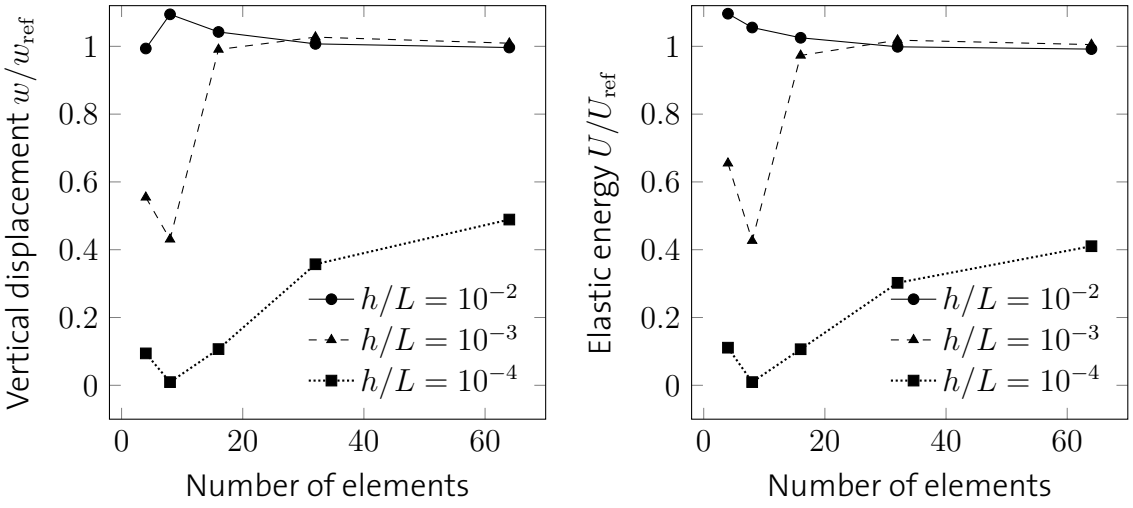

Figure 3.11: **Results of the partly clamped hyperbolic paraboloid.** Vertical displacement at $(x, y, z) = (L/2, 0, L/4)$ and total elastic energy for various shell thicknesses and mesh resolutions.

Thickness h	Pressure p_0	Displacement w_{ref}	Elastic energy U_{ref}
10^{-2}	10^{2}	5.9776929×10^{-4}	1.8779789×10^{-1}
10^{-3}	10^{-1}	5.9422579×10^{-4}	1.8668157×10^{-4}
10^{-4}	10^{-5}	5.9310827×10^{-4}	1.8616845×10^{-7}

Table 3.2: **Exact solution of the periodically pressurized free cylinder**, computed from the analytical solution in ref. [169].

Another numerical benchmark that has been proposed to investigate membrane locking is the "periodically pressurized free cylinder" [30] shown in Fig. 3.12. An open cylinder with radius R, length $L = 2R$ and unconstrained edges is loaded with a periodic pressure distribution given by $p = p_0 \cos(2\varphi)$, where φ is the angle about the cylinder axis and p_0 is a small pressure amplitude. The exact solution of the linearized problem is available in the literature. For $E = 2 \times 10^{11}$, $\nu = 1/3$, $R = 1$ and $p_0 = 10^8 (h/R)^3$, the vertical displacement w_{ref} at $(x, y, z) = (0, 0, R)$ and the total elastic energy U_{ref}, as computed from the analytical TAYLOR series expansion in ref. [169], are listed in Table 3.1. (Note that the scaling factors given there are off by a factor $(1-\nu^2)$ for the displacement and $2(1-\nu^2)^2$ for the energy, however.) In Fig. 3.13, the relative errors of the numerical solution obtained with subdivision elements are plotted. Membrane locking is much less severe than in the first benchmark, but traces of moderate locking are nonetheless in evidence from the non-uniform convergence rates.

These numerical tests indicate that membrane locking becomes prominent above a slenderness of $L/h \gtrsim 10^3$. All benchmarks carried out in the following subsections are either far away from the vanishing thickness limit or inhibit pure bending, such

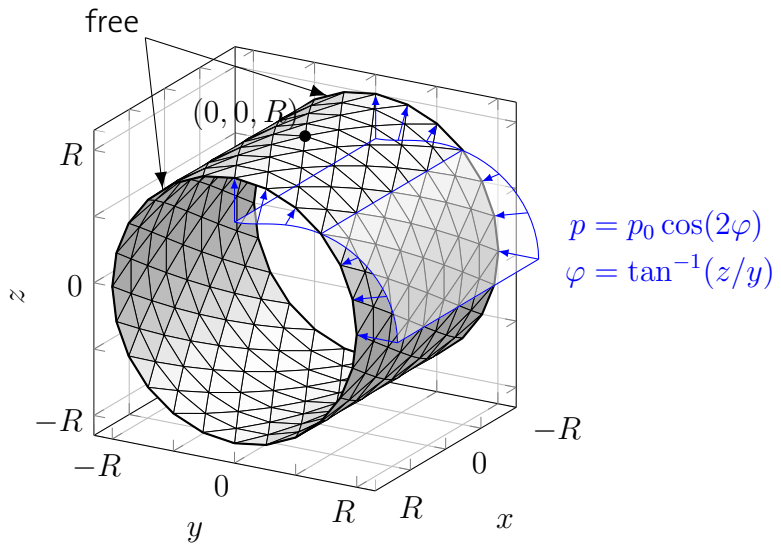

Figure 3.12: **Periodically pressurized free cylinder.** A triangulation of the middle surface with 8 elements in axial direction is shown with a fourth of the pressure distribution in blue.

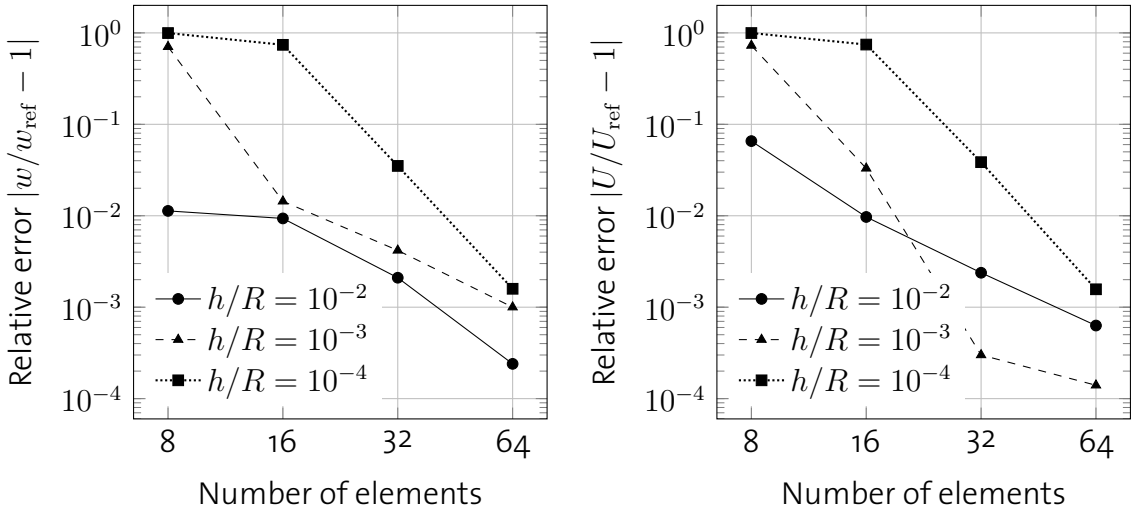

Figure 3.13: **Results of the periodically pressurized free cylinder.** The radial displacement at $(x, y, z) = (0, 0, R)$ and the total elastic energy converge non-uniformly with increasing mesh resolution for different shell thicknesses.

that effects from membrane locking should be very small or completely absent. Moreover, the thin sheet applications presented in Chapters 4 and 5 are nowhere near the pure bending regime and hence they should be unaffected by membrane locking, which justifies the use of plain LOOP subdivision surface shape functions for these purposes.

3.5.3 Inflation and isotropic growth of a sphere

Only few geometrically nonlinear problems are amenable to analytical solution. The inflation of a sphere is one of them [76]. For simplicity, the bending rigidity in equation (2.20) is set to $D = 0$ in this example, i.e., a change in energy is assumed purely due to stretching. Since a spherical shell has no boundary, this example is perfect for verifying both the pure response to large membrane stresses, and uniform in-plane growth, in a single scenario. Consider a growth tensor

$$\boldsymbol{F}_{\mathrm{g}} = \mathrm{diag}[1+g, 1+g, 1] \tag{3.103}$$

with respect to the local tangent basis $\{\mathbf{a}_1/\|\mathbf{a}_1\|, \mathbf{a}_2/\|\mathbf{a}_2\|, \mathbf{a}_3\}$, where g is a positive growth factor. The sphere with initial radius $\overline{R}$ is then trivially expected to grow uniformly according to $R/\overline{R} = 1+g$. On the other hand, in the absence of bifurcations away from the spherical symmetry [153], the pressure p needed to inflate a sphere obeying the KOITER energy density W in equation (2.19) from radius $\overline{R}$ to $R \geq \overline{R}$ is easily found by balancing internal and external forces:

$$p = \frac{\partial W}{\partial R}. \tag{3.104}$$

$W = W(R, \overline{R})$ is found using local symmetry on the GREEN strains

$$E_{\alpha\beta} = \frac{1}{2}(\lambda^2 - 1)\delta^{\beta}_{\alpha}, \tag{3.105}$$

where $\lambda = R/\overline{R} \geq 1$ is the principal stretch. The energy density of the inflated spherical membrane is thus

$$W(R, \overline{R}) = K\frac{(1+\nu)}{4}\big(\lambda^2 - 1\big)^2, \tag{3.106}$$

yielding the pressure relation

$$p = \frac{Eh}{\overline{R}(1-\nu)}(\lambda^3 - \lambda) \geq 0. \tag{3.107}$$

The meshes used for this example are shown in Fig. 3.14. They are constructed by recursive quadrisection of the faces of a regular icosahedron, followed by a radial

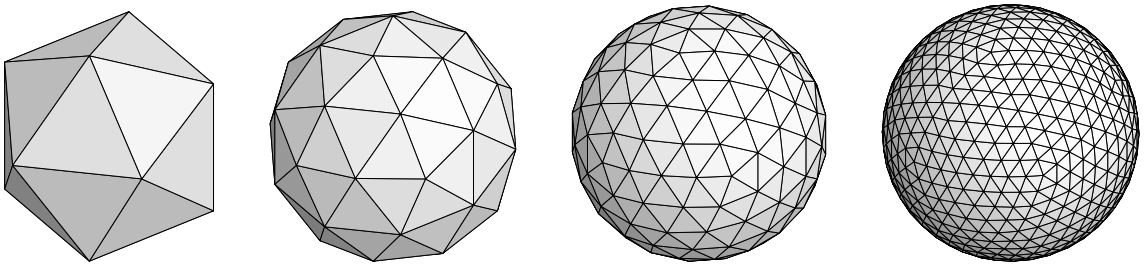

Figure 3.14: **Icosa-spherical meshes** for the inflated and growing spherical shell. From left to right, refinement recursions 0 to 3 are shown, which yield 20, 80, 320 and 1,280 triangles (36, 126, 486 and 1,926 DOFs).

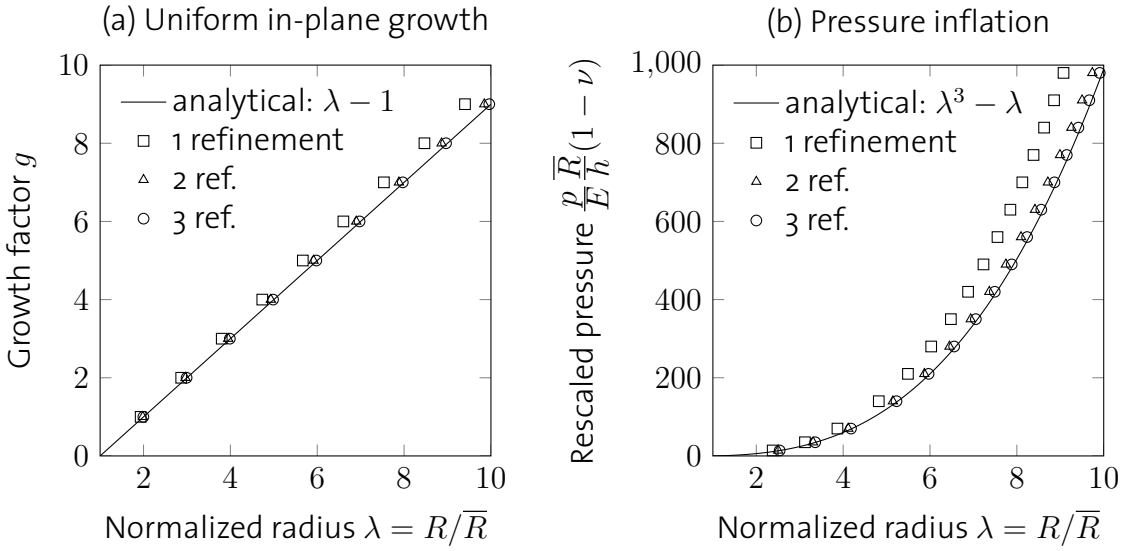

Figure 3.15: **Change of radius of a spherical shell.**

projection of the newly created vertices onto the bounding sphere on each level of recursion. The employed recursion depths are 1, 2 and 3, yielding triangulated spheres with 80, 320 and 1,280 equilateral elements, respectively. The relevant simulation parameters are $\overline{R} = 1$, $h = 10^{-3}$, $E = 1$, $\nu = 0.3$.

In Fig. 3.15, the growth-expansion and pressure-expansion curves are juxtaposed, demonstrating the high accuracy and convergence to the analytical solutions in both cases. Relatively coarse meshes are sufficient for high accuracy even at extremely large deformations.

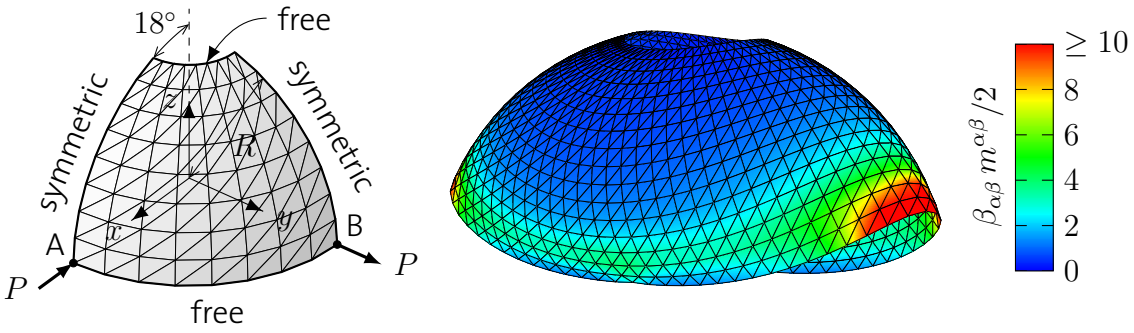

Figure 3.16: **Hemispherical shell subject to point loads.** Left: Undeformed reference configuration reduced to the first quadrant exploiting symmetry. The 8×8 control mesh is shown. Right: Final state of the 16×16 mesh at maximum load $P = 100$. The color encodes the bending energy per unit area.

3.5.4 Pinched hemisphere

Next, two numerical examples without growth are considered, for verification of the linearly elastic, geometrically nonlinear shell with coupled stretching and bending. The pinched hemisphere is a widely used benchmark for "an element's ability to represent inextensional modes" and "rigid body rotations about normals of the shell surface" [14]. In its nonlinear regime, it is a test recommended by the National Agency for Finite Element Methods and Standards (NAFEMS, test no. 3DNLG-9) [1]. The geometrical setup is shown in Fig. 3.16. A hemispherical shell with an 18° open pole and free boundaries is pinched by four equally strong, pairwise opposite diametrical point loads P acting on the equator. The shell radius is $R = 10$, its thickness $h = 0.04$, and the elastic moduli are determined by $E = 6.825 \times 10^7$, $\nu = 0.3$.

In order to minimize the impact originating from the specific choice of boundary constraints, the whole hemisphere is simulated without exploiting symmetry, and GREEN's method is used for the free boundaries, i.e., they are unconstrained. In Fig. 3.17, the displacements of points A and B on the limit surface are plotted against the applied loads for three mesh resolutions, together with some NAFEMS reference results obtained with the Abaqus FEA software [1, 220]. In the spirit of Abaqus, the subdivision shell finite elements with one-point integration are denoted by SD3R for brevity. Much more reference data for other nonlinear finite elements can be found e.g. in refs. [1, 154, 240] and references therein. The employed meshes are obtained by regularly discretizing the quarter hemisphere along the angles of inclination and the azimuth, resulting in 128, 512, and 2,048 triangles per quarter hemisphere, respectively. In Fig. 3.16, the 16×16 mesh with 512 triangles per quarter, that is also used in the NAFEMS results, is shown on the right.

The load-displacement curves for subdivision surface elements are almost identical to those of Abaqus S4R elements. High precision is obtained with SD3R at much

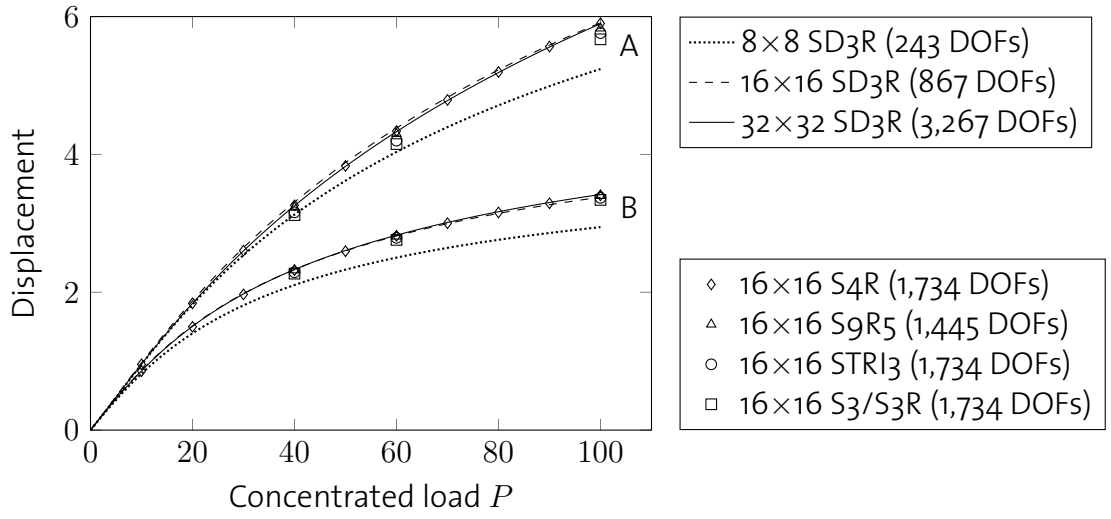

Figure 3.17: **Load-displacement curves for the pinched hemispherical shell.** The NAFEMS reference values were obtained with Abaqus.

less DOFs, mainly because subdivision shell elements go without rotational variables, unlike all other shown elements.

3.5.5 Stretched cylinder with free ends

The next example is another standard loading test, consisting of a cylindrical shell with free boundaries that is stretched transversally by two equally strong, opposite diametrical point loads P acting on the middle of the cylinder length. This test case has found vast attention in the literature. For an overview, see e.g. refs. [154, 240] and references therein. Its peculiar usefulness is due to its ability to examine two different response regimes, one after the other. At small loads, the large deformation results from low bending stiffness, while at large loads, further deformations require the stiff shell to be stretched primarily. The geometrical setup is shown in Fig. 3.18. The cylinder radius is $R = 4.953$, its length $L = 10.35$, its thickness $h = 0.094$, and the elastic moduli are determined by $E = 10.5 \times 10^6$, $\nu = 0.3125$. Like in the previous example, the full shell is simulated neglecting present symmetries, and no constraints are applied to the boundaries.

In Fig. 3.19, the resulting load-displacement curves for the points A, B and C are compared to Abaqus S4R element data from ref. [220]. In the bending regime at moderate loads, the data from 351 DOFs almost coincides with that of S4R elements using 5,550 DOFs, again demonstrating the outstanding computational efficiency of subdivision shells. In the stretching regime at large loads, SD3R elements are slightly less stiff than S4R and elements found in other literature mentioned above. Those displacements, however, are quite sensitive to changes in the mesh structure. Other

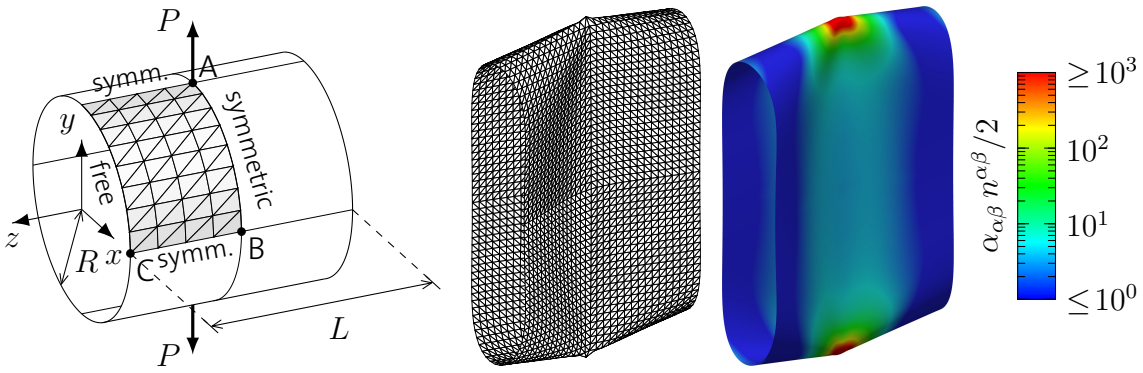

Figure 3.18: **Cylindrical shell subject to point loads.** Left: Undeformed reference configuration reduced to one eighth of the geometry exploiting symmetry. A 4×8 control mesh is shown. Middle: Buckled state of the 16×24 mesh at maximum load $P = 4\times10^4$. Right: Limit surface of the same configuration, with the stretching energy per unit area on a logarithmic color scale.

meshes than that shown in Fig. 3.18 lead to marginally shifted displacements at large loads.

Correctly capturing the snap-through transition near $P \approx 20{,}840$ has posed a tough challenge to various finite shell elements in the past. Some even fail to correctly feature it at moderate mesh resolutions [19, 83, 192]. With the subdivision shell elements, such problems are not observed here, not even for meshes much coarser than those mentioned in Fig. 3.19.

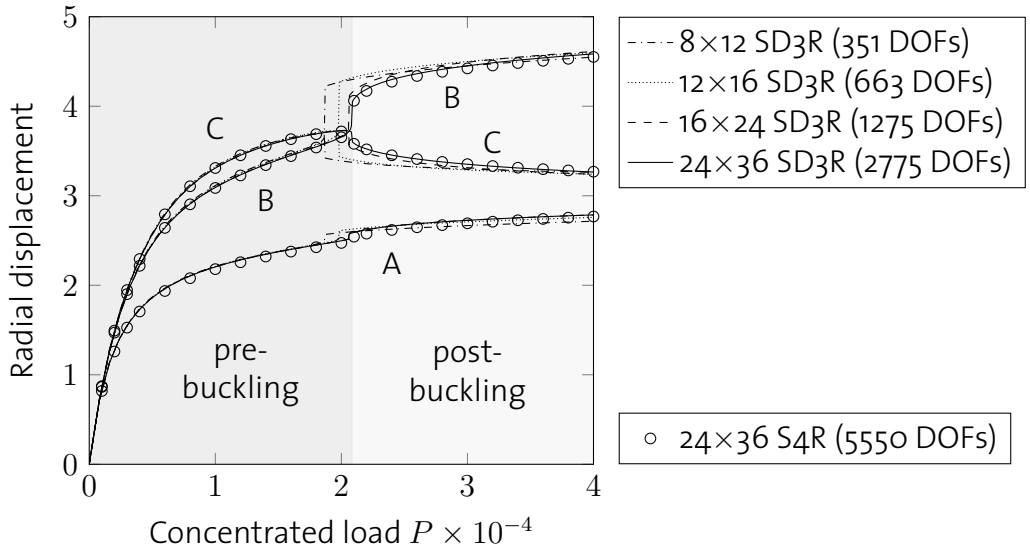

Figure 3.19: **Load-displacement curves for the stretched cylindrical shell**, with the transition near half loading.

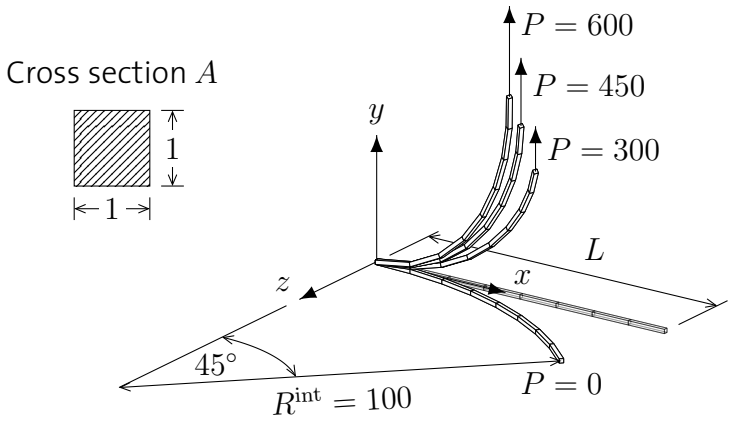

Figure 3.20: **45° bend cantilever benchmark.** An 8-element cantilever beam with square cross-section A and intrinsic radius of curvature R^{int} is subjected to transverse end loads P.

3.5.6 45-degree bend

This final numerical example is dedicated to the beam model. NAFEMS recommends the "45-degree bend" as a demanding nonlinear beam benchmark (test no. 3DNLG-5) [1]. It involves a clamped cantilever with square cross-section A, non-zero intrinsic rotation variables $\left|\widehat{\theta}_n^{\text{int}}\right| = a/2R^{\text{int}}$, $n = 0, \ldots, N$, and uniform nodal spacing $a = 2R^{\text{int}} \sin(\pi/8N)$, where N is the number of finite elements. Initially straight with length $L = Na$, it is released to form an eighth of a circle with radius R^{int} due to the intrinsic curvature, as depicted in Fig. 3.20. It is subsequently subjected to transverse end loads P leading to a three-dimensional nonlinear response that couples all element degrees of freedom. The resulting tip positions are listed in Table 3.3 for $R^{\text{int}} = 100$, $N = 8$, $A = 1 \times 1$, $E = 10^7$, $\nu = 0$, showing excellent agreement with other implementations. Since the order of the beam theory has almost no effect on such a thin rod, results for thickness 10 are also given, revealing the improved precision of corotated third-order beam theory (CR-RBT) over the first-order EULER–BERNOULLI counterpart (CR-EBT) at large transverse shear stresses.

With these favorable findings the technical part of this thesis is concluded. In the chapters to follow, the developed numerical tools are applied to explore growth, packing and interaction of thin deformable bodies.

$A = 1 \times 1$	$P = 300$	$P = 450$	$P = 600$
CR-RBT (present)	$(58.77, 40.25, 22.28)$	$(52.21, 48.59, 18.55)$	$(47.11, 53.58, 15.73)$
CR-EBT (present)	$(58.77, 40.25, 22.28)$	$(52.21, 48.58, 18.55)$	$(47.11, 53.57, 15.73)$
LI [118]	$(58.78, 40.15, 22.28)$	$(52.24, 48.46, 18.56)$	$(47.15, 53.43, 15.74)$
LEUNG at al. [117]	$(58.51, 40.46, 22.23)$	$(51.92, 48.69, 18.53)$	$(46.82, 53.6\ , 15.76)$
RHIM at al. [182]	$(58.58, 40.31, 22.16)$	—	$(47.07, 53.46, 15.59)$
LO [126]	$(58.8\ , 40.1\ , 22.3\ )$	$(52.3\ , 48.4\ , 18.6\ )$	$(47.2\ , 53.4\ , 15.8\ )$
CRISFIELD [41]	$(58.53, 40.53, 22.16)$	$(51.93, 48.79, 18.43)$	$(46.84, 53.71, 15.61)$
SANDHU et al. [191]	$(58.85, 40.04, 22.36)$	$(52.33, 48.40, 18.54)$	$(47.27, 53.34, 15.88)$
CARDONA et al. [25]	$(58.64, 40.35, 22.14)$	$(52.11, 48.59, 18.38)$	$(47.04, 53.50, 15.55)$
SIMO et al. [203]	$(58.84, 40.08, 22.33)$	$(52.32, 48.39, 18.62)$	$(47.23, 53.37, 15.79)$
BATHE at al. [9]	$(59.2\ , 39.5\ , 22.5\ )$	—	$(47.2\ , 53.4\ , 15.9\ )$
$A = 10 \times 10$	$P = 3 \times 10^6$	$P = 4.5 \times 10^6$	$P = 6 \times 10^6$
CR-RBT (present)	$(58.25, 41.49, 22.03)$	$(51.54, 49.98, 18.26)$	$(46.35, 55.09, 15.43)$
CR-EBT (present)	$(58.38, 41.22, 22.09)$	$(51.70, 49.67, 18.32)$	$(46.54, 54.75, 15.48)$

Table 3.3: **45° bend benchmark.** Comparison of centerline tip positions at different end loads and beam thicknesses. Initially ($P = 0$), it is $(70.71, 0.0, 29.29)$.

Chapter 4

Growing thin sheets

> *An organism is so complex a thing, and growth so complex a phenomenon, that for growth to be so uniform and constant in all the parts as to keep the whole shape unchanged would indeed be an unlikely and an unusual circumstance. Rates vary, proportions change, and the whole configuration alters accordingly.*
>
> – D'Arcy Wentworth Thompson, *On Growth and Form* (1917)

Before the growth evolution and interplay of *both* kinds of thin elastic bodies is studied *together* in Chapter 5, it is expedient for a number of reasons to immerse in the application-oriented part of this work by considering them separately first. In this chapter, growth of thin shells is addressed in a series of three different settings inspired by related real-world processes. To start off, the simplest sort of volumetric growth one can imagine—uniform, homogeneous and isotropic—is applied to a confined sheet, shedding light on the well-known sheet crumpling problem from a very different viewpoint. In the spirit of Thompson's perception quoted above, the growth field is then complicated to orthotropic differential extension in order to allow for complex shapes to emerge in *absence* of spatial confinement. As an example, spontaneous wrinkle formation at free edges of thin sheets is simulated, elucidating the effect of the type of growth, the involved length scales as well as geometrical constraints to morphogenesis and symmetry breaking.

4.1 Uniform growth and crumpling in rigid confinement

Take a piece of paper or foil, crumple it with your hands and then unfold it again. What you are left with is a highly complex network of scars showing where exactly the sheet buckled and folded. A similar—and in some sense converse—situation

is encountered in Nature by the millions each spring: Flower blossoms and leaves grow in tight enclosure by bud scales to eventually unfold and take a more or less flat and undamaged shape when they open. The results of these two processes are clearly different, and so one might conclude that the pathways cannot be the same either. But the comparison is unfair: Scars are owed to irreversible damage on the crumpled paper, while live plant tissue typically possesses the ability to self-heal (e.g., [96]). The question whether a membrane uniformly growing inside of a fixed confinement (like a bud, approximately) will crumple equivalently to an invariant membrane in shrinking confinement (as formed by our hands, approximately) must therefore rest upon the assumption of equal microscopic and macroscopic material properties. Even in this case the answer is not *a priori* obvious, and it was previously conjectured to be negative [215]. Here, strong numerical evidence is given against this belief.

A thin, isotropic, linearly elastic disk with radius R is placed inside of a rigid spherical container with the same radius $\overline{R} = R$. In the first setup, the container is slowly shrunk, and consequently, the disk crumples into a ball of the size of the container, developing the ridge network known from previous computer simulations [112, 124, 222, 223, 235]. In the second setup, the opposite happens, i.e., the container sustains its size while the elastic disk is subjected to a constant isotropic growth rate, both in plane and in thickness. The only relevant simulation parameter is the sheet's slenderness which is set to $\overline{R}/h = 100$ here, yielding a FÖPPL–VON KÁRMÁN number [119, 128] of

$$\widetilde{\gamma} = 12(1-\nu^2)\left(\frac{\overline{R}}{h}\right)^2 \approx 10^5, \tag{4.1}$$

a geometrical measure for a thin sheet's tendency to bend rather than stretch. POISSON's ratio is fixed to $\nu = 1/3$. To obtain equivalent time scales in the two problems, the confining sphere is shrunk in the first setup according to $\overline{R}(t) = R/(1+g(t))$, where $g(t) = \Lambda t$ is the in-plane growth factor of the growing shell in the second setup, yielding in the growth tensor

$$\boldsymbol{F}_{\mathrm{g}} = \mathrm{diag}[1+g(t), 1+g(t), 1+g(t)]. \tag{4.2}$$

Its third (normal) component is realized within the KIRCHHOFF–LOVE theory by increasing the shell thickness according to $h(t) = h(0)(1+g(t))$. The growth rate Λ is chosen small enough for the system to remain close to static equilibrium at all times and in both scenarios, and damping is subcritical. To break the initial planar symmetry, a small random transverse displacement is imposed on the disk.

No evidence is found indicating that the two processes are different. During early stages, both shells buckle to form a *developable cone* (d-cone) with a single vertex, where most curvature and bending energy is concentrated. Around $\overline{R}/R \approx 0.53$, the apex starts to nucleate, and more vertices subsequently emerge, leading to the very same ridge network as illustrated in Fig. 4.1. In the third column, the dimensionless

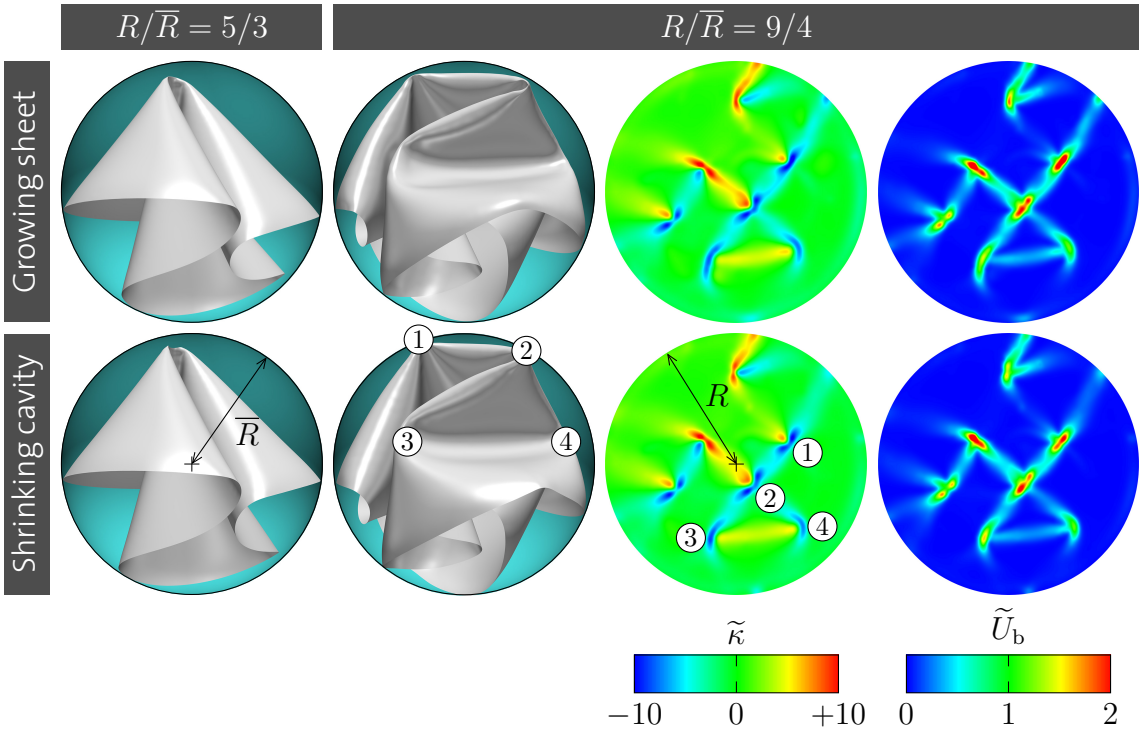

Figure 4.1: **Comparison between crumpling in shrinking confinement and confined growth.** A crumpled shell and a growing shell in spherical confinement deform equivalently. Network vertices are numbered for easy identification.

rescaled mean curvature

$$\widetilde{\kappa} = \overline{R}\,\frac{k_1 + k_2}{2} \tag{4.3}$$

is projected onto the unfolded disk, where k_1 and k_2 are the principal curvatures of the middle surface. The cross correlation of the mean curvature ridge patterns is $c = 0.89$, a very high value when compared to recent similar measurements [222]. The fourth column displays the dimensionless rescaled bending energy density

$$\widetilde{U}_\mathrm{b} = \beta_{\alpha\beta} H^{\alpha\beta\gamma\delta} \beta_{\gamma\delta}\, \overline{R}^2 \left(\frac{R(t)}{R(0)}\right)^2 . \tag{4.4}$$

No qualitative or quantitative disparity, going beyond minor local shifts resulting from the finite element size and slow but finite dynamics, is observed. This indicates that the two crumpling processes are in fact equivalent.

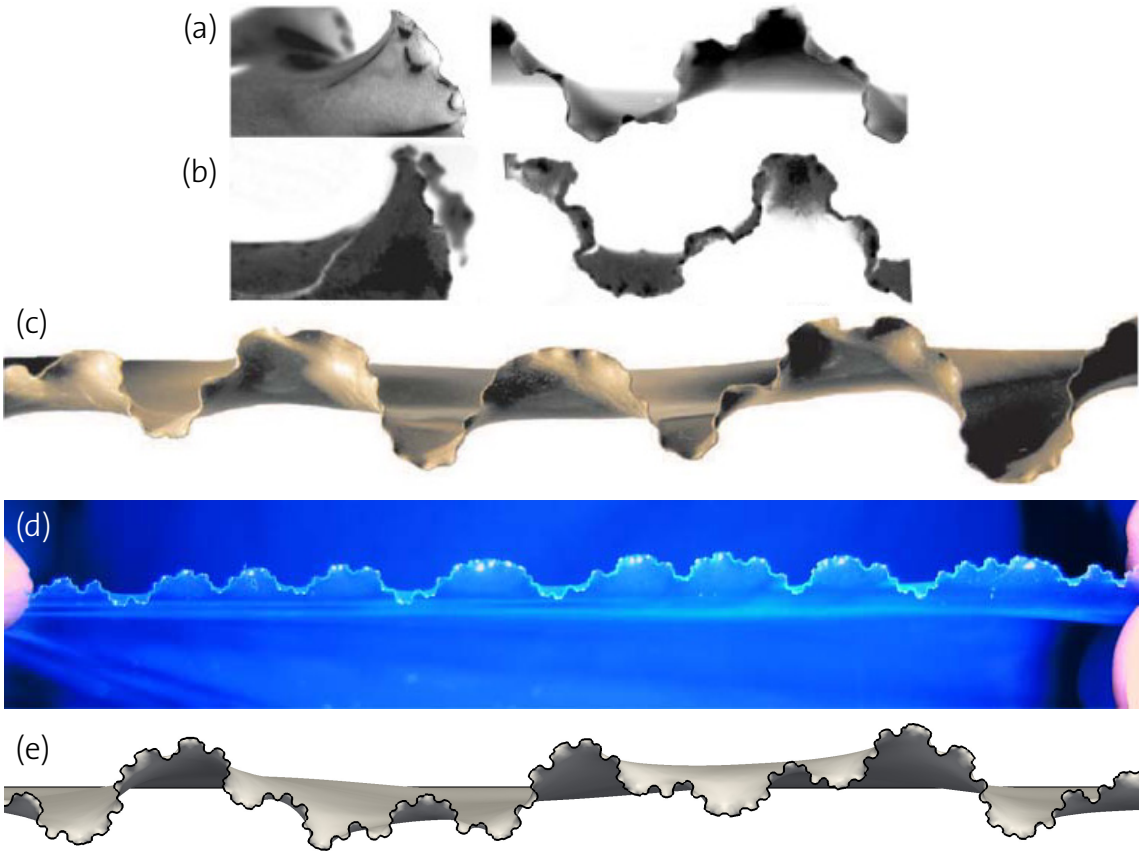

Figure 4.2: **Buckling cascades in torn plastic sheets and beet leaves.** Torn plastic (a) and beet leave (b) reproduced from ref. [198] and adapted with permission of Nature Publishing Group. (c) Reproduced with permission from ref. [138]. Copyright 2007, American Institute of Physics. (d) Photograph courtesy of E. SHARON, reproduced from ref. [196]. (e) Present computer simulation.

4.2 Wrinkling cascades in torn plastic sheets and plant leaves

A common buckling instability observed in plant growth is the occurrence of beautiful wrinkles along free tissue boundaries, such as the edges of flowers and leaves [7, 136–138, 197, 198] (Fig. 4.2). The exact nature of these wavy patterns depends on the membrane thickness and the details of growth, but it is obvious that only *differential* growth can produce them from an initially flat configuration under free boundary conditions without external loading or inelastic effects. Large planar stresses from compression due to differential in-plane growth are traded for out-of-plane bending as a result of the thin tissue's low bending rigidity. Astoundingly, the emerging buckling cascades are very similar to the shape of torn plastic sheets. Empirical measurements revealed that both phenomena are characterized by a plastic differential

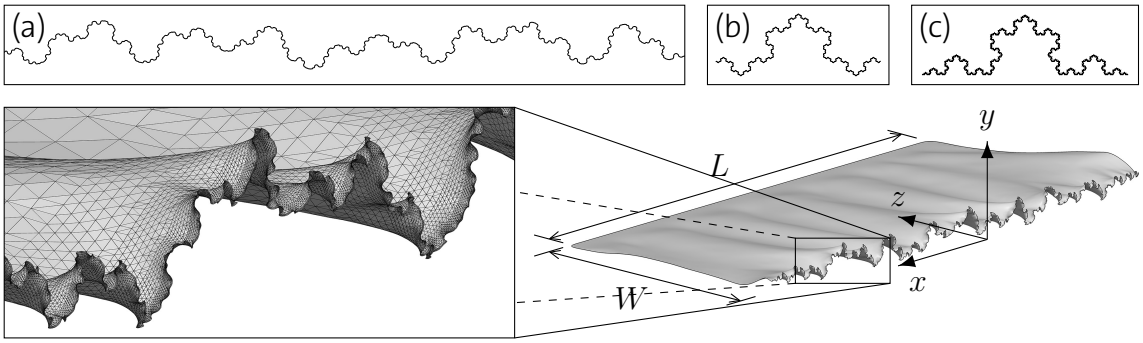

Figure 4.3: **Self-similar sheet boundary** after orthotropic differential growth according to equation (4.6). (a) Projection of the grown edge onto the xy-plane. (b) 60° FIBONACCI word fractal. (c) KOCH snowflake.

metric profile

$$g(z) = \frac{1}{1 + z/l}, \tag{4.5}$$

where $l > 0$ is a characteristic length scale and $z \geq 0$ is the in-plane coordinate perpendicular to the growing free edge (or the yielded edge in the tearing case). The developing undulation pattern has been reported to be self-similar with an odd integer scaling factor that is mostly 3 and sometimes close to 5 in experiments [7, 198]—a result that AUDOLY and BOUDAUD were able to confirm [6] by solving the FÖPPL–VON KÁRMÁN equations on the edge of a free rectangular sheet with growth profiles of the form of equation (4.5). The FÖPPL–VON KÁRMÁN equations are, however, geometrically limited in that they don't allow reentrancy, which has precluded them from examining the fractal properties of the boundary. The present nonlinear KOITER shell model with growth, on the other hand, enables a numerical solution of the problem with its full geometric nonlinearity taken into account. Consider a flat rectangular sheet of thickness $h = 10^{-4}$, length $L = 4$, and width $W = 1$, initially lying in the xz-plane. The long edge at $z = W$ is clamped and the short edges are constrained to stay at $x = \pm L/2$ so as to mimic the compressive effect of an even longer strip, while leaving them free to move in other directions. Growth is imposed by setting the growth tensor to

$$\boldsymbol{F}_{\mathrm{g}} = \mathrm{diag}[1 + g(z), 1, 1] \tag{4.6}$$

in Cartesian coordinates (x, y, z), and the characteristic length for the growth field is set to $l = 40h$ in this example. Figures 4.2 and 4.3 show the resulting equilibrated configuration after growth (or tearing). The self-similarity of the reentrant free edge at $z = 0$ is apparent, clearly resembling the wrinkling cascades observed in experiments [138, 196, 198].

The fractal dimension of the grown edge, computed using the box counting method [64] and the self-similarity method [134], is depicted in Fig. 4.4. In the former, the curve length L_{in} contained in a cubic box is determined as a function of the edge

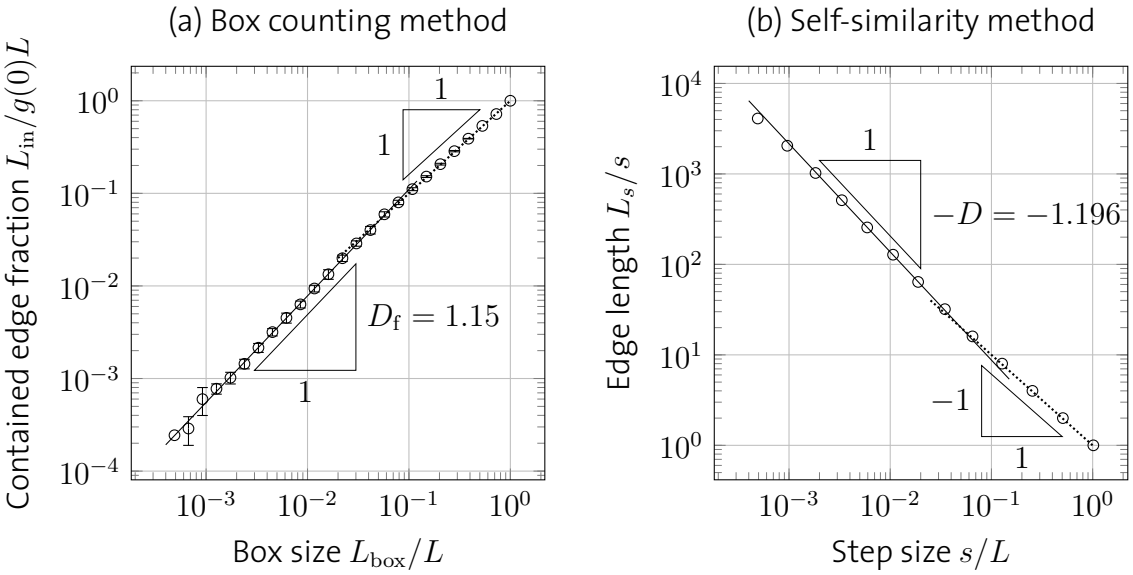

Figure 4.4: **Fractal dimension of the edge** at $z = 0$ of a thin sheet grown according to equation (4.6), measured with two standard methods.

length L_{box} of the box. A fractal curve is expected to scale as $L_{\mathrm{in}} \sim L_{\mathrm{box}}^{D_{\mathrm{f}}}$. Such scaling is indeed observed with fractal dimension $D_{\mathrm{f}} = 1.15 \pm 0.01$ (Fig. 4.4a). The scaling breaks down due to the influence of the clamped opposite edge, which introduces a global straightening effect when the box size is large ($L_{\mathrm{box}} \approx W$). The second method is more robust to global orientation and is thus better suited here. The length L_s of a piecewise linear path along the curve with segment size s is measured and expected to scale as $L_s \sim s^{1-D}$. A self-similarity dimension $D = 1.196 \pm 0.005$ is evident from Fig. 4.4b, which is very close to the HAUSDORFF dimension of a 60-degree FIBONACCI word fractal (Fig. 4.3b), $D_{\mathrm{H}} = 1.2083$ [148], and a bit lower than that of a triadic KOCH curve (Fig. 4.3c), $D_{\mathrm{H}} = 1.2619$ [135].

4.3 Unimodal wrinkling of growing cylinders

The metric profile in equation (4.5) from the previous example is not the only one yielding wrinkled edges. When it comes to wavy flowers like certain orchids for instance, single-wavelength undulations instead of self-similar edges are not uncommon. The feature responsible for wrinkle cascades is the presence of a non-constant geometric length scale defined by $l_{\mathrm{geo}}(z) = -g(z)/g'(z)$ [197]. Similar boundary instabilities are hence produced by the following generalized families of growth

metrics:

$$g_p(z) \;\propto\; \left(1+\frac{z}{p\,l}\right)^{-p}, \qquad (l>0,\ p>0,\ z\geq 0), \tag{4.7}$$

$$g_p(z) \;\propto\; \left(1-\frac{z}{p\,l}\right)^{p}, \qquad (l>0,\ p>1,\ 0\leq z\leq p\,l), \tag{4.8}$$

On the other hand, an exponential growth field

$$g(z)\propto\exp\!\left(-\frac{z}{l}\right), \qquad (l>0,\ z\geq 0) \tag{4.9}$$

yields only a single wavelength [44, 136] because $l_{\mathrm{geo}}(z)\equiv l$ is constant in this case. On some flowers, these undulations may be forced to integral wavenumbers n by angular periodicity of a single petal. Let's hence significantly increase the characteristic length l and thickness h such that only a single wavelength λ prevails even for growth in the form of equations (4.7) and (4.8), and consider a cylinder with height H and radius R instead of a flat plate, growing according to

$$\boldsymbol{F}_{\mathrm{g}}=\mathrm{diag}[1,1+g(z),1] \tag{4.10}$$

with respect to the canonical basis of cylindrical coordinates (r,φ,z). This change in geometry delivers dramatic consequences: A thin cylindrical sheet growing in circumferential direction according to $g(z)$, where z is the cylinder axis, only breaks its axisymmetry if growth leads to a circumference that changes faster than the sheet's metric can account for [137]. Such configurations have been experimentally obtained in the lab by dipping thin polyacrylamide gel tubes into water, which lets them swell, or into acetone, with lets them shrink [196] (see Fig. 4.5). A direct consequence of the GAUSS–BONNET theorem is that the continuous axisymmetry is preserved (in the vanishing thickness limit) as long as

$$\left|R\,\frac{\mathrm{d}g}{\mathrm{d}z}(z)\right|\leq 1, \quad 0\leq z\leq H, \tag{4.11}$$

and broken otherwise. The origin for this instability is the (non)existence of *embeddings* of the surface: According to GAUSS's Theorema Egregium, the creation or elimination of Gaussian curvature must be accompanied by in-plane stretching or compression, which is traded for out-of-plane buckling if the sheet is sufficiently thin.

Three instances of this kind of orthotropic differential growth are juxtaposed in Fig. 4.6 with snapshots before, at the onset, and far beyond the buckling threshold. The linear case $p=1$ excluded in equation (4.8) produces the *excess cone* (e-cone) [43, 151, 216] in the limit $R\to 0$, which is a developable surface that doesn't wrinkle at the boundary as shown in the top row of Fig. 4.6, because $g_1''(z)\equiv 0$. Unimodal wrinkling is observed in superlinear growth (bottom rows), where the axisymmetry is spontaneously broken to n-fold rotational symmetry C_n. A relatively short cylinder

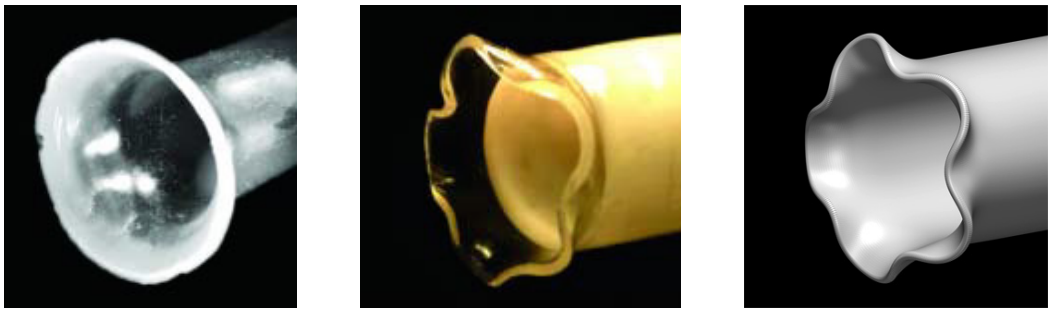

Figure 4.5: **Boundary instability of a swollen gel cylinder.** Left and middle: Dipping polyacrylamide gel tubes into water grows their metric profile. If the immersion depth is confined to a narrow boundary layer (short l, large metric gradient), the continuous axisymmetry is broken into a discrete one. Photographs courtesy of E. SHARON, M. MARDER and H. L. SWINNEY, reproduced from ref. [196]. Right: Computer simulation with differential growth of the form of equation (4.8).

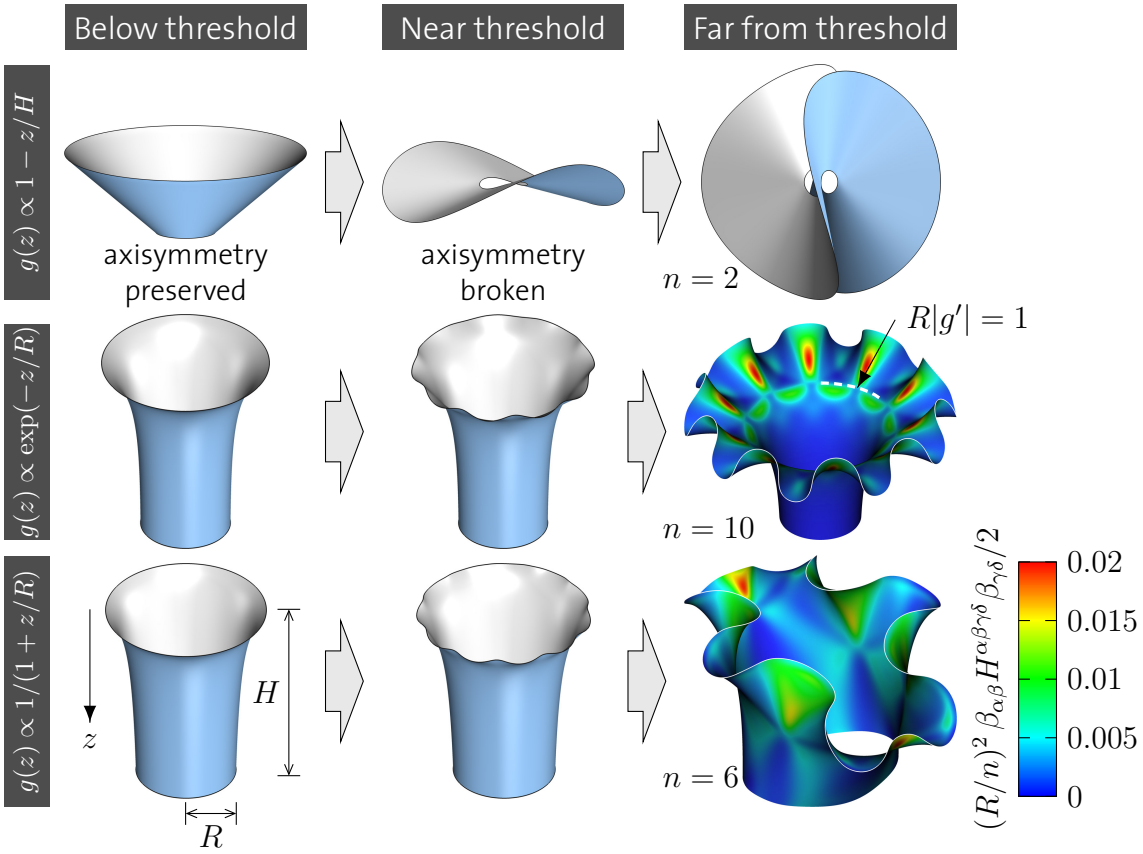

Figure 4.6: **Differential circumferential growth of a cylinder.** Linear growth profiles (top row) preserve the vanishing Gaussian curvature. In superlinear growth (bottom rows), the axisymmetry is spontaneously broken to discrete rotational symmetry C_n. From left to right, the proportionality prefactor is increased. The rescaled bending energy density is shown in color, revealing the buckling threshold where equation (4.11) holds equally. The simulation parameters are $H/R = 4, l/R = 1, h/R = 0.01$.

(small H/l) with free boundaries can also buckle at the opposite edge if the metric grows large enough, breaking C_n symmetry further to C_2 (bottom right image).

How does the number n of boundary waves scale with l, h, R when axisymmetry is broken, and is it universal for all positive, monotonically decreasing and strictly convex growth profiles satisfying

$$\lim_{z\to 0} l_{\mathrm{geo}}(z) = l \; ? \tag{4.12}$$

Since the preferred wavelength λ is a local feature independent of global geometry and topology (independent of H and R), the only involved length scales are h and l_{geo}, so one may use the ansatz [197]

$$\lambda \sim h^{\alpha}\, l_{\mathrm{geo}}^{1-\alpha}, \qquad \text{i.e.,} \qquad \frac{\lambda}{h} \sim \left(\frac{l_{\mathrm{geo}}}{h}\right)^{1-\alpha}. \tag{4.13}$$

On the other hand, geometry implies that

$$\lambda = \frac{2\pi R}{n}(1 + g(0)). \tag{4.14}$$

since $z = 0$ is where equation (4.11) is violated at the buckling threshold, given that $g' < 0$ and $g'' > 0$. After combining equations (4.11) to (4.14), one thus finds a scaling for the number of wrinkles

$$n \sim \left(1 + \frac{R}{l}\right)\left(\frac{l}{h}\right)^{\alpha}. \tag{4.15}$$

Up to the first term, which accounts for the mean curvature of the cylinder, this coincides with the scaling law reported in ref. [6] for the wrinkling hierarchies in initially flat sheets, where $\alpha = 2/5$ has been found for the family in equation (4.5). The present numerical data, which best fits equation (4.15) with $\alpha = 0.39 \pm 0.02$, shows that the wrinkles studied here fall in the same category, see Fig. 4.7. Moreover, the data collapse of all employed growth profiles on a single line indicates that the scaling is universal in this respect.

To summarize this chapter, different growth concepts were applied to thin shells, breeding fundamentally different shape transformations. *Uniform* isotropic swelling doesn't alter the sheet's equilibrium form, letting it crumple in a container exactly as if the latter was shrinking. *Differential* growth on the other hand explains the boundary instabilities found in torn plastic foils and thin plant tissue based purely on mechanical principles, i.e., as a "dead" process. As simulations showed, the growth profile previously observed empirically leads to a self-similar free boundary with a fractal dimension that doesn't seem to coincide with that of any other known fractal curve. Finally, a universal scaling function for the number of spontaneously emerging wrinkles was derived for a general class of growth metrics on thin cylinders, illustrating the effect of competing length scales on growth instabilities.

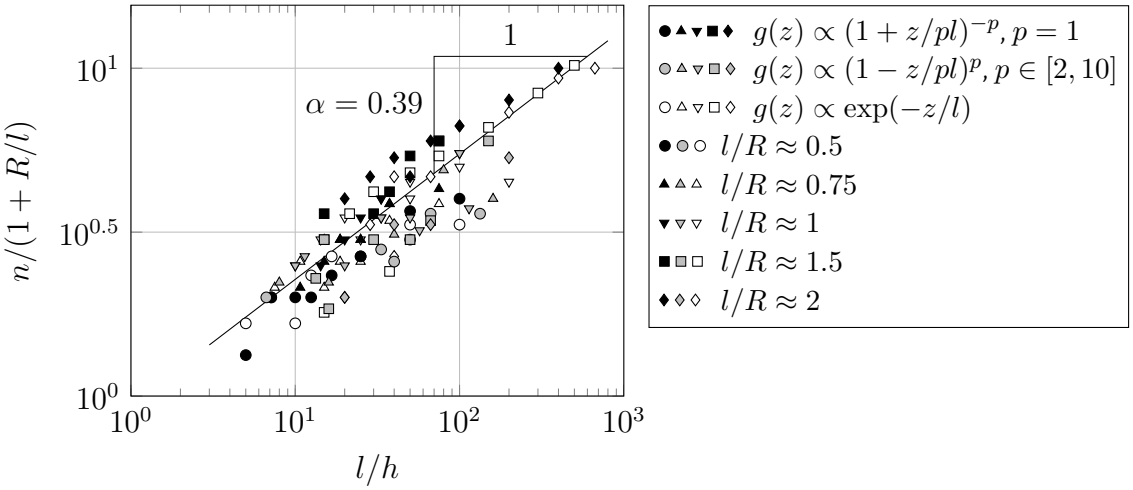

Figure 4.7: **Scaling of the wrinkle number** n along the edge of a circumferentially growing cylinder. The mode with the lowest energy is the integer n closest to the power law of equation (4.15), but excited modes also randomly occur and are metastable (data points lying significantly above or below the straight line).

Thin sheets are quasi-two-dimensional. Their two principal tangential directions offer much room for multifarious morphogenesis due to in-plane anisotropy. In thin filaments, whose tangent space is quasi-one-dimensional, this degree of freedom is absent, essentially leaving only two kinds of tangential growth: uniform and non-uniform. These will be addressed in the next chapter in the context of filament packing with a focus the mechanical interaction between thin elastic bodies.

Chapter 5

Filament packing and growth in spatial confinement

> *[...] while growth is a somewhat vague word for a very complex matter [...], it deserves to be studied in relation to form: whether it proceed by simple increase of size without obvious alteration of form, or whether it so proceed as to bring about a gradual change of form and the slow development of a more or less complicated structure.*
>
> – D'Arcy Wentworth Thompson, *On Growth and Form* (1917)

In this main chapter, the previously developed concepts and methods culminate in the study of filament growth and packing in flexible shells. The problem is approached in a gradual fashion, starting from the well-understood case of a rigid container with spherical symmetry into which an elastic thread is radially injected through a small opening. A natural question to ask is how stable the packing processes and morphologies observed in spherical cavities are with respect to perturbations to the global shape dictated by the rigid confinement, and so the first step toward more general, deformable cavities is to consider spheroids with an eccentricity in Section 5.1. As argued in Chapter 1, many related biological and medical examples of filament packing occur within confinements that—in one way or another—conform to the shape assumed by the packed threads, thus giving them more freedom to release residual stresses. Generalizing the type of container to an elastic thin shell therefore constitutes the next natural step, which is made in Section 5.2 only to find the role of friction redefined. Finally, in Section 5.3, a change in topology of the filament from an open thread to a closed ring delivers a very comprehensive, novel view on the problem of strongly interacting thin sheets and wires, as the full morphological phase space is quantitatively uncovered.

5.1 Dense packing in rigid containers

When a thin elastic filament is forced into a rigid hollow sphere, its morphogenesis is mainly determined by the amount of contained torsion. This was previously shown by considering two different packing scenarios [152, 214]. In the first, an intrinsically curved wire was injected. If the larger two of the three inherent length scales—the cavity radius R and the equilibrium radius of curvature of the pre-curved wire R^{int}—are incompatible, torsion can be minimized only at the expense of further bending, which induces frequent reorientations in the coils as well as large residual twist, giving rise to very disordered packings. In the second setup, the elastic thread was intrinsically straight, which removed this degree of freedom coupling. It was furthermore allowed to rotate about its own axis at the insertion point such that all torsional elastic energy could dissipate out of the packed system, yielding an ordered structure made of layered coils. While the size of the confining sphere was found to strongly affect the required injection force in the disordered morphology, no account was given on the specific choice of confinement *shape*.

The goal of the simulation series presented in the following is to investigate the packing patterns and energy levels arising purely from imposed global asphericity, and to demonstrate that spherical coils are not naturally found in conforming confinements. To this end, the same two packing conditions (intrinsic curvature vs. free axial rotation) are simulated in rigid isochoric ellipsoids at different aspect ratios (R_x:R_y:R_z, where x is the filament injection axis). The set of cavities comprises a sphere ($1:1:1$), two oblate spheroids ($1:2:2$ and $2:2:1$), two prolate spheroids ($1:1:3$ and $3:1:1$), and three scalene ellipsoids ($1:3:2$, $2:1:3$ and $3:2:1$) so as to capture also the influence of different insertion directions.

Since POISSON's ratio plays only a minor role in thin filament packings, it is fixed to $\nu = 1/3$ here. Similar to the preceding study on spherical confinements [214], the filament is pre-curved with intrinsic radius $1/\kappa^{\mathrm{int}} = R^{\mathrm{int}} = 2R$ in the first setup, where $R = (R_x R_y R_z)^{1/3}$ denotes the equivalent spherical confinement size. Aside from the ellipsoidal eccentricities, this leaves the ratio $q = R/r$ as the only geometric parameter. COULOMB friction is assumed between any two contacting surfaces (filament-filament and filament-cavity) with a static friction coefficient, $\mu_{\mathrm{s}} = 0.2$, and a slightly lower dynamic friction coefficient, $\mu_{\mathrm{d}} = 0.9\mu_{\mathrm{s}}$, like was found to match well experiments on nylon cords in ref. [214]. Generally, frictional forces have no significant morphological influence on this kind of packings in rigid containers, as was verified in various test simulations. The filament is radially inserted at a constant speed, which is set slow enough to make inertial effects negligible on the outcome. Its axisymmetry is broken by imposing a small random initial transverse deflection on the two foremost nodes, which also serves as a convenient method to obtain statistically independent realizations of the same setup. As the filament is injected into the cavity, the computational mesh is gradually extended with additional elements.

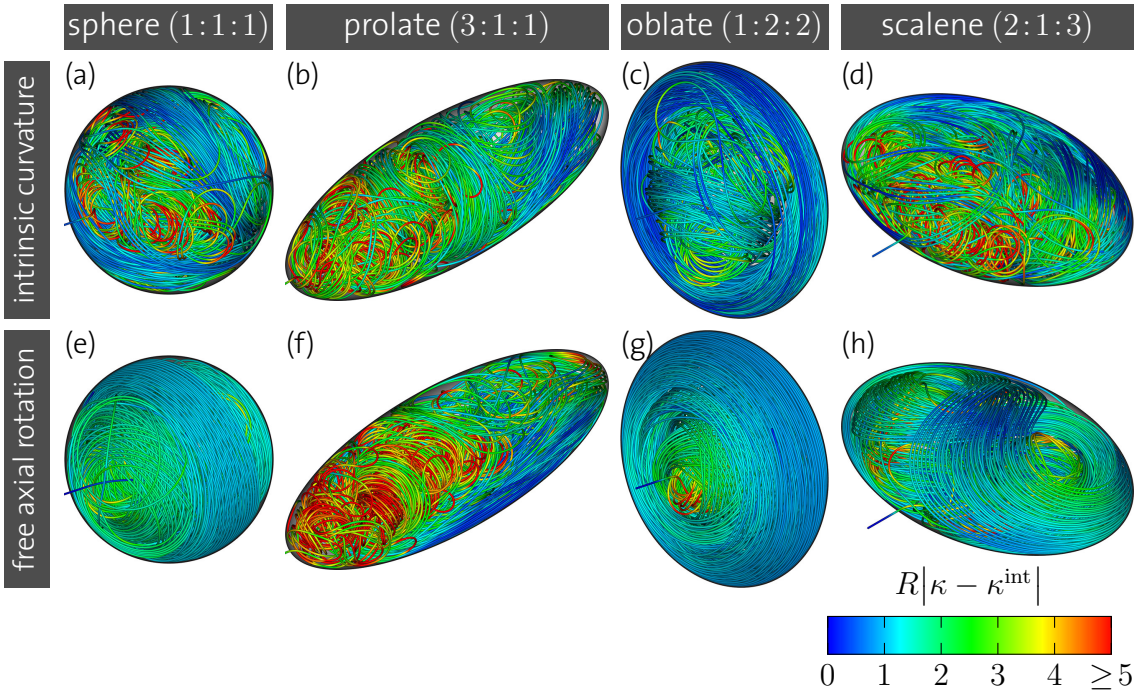

Figure 5.1: **Influence of confinement shape on coiling and crumpling.** A selection of simulated isochoric ellipsoidal cavities with volume $V = \frac{4}{3}\pi R^3$ is shown, where $R = (R_x R_y R_z)^{1/3} = 50r$ is the equivalent sphere radius. The color represents the rescaled elastic curvature. All images to scale, except that the wire radius is halved to reveal the inner structures. The packing densities are $\phi = 40\%$ (sphere), $\phi = 33\%$ (prolate), $\phi = 35\%$ (oblate, intrinsic curvature), $\phi = 48\%$ (oblate, free rotation) and $\phi = 37\%$ (scalene).

5.1.1 Energetics and order

Figure 5.1 shows a selection of the resulting densely packed isochoric ellipsoids at $q = 50$. An exact spherical geometry imposes no preferential orientation to the packed filament, leaving it fully exposed to the effect of coupled or uncoupled bending and torsion, eventually yielding the already known disordered packings and regular layered coils. But the situation changes dramatically when the rotational invariance is broken: Prolate spheroids, for instance, dictate the filament arrangement in early stages through their limited spatial extent perpendicular to the long axis of revolution. In an attempt to minimize large bending stresses, the packed thread coils primarily along the major axis, tilted such that the apical region of high curvature is avoided, which is particularly apparent in Fig. 5.1b. Such inclined coils are indeed found in the slightly elongated hagfish gland thread cells (see Fig. 1.2). As more thread gets injected, the central part of the cavity is filled with a coiling pattern similar that of spheres, because the elongated tip has been filled already, restoring more or less isotropic geometrical constraints in the middle. Further filament insertion finally leads to *crumpling*: Since there is almost no more room to fill, the bulk

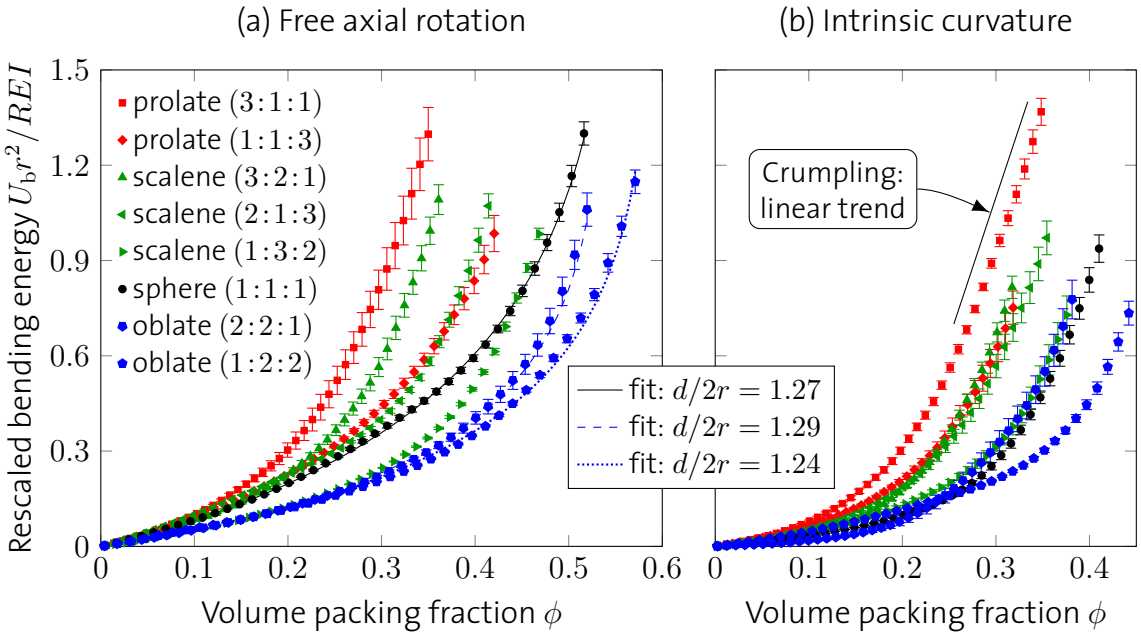

Figure 5.2: **Bending energy for different isochoric ellipsoidal cavities.** Error bars denote standard errors from $8-9$ independent simulations at $q = 40$. The fitted curves correspond to the analytical approximation in equation (5.7), which holds only for the setup without intrinsic curvature in spheres and oblate spheroids.

structure is axially compressed by the pushing filament. In turn, succeeding thread segments tightly curve under the action of bulk pressure.

Not surprisingly, oblate spheroids (Fig. 5.1c,g) exhibit a very different packing process. The preferred winding direction imposed by the single short principal axis leads to a highly ordered coil early on, largely independent of the (moderate) filament pre-curvature. Only at larger densities, when the coiling radius starts to compete with the transverse length scale R_x, loop reorientations let the coiling behavior known from spherical confinement be retrieved. The final morphology is thus split into an ordered coil at the outer rim and an inner part with the same characteristics as in a sphere. Scalene ellipsoids lie somewhat in between these two extremes, blurring the aforementioned effects. The typical trait at moderate aspect ratios is a figure-eight coil when intrinsic curvature is absent (Fig. 5.1h).

Owing to their slenderness, packed thin filaments favor bending deformations over compression, tension or twist, letting the bending energy U_b dominate all other elastic energy contributions. In order to compare the energetics in different packing geometries, it is hence sufficient to consider U_b only. Figure 5.2 shows the dimensionless bending energy for all simulated configurations as a function of the volume density

$$\phi = \frac{AL}{4/3\,\pi R_x R_y R_z} = \frac{3}{4q^3}\frac{L}{r}, \tag{5.1}$$

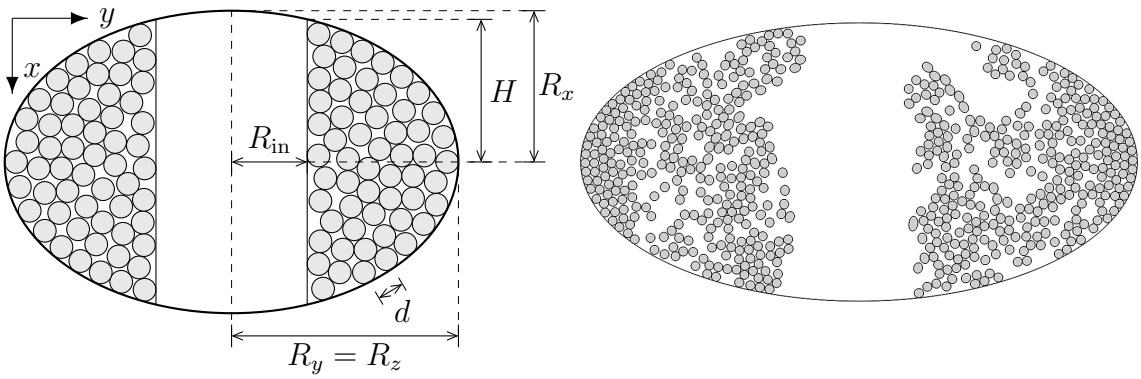

Figure 5.3: **Cross section of wire coils in oblate spheroids.** Left: PUROHIT hoop model with its geometric parameters. Right: Simulation snapshot of the $1:2:2$ oblate.

which is perhaps the most natural measure of the packing progress. Here, $L = \int_\Gamma \mathrm{d}s$ represents the injected filament length and $A = \pi r^2$ is its cross section area. It is evident that prolate spheroids are the energetically least favorable shapes, independent of whether the thread is slightly pre-curved or not. When crumpling sets in at large packing density, the bending energy transitions to a linear increase $U_\mathrm{b} \sim \phi$. The competitive position of scalene ellipsoids strongly varies with the axis along which the filament is injected—only if it points in the direction of least cavity extent (as in $1:3:2$), scalene shapes can keep up with spheres. As intuitively expected, oblate spheroids win the race from beginning to end.

The ordered coils observed in packed spheres or oblate spheroids with $R_x \leq R_y = R_z$ can be approximated analytically following the ideas of PUROHIT et al. [172]. Their geometrical model, which was originally devised for the description of DNA strands in viral capsids, has been successfully applied to ordered coiling in spherical wire packings [214] and is generalized here for oblate cavities. It is based on the approximation that thin filaments coil such that their binormal vectors are always parallel to the feeding axis x, and that their radius of curvature about this axis is maximal, resulting in an empty cylindrical region about x as sketched in Fig. 5.3. Let R_in be the radius of this empty column, and H its half height, which is determined by

$$H^2(R_\mathrm{in}) = R_x^2 - \left(R_\mathrm{in}\frac{R_x}{R_y}\right)^2 \tag{5.2}$$

for an oblate spheroid. Assuming that the centerlines of individual strands in the coil are separated by $d(\phi) \geq 2r$ on average, the number of windings along the height is given by

$$\omega(R_\mathrm{in}) = \frac{2H(R_\mathrm{in})}{d(\phi)}. \tag{5.3}$$

The total filament length L and bending energy U_b are now approximated by replacing the sum over a discrete set of closed hoops by integrals over the packed volume,

leading to

$$L(R_{\mathrm{in}}) = \frac{2}{\sqrt{3}d(\phi)} \int_{R_{\mathrm{in}}}^{R_y} 2\pi y \omega(y)\ \mathrm{d}y, \tag{5.4}$$

$$U_{\mathrm{b}}(R_{\mathrm{in}}) = \frac{2}{\sqrt{3}d(\phi)} \int_{R_{\mathrm{in}}}^{R_y} \frac{\pi EI}{y} \omega(y)\ \mathrm{d}y, \tag{5.5}$$

where the prefactor $2/\sqrt{3}d(\phi)$ stems from the further assumption of hexagonal packing with spacing $d(\phi)$ in any cross section perpendicular to the coil. By recalling the definition of the packing density from equation (5.1),

$$\phi(R_{\mathrm{in}}) = \frac{3r^2 L(R_{\mathrm{in}})}{4R_x R_y^2}, \tag{5.6}$$

the auxiliary inner radius R_{in} in equations (5.4) and (5.5) can be substituted for ϕ. Evaluating these integrals then results in the sought approximation for the total bending energy:

$$U_{\mathrm{b}}(\phi) = \frac{4\pi}{\sqrt{3}} \frac{R_x EI}{d^2(\phi)} \left(\log \left[\frac{1 + k(\phi)}{\sqrt{1 - k^2(\phi)}} \right] - k(\phi) \right) \tag{5.7}$$

where

$$k^3(\phi) = \frac{2\sqrt{3}\phi}{\pi} \left(\frac{d(\phi)}{2r} \right)^2. \tag{5.8}$$

Note in particular that $U_{\mathrm{b}} \sim R_x$ independent of R_y (at fixed ϕ and assuming constant d), i.e., the thinner the oblate cavity, the lower the bending energy of the packed coil. The only remaining unknown variable is the segment distance $d(\phi)$, that is in general a function of the packing density. Motivated by the observation that the density dependence of d is very weak in the spherical limit [214], it is used here as a constant parameter to fit equation (5.7) to the numerical data plotted in Fig. 5.2, with excellent agreement in all cases.

From the bending energy in equation (5.7), one can deduce the elastic force F required to inject the wire as the derivative with respect to the wire length L, which, after some algebra, reduces to the remarkably simple form

$$F(\phi) = \frac{\mathrm{d}U_{\mathrm{b}}(\phi)}{\mathrm{d}L} = \frac{EI}{R_y^2} \frac{1}{2(1 - k^2(\phi))}. \tag{5.9}$$

A beautiful property of this analytical model is that both the bending energy and the insertion force diverge as $k(\phi) \to 1$, which is the case when the packing density reaches its theoretical maximum

$$\phi_{\max} = k^{-1}(1) = \frac{\pi}{2\sqrt{3}} \left(\frac{2r}{d} \right)^2. \tag{5.10}$$

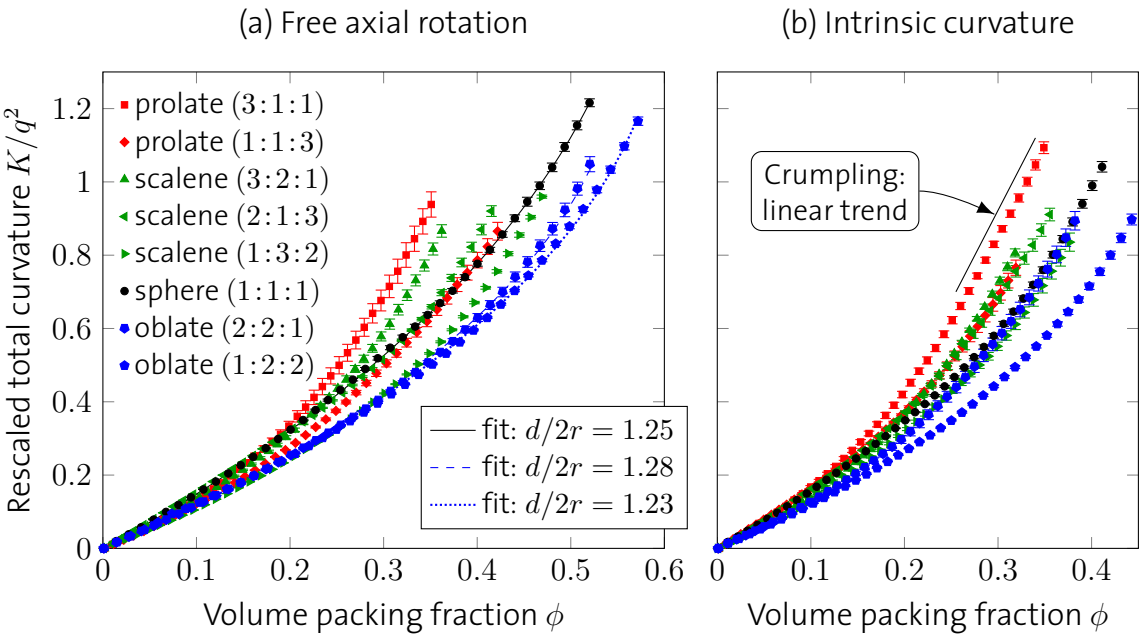

Figure 5.4: **Total curvature for different isochoric ellipsoidal cavities.** Error bars denote standard errors from $8-9$ independent simulations. The fitted curves correspond to the analytical approximation in equation (5.11).

For $d \to 2r$, this corresponds to hexagonal close-packing of the circular wire cross sections ($\phi_{\max} \approx 0.9069$).

Following the same lines, one can determine the total curvature K of the inserted wire as

$$\begin{aligned} K(\phi) &= \int_0^{L(R_{\text{in}})} \frac{1}{R_{\text{in}}(s)}\,\mathrm{d}s \\ &= \frac{4\pi}{\sqrt{3}}\frac{R_x R_y}{d^2(\phi)}\left(\sin^{-1}[k(\phi)] - k(\phi)\sqrt{1-k^2(\phi)}\right) \end{aligned} \tag{5.11}$$

for $\phi \leq \phi_{\max}$, in which the local radius of curvature $1/\kappa(s) = R_{\text{in}}(s)$ is the inverse of equation (5.4). Numerical measurements of the total filament curvature are plotted in Fig. 5.4 for all eight ellipsoidal cavities and for the configurations with and without intrinsic curvature. Equation (5.11) approximates the data with excellent agreement in oblate spheroids and spheres. In accordance with the previous observation on bending energy, the total curvature is more affected by confinement asphericity than by pre-curvature, and also the fit parameters d are consistent. Likewise, the crumpling regime in prolate cavities can be recognized by a linear trend $K \sim \phi$.

As proposed in ref. [215], the radius of gyration of the filament,

$$R_{\text{g}}^2 = \frac{1}{M}\int_V \|\mathbf{r}-\overline{\mathbf{r}}\|^2 \rho\,\mathrm{d}V, \qquad \overline{\mathbf{r}} = \frac{1}{M}\int_V \mathbf{r}\rho\,\mathrm{d}V, \qquad M = \int_V \rho\,\mathrm{d}V, \tag{5.12}$$

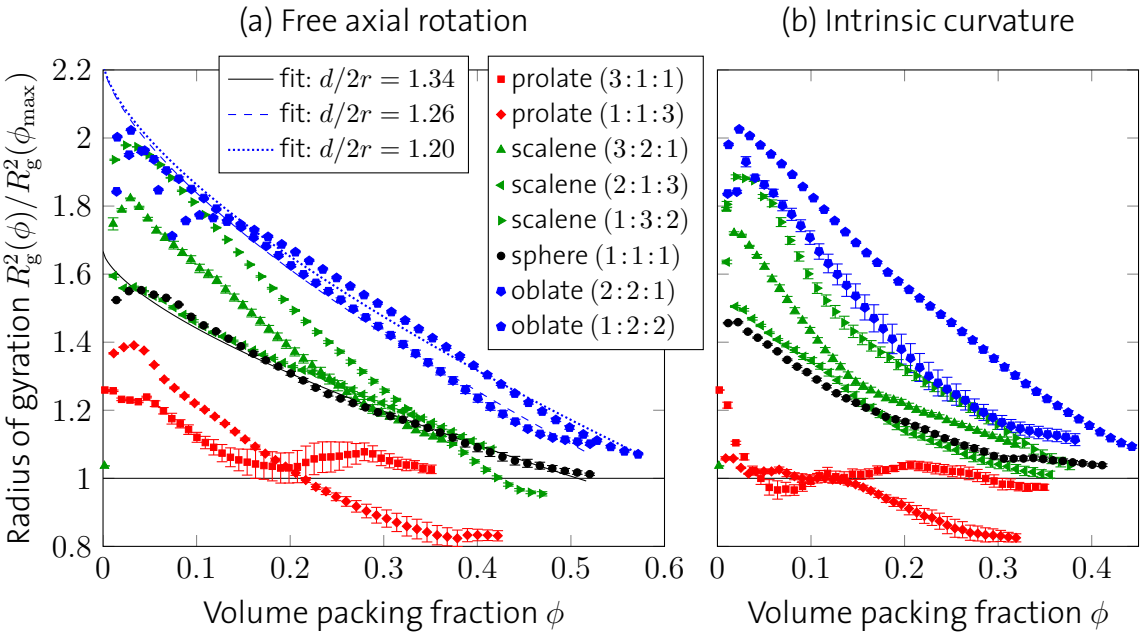

Figure 5.5: **Radius of gyration for different isochoric ellipsoidal cavities.** Error bars denote standard errors from $8-9$ independent simulations. The fitted curves correspond to the analytical approximation in equation (5.14).

can be used to further quantify the packing morphology. In the analytical hoop model it is approximated as

$$R_g^2 = \frac{1}{M}\int_{R_{in}}^{R_y}\int_{-H(y)}^{H(y)} 2\pi y(x^2+y^2)\rho \,\mathrm{d}x\,\mathrm{d}y, \tag{5.13a}$$

$$M = \int_{R_{in}}^{R_y}\int_{-H(y)}^{H(y)} 2\pi y\rho \,\mathrm{d}x\,\mathrm{d}y. \tag{5.13b}$$

By writing $R_{in}(\phi) = R_y\sqrt{1-k^2(\phi)}$, one thus easily finds

$$R_g^2(\phi) = \frac{1}{5}\big(k^2(\phi)R_x^2 + \big[5-3k^2(\phi)\big]R_y^2\big), \tag{5.14}$$

which nicely converges to the radius of gyration of a solid ellipsoid with uniform spatial mass distribution,

$$R_g^2(\phi_{max}) = \frac{1}{5}\big(R_x^2+R_y^2+R_z^2\big). \tag{5.15}$$

As demonstrated in Fig. 5.5, equation (5.14) is a reasonable approximation to the effectively observed data. It is no surprise that during early stages ($\phi \lesssim 0.1$), the analytical model is an overestimation, because it takes a few windings for the coil to mask the effect of the short piece that has just entered and is therefore still located close to the center. Once again, confinement shape is more determinant for the

packing process than the imposed intrinsic curvature. An apparent morphological feature of prolate packings that can be read off Fig. 5.5 is that the radius of gyration drops well below its theoretical bulk value at full packing, indicating that the filament fills the elongated container very inhomogeneously, avoiding the outer regions near the tip. This quantitatively confirms the impression one gets from Fig. 5.1b,f.

5.1.2 Entanglement

Thinking about how easily an earphone cord gets tangled up in one's pockets, it is natural to ask how much a thin thread will do the same when injected into a container in the present, more controlled environment. Does it form knots, which will prevent one from pulling it out again? This question is particularly relevant for DNA packing in capsids, where a deadlock would have fatal consequences. Entanglement of a space curve $\Gamma\colon\, s \mapsto \mathbf{x}(s)$ can be quantified in a multitude of ways. Among the most common measures is the linking number

$$\mathrm{LN} = \frac{1}{4\pi} \int_{s\in\Gamma} \int_{s'\in\Gamma} \frac{(\mathbf{x}(s) - \mathbf{x}(s')) \cdot (\mathrm{d}\mathbf{x}(s) \times \mathrm{d}\mathbf{x}(s'))}{\|\mathbf{x}(s) - \mathbf{x}(s')\|^3} \tag{5.16}$$

that dates back to the famous works of GAUSS [68]. It counts the number of (signed) filament crossings averaged over all vantage points, and is an integral number for closed Γ. Albeit it is most frequently and fruitfully employed in the theory of knots, which are embeddings of closed circles in Euclidean space, nothing prevents one from calculating the linking number also for filaments with open ends, such as the ones injected into cavities here, as it conveys morphological information on how the filament coils or crumples. The linking number is a chiral property, meaning that its sign is coincidental here and on average it will cancel out. The quantity of interest is thus its magnitude $|\mathrm{LN}|$.

A closely related measure of entanglement is the average crossing number [67]

$$\mathrm{ACN} = \frac{1}{4\pi} \int_{s\in\Gamma} \int_{s'\in\Gamma} \frac{|(\mathbf{x}(s) - \mathbf{x}(s')) \cdot (\mathrm{d}\mathbf{x}(s) \times \mathrm{d}\mathbf{x}(s'))|}{\|\mathbf{x}(s) - \mathbf{x}(s')\|^3} \tag{5.17}$$

whose only distinction from LN is that it neglects the type (sign) of the crossings, making it an achiral invariant. ACN has been used for instance to characterize the spontaneous knotting of open strings agitated in spatial confinement [176]. Only recently its relationship with the total curvature has been rigorously established [22, 59]. The average crossing number of a knot is bounded by the total curvature K and the normalized filament length $l = L/R$ as

$$\mathrm{ACN} \leq cK\sqrt{l} \tag{5.18}$$

where c is a constant independent of the knot. In Fig. 5.6 it is shown that this upper bound does not apply in the present thread packing problem. Instead, the

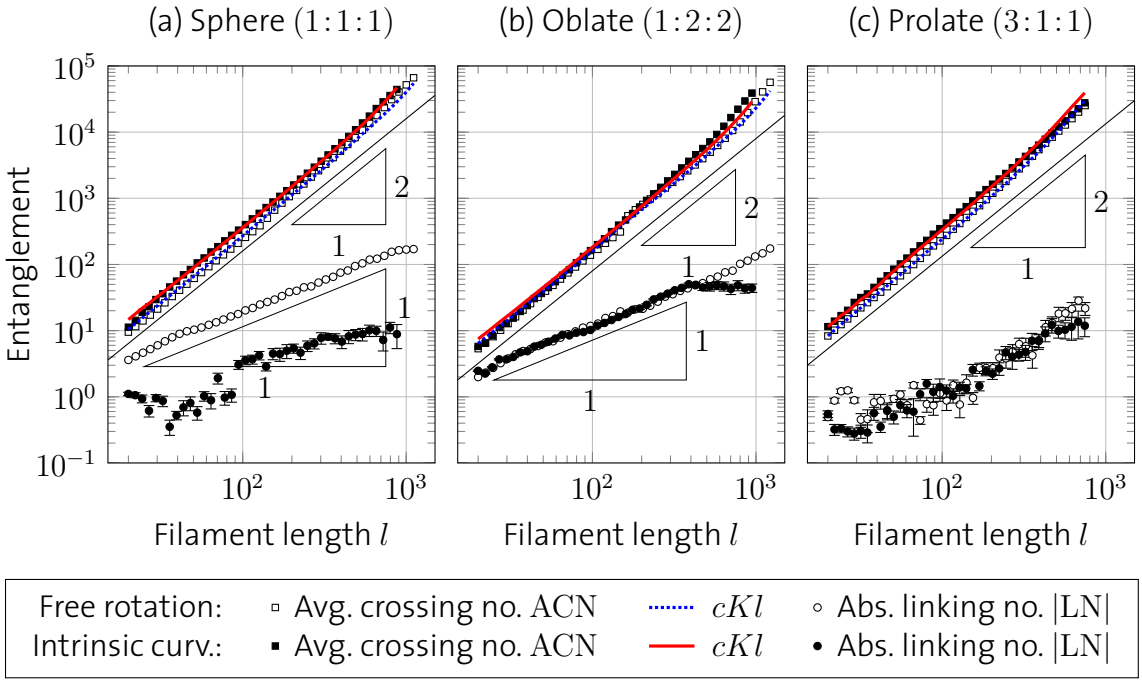

Figure 5.6: **Filament entanglement in different isochoric ellipsoidal cavities.** Error bars denote standard errors from $8-9$ independent simulations, and are omitted where significantly smaller than the symbols or line widths.

relationship

$$\mathrm{ACN} \approx cKl \tag{5.19}$$

is empirically observed, independent of the ellipsoidal shape. For random circles in a sphere, it is known that $\mathrm{ACN} \sim l^2$ [21]. K is superlinear in l here (recall Fig. 5.4), however, and indeed the measured ACN deviates accordingly from the quadratic scaling l^2. Although ACN is merely an *estimate* of entanglement, the violation of equation (5.18) is a clear indication that the packed filaments are not knotted. Preliminary simulations in which the threads could be pulled out of their confinement again without blockage confirmed this conjecture (data not shown).

Unlike ACN, LN is strongly dependent on the imposed global geometry and intrinsic curvature. In ordered coils, its absolute value scales linearly with the packing density, $|\mathrm{LN}| \sim l \sim \phi$ (at fixed q). The frequent loop reorientations in disordered morphologies, on the other hand, let LN fluctuate about zero and its magnitude consequently shows no clear functional relationship with l. The kink of $|\mathrm{LN}|$ in Fig. 5.6b reveals the point where the pre-curved wire changes its inner coiling orientation for the first time in an oblate spheroid, as displayed in Fig. 5.1c.

In summary of Section 5.1, the systematic variation of ellipsoidal aspect ratios unveiled how geometric restrictions imposed by the container shape dictate how an injected thread coils and crumples. Oblate shapes offer a clear energetic advantage

over spheres or more elongated confinements, leaving no doubt that a sufficiently deformable cavity will not naturally take a spherical form when filled with a thin thread. This fundamental finding suggests that recently acquired knowledge on filament packings in rigid spheres [152, 214] could be of limited applicability to biological or medical applications where the confining hull is conforming in one way or another, like in the surgical occlusion of cerebral aneurysms. There is hence a strong motivation to generalize the rigid cavities to flexible shells, which is the main subject of Sections 5.2 and 5.3.

5.2 Dense packing in flexible containers

As a consequence of the numerical and analytical considerations in the previous section, an obloid configuration suggests itself as the equilibrium shape of a deformable membrane a thin wire is forced into. In fact, similar forms have been experimentally obtained by enclosing elastic nanotubes and nanowires with polymer shells and emulsion droplets, which were then intentionally contracted [32, 33, 242]—a technique that has been advocated as a way to store and deploy mechanical work on the nano- to microscale through spatial confinement. Monte Carlo simulations at finite temperature have likewise indicated [66, 139] that soft vesicles deform into obloids when enclosing a fluctuating polymer chain whose persistence length grows much larger than the vesicle diameter. These studies, however, were limited in a combination of the following ways:

- Thermal fluctuations masked the ground state configurations in MC simulations, bounding their direct significance to the molecular scale.
- The exact equilibrium confinement shape wasn't quantitatively measured.
- Friction was disregarded.
- The effects of either in-plane shearing, stretching or bending of the flexible hull were disregarded.

In the following, these restrictions are all eliminated. The goal of this section is to identify the inherent macroscopic parameters that govern morphogenesis of a long, slender filament as it is fed into a flexible shell, to quantitatively characterize the emerging forms and packing patterns, and to emphasize on the differences to the packing process in rigid cavities.

Figure 5.7 shows a cutout of the computational model with all essential control parameters. Both filament and sheet are characterized by three homogeneous isotropic material parameters, henceforth labelled with subscripts f and s for easy distinction between the two elastic bodies: the YOUNG's modulus E, POISSON's ratio ν, and the mass density ρ. POISSON's ratios are fixed to $\nu_\mathrm{f} = \nu_\mathrm{s} = 1/3$. COULOMB's law is assumed for dry stick-slip friction between any two contacting surfaces (filament-

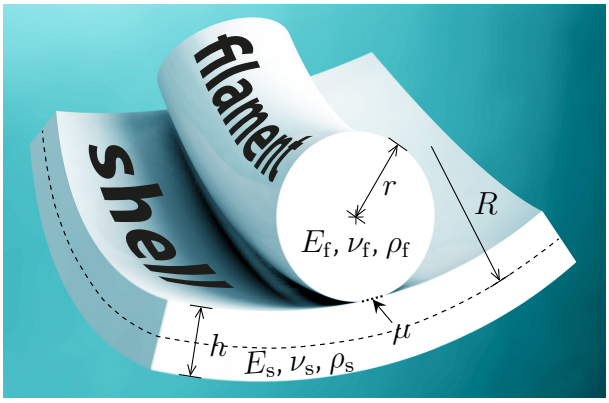

Geometry:
Nominal confinement size $q = R/r$
FÖPPL–VON KÁRMÁN number $\gamma = (R/h)^2$

Material:
Relative confinement flexibility $f = E_\mathrm{f}/E_\mathrm{s}$
COULOMB friction coefficient $\mu = \mu_\mathrm{s}$

Figure 5.7: **Schematic of the interaction model.** Both the filament and the confining spherical sheet are characterized by a YOUNG's modulus E, POISSON's ratio ν and mass density ρ. Stick-slip COULOMB friction between any contacting surfaces is assumed. The morphogenesis is governed by only four dimensionless numbers: q, γ, f and μ.

filament, filament-shell, shell-shell) with $\mu_\mathrm{s} = 0.9\mu_\mathrm{d}$ as before, which is adequate for a broad class of materials [62]. To simplify the parameter space further, the same coefficients are used for all three contact types. An intrinsically straight thread is radially injected into a thin shell whose unstrained equilibrium configuration is a sphere with radius R and thickness h as shown in the figure. Like in the previous section, the feeding velocity is kept constant and small enough to let the system continuously relax close to static equilibrium at all times, and a small random transverse deflection is initially added to the wire to break the rotational symmetry about the feeding axis. The confining shell is held in place by imposing zero displacement on a narrow rim about the small opening through which the thread is injected.

A key result from the computer simulations is that this morphogenesis is controlled by four independent dimensionless non-negative quantities,

$$q = \frac{R}{r}, \quad \gamma = \left(\frac{R}{h}\right)^2, \quad f = \frac{E_\mathrm{f}}{E_\mathrm{s}}, \quad \mu = \mu_\mathrm{s}, \tag{5.20}$$

if inertial effects are negligible. Up to an irrelevant prefactor, γ is the FÖPPL–VON KÁRMÁN number as defined in equation (4.1). f is the relative filament rigidity, which conversely may also be thought of as the confinement flexibility. γ and f generalize the previously studied rigid cavities, which are attained in the limits $\gamma \to 0$ and $f \to 0$. Together with γ, expressing the nominal system size by the non-dimensional ratio q renders the problem scale-invariant, which attests to the wide applicability of the results from microscopic to macroscopic scales. Since the volume enclosed by the flexible shell is not constant, the packing density ϕ as defined in equation (5.1) is no longer proportional to the inserted filament length L, and can well be non-monotonic. $l = L/R$ instead of ϕ therefore lends itself as a suitable measure for the packing progress.

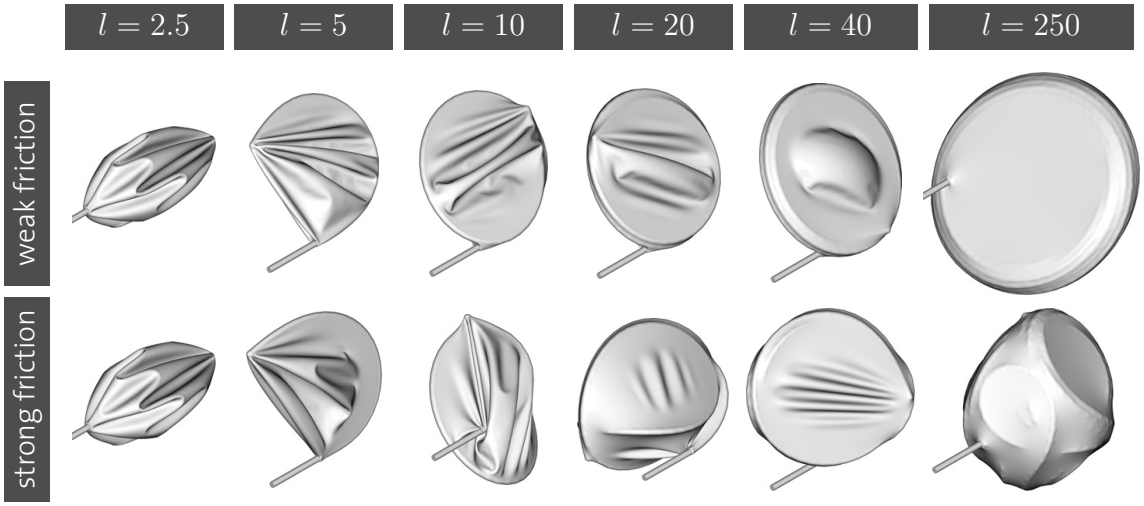

Figure 5.8: **Packing evolution in flexible confinement.** Series of simulation snapshots at $\mu = 0$ (top row) producing aligned coils, and at $\mu = 0.5$ (bottom row) producing disordered space-filling packings. The remaining parameters are $q = 20$, $\gamma = 200^2$, $f = 100$. All images to scale.

5.2.1 Morphological phases

The typical packing evolution obtained in very elastic or very thin shells is displayed in Fig. 5.8. At weak frictional forces, a highly ordered packing pattern is observed in which the filament bundles into a tight circular *coil* that continues to grow and stretch the confining shell as more thread is injected. Eventually, both upper and lower faces of the membrane are fully flattened by the stretch, turning it into the convex hull of the enclosed coil. When friction is activated, however, the situation is dramatically changed: Tangential sliding is hampered, which lets the wire tip poke the surrounding shell significantly. The compressive forces acting on the inserted thread are much higher in consequence, and soon let it buckle out of the coiling plane to form a more three-dimensional packing process. Clearly, only sufficiently flexible shells allow for this kind of spontaneous loop reorientation. As more and more wire is fed in, the reorientation process is frequently repeated, yielding a *crumpled* structure that tends toward an approximately spherical bulk shape—a feature that previous works didn't capture [66, 139]. Due to the thin shell's tensile flexibility, frictional forces between the two thin objects let the pushing filament locally drag its confinement along a small distance, making static friction much more relevant in deformable than in rigid confinements. This unique feature explains the main observation reported here: unlike in rigid cavities, frictional forces become a key player for filament morphogenesis in deformable shells. This characteristic crumpling behavior is easy to reproduce manually in table-top experiments, an example of which is shown in Fig. 5.9. Note the manifest resemblance between the experimentally obtained structure and the computer simulation in the lower right panel of Fig. 5.8.

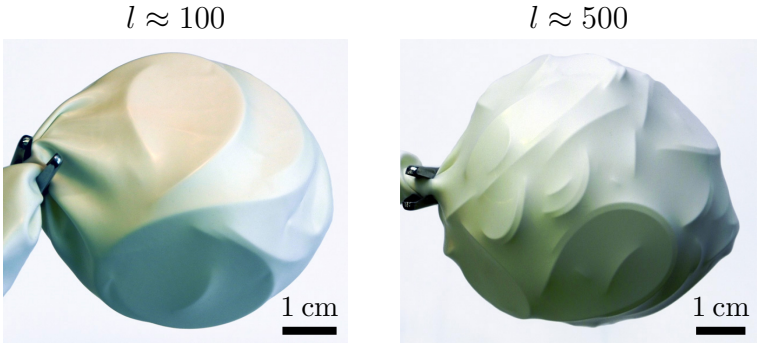

Figure 5.9: **Experimental realization of the crumpled morphology.** A polycaprolactam wire ($r = 0.5\,\mathrm{mm}$), manually fed into a customary inflatable balloon made of natural rubber ($R = 27\,\mathrm{mm}$, $h = 0.25\,\mathrm{mm}$), spontaneously crumples due to friction.

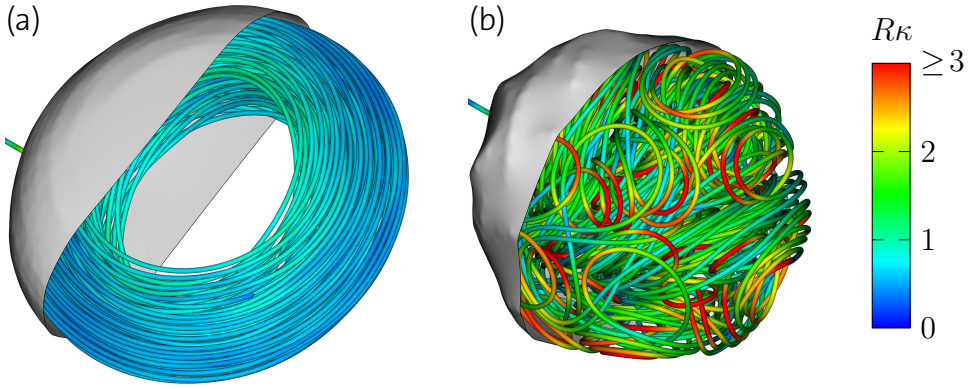

Figure 5.10: **Packing morphologies in flexible confinement.** (a) Toroidal coiling at weak friction ($\mu = 0$). (b) Space-filling crumpling at strong friction ($\mu = 0.5$). The further relevant simulation parameters are $q = 20$, $\gamma = 10^2$, $f = 10^3$, and the packed filament length is $l = 800$. In color, the rescaled filament curvature is shown. Images to scale, except that the wire radius is halved to reveal the inner structure.

In the remainder of Section 5.2, these two distinct morphologies and the transition between them are quantitatively analyzed. For simplicity, the system parameters are fixed to $q = 20$, $\gamma = 10^2$, $f = 10^3$, $\mu = 0, 0.5$—a choice for which the morphological characteristics of the two phases are pronounced most clearly. Fig. 5.10 provides insight into the inner packing structure for these two settings.

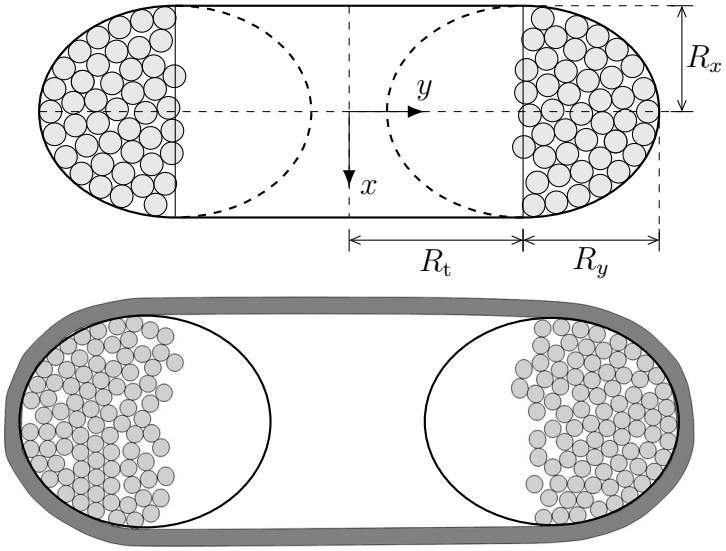

Figure 5.11: **Cross section of a coiled wire in a flexible shell at low friction.** Top: PUROHIT hoop model with its geometric parameters. Bottom: Simulation snapshot at $l = 800$ with superposed ellipses.

5.2.2 Energetics and order

An intriguing feature in the frictionless case is that the long, flexibly confined filament coils into a dense circular bundle whose cross section is very well approximated by two half ellipses. The central portion of the cavity is left unoccupied just like in rigid oblate spheroids (see Section 5.1) as a result of the wire's tendency to minimize its dominant elastic energy contribution, the bending energy. A typical cross section of the coil with fully stretched lateral faces of the thin shell is displayed in Fig. 5.11 in support of this statement. It is thus an easy task to generalize PUROHIT's hoop model, that proved to capture the energetic and structural properties of ordered coiling in rigid oblates extremely well, to the present flexible cavities. Aside from the filament spacing $d(L)$, the unknown cross-sectional parameters are the major radius of the toroidal coil, R_t, and its two minor radii R_x, R_y, as labeled in the upper panel of Fig. 5.11. The evolution of these three radii with the packed thread length depends on the system parameters q, γ, f, but the common typical functional form is well approximated by a power-law scaling

$$\frac{R_t}{R} \sim l^{\alpha}, \qquad \frac{R_x}{R} \sim l^{\beta}, \qquad \frac{R_y}{R} \sim l^{\gamma} \tag{5.21}$$

within a certain range of the rescaled thread length $l = L/R$, as demonstrated in Fig. 5.12. The best fits for $q = 20$, $\gamma = 10^2$, $f = 10^3$ are $\alpha = 0.04 \pm 0.01$, $\beta = 0.35 \pm 0.01$, $\gamma = 0.46 \pm 0.01$, indicating that while the minor radii grow quickly, the major radius R_t remains approximately constant. $\alpha \approx 0$ is indeed expected for very flexible cavities, since $1/R_t$ is the maximum curvature in the coil, the square of which is minimized according to the principle of minimum energy.

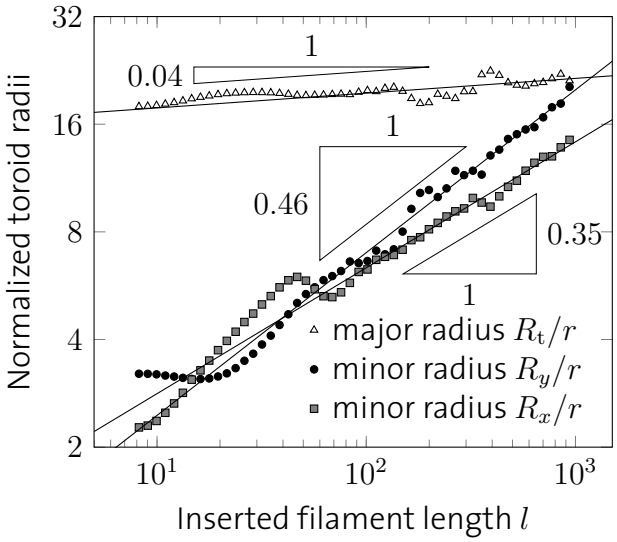

Figure 5.12: **Scaling of the shape of the filament coil in flexible confinement.** Data obtained by fitting semi-ellipses to the cross sections of a numerical simulation at $q = 20$, $\gamma = 10^2$, $f = 10^3$, $\mu = 0$, as shown in Fig. 5.11.

Carrying on in the derivation of an analytical model for the toroidal coil, in place of equation (5.4), the packed thread length follows as

$$\begin{aligned} L &= \frac{2}{\sqrt{3}d(L)} \int_0^{R_y} 2\pi(R_\mathrm{t} + y)\omega(y)\ \mathrm{d}y \\ &= \frac{4\pi}{\sqrt{3}} \frac{R_x R_y^2}{d^2(L)} \left(\frac{2}{3} + \frac{\pi}{2}\varrho \right) \end{aligned} \tag{5.22}$$

where $\varrho = R_\mathrm{t}/R_y$ and the number of windings ω is given by equations (5.2) and (5.3). This fixes the average strand separation $d(L)$ given that $L, R_\mathrm{t}, R_x, R_y$ are known. Analogously, one can calculate the volume V enclosed by the deformed shell as the sum of the unoccupied cylinder and the packed toroidal rim, which yields

$$\begin{aligned} V(L) &= 2\pi R_x R_\mathrm{t}^2 + \int_0^{R_y} \int_{-H(y)}^{H(y)} 2\pi(R_\mathrm{t} + y)\ \mathrm{d}x\,\mathrm{d}y \\ &= 2\pi R_x R_\mathrm{t}^2 \left(\frac{2}{3} + \frac{\pi}{2}\varrho\left[\varrho + \frac{\pi}{2}\right] \right). \end{aligned} \tag{5.23}$$

As shown in Fig. 5.13a, equation (5.23) approximates the effective measured volume quite well, except at the early stage where the wire is not yet stretching the confining thin shell to a convex hull. In contrast, the enclosed volume of the *crumpled* morphology at $\mu = 0.5$ increases linearly with l—a direct consequence of the uniform disorder in the system.

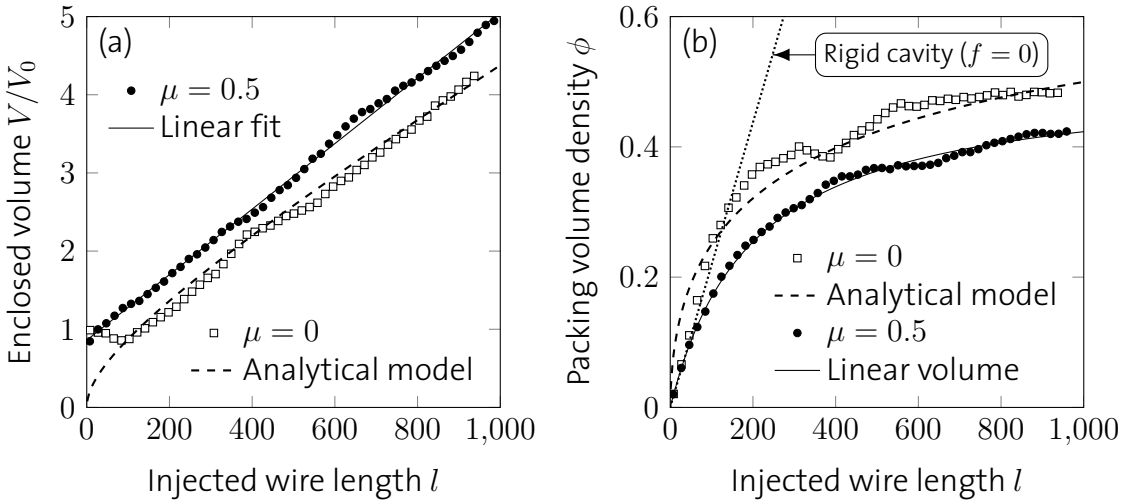

Figure 5.13: **Filament packing progress in flexible confinement.** For normalization, the initial volume $V_0 = 4\pi(R-h/2)^3/3$ is used. The dashed analytical curves for $\mu = 0$ are obtained by plugging the power law fits of equation (5.21) into equation (5.23).

From the volume, one can derive the volume packing density $\phi = AL/V$, where A is the cross-sectional area of the filament. It is plotted against l in Fig. 5.13b together with the linear relationship for rigid cavities ($f = 0$), to demonstrate that the packing process of thin wires in flexible containers can typically be divided into two regimes: Early on, the shell is stretched such that $\phi(f > 0) > \phi(f = 0)$, but upon further packing, the shell expands such that $\phi(f > 0) \ll \phi(f = 0)$. Not surprisingly, the power-law scaling of the coil dimensions in equation (5.21) sets in only after the crossover point $\phi(f > 0) = \phi(f = 0)$ has been passed.

The toroidal analog of equation (5.7) for the filament bending energy in flexible shells reads

$$\begin{aligned} U_\mathrm{b}(L) &= \frac{2}{\sqrt{3}d(L)} \int_0^{R_y} \frac{\pi E_\mathrm{f} I}{R_\mathrm{t} + y} \omega(y)\ \mathrm{d}y \\ &= \frac{4\pi}{\sqrt{3}} \frac{R_x E_\mathrm{f} I}{d^2(L)} \left(\sqrt{1-\varrho^2} \log\left[\frac{1+\sqrt{1-\varrho^2}}{\varrho} \right] + \frac{\pi}{2}\varrho - 1 \right). \end{aligned} \tag{5.24}$$

Using equation (5.22), the unknown $d(L)$ can be eliminated to yield the final expression

$$U_\mathrm{b}(L) = \frac{L E_\mathrm{f} I}{R_y^2} \left(\sqrt{1-\varrho^2} \log\left[\frac{1+\sqrt{1-\varrho^2}}{\varrho} \right] + \frac{\pi}{2}\varrho - 1 \right) \Big/ \left(\frac{2}{3} + \frac{\pi}{2}\varrho \right). \tag{5.25}$$

Note that equation (5.25) is real-valued even for $\varrho > 1$. U_b is monotonically decreasing in ϱ, and thus the filament favors toroidal configurations with large major radius R_t but small minor radii R_x, R_y. This tendency of the filament competes with the shell

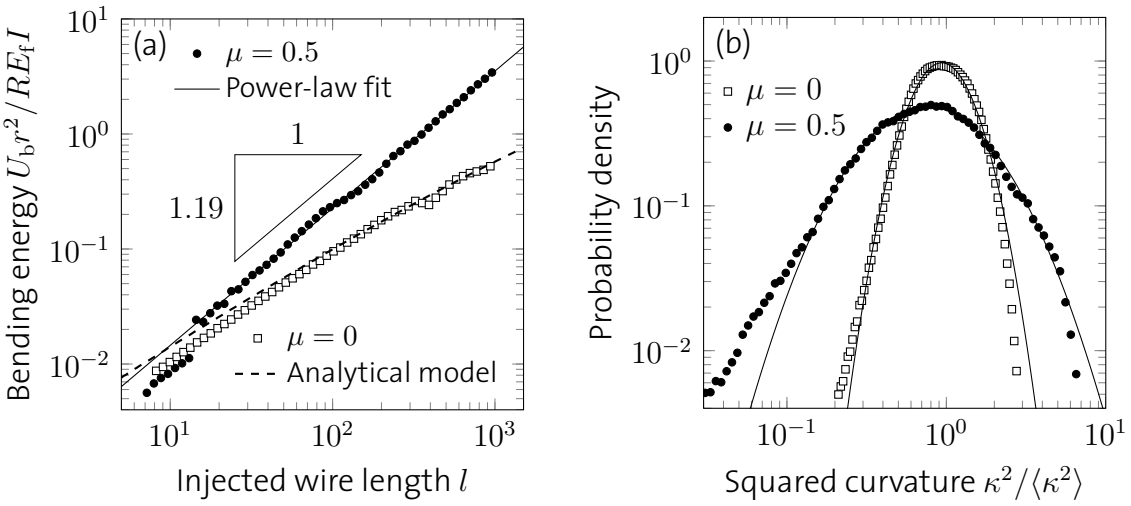

Figure 5.14: **Filament energetics in flexible confinement.** The dashed line in (a) corresponds to the analytical approximation in equation (5.25) with the fitted power laws from equation (5.21) plugged in. In (b), best-fitting log-normal distributions are represented by solid lines.

deformations necessary to adopt such a shape. In Fig. 5.14a, the rescaled bending energies of both morphologies are compared. The numerically measured bending energy of the coiled morphology is very well approximated by Eq. 5.25, with only a slight overestimation at low packing. The crumpled morphology at $\mu = 0.5$, on the other hand, exhibits a clear power-law trend

$$\frac{U_b r^2}{RE_f I} \sim l^{1.19}, \tag{5.26}$$

with exponent 1.192 ± 0.006, which hints at a hierarchic inner packing structure: The more filament is injected, the more spatial freedom is limited, resulting in higher bending curvature in the newly formed loops. The bulges visible in Fig. 5.9 provide some intuition on this phenomenon. Generally, the packing structure in flexible shells is much more stable than in rigid cavities. Once a certain filament segment has taken position, the enclosing membrane fits the structure so tightly that it won't reorient much later on.

In rigid spheres, the distribution of bending energies in disordered wire packings is well fit by a log-normal probability density, with the exception of a larger tail toward low values [214]. The same holds here for the crumpled morphology in elastic shells, albeit with quite a different origin. In rigid spheres, such hierarchic disorder needed to be introduced by artificially pre-curving the wire, whereas tight membrane confinement induces this hierarchy naturally even with straight threads. Figure 5.14b shows that the logarithm of the normalized local squared curvature follows a normal

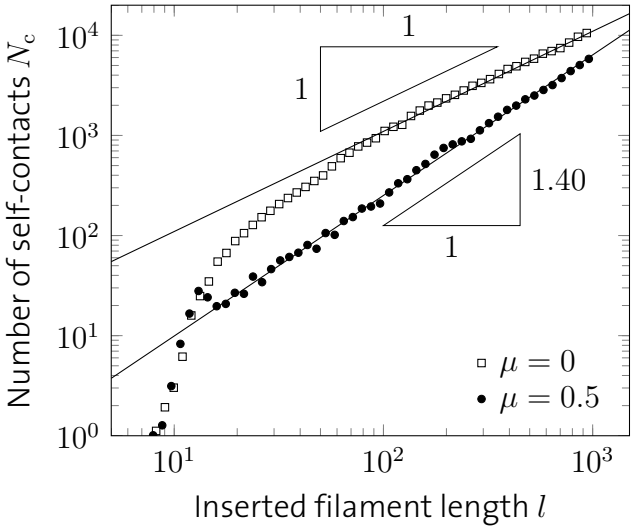

Figure 5.15: **Number of filament self-contacts in flexible confinement.** Low friction leads to dense filament alignment with hexagonal packing, hence $N_c \sim l$ once a few coil windings are established. The hierarchic crumpling pattern at strong friction manifests itself in a power law for the number of wire-wire contacts with exponent 1.40 ± 0.01 at $\mu = 0.5$.

distribution,

$$\log\left(\frac{\kappa^2}{\langle\kappa^2\rangle}\right) \sim \mathcal{N}(\mu, \sigma^2) \tag{5.27}$$

with probability density function

$$f(x) = \frac{1}{\sqrt{2\pi}\sigma} \exp\left[-\frac{1}{2}\left(\frac{x-\mu}{\sigma}\right)^2\right]. \tag{5.28}$$

Equation (5.28) is best fit by the mean and standard deviation values $\mu = -0.29$, $\sigma = 0.83$ for the crumpled morphology. In contrast to what the well-defined geometry of the hoop model (Fig. 5.11) suggests, the distribution of bending energies in the toroidal coil at low friction is also relatively close to a log-normal probability density (albeit much more narrow), with a slight tendency toward lower values in the tails. The best fit is obtained with $\mu = -0.07$, $\sigma = 0.41$.

The hierarchic nature of the crumpled morphology is manifest also in the number of contacts observed between filament segments, N_c, as Fig. 5.15 shows. After the two morphological phases have bifurcated, N_c follows a superlinear power law with exponent 1.40 ± 0.01 at $\mu = 0.5$:

$$N_c \sim l^{1.40}. \tag{5.29}$$

On the contrary, low friction leads to dense filament alignment with hexagonal packing in the coiled morphology, hence $N_c \sim l$ once a few coil windings are established.

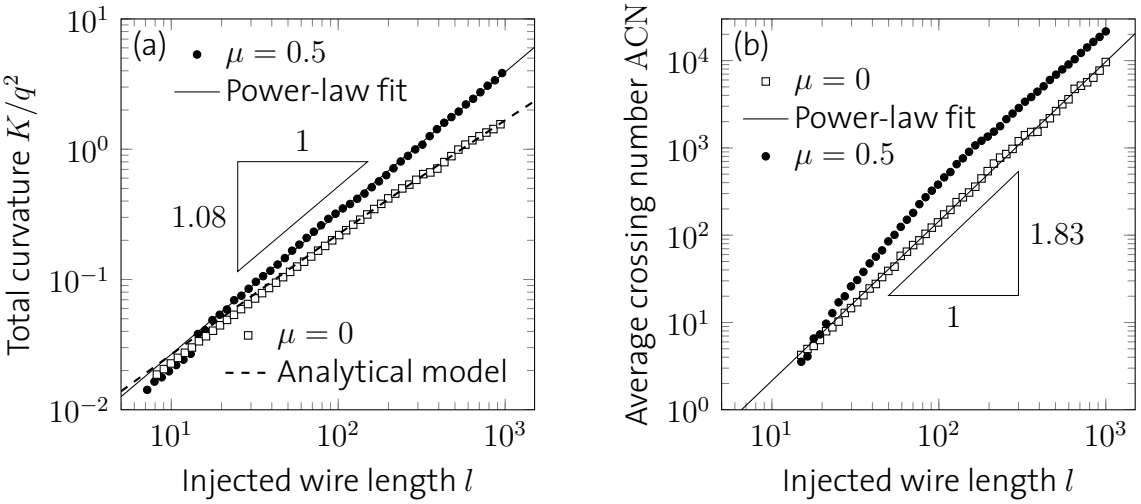

Figure 5.16: **Entanglement in flexible confinement.** The dashed line in (a) represents to the analytical model of equation (5.30) with the power laws from equation (5.21) plugged in. ACN scales with the injected thread length with an exponent of less than two in the coiled morphology (b), unlike in the disordered phase at strong friction.

5.2.3 Entanglement

In Section 5.1.2, filament entanglement in undeformable containers was measured in terms of the average crossing number ACN, defined in equation (5.17), to empirically find the approximate relationship $\mathrm{ACN} \approx cKl$. Since the total curvature K was superlinear in l, ACN grew quicker than l^2, which is the theoretical scaling for random circles in a sphere. This behavior breaks down in flexible cavities, as is demonstrated here. In the hoop model for the coiled phase, the total curvature reads

$$\begin{aligned} K(L) &= \frac{2}{\sqrt{3}d(L)} \int_0^{R_y} 2\pi\omega(y)\ \mathrm{d}y \\ &= \frac{L}{R_\mathrm{t} + 4R_y/3\pi}, \end{aligned} \tag{5.30}$$

where the strand distance $d(L)$ was eliminated using equation (5.22). Just like the bending energy, this excellently approximates the effective measurement with a slight initial overestimation, which is shown in Fig. 5.16a. Consistently with the energetics (equation (5.26)), a superlinear power law with exponent 1.083 ± 0.004 is found for the total curvature in the hierarchic crumpled morphology:

$$K \sim l^{1.08}. \tag{5.31}$$

Nonetheless, Fig. 5.16b shows that there is no apparent simple functional relationship between ACN and l in the crumpled phase. The frictionless toroidal coil, on the

other hand, exhibits a scaling that is consistent with a power law with exponent $\delta < 2$,

$$\mathrm{ACN} \sim l^{\delta}. \tag{5.32}$$

$\delta = 1.83 \pm 0.01$ fits the present numerical data best. The origin of this exponent is not precisely clear at this point—it must be put into context with analytically known values in related systems. For random circles in a sphere, it is known that $\delta = 2$, while free coils of rope have $\delta = 4/3$ [21]. The ordered coiling in flexible frictionless shells lies in between these two well-understood cornerstones.

5.2.4 Coiling-to-crumpling transition

To complete the quantitative characterization of the two morphological phases discussed above, an order parameter is required that discriminates them rigorously. Intuitively, what defines the order of the filament coil at low friction is *alignment* between the individual loops. All thread segments turn in the same direction about the toroidal axis of revolution. The hierarchic packing pattern in the crumpled morphology emerges due to frequent three-dimensional loop reorientations, which break this alignment. Denote by $\mathbf{n} \in \mathbb{R}^3$ the unit vector pointing in direction of the filament's principal axis of minimal moment of inertia. Then the curvature of the filament about $\mathbf{n}$ reads

$$\kappa(s) = \mathbf{n} \cdot \left(\frac{\partial \mathbf{x}}{\partial s} \times \frac{\partial^2 \mathbf{x}}{\partial s^2} \right)(s) \tag{5.33}$$

and the sign of the rescaled quantity $r\kappa(s)$ indicates its turning direction about the main coiling axis. Consequently, its average value

$$T = \langle \mathrm{sgn}(r\kappa) \rangle = \frac{1}{L} \int_0^L \mathrm{sgn}\left(r\kappa(s) \right) \, \mathrm{d}s \ \in [-1, 1] \tag{5.34}$$

measures the fraction of the filament turning in either direction about that axis. While a balance between left- and right-turning wire segments yields $T = 0$, T takes one of its extreme values ± 1 if and only if the wire coil never changes its orientation. Since this coiling direction is initially selected at random by imperfections of the material and geometrical setup, or by a random initial perturbation to the displacement field in numerical simulations, the sample average of T vanishes. The decisive non-trivial quantity is thus its absolute value $|T|$. The quantity

$$D = 1 - |T| \tag{5.35}$$

can serve as an order parameter to discriminate the ordered coiling at low friction from the disordered crumpling at high friction. As shown in Fig. 5.17, D vanishes exactly in the coiled phase, whereas it takes a finite value in the crumpled phase. $D = 1$ is attained only if the loops are perfectly isotropically distributed. Evidently, the phase transition is continuous and occurs at very low values of the friction coefficient

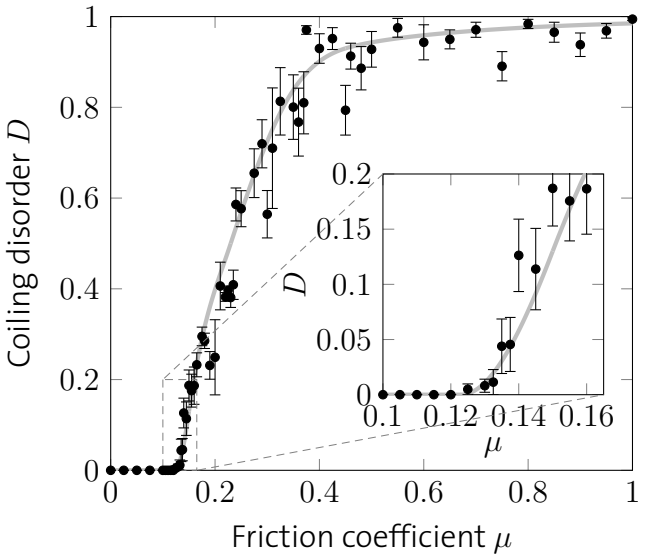

Figure 5.17: **Order parameter for the coiling-to-crumpling transition.** The transition is continuous and occurs at $\mu \approx 0.12$. The inset shows a magnification about the transition point. Error bars indicate standard errors from 10 independent simulations at $q = 20$, $\gamma = 10^2$, $f = 10^3$. The solid gray line is used as a guide to the eye. Data maximized over $l \in [5, 50]$.

(already $\mu = 0.2$ is sufficient to inhibit perfect alignment), which accentuates the fundamental difference between rigid and flexible confinements once again.

To summarize Section 5.2, the generalization from infinitely stiff to more flexible containers brought along a dramatic change in the packing of long filaments. Rigid cavities dictate the coiling process through their inviolable geometrical constraints, making friction a component of subordinate importance. Elastic shells, however, conform to the preferred shape of the packed thread, embracing it tightly. At weak frictional forces, this leads to a high degree of alignment through dense bundling, whereas even moderate friction between the elastic objects lets the shell get dragged along with the pushing filament, leading to higher compressive forces. Consequently, filament loops frequently reorient in space, leading to a hierarchic, disordered packing process. The role of friction is completely redefined in strongly deformable cavities.

A point that has not been addressed so far is the transition between rigid and flexible cavities. In particular, three out of four control parameters (q, γ, f) were fixed. How stiff is "rigid"? At which slenderness will a confining thin shell become flexible enough to alter morphogenesis of a contained long thread? Among others, these questions are pursued in the next section.

5.3 Growing rings in flexible containers

So far, the packing problem in deformable cavities was tackled for the particular case of radial injection of a linear filament through a small opening from outside. From a viewpoint of biological systems—especially if a cell wall or lipid bilayer acts as the confining membrane—another frequently encountered scenario is the growth of a filamentous structure *within a closed hull*, or the shrinkage of said hull. These fully enclosed strings may be linear, or as in the case of DNA in a wealth of organisms, of circular topology [174, and referenced therein]. Microtubules confined by erythrocytes [39, 155] and actin/filamin networks in giant vesicles [91, 123] are known for their capability to spontaneously take a ring-like shape, even though they aren't typically closed circles by construction. With these real-world problems in mind, a change of filament topology is in order. In the remainder of this chapter, the buckling, folding, bundling and coiling of a growing elastic circular thread is studied as it results from mechanical interaction with a confining flexible shell.

The initial condition at time $t = 0$ consists of a ring filament with length $L(0) = \overline{L}$ and cross-sectional radius r, surrounded by a close-fitting spherical shell with thickness h, whose middle surface has radius R. Since the system is made of the same two thin bodies as in Section 5.2 (except for the filament topology), it is fully characterized by the four dimensionless control parameters of equation (5.20): q, γ, f and μ. A tiny random perturbative deflection is imposed on the elastic ring to allow it to break the system's initial reflective and rotational symmetries by buckling and to allow for independent repetitions of the simulations. The filament is grown uniformly in length according to

$$\lambda = \frac{L(t)}{L(0)} = \exp(\Lambda t). \tag{5.36}$$

The growth rate Λ is set sufficiently small for inertial effects to have a negligible effect on the outcome. Uniform filament extension stands in sharp contrast to the packing problems addressed in Sections 5.1 and 5.2, where the feeding of more thread into the cavity could be considered as growth that is localized to the point of insertion. The difference between these two extreme cases of growth distributions is discussed toward the end of this section.

As the filament grows, it bears against the confining wall until the critical buckling load is exceeded and it buckles out of plane with harmonic mode n. Excited modes $n > 2$ are unstable in the quasi-static frictionless limit [87], but the simulations show that they can be observed when inertia is not negligible (i.e., large mass densities, fast growth or viscous overdamping) and in the presence of significant friction. The ground state buckling mode $n = 2$, which is most relevant in practice, develops a saddle shape until two filament segment pairs touch. This first contact occurs at

$$\lambda = \lambda^* \approx 2.127 \tag{5.37}$$

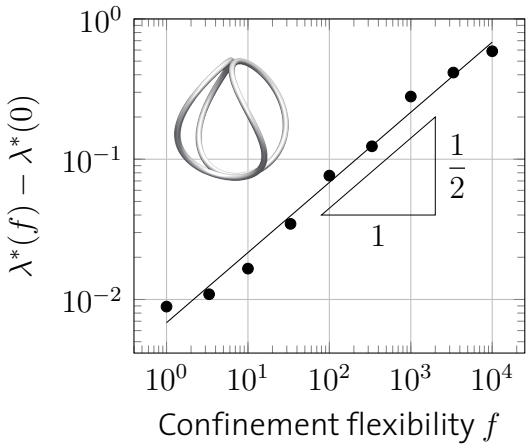

Figure 5.18: **Scaling of the point of first contact in flexible confinement** for fixed $q = 30$, $\gamma = 80^2$. At these values, $\lambda^*(f = 0) = 2.095$, and the best fit for a power-law exponent is 0.51 ± 0.02.

for rigid spherical cavities ($f = 0$) in the theoretical thin filament limit $q \to \infty$ [87]. The scaling of this point of first contact in finite systems is well approximated by $\lambda^*(f) - \lambda^*(0) \sim \sqrt{f}$, as Fig. 5.18 shows. Growth beyond λ^* with real self-avoiding materials has never been explored to date. The simulations and experiments presented below dispel this limitation, showing that four distinct morphologies emerge by bifurcation as the filament grows longer, which are illustrated in Fig. 5.19. They shall be denominated *spiral*, *classical*, *folded* and *warped*, motivated by their characteristics as detailed in the following.

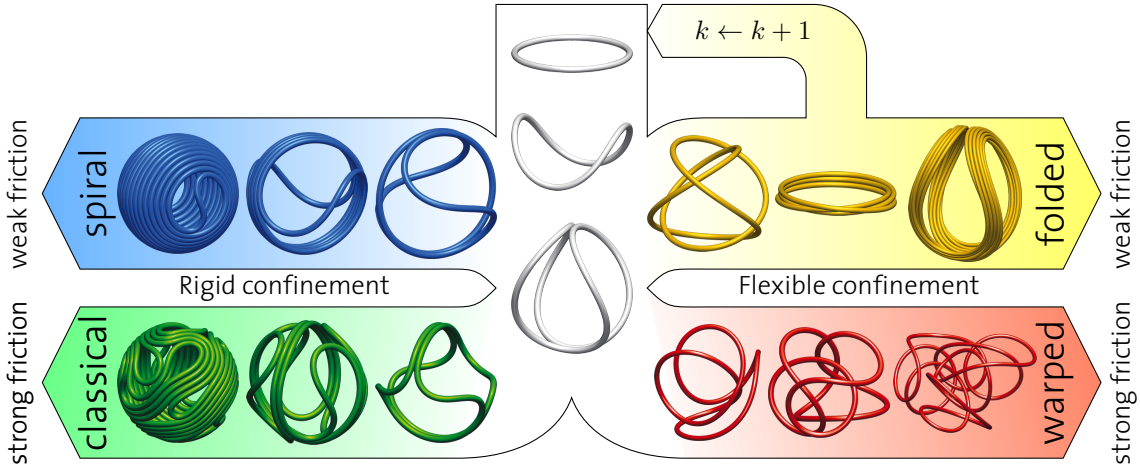

Figure 5.19: **Packing evolution depending on friction and confinement rigidity.** A confined growing ring buckles to a saddle shape (mode $n = 2$, middle). Beyond the point of first contact $\lambda = \lambda^*$, four distinct morphologies can emerge. The folding at low friction in flexible confinement is repeated during growth: Filament bundles refold self-similarly, each time tripling the number of bundle strands ($\omega = 3^k$).

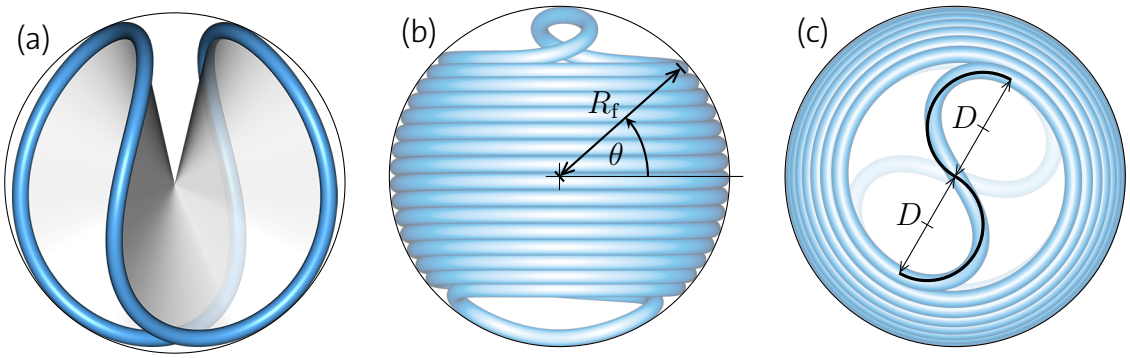

Figure 5.20: **Geometrical approximation of the spiral morphology.** (a) Before self-contact, the ring filament follows the rim of an e-cone. After contact, the filament can be divided into three parts: a coil with inclination θ (b) and two S-shaped curves (c).

5.3.1 The spiral phase

The packing in frictionless rigid spheres can serve as a reference model for less idealized systems. The limit $f, \mu \to 0$ is therefore considered first here. When $\lambda > \lambda^*$, a spiral (depicted in Fig. 5.19, top left, and Fig. 5.20b,c) develops analogous to unconfined *excess cones* e-cones [216]. In the spirit of refs. [18, 213], this configuration is here referred to as the *spiral phase*. Already D'ARCY THOMPSON postulated the existence of spiral packing patterns in the context of linearly growing spicules confined to ellipsoidal cell walls [227, page 676], albeit he didn't quantify his arguments.

The bending energy U_b of the filament before the first self-contact occurs ($\lambda < \lambda^*$) can be approximated analytically by integrating the square FRENET curvature over the centerline:

$$\frac{U_\mathrm{b} R_\mathrm{f}}{E_\mathrm{f} I} = \frac{1}{2} \int_0^{2\pi l} \left[\kappa_\mathrm{g}^2(s) + 1\right] \, \mathrm{d}s \tag{5.38}$$

where

$$R_\mathrm{f} = \frac{\overline{L}}{2\pi} = R - \frac{h}{2} - r \tag{5.39}$$

is the initial filament radius and $\kappa_\mathrm{g}(s)$ is the geodesic curvature of the rim of a unit e-cone given by [151]

$$\kappa_\mathrm{g}(s) = 2Q\sqrt{m}\ \mathrm{sn}(sQ \mid -m), \tag{5.40a}$$

$$Q = \frac{4n}{2\pi\lambda} K(-m). \tag{5.40b}$$

$K(m)$ denotes the complete elliptic integral of the first kind, while $\mathrm{sn}(u \mid m)$ is the sine of the JACOBI amplitude $\mathrm{am}(u \mid m)$, and the elliptic parameter $m \geq 0$ is found by

solving

$$2\pi = \frac{J^2 - 2C}{2JQ}\,\Pi\left[4m\frac{Q^2}{J^2}; \mathrm{am}(2\pi\lambda Q \mid -m) \mid -m\right] - J\pi\lambda, \tag{5.41a}$$

$$J^2 = C^2 + 4mQ^4, \tag{5.41b}$$

$$C = 1 + (m-1)Q^2 \tag{5.41c}$$

numerically [86], in which $\Pi[\eta; \varphi \mid m]$ stands for the incomplete elliptic integral of the third kind.

Beyond the point of first contact ($\lambda > \lambda^*$), frictionless rigid spherical confinements give rise to chiral surface-covering filament packings consisting of a dense coil and two spiral S-curves located at the poles (Fig. 5.20). This high degree of order grants access to an approximate closed-form solution of the predominant elastic contribution, the bending energy of the confined filament. The length L^{coil} of the coiled part can be estimated by summing up coplanar rings over an equatorial band on the surface of a sphere with radius R_{f}. The angular width of the band is 2θ, where θ is the inclination of the coil as depicted in Fig. 5.20, yielding

$$\begin{aligned} L^{\mathrm{coil}} &\approx \frac{1}{2r}\int_{-\theta}^{\theta}\int_{0}^{2\pi} R_{\mathrm{f}}^2 \cos\theta' \,\mathrm{d}\varphi \,\mathrm{d}\theta' \\ &= 2\pi\frac{R_{\mathrm{f}}^2}{r}\sin\theta. \end{aligned} \tag{5.42}$$

Like in the hoop model developed in Sections 5.1 and 5.2, the helical pitch of the coil is disregarded. A noteworthy difference between the present spiral coil and those in the earlier packing problems is that the equilibrium strand spacing d always attains its minimum value $d = 2r$ here, i.e., the spiral coil is always tight. There is hence no fitting parameter in this analytical model. The bending energy of the coil follows as

$$\begin{aligned} U_{\mathrm{b}}^{\mathrm{coil}} &\approx \frac{1}{2r}\int_{-\theta}^{\theta}\int_{0}^{2\pi} \frac{E_{\mathrm{f}} I R_{\mathrm{f}}}{2R_{\mathrm{f}}\cos\theta'} \,\mathrm{d}\varphi \,\mathrm{d}\theta' \\ &= \pi\frac{E_{\mathrm{f}} I}{r}\log\left[1 + \frac{2}{\cot(\theta/2) - 1}\right]. \end{aligned} \tag{5.43}$$

The relative error resulting from the neglected pitch is $|1 - (1 + [r/\pi R_{\mathrm{f}}]^2)^{-2}|$, which is as low as 0.1% already for filaments as thick as $R_{\mathrm{f}}/r = 14$. A rough estimate for the contribution from the two central spiral patterns is given by four semicircles with a diameter of $D = R_{\mathrm{f}}(\pi/2 - \theta)$. (An alternative estimate can be found in ref. [18].) Adding these contributions up, one finds the total filament length $L \approx L^{\mathrm{coil}} + 2\pi D$ and its total bending energy $U_{\mathrm{b}} \approx U_{\mathrm{b}}^{\mathrm{coil}} + 4\pi E_{\mathrm{f}} I/D$, such that

$$\frac{U_{\mathrm{b}} R_{\mathrm{f}}}{E_{\mathrm{f}} I} \approx \pi\frac{R_{\mathrm{f}}}{r}\log\left[1 + \frac{2}{\cot(\theta/2) - 1}\right] + \frac{4\pi}{\pi/2 - \theta}. \tag{5.44}$$

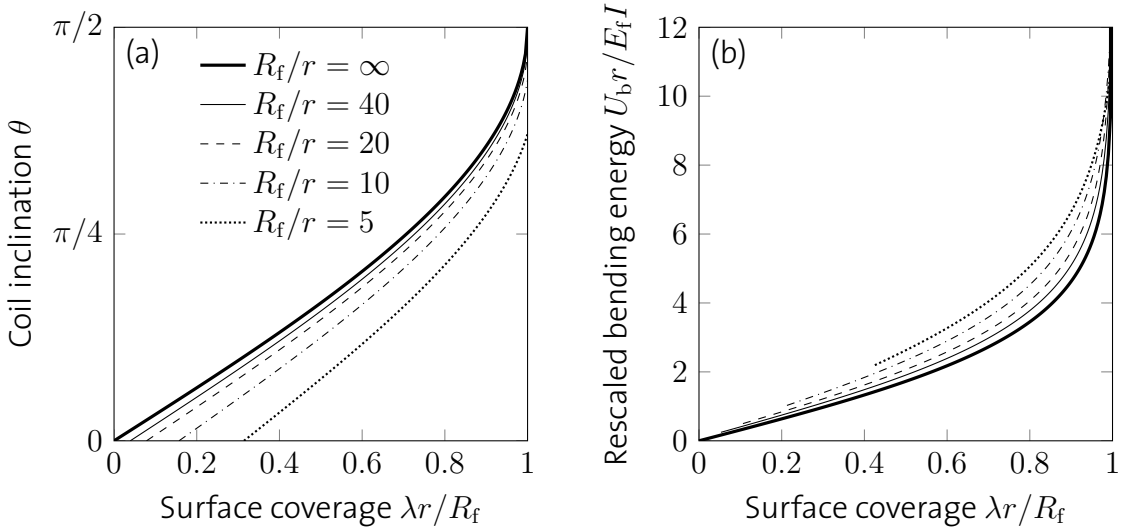

Figure 5.21: **Analytical approximation to the spiral filament after self-contact.** (a) Inclination of the spiral coil as shown in Fig. 5.20, obtained through numerical solution of equation (5.45). For very thin filaments ($R_f/r \to \infty$), it is $\theta = \sin^{-1}(\lambda r/R_f)$. (b) The bending energy after the first contact (equation (5.44)) transitions from an early linear regime ($\lambda r/R_f \ll 1$) to divergence at full surface coverage ($\lambda \to R_f/r \to \infty$).

To obtain the bending energy as a function of the normalized filament length λ, the coil inclination θ can be eliminated from equation (5.44) by numerically solving

$$\lambda = \frac{L}{2\pi R_f} \approx \frac{R_f}{r} \sin\theta + \pi/2 - \theta \tag{5.45}$$

for θ. The number of windings in the coil is given by $\omega = \theta R_f/r$. In Fig. 5.21 the numerical solutions for θ and U_b are plotted as a function of how much of the spherical surface is covered with filament.

In Fig. 5.22a it is shown that both analytical descriptions before and after contact, equations (5.38) and (5.44), are in excellent agreement with the numerical measurements. The measured energy after contact weakly oscillates because the coil is slightly bent by the S-curves. These oscillations increase for larger q. As the surface gets fully covered with a single layer of filament (i.e., as λ approaches R_f/r), the growing filament eventually buckles inward to release a large amount of elastic energy, and the packing process continues in a less ordered fashion much like some DNA molecules in phage capsids [5, 104].

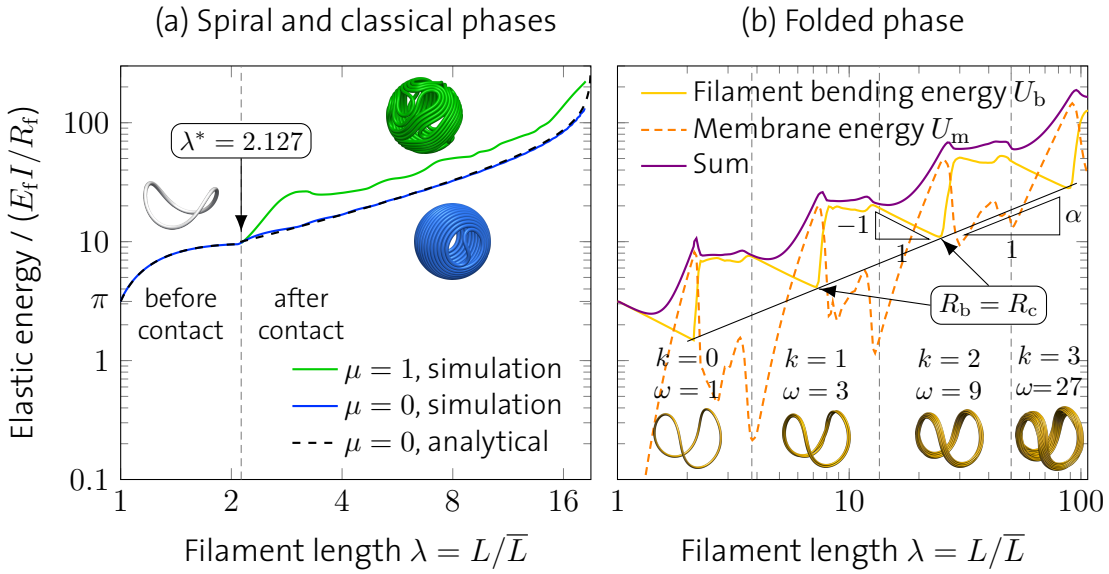

Figure 5.22: **Comparison of energetics.** (a) Filament bending energy in the spiral (blue) and classical (green) morphology at $q = 20$. (b) Folded morphology at $q = 20$, $\gamma = 20^2$, $f = 10^4$, $\mu = 0$. The predominant elastic energy contribution alternates between the filament bending energy U_b and the membrane energy U_m (stretching term of equation (2.23)). A cascade of four self-similar folds can be recognized by the repeated power law regions.

5.3.2 Morphological phases and phase transitions

A crucial requirement for a growing filament to coil is tangential sliding, giving rise to the high degree of order in the spiral morphology by continuous rearrangements. The presence of friction induces locality by limiting rearrangements to the local neighborhood, inhibiting relaxations to lower global energy conformations, thus trapping growing filaments in a disordered state (Fig. 5.19, bottom left). Figure 5.22a clearly shows that the bending energy of a growing ring filament with friction is bounded from below by the spiral phase. A similar situation is encountered in flat two-dimensional wire packings [213], from where the term *classical phase* is adopted. There, friction was found to account for a morphological phase transition from a spiral to a hierarchic loop pattern due to locality, as depicted in Fig. 5.23. The same phenomenon is observed here on the inner wall of a rigid spherical cavity. To quantify the spontaneous breaking of spiral symmetry with increasing μ, the following order parameter is proposed in analogy to the coiling-to-crumpling transition in Section 5.2.4. Define the signed coiling curvature $\kappa(s)$ as in equation (5.33) and extend it periodically such that $\kappa(s) = \kappa(s + L)$. Then, the circular convolution

$$c(s') = \frac{1}{L} \int_0^L \operatorname{sgn}\left[\left(s - \frac{L}{2}\right) \kappa(s + s')\right] \, \mathrm{d}s \;\in [0, 1] \tag{5.46}$$

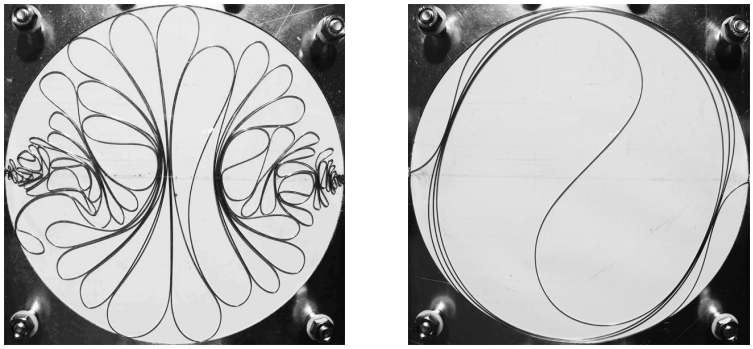

Figure 5.23: **Morphologies of elastic wires in flat rigid confinement.** Steel wires forced into flat rigid circles exhibit morphologies that share their essential features with the spiral and classical phases reported in the present work. Photographs by N. B. STOOP and F. K. WITTEL, reprinted with permission from ref. [213]. Copyright (2008) by the American Physical Society.

is a natural measure for the degree of order of the filament when cut in half at $s = s'$ and $s = s' + L/2$. If the two halves equally contain right- and left-turning segments, one has $c(s') = 0$. Conversely, only if one half turns only left and the other half only right, one has $c(s') = 1$. Thus, if one accounts for the periodic nature of the ring filament by maximizing over all bisection points s', the turning disorder

$$D = 1 - \max\{c(s') \mid s' \in [0, L]\}, \tag{5.47}$$

which is the analog of equation (5.35) for a ring-like thread, can serve as an order parameter to discriminate the spiral from the classical phase. It is evident from Fig. 5.28a that the transition occurs near $\mu \approx 0.5$, with a slight dependence on the system size q. In stiff confinement, friction must thus be fairly strong to introduce local order, which contributes to explaining why viral DNA is often condensed into layered spools [28, 53, 98, 160].

The surface-covering spiral and classical morphologies bear resemblance to liquid crystals, an analogy that has already been drawn in the context of DNA packing in viral capsids [100]. Define a loop by an area surrounded by a filament segment with only one inner point of contact [11, 213]. The spiral phase has only four such loops (two at each pole), while the classical phase is characterized by a broader spatial distribution of loops. At very high surface packing ($\lambda \to R_\mathrm{f}/r$), classical loops are compressed to point singularities with strength $\pm 1/2$ delimiting line disclinations known from nematic liquid crystals [29] (see Fig. 5.24). The spiral phase is in turn reminiscent of spherical smectic liquid crystals with two closely bound disclinations ending at two $1/2$-singularities at each pole [97]. The total disclination strength of a spherical liquid crystal is always two, which is a direct consequence of the GAUSS–BONNET theorem. Indeed, this identity holds for growing ring filaments for all q, μ in the spiral and classical phases. The number of topologically nontrivial loops is always four, but the classical phase can exhibit an arbitrary additional number of topologically trivial

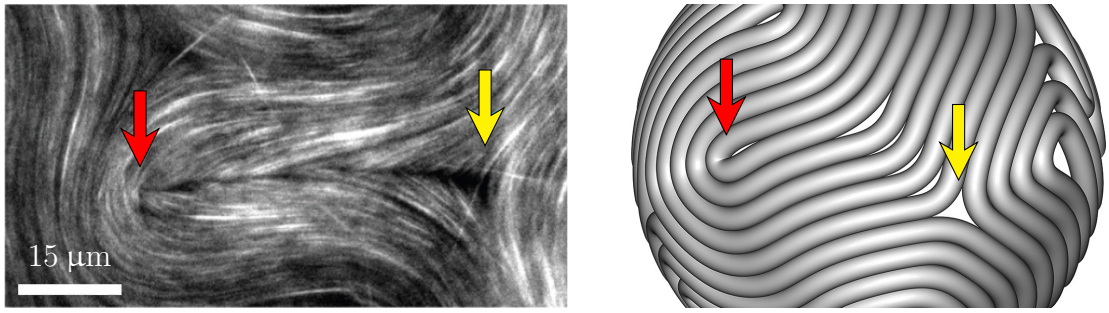

Figure 5.24: **Relationship of the classical morphology to 2D nematic liquid crystals.** Left: Active liquid crystals confined to fluid interfaces feature disclination defects with charge $+1/2$ (red arrow) and $-1/2$ (yellow arrow). Picture reproduced from ref. [190] and adapted with permission of Nature Publishing Group. Right: The same topological defects occur in the classical morphology of growing ring filaments in rigid confinement.

loops. However, it is stressed here that the existence of topologically trivial loops is sufficient, but not necessary for $D > 0$, and is thus not an order parameter.

The spiral and classical morphologies are highly metastable as the filament inevitably buckles away from the rigid wall. A qualitative stability condition was derived in ref. [100] and translates to $\lambda \ll q^2$ in the present terms, suggesting that dense single-layered surface packings (λ close to q) are found only in sufficiently small cavities, such as the one depicted in Fig. 5.24. This explains why they are not common in biophysical environments with very thin confined threads. Instead, such systems gain ultimate stability from weak or flexible confinement. In the computer simulations, the parameters γ and f were increased to discover a completely altered morphogenesis beyond a certain transition. As the confining sheet is elasticized or thinned, suddenly, the filament folds on itself as illustrated in the top right of Fig. 5.19 instead of coiling at low friction. Bundles of ω subthreads are formed similar to actin/filamin rings and microtubules in vesicles [91, 123, 168]. The same principle has found its way into everyday appliances: Pop-up tents or laundry baskets (Fig. 5.25) can be folded in the same fashion to save space [150]. This is hence referred to as the *folded* morphology. The folding process is repeated as the filament continues to grow. The winding number ω obeys

$$\omega = \prod_k (2n_k - 1), \tag{5.48}$$

where $n_k \in \{2, 3, 4, \dots\}$ is the buckling mode ($n_k = 0, 1$ are out of play because they represent rigid body movements) and $k = 0, 1, 2, \dots$ is the number of folds in the cascade. The ground state ($n_k \equiv 2$) energy is plotted in Fig. 5.22b, revealing a series of self-similar folds that define the folded phase. Prior to buckling, the circular filament bundle with effective average radius R_b linearly expands to release bending energy

Figure 5.25: **Examples of the folded morphology in daily life.** Folded elastic rings confined by thin sheets occur in daily-life items like pop-up tents, kids' soccer goals and laundry baskets (pictured, from left to right). All images show the unfolded state ($\lambda < \lambda^*$) which can be folded into $n = 3$ loops to save space. Reproduced from ref. [150] and adapted with permission of Nature Publishing Group.

according to

$$\frac{U_\mathrm{b} R_\mathrm{f}}{E_\mathrm{f} I} \sim \frac{R_\mathrm{f}}{R_\mathrm{b}} \sim \lambda^{-1}, \tag{5.49}$$

stretching the circumjacent sheet until a critical radius R_c is reached where the bundle buckles. The critical force F_c exerted by the shell onto the filament at the point of buckling ($R_\mathrm{b} = R_\mathrm{c}$) can be calculated by balancing the internal and external energies. For a circular single-fiber ring with buckling mode n, it is given by [230]

$$F_\mathrm{c} = 2\pi(n^2 - 1)\frac{E_\mathrm{f} I}{R_\mathrm{c}^2}. \tag{5.50}$$

After the bundle has folded onto itself, it again assumes a linearly growing toroidal shape that is governed by equation (5.49) until $R_\mathrm{b} = R_\mathrm{c}$, and the buckling repeats in this fashion (Fig. 5.26f). Numerical simulations show that the long-term trend of the bending energy at the buckling points is

$$\frac{U_\mathrm{b} R_\mathrm{f}}{E_\mathrm{f} I} \sim \lambda^\alpha \tag{5.51}$$

with an exponent that is at least bounded by $0 < \alpha < 1$. For the set of parameters in Fig. 5.22b, $\alpha = 0.80 \pm 0.02$. By supposing that

$$U_\mathrm{b} \approx \omega\pi \frac{E_\mathrm{f} I}{R_\mathrm{c}} \sim \frac{E_\mathrm{f} I}{R_\mathrm{f}} \lambda \left(\frac{R_\mathrm{f}}{R_\mathrm{c}}\right)^2 \tag{5.52}$$

because $\lambda \approx \omega R_\mathrm{c}/R_\mathrm{f}$, the critical radius is expected to slowly increase according to

$$\frac{R_\mathrm{c}}{R_\mathrm{f}} \sim \lambda^\beta, \qquad \beta = (1 - \alpha)/2, \tag{5.53}$$

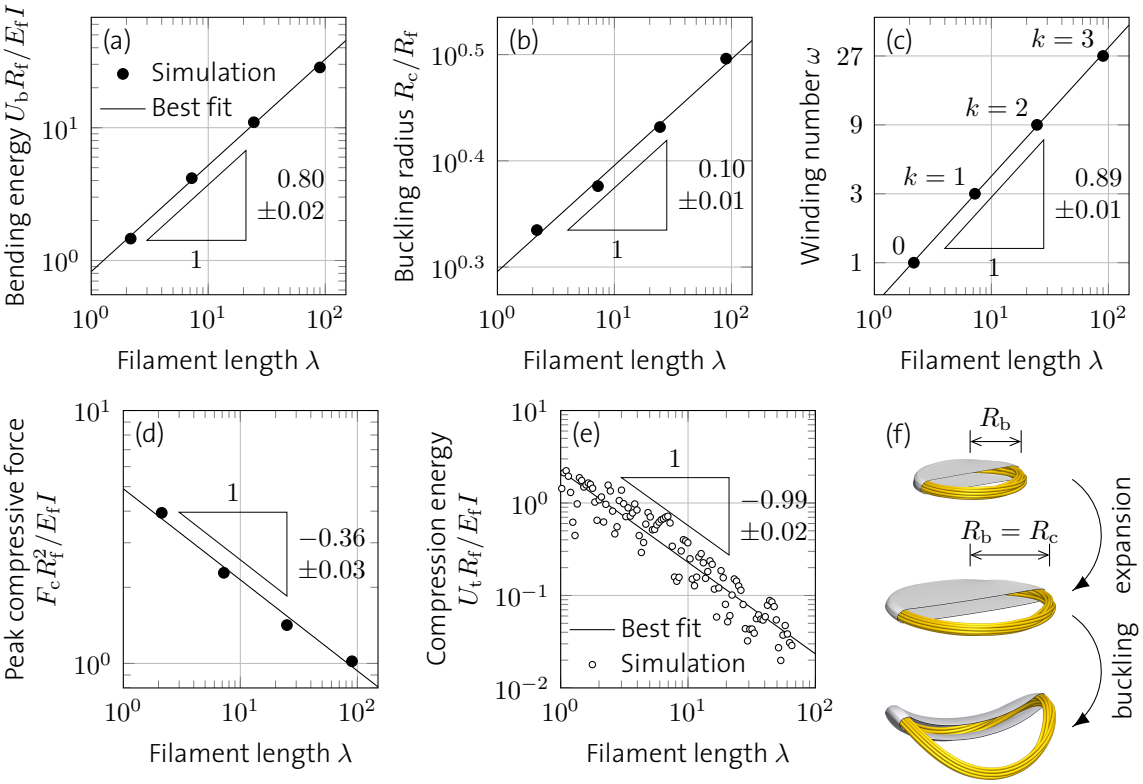

Figure 5.26: **Self-similarity of the folded morphology.** Power-law scaling of the filament bending energy (a), critical buckling radius (b), number of subthreads (c), compressive force (d) and compressive energy (e) with the relative filament length at the buckling points $R_b = R_c$. (f) Typical evolution of the bundle shape in the folded morphology ($n = 2, k = 2, \omega = 9$).

and accordingly, the ground state winding number should scale as

$$\omega \sim \lambda^\gamma, \qquad \gamma = (1+\alpha)/2. \tag{5.54}$$

This simple reasoning is indeed very well matched by the numerical data (see Fig. 5.26), which is best fit by $\beta = 0.10 \pm 0.01$ and $\gamma = 0.89 \pm 0.01$. As the buckling radius R_c slowly increases, the compressive force F_c experienced by the filament weakens (Fig. 5.26d). The associated compression energy U_t, while starting off at the same order of magnitude at $\lambda = 1$ as the bending energy, shows a pronounced decay with exponent ≈ -1 in Fig. 5.26e. This reveals an intriguing property of filament growth in flexible confinement that can't be found in rigid containers. By folding into bundles, the filament experiences an ever weakening compression and thus further stabilizes while growing longer, even though the confining shell is progressively stretched. This striking refolding of bundled rings provides a purely mechanical explanation for the spontaneous bundling of flexibly confined filaments such as actin networks [91, 123] (Fig. 5.27) and marginal microtubule bands in developing erythrocytes [39, 155] as a result of membrane or shell enclosure instead of cross-linkage. Only sufficiently deformable containers conform to pushing filaments, allowing

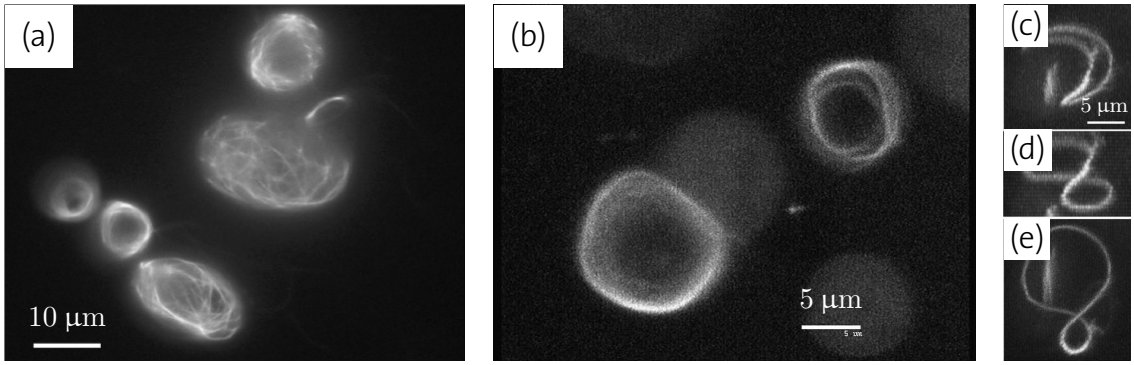

Figure 5.27: **Spontaneous bundling of actin networks in giant vesicles.** Actin/α-actinin networks spontaneously bundle in giant vesicles when quenched (a) or if the vesicle diameter is relatively small (b). (c-e) Ring-like actin/filamin bundles buckle to the characteristic saddle rim shape if the coil radius is larger than the vesicle radius. All micrographs reprinted with permission from ref. [123]. Copyright (2002) by the American Physical Society.

them to pass one another to fold into energetically more favorable bundle configurations. This might also provide a paradigm to explain layered slime thread bundling in hagfish gland thread cells [239], where the cell membrane deforms under high packing pressure. The presented findings suggest that such thread bundle packings may be obtained only in systems where frictional forces are rather small. Other biological systems in which filament bundling provides a mechanism of mechanical stabilization in membrane confinement include filopodial protrusion [125, 147, 219].

Remarkably, the gain in mechanical stability in flexible cavities goes hand in hand with the loss of chirality. Denote by $\mathbf{p}(s) = \mathbf{x}(s) - \langle \mathbf{x} \rangle$, $s \in [0, L]$, the position of the filament centerline relative to its own center of mass, $\langle \mathbf{x} \rangle$. A convenient order parameter describing the transition from the spiral to the folded phase is the geometric chirality coefficient

$$\chi = 1 - \max\{o(\mathbf{p}, \widetilde{\mathbf{p}}(\mathbf{a})) \mid \mathbf{a} \in S^2\} \in [0, 1] \tag{5.55}$$

where $S^2 = \{\mathbf{a} \in \mathbb{R}^3 \mid \|\mathbf{a}\| = 1\}$ is the set of vectors on the unit 2-sphere,

$$\widetilde{\mathbf{p}}(\mathbf{a}) = \mathbf{p} - 2\frac{\mathbf{p} \cdot \mathbf{a}}{\mathbf{a} \cdot \mathbf{a}}\mathbf{a} \tag{5.56}$$

is the reflection of the filament centerline $\mathbf{p}$ on the plane perpendicular to $\mathbf{a}$ and

$$o(\mathbf{p}, \widetilde{\mathbf{p}}) = \frac{1}{L}\int_0^L H\left(1 - \min_{s \in [0,L]}\left\{\frac{\|\mathbf{p}(s) - \widetilde{\mathbf{p}}(s')\|}{2r}\right\}\right) \mathrm{d}s' \tag{5.57}$$

gives the fraction of overlap between the filaments described by $\mathbf{p}$ and $\widetilde{\mathbf{p}}$. In equation (5.57), $H(\cdot) = (1 + \mathrm{sgn}(\cdot))/2$ denotes the HEAVISIDE step function. If and only if all spheres with radius r along the thread centerline overlap with the volume of the

thread mirrored on the plane perpendicular to $\mathbf{a}$, one has $o(\mathbf{p}, \widetilde{\mathbf{p}}) = 1$. Conversely, if and only if the thread volumes are disjunct, $o(\mathbf{p}, \widetilde{\mathbf{p}}) = 0$. By maximizing the overlap over all mirror images in equation (5.55), the chiral dissimilarity of the filament and its own mirror image, χ, can thus be obtained. A very similar measure [70, 144] is rooted in the pattern recognition community [188] and has also been applied in chemistry to compare the structure of molecules [24]. In Fig. 5.28b, a pronounced discontinuity in χ is in evidence, suggesting that the phase transition between the spiral and the folded morphology is of first order.

Chirality of confined rods is know to play a key role in morphogenesis of *Escherichia coli* cells for instance, where the bacterial rod grows into a helical spiral, guided by proteins [237]. The present data provide evidence that, conversely, filament chirality can emerge as a purely mechanical consequence of non-flexible confinement.

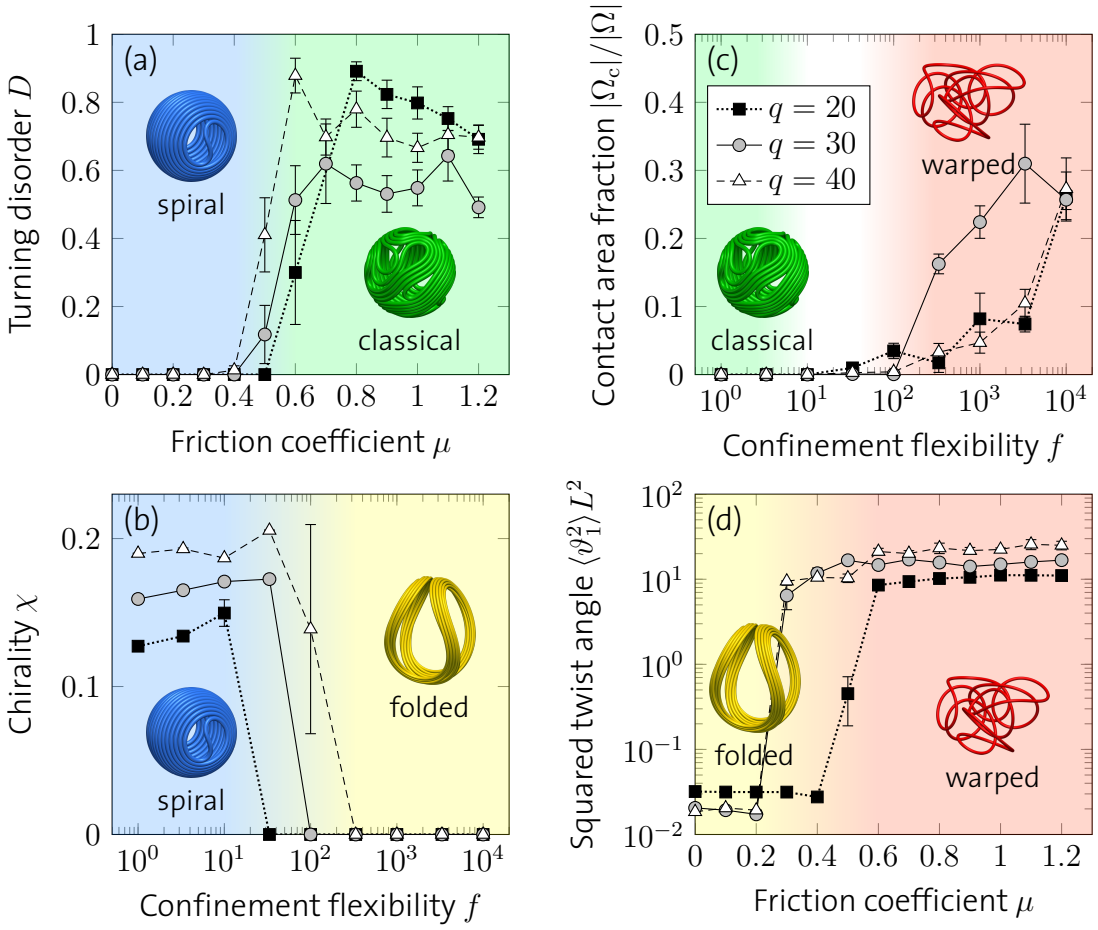

Figure 5.28: **Order parameters for the morphological phase transitions.** (a) Half of the spiral filament turns right and half of it left, which is not the case in the classical phase ($f = 0$, $\lambda = 10$). (b) The dissimilarity between the filament and its own mirror image is strictly positive in the chiral spiral phase, but vanishes in the achiral folded phase ($\gamma = 10^4$, $\mu = 0$, $\lambda = 5$). (c) The fraction of the sheet surface in contact with itself vanishes when the warped phase transitions to the classical phase ($\gamma = 10^4$, $\mu = 1.4$, data maximized over $\lambda \in [1, 10]$). (d) The amount of twist quantifies the transition from the folded to the warped phase ($\gamma = f = 10^4$, $\lambda = 5$). Error bars represent standard errors from $6 - 10$ independent realizations.

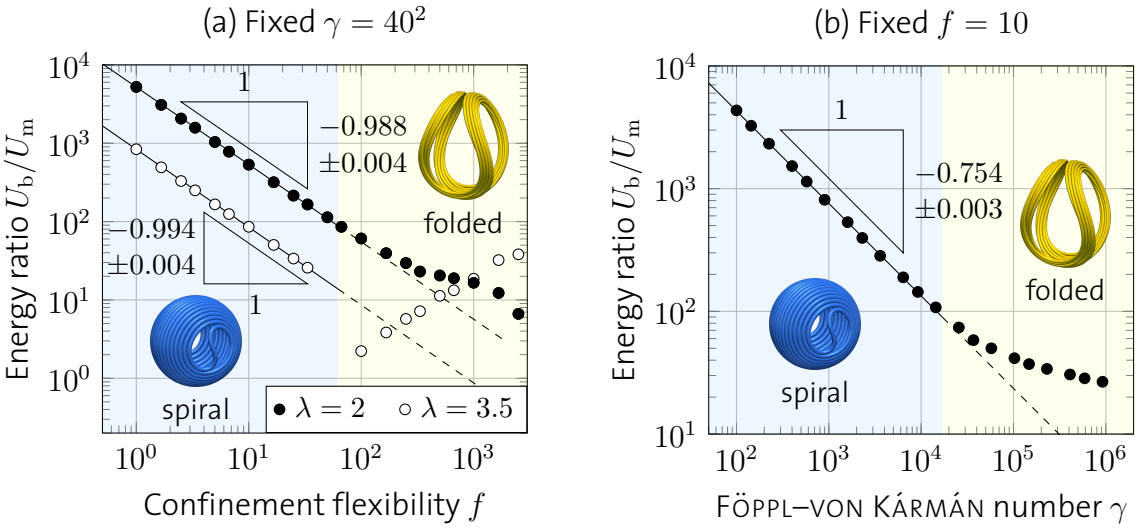

Figure 5.29: **Breakdown of energy scaling in the spiral-to-folded transition.** Data from simulations at fixed $q = 20$, $\mu = 0$. Filled symbols are prior to the first filament contact ($\lambda = 2$), open ones are post contact ($\lambda = 3.5$). The solid lines correspond to best power-law fits in the spiral phase.

The shape of the spiral filament is almost unaltered by changes in f and γ, given that these control parameters are lower than their critical values where the system transitions to the folded phase. The filament bending energy U_b is hence approximately constant (for fixed l and q) within the spiral phase, while the energetics of the shell strongly vary with f and γ. In the spiral phase, the elastic membrane energy U_m scales according to

$$\frac{U_m}{U_b} \sim f\gamma^{3/4}, \tag{5.58}$$

as is demonstrated in Fig. 5.29—a result which may appear counter-intuitive at first glance, because one might expect $U_m/U_b \sim f^{-1}$ by definition of f in equation (5.20). Such intuition is misguided by the false assumption of equal straining of the two slender objects. Instead, as f and γ are increased, the shell is increasingly strained. The scaling equation (5.58) breaks down at the transition to the folded phase (Fig. 5.29), which comes as no surprise since that is where the filament bending energy deviates significantly from that of the spiral phase (see also Fig. 5.22).

If growing filaments are inclined to form highly ordered bundles inside of deformable membrane cavities (without friction), the question naturally arises whether purely mechanical material properties can also give rise to disordered patterns with strongly warped or tangled filaments. Developing vertebrate intestines, where the gut tube grows into the body cavity at a different rate than the adhering mesenteric sheet, are in fact one example [193] (Fig. 5.30). Here, this particular result can be put in a broader, more general framework by controlling friction. As μ is increased, the thin flexible sheet grabs hold of the pushing filament, tightly wrapping around it. Just like in the classical phase, and similarly to the crumpled morphology in

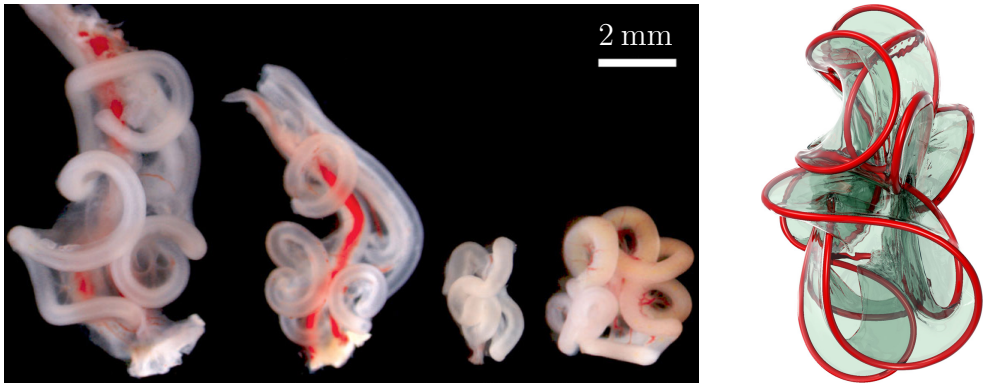

Figure 5.30: **Example of the warped morphology in biology.** Growing gut tubes of various vertebrates develop loop patterns as a result of differential growth rates, similar to the warped morphology at large frictional forces, pictured on the right. Left image reproduced from ref. [193] and adapted with permission of Nature Publishing Group. From left to right: chick, quail, finch and mouse.

Section 5.2, friction enforces locality: The filament can no longer just freely fold up inside, and further growth causes it to locally twist in frustration, leading to a *warped* morphology (depicted in Fig. 5.19, bottom right, and in Fig. 5.30, right). For $\gamma, \mu \to \infty$, this behavior is reminiscent of the EULER–PLATEAU problem [71] but significantly more complex due to the crucial role of twist and volumetric exclusion. The transition from the folded to the warped phase is accompanied by the breaking of torsional symmetry. As order parameter the non-dimensional torsional energy

$$\langle \vartheta_1^2 \rangle L^2 = \frac{2LU_\mathrm{t}}{GJ} \tag{5.59}$$

may be used with ϑ_1 from equation (2.33), since it vanishes in the folded phase for $q \to \infty$ and takes a significant, finite value in the warped phase. As can be recognized from Fig. 5.28d, the exact value of the corresponding critical friction coefficient, while depending on the system size q, is generally very low, implying that the warped phase is relevant even in systems with moderate friction. This is in striking agreement with the case where a long thread is injected from outside, see Section 5.2.4. Within the warped phase, the stored torsional energy quickly levels off. These measurements thus provide a tight lower bound for the amount of twist in vertebrate guts [193].

The direct transition from the classical to the warped morphology is less obvious. A large portion of the phase space is occupied by *mixed* states in which the confinement is not stiff enough to keep the filament from buckling into the sphere, but at the same time not flexible enough to wrap around it and force it to twist. Such configurations are prevalent, e.g., in brain aneurysms occluded by detachable coils (see e.g. ref. [185]). It is nonetheless possible to define a sharp phase boundary by considering as an order parameter the area fraction of the membrane that is in contact with itself, $|\Omega_\mathrm{c}|/|\Omega|$ (where $|\Omega| = \int_\Omega \mathrm{d}\Omega$), because it is non-zero only in the warped phase, as shown in Fig. 5.28c.

5.3.3 Full phase diagram

For the design and optimization of new materials and structures, e.g. in nanorobotics or endovascular coiling, reliably predicting the packing behavior is essential. Here, computer simulations are used to acquire a quantitative image of the morphological phase space, allowing one to accurately predict morphogenesis depending on the geometry and material parameters. In the low friction regime (upper half of Fig. 5.31), the spiral and folded phases are separated by a smooth phase boundary. Evidently, if the confining sheet is thin enough, filaments don't need to be substantially more rigid to fold instead of coiling. Bigger systems (larger q) favor the spiral morphology as the phase boundary is shifted toward flexible confinements (large γ, f). Very close to the phase boundary, mixed configurations such as the one shown in Fig. 5.31e occur when the filament folds at only one of the two contact points, which is a dynamic effect.

A cut through the phase space at fixed q and γ unveils its full complexity (lower half of Fig. 5.31). All phase boundaries are q-dependent. Perhaps most intriguingly, straight single-parameter lines are found along which all morphologies are traversed, including the mixed region (uncolored area). An example is the line along the f-axis, at $q = 40$, $\gamma = 10^4$, $\mu = 0.5$. This shows how delicate the choice of parameters is for targeting a specific morphology—possibly too delicate for Nature to rely on this selection in some parameter regions. Another striking feature is reentrancy of the warped phase in small systems with strong friction (Fig. 5.31 at $q = 20$, $\gamma = 10^4$, $f \approx 10^2 - 10^3$, $\mu \approx 1.2$), where the folded phase extends far into the large-μ region. In its low-μ end near the boundary to the folded phase, the warped morphology is just a temporary interstate. The filament first warps (including the characteristic twist and shell-shell contact), but upon further growth, some sliding allows it to rearrange and fold nevertheless, defining a region in phase space where the warped and folded phases coexist, which is illustrated by a color gradient in the phase diagram. The individual simulation runs that gave rise to this quantitative image of the phase space are documented in Appendix A.

The four morphologies discussed here are almost as easy to reproduce in tabletop experiments as the crumpled configuration of Fig. 5.9. In the experiments shown in Fig. 5.31b,c, straight steel pipes were tangentially attached to rigid polystyrene spheres and polyurethane wires were manually fed from both sides at equal speed through the pipes into the spheres. Starting from an initially preset loop inside, the wire then developed into the spiral or classical morphology depending on friction, which was controlled with a silicone lubricant. For the morphologies in flexible confinement (Fig. 5.31a,d), stiffer polycaprolactam wires and customary stretchable balloons made of natural rubber were used, into which the wires were tangentially pushed by hand.

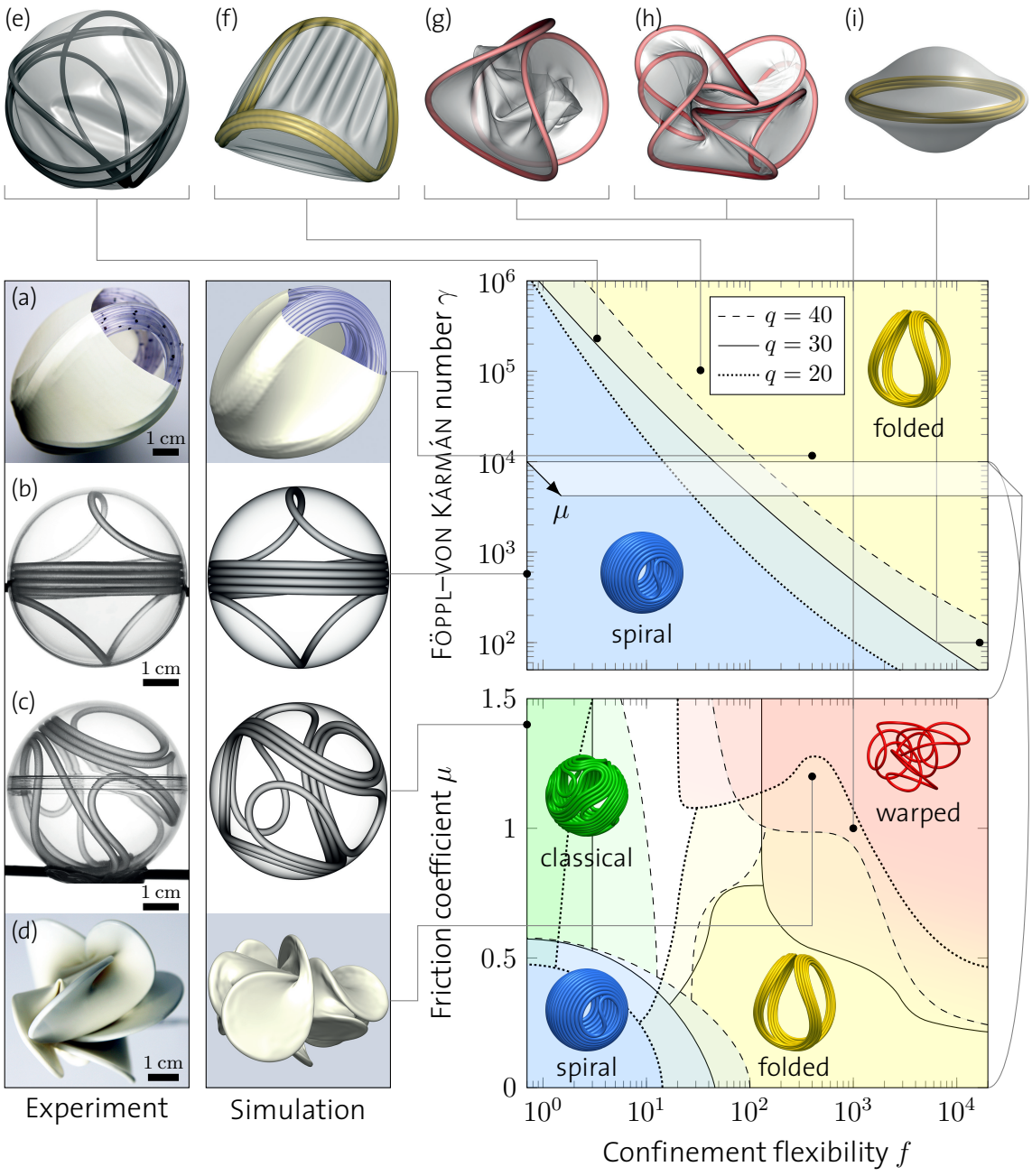

Figure 5.31: **Morphological phase diagram.** The lines represent least-squares-fitted phase boundaries. (b,c) Polyurethane wires ($r = 1\,\mathrm{mm}$) tangentially fed from opposite directions into rigid polystyrene spheres ($R = 24\,\mathrm{mm}$, $h = 1\,\mathrm{mm}$). (a,d) Polycaprolactam wires ($r = 0.75\,\mathrm{mm}$) in natural rubber balloons ($R = 27\,\mathrm{mm}$, $h = 0.25\,\mathrm{mm}$). (e-i) Simulation snapshots at $q = 30$, $\lambda = 4$. (e) An exemplary mixed configuration close to the phase boundary. (f) Very thin confinements exhibit tension wrinkles [27]. (g) Very flexible confinements are stretched similar to lipid vesicles [114]. Warped filaments typically first crumple the sheet (h, $\lambda = 2$) before strongly twisting (i, $\lambda = 4$).

The presented morphological phase diagram is independent of how growth is realized in detail. In the simulations the filament was grown uniformly everywhere, whereas the tangential injection of an invariant wire in the experiments corresponds to concentrated growth at the point of insertion. These two extremes are exactly equivalent in the low friction phases owing to global rearrangements, and they similarly produce the high-friction morphologies with the exception that reorganization is somewhat condensed to a neighborhood about the localized growth zones if growth is non-uniform.

In Section 4.1 it was found that sheet growth in invariant confinement and crumpling in shrinking confinement are equivalent in the elastic limit. This begs the question to which degree the same analogy applies to the filament morphogenesis described in this chapter. Simulations (not shown) revealed that an invariant filament getting gradually compressed by a shrinking shell yields the same morphologies as reported here for a growing filament. The only difference is that q (and possibly γ) decrease over time and the phase diagram must be interpreted accordingly. All presented analytical and scaling arguments hold also for this case without modification (where R_f is no longer constant, and $\lambda = \overline{L}/2\pi R_\mathrm{f}$).

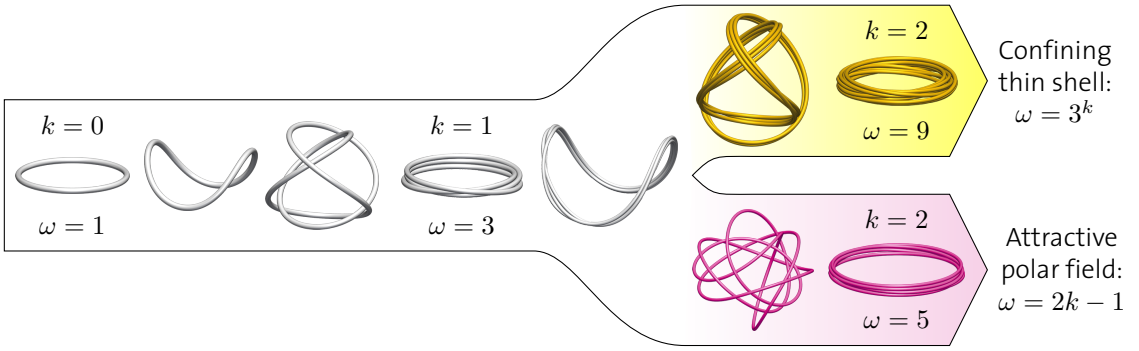

Figure 5.32: **Folding of a loop filament in weak confinements.** The folding behavior of growing filament loops strongly depends on the type of confinement. The number of windings ω scales exponentially with the number of folds k in thin elastic sheets, and linearly in polar attractive force fields.

5.3.4 Comparison with another type of weak confinement

The exponential scaling of the winding number $\omega = (2n-1)^k$ in the folded morphology is a particular feature of the type of flexible confinement considered here. By replacing the confining thin shell by an attractive polar force field with potential $\Phi(r) \sim r^p$, $p \geq 1$, where r is the distance from the center, a cascade of folds emerges with winding number $\omega = 2k - 1$ for the stable buckling mode $n = 2$ (Fig. 5.32) similar to phantom rings confined to the surface of a sphere [87]. This dramatic difference in scaling stems from the anisotropic spatial confinement exerted by a flexible membrane: In a polar field, the single strands in the buckling rope have room to separate and disentangle during the transition to a higher winding number, resulting in the low energy modes $\omega = 2k - 1$. This is prevented by the interaction with an elastic thin shell, which wraps around the folded strands, enforcing the exponential law by keeping the bundle together.

Note that spatial confinement is not the only way of obtaining the saddle shape shown in Fig. 5.32 from a buckled single-stranded ring. The necessary excess curvature can also be imposed by creasing an annulus or by attaching two open ends of a ring at an excess angle [150]. Without the flexible confinement exerted by an enclosing thin sheet, however, the cascade of self-similar folds that is observed here in the folded phase has not been reported before. An unconstrained over-curved ring or annulus will just wind $\omega = 2k - 1$ times.

With this comprehensive insight into the morphological phase space of growth, packing and interaction of thin elastic bodies, the main part of this thesis is concluded. In the final part that starts with the next chapter, possible extensions are discussed, which are mainly focused on a computationally efficient stress resultant implementation of material nonlinearity in the form of elasto-plasticity.

Chapter 6

Plasticity in thin filaments

[...] when the engineer talks of repeated loading, of elastic fatigue, of hysteresis, and other phenomena associated with plasticity and strain, the physiological analogues of these physical phenomena are perhaps not far away.

– D'Arcy Wentworth Thompson, *On Growth and Form* (1917)

Apart from permanent deformations imposed by growth, Chapters 2 to 5 considered thin body mechanics under the hypothesis of linear elasticity. The wire packing problem in 2D, however, is known to strongly depend on plastic yielding [213], and a preliminary experiment briefly mentioned in ref. [72], which appears to be the only attempt made so far at investigating the packing of ductile wires in 3D, suggests a similar dependency for the 3D counterpart. Plasticity in thin sheets, on the other hand, has been included in recent numeric studies on crumpling [124, 223], but was found to have a somewhat less dramatic effect than for wires, presumably due to the reduced spatial freedom. The computational models cited above were strongly limited in the simplistic way they approximated the irreversible, three-dimensional material response under yield: the degrees of freedom were decoupled in the nonlinear constitutive modeling, and one-dimensional elasto-plasticity was implemented in a subset of them.

Coupled three-dimensional elasto-plasticity is a notoriously difficult problem to solve in the context of thin beams and shells, especially in combination with strain hardening. The concept is fundamentally inconsistent with the assumptions made to develop reduced-dimensionality models using stress resultants. In the elastic regime, all material points across the structural thickness obey the same elastic field equations, allowing them to be integrated analytically in the thickness direction under given kinematic assumptions to yield resultant fields. The same does not hold in elasto-plasticity, where different points in the cross section are in different elastic or plastic states. Even the definition of a consistent yield surface in

stress resultant space under the assumption of *ideal plasticity*, i.e. without strain hardening, is a very non-trivial task for thin shells [23, 183], let alone cases that include hardening. A serious amount of literature is available on how to cope with these difficulties in a number of different ways, including techniques to capture the variation across the thickness by numerical integration or partition into a layered "sandwich", and iterative return mapping procedures. For a concise overview, see e.g. refs. [8, 52, 111] and references therein. Needless to say, such methods typically come with substantial computational costs.

Here, a simplification is proposed for thin elasto-plastic filaments, based on the concept of *plastic hinges*, that sidesteps the aforementioned difficulties by employing a particularly convenient ellipsoidal approximation of the yield surface in coupled stress resultant space. Together with linearized hardening laws, this enables a direct solution of the return mapping problem without iterative procedures and without the need to distinguish different cases near creases of multi-surface yield functions. The focus is on simplicity and computational efficiency, without decoupling the degrees of freedom, in line with the assumptions of the underlying kinematic theory. Specifically, the plasticity model is characterized by the following assumptions:

- *Yield condition.* – The VON MISES yield surface is approximated in stress resultant space.
- *Hardening law.* – Linear strain hardening is assumed, which is essential for non-iterative return to the admissible region. To account for the BAUSCHINGER effect, *isotropic* hardening is complemented by *kinematic* hardening.
- *Flow rule.* – A rate-independent associative flow rule is assumed. For viscoplastic regularization, it is trivial to extend the algorithm by introducing a relaxation time in the return mapping in Section 6.1.3 [202].

6.1 A stress resultant plasticity model for thin filaments

6.1.1 One-dimensional constitutive laws

In a first step, each of the four beam degrees of freedom (torsion, bending in two directions and axial compression/tension) is considered separately to determine the respective plastic resultants, i.e., the stress resultants at which the plastic hinge yields under unidirectional deformation purely in the respective mode. Suppose linear strain hardening at each material point in any beam cross section with *isotropic* hardening modulus H^{iso} and *kinematic* hardening modulus H^{kin}. The stress-strain curve at each of these points is then given by a linear elastic regime with slope E,

and a linear hardening regime with slope $SE < E$, where [202]

$$S = \frac{H^{\text{kin}} + H^{\text{iso}}}{E + H^{\text{kin}} + H^{\text{iso}}}. \tag{6.1}$$

Let x be the axis perpendicular to the cross section under consideration. The torque T about x resulting from pure torsion τ reads

$$T = \int_A \sigma_{13}(r')r' \, \mathrm{d}A = \int_0^{2\pi} \int_0^r \sigma_{13}(r')r'^2 \, \mathrm{d}r' \, \mathrm{d}\varphi \tag{6.2}$$

where $\sigma_{13}(r') = Gr'\tau$ is the torsional stress at distance r' from the centerline (see equation (2.37b)). Denote by σ_{Y} the yield stress of the isotropic material in uniaxial tension. The circular cross section is divided into a circular inner elastic region $0 \le r' \le r_{\text{Y}}$, where $6\sigma_{13}(r')^2 \le \sigma_{\text{Y}}^2$ in VON MISES plasticity, and an outer plastic rim $r_{\text{Y}} < r' \le r$, where all material points have yielded, as shown in Fig. 6.1a. The yield radius r_{Y} is defined by $6\sigma_{13}^2(r_{\text{Y}}) = \sigma_{\text{Y}}^2$:

$$r_{\text{Y}}(\tau) = \frac{\sigma_{\text{Y}}}{\sqrt{6}G\tau}. \tag{6.3}$$

Conversely, the torsion required to let the cross section yield at radius $r' = r_{\text{Y}}$ is

$$\tau_{\text{Y}}(r') = \frac{\sigma_{\text{Y}}}{\sqrt{6}Gr'}. \tag{6.4}$$

Using the point-wise bilinear stress-strain relationship with equation (6.1), the torque as a function of torsion can be integrated over the two regions, according to

$$\begin{aligned} T(\tau) &= 2\pi \int_0^{\min\{r,r_{\text{Y}}\}} Gr'^3\tau \, \mathrm{d}r' + 2\pi \int_{\min\{r,r_{\text{Y}}\}}^r \frac{\sigma_{\text{Y}}}{\sqrt{6}} r'^2 + SGr'^3\big[\tau - \tau_{\text{Y}}(r')\big] \, \mathrm{d}r' \\ &= SGJ\tau + (1-S)G\tau\frac{\pi}{2}\left[\min\{r, r_{\text{Y}}\}^4 + \frac{4}{3}\big(r^3 - \min\{r, r_{\text{Y}}\}^3\big)r_{\text{Y}}\right]. \end{aligned} \tag{6.5}$$

This is the exact nonlinear torque-torsion relationship for linear hardening, and it is plotted in Fig. 6.1c. For computational reasons mentioned in the introductory part of Chapter 6, it is replaced here by its optimal bilinear approximation in stress resultant space,

$$T_2(\tau) = \begin{cases} GJ\tau & \text{if } \tau \le \lambda\tau_{\text{Y}}(r) \\ GJ\big(\lambda\tau_{\text{Y}}(r) + S\big[\tau - \lambda\tau_{\text{Y}}(r)\big]\big) & \text{otherwise} \end{cases}. \tag{6.6}$$

The only remaining unknown is the effective average yield multiplier λ, which can be determined by imposing correct asymptotics. In the limit of a fully plastic cross section, the bilinear approximation must coincide with the exact nonlinear torque-torsion relationship:

$$\lim_{\tau\to\infty} \frac{T(\tau)}{T_2(\tau)} = 1. \tag{6.7}$$

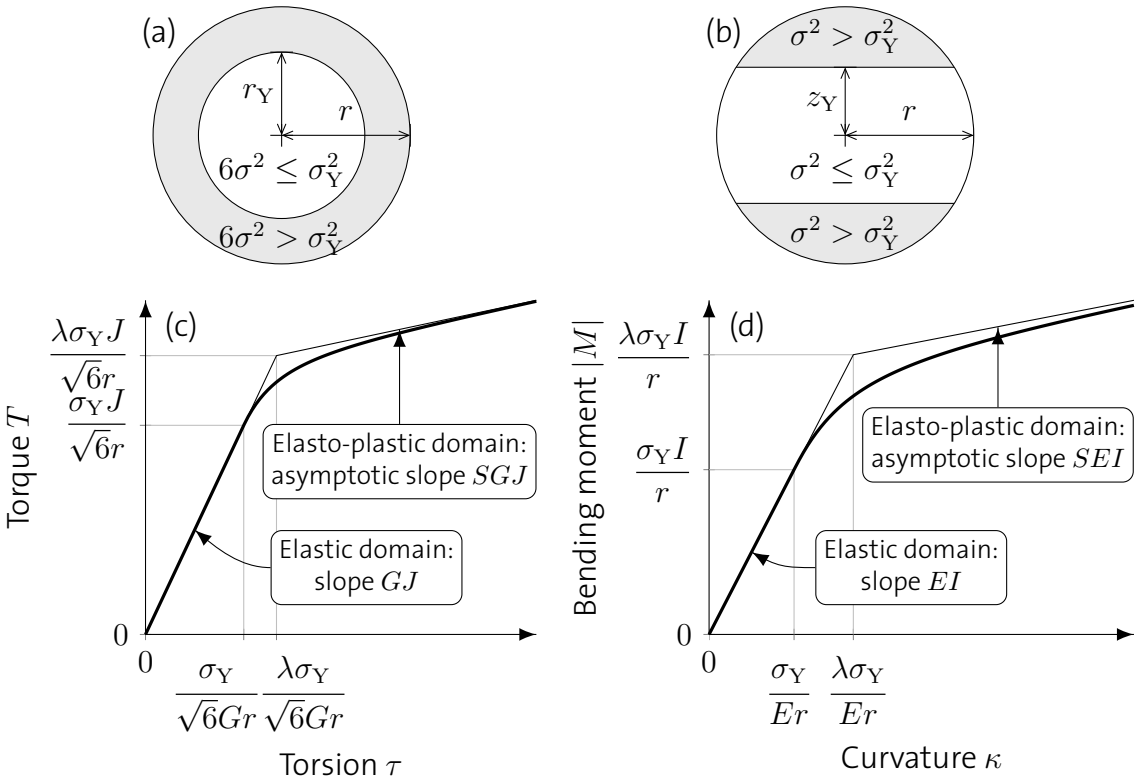

Figure 6.1: **Stress resultant plasticity model.** Elasto-plastic filament cross section in pure twist (a) and uniaxial bending (b). The gray regions are plastic, while the inner white region is elastic. Exact stress-strain relationship for linear hardening in stress resultant space for pure torsion (c) and uniaxial bending (d) (thick line) and their optimal bilinear approximations T_2 and M_2 (thin lines).

Substituting equations (6.5) and (6.6) into this condition yields the sought $\lambda = 4/3$, which is a purely geometric factor independent of the material properties. The yield point of the plastic hinge in torsion is thus given by the *plastic torque*

$$T_Y = T_2\big(\lambda\tau_Y(r)\big) = \lambda\frac{\sigma_Y J}{\sqrt{6}r} = \frac{2\pi}{3\sqrt{6}}\sigma_Y r^3. \tag{6.8}$$

To arrive at the *plastic moment* in uniaxial bending, the procedure is analogous. Bending with centerline curvature κ_y about the y-axis yields a moment of

$$M_y = \int_A z\sigma_{11}(z)\ \mathrm{d}A \tag{6.9}$$

where $\sigma_{11}(z) = -Ez\kappa_y$ is the bending stress distribution across the beam thickness in EULER–BERNOULLI theory (see equation (2.37c)). Similar to torsion, the wire cross section consists of two parts, an central elastic region $0 \le |z| \le z_Y$, where $\sigma_{11}(z) \le \sigma_Y$, and an inner/outer plastic lid $z_Y < |z| \le r$, where all material points have yielded,

as illustrated in Fig. 6.1b. The yield height z_Y is defined by $\sigma_{11}^2(z_\mathrm{Y}) = \sigma_\mathrm{Y}^2$:

$$z_\mathrm{Y}(\kappa_y) = \frac{\sigma_\mathrm{Y}}{E\kappa_y}. \tag{6.10}$$

Conversely, the curvature required to let the cross section yield at height $\pm z = z_\mathrm{Y}$ is

$$\kappa_\mathrm{Y}(z) = \frac{\sigma_\mathrm{Y}}{Ez}. \tag{6.11}$$

The exact nonlinear moment-curvature relationship for linear hardening hence follows by integration over the cross section as

$$\begin{aligned} |M_y(\kappa_y)| &= 4\int_0^{z_\mathrm{m}} \int_0^{\sqrt{r^2-z^2}} Ez^2\kappa_y \,\mathrm{d}y\,\mathrm{d}z + 4\int_{z_\mathrm{m}}^{r} \int_0^{\sqrt{r^2-z^2}} \sigma_\mathrm{Y} z + SEz^2\big[\kappa_y - \kappa_\mathrm{Y}(z)\big] \,\mathrm{d}y\,\mathrm{d}z \\ &= SEI\kappa_y + (1-S)E\kappa_y\left[\frac{r^4}{2}\tan^{-1}\left(\frac{z_\mathrm{m}}{y_\mathrm{m}}\right) + z_\mathrm{m}y_\mathrm{m}\left(z_\mathrm{m}^2 - \frac{r^2}{2}\right) + \frac{4}{3}y_\mathrm{m}^3 z_\mathrm{Y}\right] \end{aligned} \tag{6.12}$$

where $z_\mathrm{m} = \min\{r, z_\mathrm{Y}\}$ and $y_\mathrm{m} = \sqrt{r^2 - z_\mathrm{m}^2}$ are used for shorthand notation. Equation (6.12) is plotted in Fig. 6.1d. Analogous to equation (6.6), a bilinear approximation of the form

$$|M_2(\kappa)| = \begin{cases} EI\kappa & \text{if } \kappa \le \lambda\kappa_\mathrm{Y}(r) \\ EI\big(\lambda\kappa_\mathrm{Y}(r) + S\big[\kappa - \lambda\kappa_\mathrm{Y}(r)\big]\big) & \text{otherwise} \end{cases} \tag{6.13}$$

is used. Substituting equation (6.12) and equation (6.13) into the asymptotic convergence condition

$$\lim_{\kappa_y\to\infty} \frac{M_y(\kappa_y)}{M_2(\kappa_y)} = 1 \tag{6.14}$$

yields $\lambda = 16/3\pi$, so that the sought *plastic bending moment* for the hinge reads

$$M_\mathrm{Y} = \big|M_2\big(\lambda\kappa_\mathrm{Y}(r)\big)\big| = \lambda\frac{\sigma_\mathrm{Y} I}{r} = \frac{4}{3}\sigma_\mathrm{Y} r^3. \tag{6.15}$$

For the fourth and final internal degree of freedom, axial tension or compression, the situation simplifies substantially, as the stress resultant of equation (2.37a),

$$N = \int_A \sigma_{11} \,\mathrm{d}A = EA\zeta, \tag{6.16}$$

is constant across the beam cross section, and thus all points yield simultaneously, implying that the exact stress-strain relationship for linear hardening is bilinear also in stress resultant space. Therefore $\lambda = 1$, and the *plastic force* is given by

$$N_\mathrm{Y} = \lambda\sigma_\mathrm{Y} A = \pi\sigma_\mathrm{Y} r^2. \tag{6.17}$$

6.1.2 Yield condition

Various stress resultant yield criteria have been proposed as approximations to the VON MISES yield surface. A very common one is [170, 189]

$$\sqrt{\left(\frac{T}{T_\mathrm{Y}}\right)^2+\left(\frac{M_z}{M_\mathrm{Y}}\right)^2+\left(\frac{M_y}{M_\mathrm{Y}}\right)^2}+\left(\frac{N}{N_\mathrm{Y}}\right)^2-1=0 \tag{6.18}$$

where, for the moment being, the hardening variables and plastic strains are omitted. The computational disadvantage of this choice is that return mapping with work hardening requires costly iterative techniques. A simple and expedient alternative, that permits a single-step return to the admissible region even in combination with hardening, is obtained by not taking the square root in equation (6.18), which renders the yield surface an ellipsoidal approximation in four-dimensional resultant space. Clearly this overestimates the yield point in combined traction and torsion/bending, but for packing problems with very thin filaments such as in Chapter 5, the beam can be considered almost inextensible ($N \approx 0$), so that the square root becomes irrelevant and equation (6.18) is retrieved in close approximation.

In order to apply the standard direct radial return mapping procedure [202], all four degrees of freedom are rescaled to effective strains ε^eff such that the yield stress is given by the YOUNG's modulus times the effective strain at yield,

$$\sigma_\mathrm{Y}=E\varepsilon_\mathrm{Y}^\mathrm{eff}. \tag{6.19}$$

By recalling from equation (6.8) that the torque at the effective yield point of the plastic hinge reads $T_\mathrm{Y}=GJ\tau$ one immediately finds that equation (6.19) holds with

$$\varepsilon^\mathrm{eff}=\frac{G}{\lambda E}r\tau=\frac{3\sqrt{6}}{8(1+\nu)}r\tau=:\alpha\tau. \tag{6.20}$$

The analogous calculation carried out on equation (6.15) gives the effective bending strain

$$\varepsilon^\mathrm{eff}=\frac{1}{\lambda}r\kappa_y=\frac{3\pi}{16}r\kappa_y=:\beta\kappa_y, \tag{6.21}$$

and by virtue of equation (6.17) the trivial identity

$$\varepsilon^\mathrm{eff}=\zeta \tag{6.22}$$

follows for the fourth variable, axial strain. In this transformed stress-strain space, the approximate ellipsoidal VON MISES yield condition is recast into the convenient spherical form

$$\frac{\sigma^\mathrm{eff}}{\sigma_\mathrm{Y}}-1=0 \tag{6.23}$$

in which

$$\sigma^\mathrm{eff}=E\varepsilon^\mathrm{eff},\qquad \varepsilon^\mathrm{eff}=\left\|\boldsymbol{\varepsilon}^\mathrm{eff}\right\|,\qquad \boldsymbol{\varepsilon}^\mathrm{eff}=[\alpha\tau,\,\beta\kappa_z,\,\beta\kappa_y,\,\zeta]^\mathsf{T}, \tag{6.24}$$

according to equations (6.20) to (6.22).

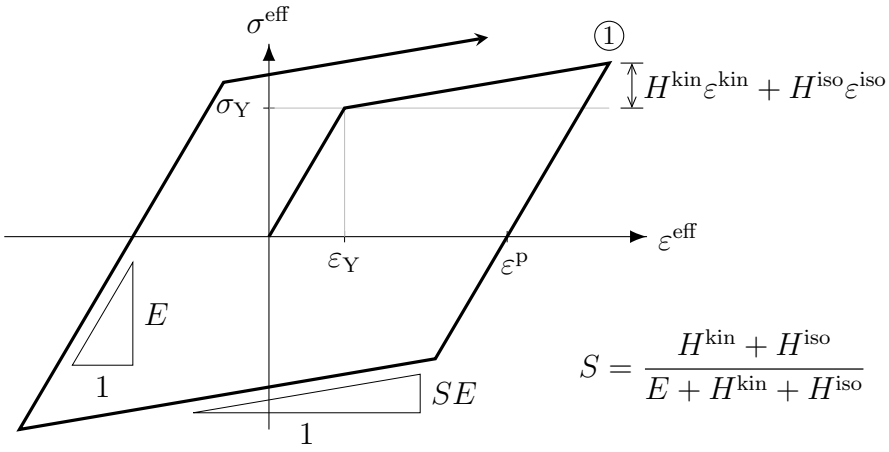

Figure 6.2: **Effective one-dimensional plasticity model** with combined linear kinematic and isotropic hardening, visualized for an example of cyclic loading. The plastic strain ε^{p}, the kinematic back strain ε^{kin} and the isotropic hardening strain ε^{iso} are labeled for point ①, at the beginning of unloading.

6.1.3 Return mapping

With the yield condition established in equation (6.23), it becomes straightforward to implement elasto-plastic beams with linear hardening efficiently by means of the standard radial return algorithm [202]. The full step-by-step procedure is given here for completeness. Up to nine additional internal variables are required per beam element to store the current plastic state:

- Four *plastic strains* $\boldsymbol{\varepsilon}^{\text{p}} = [\varepsilon_1^{\text{p}}, \varepsilon_2^{\text{p}}, \varepsilon_3^{\text{p}}, \varepsilon_4^{\text{p}}]^{\mathsf{T}}$ which hold the residual deformations after complete unloading
- Four *kinematic back strains* $\boldsymbol{\varepsilon}^{\text{kin}} = \left[\varepsilon_1^{\text{kin}}, \varepsilon_2^{\text{kin}}, \varepsilon_3^{\text{kin}}, \varepsilon_4^{\text{kin}}\right]^{\mathsf{T}}$ that represent the center of the elastic domain, which moves in the transformed strain space due to kinematic hardening
- A non-negative *isotropic strain* $\varepsilon^{\text{iso}} \geq 0$ that stores the increase of the elastic domain due to isotropic hardening

All of them vanish in the initial, stress-free configuration. A one-dimensional projection of the work hardening model and its internal variables is visualized in Fig. 6.2 for convenience. Given a new trial state in the corotated frame for element e, $\widehat{\mathbf{u}}_e = [\widehat{\varphi}_1, \widehat{\psi}_1, \widehat{\theta}_1, \widehat{u}_{12}, \widehat{\varphi}_2, \widehat{\psi}_2, \widehat{\theta}_2]^{\mathsf{T}}$, rescale it to obtain the effective strains along the element,

$$\boldsymbol{\varepsilon}^{\text{eff}} = \left[\alpha\frac{\widehat{\varphi}_1 - \widehat{\varphi}_2}{a_e},\ \beta\frac{\widehat{\psi}_1 - \widehat{\psi}_2}{a_e},\ \beta\frac{\widehat{\theta}_1 - \widehat{\theta}_2}{a_e},\ \frac{\widehat{u}_{12}}{a_e}\right]^{\mathsf{T}}. \tag{6.25}$$

Subtract the plastic and kinematic strains:

$$\boldsymbol{\varepsilon} = \boldsymbol{\varepsilon}^{\text{eff}} - \boldsymbol{\varepsilon}^{\text{p}} - \boldsymbol{\varepsilon}^{\text{kin}}. \tag{6.26}$$

Evaluate the yield condition:

$$f = \|\boldsymbol{\varepsilon}\| - \varepsilon_{\mathrm{Y}}^{\mathrm{eff}} - \varepsilon^{\mathrm{iso}}, \tag{6.27}$$

where ε_{Y} is the effective yield strain from equation (6.19). If $f > 0$, the current trial state lies outside of the admissible domain, and is hence projected onto its boundary by performing the following steps. Compute the change in the consistency parameter associated with the projection,

$$\Delta\gamma = \frac{Ef}{E + H^{\mathrm{kin}} + H^{\mathrm{iso}}}, \tag{6.28}$$

and the direction vector

$$\mathbf{n} = \frac{\boldsymbol{\varepsilon}}{\|\boldsymbol{\varepsilon}\|}. \tag{6.29}$$

Update the internal variables according to

$$\boldsymbol{\varepsilon}^{\mathrm{p}} \leftarrow \boldsymbol{\varepsilon}^{\mathrm{p}} + \Delta\gamma\mathbf{n}, \tag{6.30a}$$

$$\boldsymbol{\varepsilon}^{\mathrm{kin}} \leftarrow \boldsymbol{\varepsilon}^{\mathrm{kin}} + \Delta\gamma\frac{H^{\mathrm{kin}}}{E}\mathbf{n}, \tag{6.30b}$$

$$\boldsymbol{\varepsilon}^{\mathrm{iso}} \leftarrow \boldsymbol{\varepsilon}^{\mathrm{iso}} + \Delta\gamma\frac{H^{\mathrm{iso}}}{E}, \tag{6.30c}$$

which results in $f = 0$. Finally, independent of whether the plastic variables needed to be updated or not, subtract the plastic strains from the element DOFs to obtain the purely elastic part, which is then used to compute the forces and moments in equation (3.67):

$$\widehat{\mathbf{u}}_e \leftarrow \widehat{\mathbf{u}}_e - \left[\frac{a_e}{2\alpha}\varepsilon_1^{\mathrm{p}},\ \frac{a_e}{2\beta}\varepsilon_2^{\mathrm{p}},\ \frac{a_e}{2\beta}\varepsilon_3^{\mathrm{p}},\ a_e\varepsilon_4^{\mathrm{p}},\ -\frac{a_e}{2\alpha}\varepsilon_1^{\mathrm{p}},\ -\frac{a_e}{2\beta}\varepsilon_2^{\mathrm{p}},\ -\frac{a_e}{2\beta}\varepsilon_3^{\mathrm{p}}\right]^{\mathsf{T}}. \tag{6.31}$$

6.2 The effect of plasticity on filament packing

In two-dimensional systems, wire ductility is known to act as a local stabilizer in dense packings, leading to more curvature in the inner regions of the cavity [213]. Due to the missing third dimension, spatial constriction can essentially be skirted only by bending in a single direction, which is why plastic bending soon governs local arrangements. In three dimensions, on the other hand, more spatial alternatives are available to bypass states of high stress by lateral evasion. Consequently, it seems reasonable to assume that plasticity affects filament packing processes less dramatically in 3D than in 2D. As already mentioned in the introductory part of this chapter, however, quantitative arguments in this direction are still missing to date, with the exception of a single experimental realization presented by GOMES et al. [72], which is shown in Fig. 6.3.

Figure 6.3: **Three-dimensional packing of a ductile wire in a rigid sphere.** The wire is made of a tin/lead alloy and was fed from opposite sides into a rigid hollow sphere of size $q = 50$, of which only the lower half is pictured. Photograph from ref. [72], published under a Creative Commons license CC BY-NC.

In this final section, a first step toward a more systematic study of ductile filament packings in three-dimensional spatial confinement is made by employing the elasto-plastic constitutive model developed in Section 6.1. The results obtained so far are of merely preliminary character and are presented below to provide a starting point for further research on the subject.

In a series of computer simulations, an intrinsically straight wire was perpendicularly injected into a rigid spherical cavity. The relevant simulation parameters were fixed to an effective system size of $q = R/r = 50$, a static COULOMB friction coefficient of $\mu_\mathrm{s} = 0.3$ ($\mu_\mathrm{d} = 0.9\mu_\mathrm{s}$ as before), a kinematic hardening modulus of $H^\mathrm{kin}/E = 5\%$, and no isotropic hardening. The dimensionless yield strength $\varepsilon_\mathrm{Y} = \sigma_\mathrm{Y}/E$ was varied systematically to explore how it affects the packing process. For inertial effects to be insignificant for the result, the injection speed had to be slowed down up to ten times compared to the purely elastic simulations carried out in Sections 5.1 and 5.2.

As the ductile wire is fed in, it coils up along the inner wall of the cavity, where the radius of curvature is largest, very much like in the elastic limit (recall Fig. 5.1). This stands in sharp contrast to the two-dimensional case, where helical coils are inhibited because the filament is forced to stay planar, making a frequent alternation between clockwise and counter-clockwise bending necessary, which eventually gives rise to a characteristic loop pattern at sufficiently low plastic moments. In 3D, no such reorientation is observed at moderate packing densities, no matter how small the yield strength. Figures 6.4 and 6.5 reveal three regimes along the axis of varying yield points, that are very similar in morphology, but vastly different in energetics. Plasticity kicks in below a yield curvature of $\kappa_\mathrm{Y} = \varepsilon_\mathrm{Y}/\beta \approx 2.5/R$, with β from equation (6.21). This corresponds to the maximum curvature encountered on the juvenile piece of wire that has just entered the container but is not yet part of the coil.

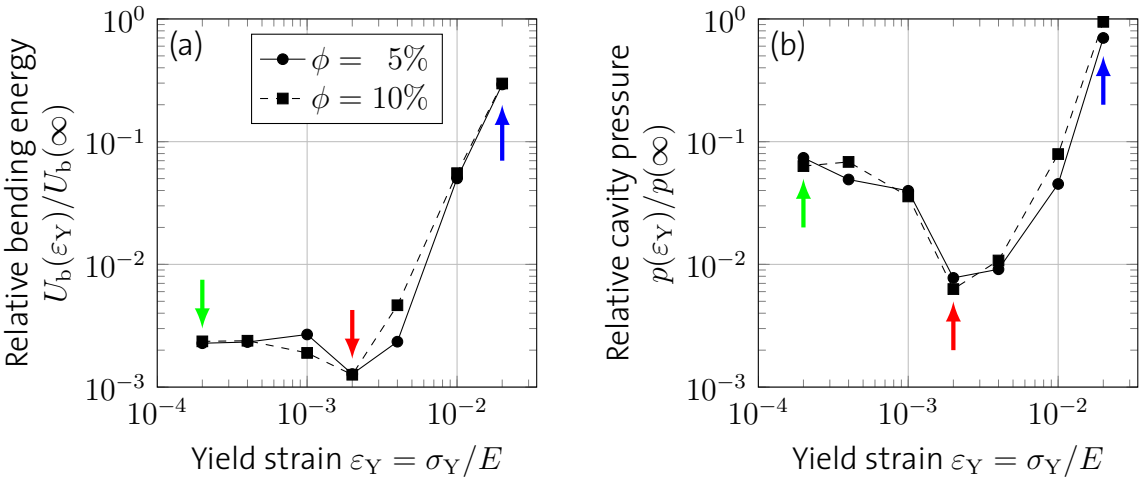

Figure 6.4: **Influence of the yield point on filament packing energetics.** Both the filament bending energy (a) and the pressure exerted on the spherical container (b) take a minimum at $\varepsilon_Y \approx 0.002$, independent of the packing densities examined here ($\phi \leq 10\%$). Arrows indicate the snapshot positions of Fig. 6.5.

As the yield strength is further decreased, the total elastic bending energy rapidly drops, indicating that more and more of the local wire curvature $\kappa = \kappa^e + \kappa^p$ is due to a permanent plastic deformation

$$\kappa^p = \frac{1}{\beta}\sqrt{(\varepsilon_2^p)^2 + (\varepsilon_3^p)^2}. \tag{6.32}$$

Not surprisingly, the pressure p exerted by the packed filament on the cavity wall sharply decreases accordingly. At a yield strain of $\varepsilon_Y \approx 0.002$ (corresponding to $\kappa_Y \approx 1/6R$), a minimum is attained in which the bending energy and bulk pressure almost vanish. Figure 6.5 shows why this is the case: Early plastic yielding allows the juvenile filament part to permanently bend with higher curvature than dictated by the cavity radius, at no energetic penalty. Consequently, the plastic coil does not bear strongly against the confining wall and packing is focused more on the interior regions. $\varepsilon_Y = 0.002$ is a typical value for, e.g., various copper alloys such as brass. As the yield strain is lowered even further to the regime of more ductile materials like aluminium or tin ($\varepsilon_Y \approx 0.0002$), the yield curvature is exceeded nearly everywhere in the packing, letting the packing process be governed by the hardening law almost entirely. Since linear work hardening is assumed here, the constitutive relationship therefore becomes effectively linear again and the ordered coiling of high ε_Y recurs at low ε_Y, which is evident from Fig. 6.5. Aligned coiling at minimum curvature is thus a *reentrant* feature in this regard. Consequently, the bending energy increases again to level off at a value determined by the hardening modulus (Fig. 6.4a) and the bulk pressure exhibits a similar behavior (Fig. 6.4b).

Although the packing morphologies at very low and high yield strengths are visually indistinguishable, their internal stress states differ fundamentally. At low

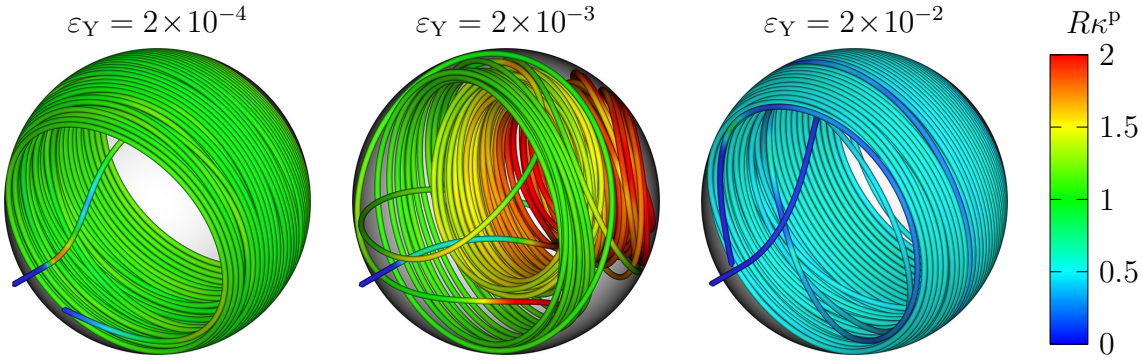

Figure 6.5: **Influence of the yield point on filament packing morphology.** The coiling morphology of thin wires with very low yield strength (left) is almost indistinguishable to that of nearly elastic wires (right). In between (middle), a regime exists where coils of higher curvature are formed, allowing the wire to detach from the inner wall. Simulation snapshots for Fig. 6.4 at a packing density of $\phi \approx 10\%$. The dimensionless plastic curvature is shown in color.

ε_Y, the plastic curvature is close to the value preferred by the local geometrical environment ($1/(R-r)$ in the outermost layer), whereas it naturally approaches zero as ε_Y gets closer to the elastic limit. This accentuates how elasto-plasticity decouples form from potential energy: Different internal stress levels do not necessarily imply different coiling, and conversely, similar shapes can store vastly different amounts of elastic energy.

These preliminary results offer first insights into the packing of elasto-plastic filaments in constrained three-dimensional spaces. Unlike in 2D [213], dry friction is not crucial for the packing process in rigid containers—the data presented above is largely insensitive to changes in μ. In this sense, plastically deforming wires are no different than purely elastic ones. The interplay of friction and filament yielding in *deformable* membranes, however, remains an open question, as does the packing at higher volume densities. It should also be noted that the pattern found experimentally (Fig. 6.3) significantly deviates from the coiled morphology observed here (Fig. 6.5), which is seemingly owed to the precise form of the nonlinear constitutive relationship. To test this hypothesis, different hardening moduli, and possibly also nonlinear hardening, should be examined in future research, as it appears to have a dramatic influence on the packing.

Understanding the effect of ductility on wire packing problems is particularly important in the optimal design of detachable coils for the stable embolization of saccular aneurysms. Strong cavity pressure might lead to further damage on the arterial wall, and highly ordered alignment of coils is undesirable for complete occlusion at moderate packing densities. With a more detailed quantitative analysis, it might be possible to formulate precise recommendations for the best choice of geometrical and material properties.

Chapter 7

Outlook and Conclusion

7.1 Extensibility and future prospects

Large deformation mechanics of thin objects is an extremely multifaceted topic, and apart from the questions raised in the previous chapter, many questions that go beyond the scope of the present work can be asked, with both practical and scientific relevance. A short list of open problems that can be tackled easily without any or with only minor extensions of the presented finite element program is given below, together with a summary of preliminary results where available.

Packing and statistical properties of filaments with intrinsic curvature or twist

In the framework of large-scale filament packing, a comprehensive study on the morphological phase space of strongly curved or twisted strings is still missing. Up to this point, moderate intrinsic curvature has been used to couple bending and twist only weakly, i.e., with a radius of curvature that is no smaller than the confinement radius. There are, however, many systems where intrinsic curvature is much higher. Various forms of DNA come to mind, especially *fractal globules* [82, 120, 146].

A related phenomenon occurring in helical structures such as tendrils and telephone cords is *helical perversion* [74, 143], which describes the spontaneous change of handedness in helices. In a preliminary computer simulation, an initially straight elastic rod of net length $L/r = 8 \times 10^4$ with net intrinsic radius of curvature $R^{\mathrm{int}}/r = 10$ was released to develop such perversions. Its relaxed static end configuration is shown in Fig. 7.1a, where a change of handedness every few windings is in evidence. The filament cannot fully relax to a stress-free configuration due to excluded volume, thus taking a locally helical shape with radius $\approx R^{\mathrm{int}}$ and pitch $2r$. The torsion of

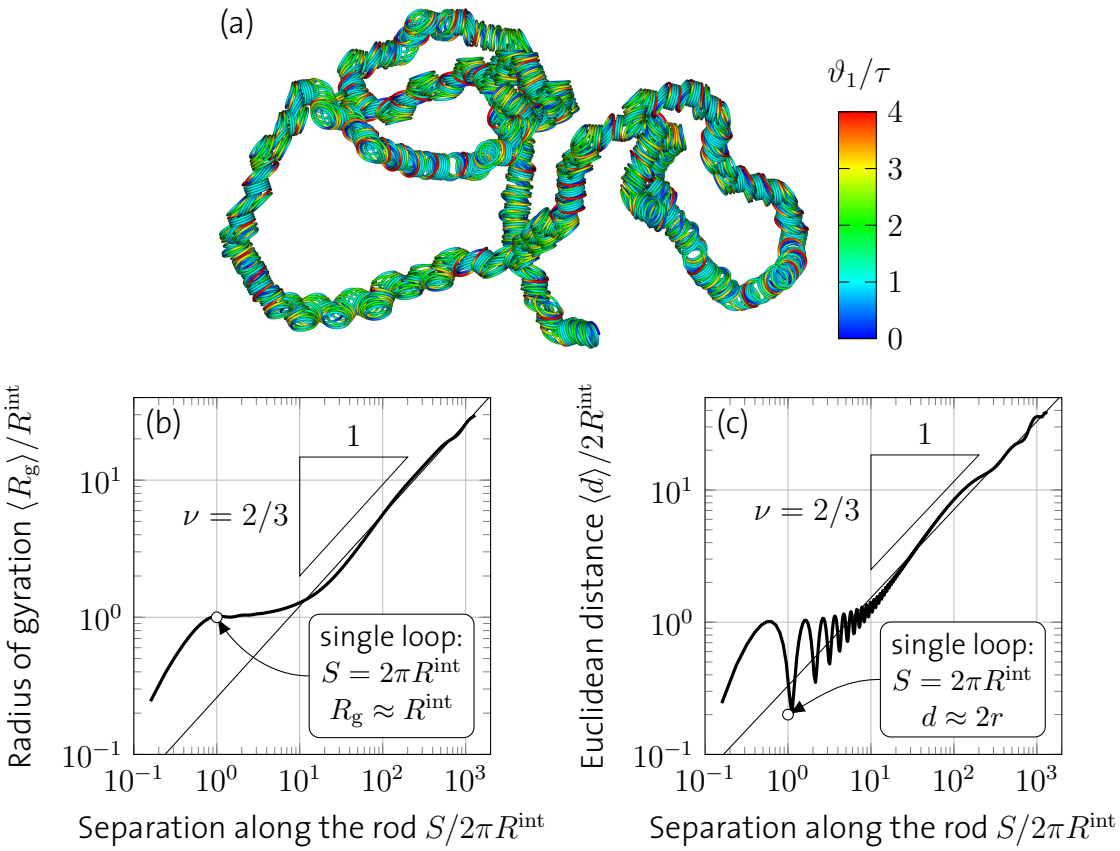

Figure 7.1: **Helical perversion of a rod with intrinsic curvature.** (a) Locally, the torsion ϑ_1 can be significantly larger than that of an equivalent dense helix, τ (see equation (7.1)). (b,c) Large-range scaling of the radius of gyration and the point-to-point distance with the axial separation S. The straight lines correspond to an exponent of $\nu = 2/3$.

such a helix is

$$\tau = \frac{r/\pi}{(r/\pi)^2 + (R^{\mathrm{int}})^2}, \tag{7.1}$$

which is used for normalization of the torsion ϑ_1 in the color scale. Each perversion induces a change of direction at the helical length scale, resulting in a relatively disordered global path of the structure. The Euclidean distance of two mass points separated by a distance S along the rod centerline,

$$d(s, S) = \|\mathbf{x}(s + S) - \mathbf{x}(s)\|, \qquad s, s + S \in [0, L], \tag{7.2}$$

as well as the radius of gyration,

$$R_{\mathrm{g}}^2(s, S) = \frac{1}{S} \int_s^{s+S} \|\mathbf{x}(s') - \overline{\mathbf{x}}(s, S)\|^2 \, \mathrm{d}s', \tag{7.3a}$$

$$\overline{\mathbf{x}}(s, S) = \frac{1}{S} \int_s^{s+S} \mathbf{x}(s') \, \mathrm{d}s' \tag{7.3b}$$

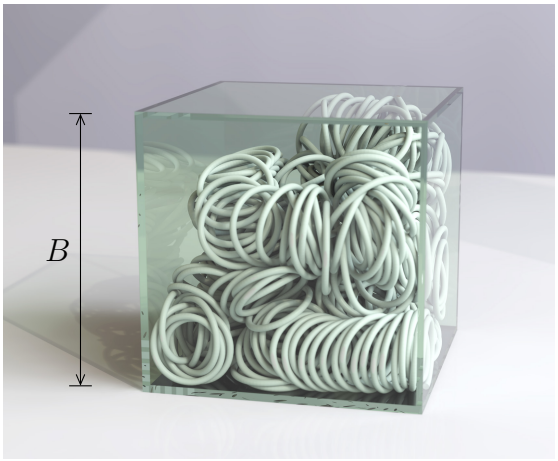

Figure 7.2: **Packing of a pre-curved cord.** Simulation snapshot at a packing density of $\phi \approx 13\%$ of an intrinsically curved wire with $R^{\text{int}}/r = 10$ that was fed through a small hole into a rigid cube with edge length $B/r = 80$.

are consistently found to scale as

$$\langle R_{\text{g}}(s,S)\rangle \sim \langle d(s,S)\rangle \sim S^{\nu}. \tag{7.4}$$

with exponent $\nu \approx 2/3$, as shown in Fig. 7.1b,c. $\langle\cdot\rangle = (1/L)\int_0^L \cdot\, \mathrm{d}s$ denotes the average over the filament length. The global path does hence *not* follow a random walk, for which $\nu = 1/2$. It could be worthwhile to verify this presumed exponent with simulations on longer rods, to investigate its dependence on the ratio R^{int}/r, and to clarify its relation to the FLORY exponent for self-avoiding polymers in three dimensional space, $\nu = 3/5$ [63].

Helical perversions also emerge when an intrinsically curved filament is injected into spatial confinement. Figure 7.2 shows an example simulation in a box cavity. A systematic study of entanglement, interlocking and maximum packing density of helical wires as a function of helical radius and pitch could be of particular value for the medial industry dedicated to the optimal design of detachable microcoils for the stable surgical occlusion of cerebral aneurysms. All required features are readily implemented in the presented finite element program; intrinsic rotations can be set via equation (3.63).

Unpacking and disentanglement of packed filaments

A natural next step in the study of filament packing and entanglement is to explore the reverse process: extraction and disentanglement. Although long filaments tightly packed in spatial confinement can be extracted without obstruction, as already mentioned in Section 5.1.2, abrupt removal of the container does not allow

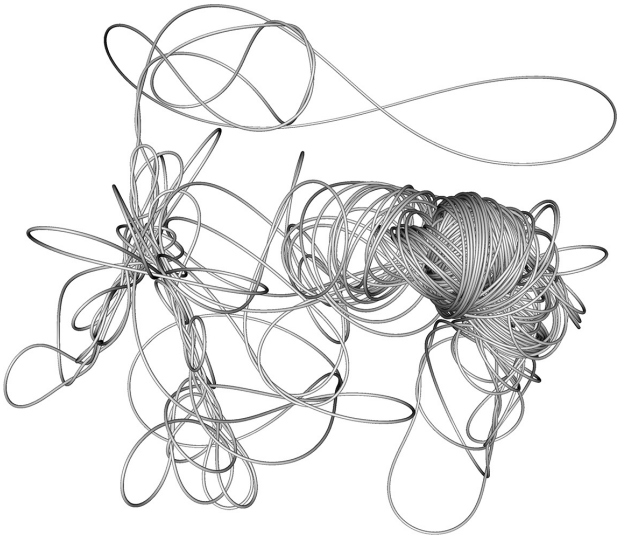

Figure 7.3: **Disentanglement of a released coil.** Computer simulation of a packed rigid sphere ($q = 40$, packing density $\phi \approx 50\%$) which is instantaneously removed. Even though packed elastic wires aren't knotted, removal of the confinement doesn't lead to entire disentanglement when friction is involved.

the elastic thread to completely disentangle without further external effort. Very heterogenous tangled coils are left behind, whose structure is expected to depend strongly on the initial packing density and friction. An example configuration is pictured in Fig. 7.3. A better understanding of this dependency could shed some light on why it can be so cumbersome to unsnarl even seemingly ordered coils, and might be useful e.g. for DNA extraction.

Fracture and segmentation

Perhaps even more prevalent in Nature and our daily life than the packing of a single long filament is that of multiple ones. A bowl of pasta (Fig. 7.4) or a haystack are just two out of many examples. Segmentation can also occur spontaneously as a mode of material failure. A question that has not been pursued exhaustively is the effect of segment length and fracture on packing processes, in either rigid or deformable confinements. Figure 7.5 shows a preliminary two-dimensional simulation of a ductile and fragile wire injected into a circular container. Fragmentation clearly has a increasing effect on the maximum packing density, as is breaks up loops at the point of highest curvature, allowing the filament to occupy space that is otherwise excluded by the inner void of loops. Whether the same holds in 3D, too, remains unclear. The relationship of such configurations to the random packing of rigid rods [167], and the impact of flexibility of segmented fibers on the maximum packing fraction, which is barely known [115], could be studied easily on a large scale with the presented computational model.

Figure 7.4: **A bowl of spaghetti.** Left: Photography copyright by STUART MONK / 123RF Stock Photo. Right: Simulation in which a pliable segmented cord (the spaghetti) was dropped into an oblate cavity (the bowl) under the effect of gravity and significant frictional forces.

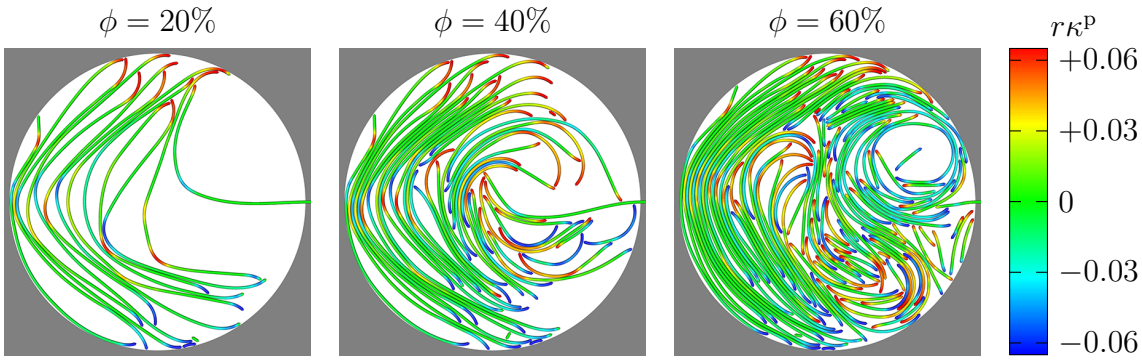

Figure 7.5: **Fracture of a ductile wire in a two-dimensional cavity.** The relevant simulation parameters are $q = 100$, $\mu = 0.5$, a plastic yield strain of $\sigma_{\mathrm{Y}}/E = 1\%$, a kinematic hardening modulus of $H^{\mathrm{kin}}/E = 5\%$, and a fracture strain of $\sigma_F/E = 1.2\%$. In color, the signed plastic curvature κ^{p} is shown, rescaled by the wire radius r.

7.2 Summary and significance

When thin deformable bodies grow or are spatially confined to length scales that are much larger than their thickness, but much shorter than their longitudinal equilibrium extent, they develop a wealth of complex shapes and patterns, in the first instance owing to their low bending rigidity. Nature and our daily environment are rife with examples. As soon as deformations are so large that the objects come in contact with themselves or with one another, contact phenomena give rise to even more morphological diversity. The presented thesis considered shape transformation and pattern formation due to different kinds of growth, confinements and mechanical interactions of thin bodies. The main focus was on a specific subclass of problems that couples these effects in a particularly challenging way: the packing of long filaments in flexible cavities.

In the first part, a highly capable finite element program was developed to study the dynamic morphogenesis, interplay and packing of thin wires and shells undergoing very large deformations and growth. It was thoroughly implemented and verified, and its capabilities and limitations were assessed. In the second part, numerical simulations were carried out to quantitatively explore the morphological phase space under the aforementioned constraints on a series of example settings. For each, the respective non-dimensional geometric and material control parameters were identified that govern the process of shape transformations or packing. A set of distinct morphological phases were found, and their characteristic statistical and energetic properties were measured and compared. For the rigorous definition of these phases and the transitions between them, appropriate order parameters were defined and the associated broken symmetries were identified. The results from computer simulations are fully consistent with experiments conducted on off-the-shelf materials at the human length scale.

Different types of growth give rise to very different shapes. A *uniformly* and *isotropically* swelling thin elastic sheet exhibits the exact same crumpling behavior in spatial confinement as an invariant sheet under external compression. *Differential* in-plane growth, on the other hand, lets even an unconstrained shell buckle out of plane. The fractal dimension of wrinkled edges of beet leaves and torn plastic sheets, that are due to differential orthotropic growth with steep metric gradients, was determined and compared to related self-similar curves. A broad family of differential orthotropic growth fields yield unimodal boundary wrinkling reminiscent of flower petals, with a universal scaling law for the number of wrinkles. Thin wires, however, don't offer the same amount of freedom due to their quasi-one-dimensionality, which essentially limits the scope of growth to the axial direction. Two extreme cases of axial filament growth in constrained spaces were studied: localized to a point (in the form of injection from outside) and uniformly distributed.

Previous scientific work on the filament packing problem concentrated on the ideal case of rigid spherical confinement, precluding their results from being directly applicable to biophysical and medical systems in which long threads are enclosed by deformable membranes. In the present thesis, for the first time, the morphological phase space of filament packings was explored in a regime that is conceptually very different. A regime where the growing filament can strongly deform the cavity, allowing for a surprisingly enriching mutual feedback between the two structures. This change of paradigm delivers dramatic consequences. While friction has relatively little influence on the filament coiling in rigid three-dimensional spheres, it plays a key role in flexible shells. Even moderate frictional forces lead to a large amount of disorder in the packing, effectively inhibiting ordered coiling and bundling of the thread. This novel insight sheds light on daily mysteries like the spontaneous entanglement of earphone cords in one's pockets. In combination, container flexibility and friction can give rise to bundling, coiling, folding or crumpling, to order or disorder, and to the spontaneous breaking of various symmetries. Scaling laws have been found that characterize or separate these different regimes, and power laws unveiled hierarchic or self-similar processes in the packing of flexibly confined filaments.

The presented findings establish a paradigm for understanding morphogenesis of thin filaments in a multitude of biological mechanisms. It was shown how Nature may employ flexible envelopment and low frictional forces as a mechanical trick to realize spontaneous bundling and alignment of confined threads, as it is observed in giant vesicles, erythrocytes, hagfish cells etc., without need for filament interlinking. On the technological side, the morphologies discovered in flexible confinement should find direct impact in nanorobotics and nanomotors, for which the reported folding of elastic rings provides a new method to stably store and deploy mechanical work in tightly confined spaces. Unlike linear nanowires, which coil into quasi-two-dimensional spirals or tori, ring-like filaments fold in a three-dimensional fashion and possess no sharp ends that could pierce their environment. Such systems need to be designed with as little friction as possible in order to avoid energetically and spatially less optimal disordered configurations.

Growth, packing and mutual interaction of slender objects were addressed from a continuum mechanical perspective, considering shapes and shape transformations as they emerge from "dead" physical principles even in living organisms—or as the famous mathematical biologist, whose pioneering ideas have served as a guiding keynote for this work, put it:

> *Cell and tissue, shell and bone, leaf and flower, are so many portions of matter. [...] Their problems of form are in the first instance mathematical problems, their problems of growth are essentially physical problems, and the morphologist is,* ipso facto*, a student of physical science.*
>
> – D'Arcy Wentworth Thompson, *On Growth and Form* (1917)

Appendix A

Individual numerical realizations

To arrive at the quantitative morphological phase diagram in Fig. 5.31, a series of numerical simulations at different phase space parameters were carried out. Each of them produced one of the morphologies as detailed in Section 5.3, and is represented in Fig. A.1 by a colored data point. Black symbols denote simulations that yielded the mixed configuration described in Section 5.3.

The phase boundaries were obtained from a fit to these individual realizations. In the frictionless case, the phase boundary is well approximated by a quadratic curve in $\log(f) - \log(\gamma)$ space at all fixed system sizes q examined, and thus this functional relationship is used for the least-squares fits at $\mu = 0$.

In Fig. A.1 the classical morphology is bounded toward large shell flexibilities f by a dashed line to indicate where the stability criterion $l \ll q^2$ mentioned in Section 5.3 is no longer fulfilled and the filament detaches from the confining wall to buckle inward. The uncolored area in the phase diagram may hence be considered a fifth morphology, and the transition from the classical and spiral phases to this *buckled* phase can be quantified by considering as order parameter the fraction of filament length that is not in contact with the enclosing shell (at fixed l). It vanishes for the classical and spiral morphologies while taking a strictly positive value in the buckled configurations.

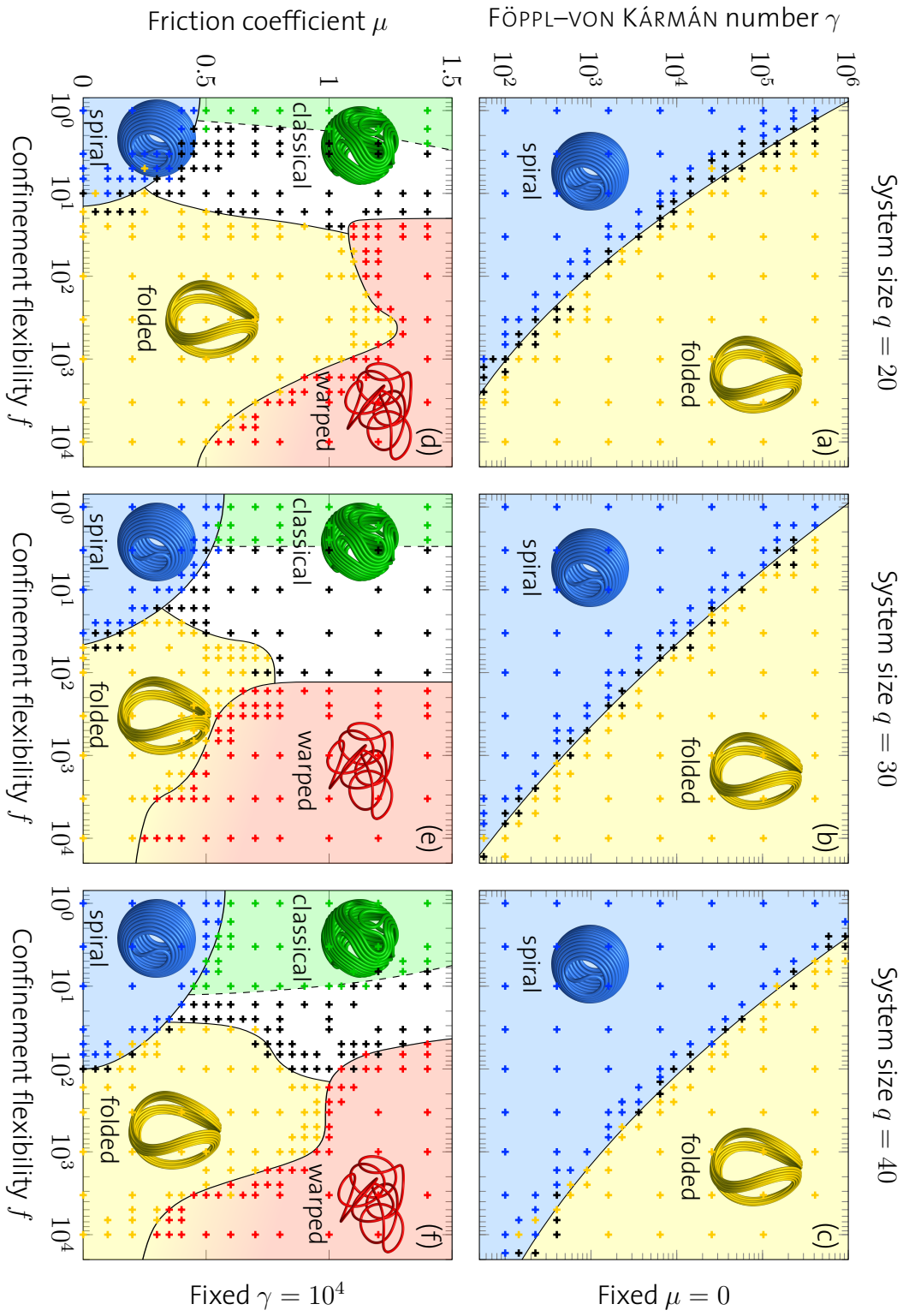

Figure A.1: **Morphological phase diagram with individual realizations** for different system sizes q. (a-c) Cuts through the phase space for the frictionless case ($\mu = 0$). (d-f) Cuts through the phase space for thin shells ($\gamma = 10^4$).

References

[1] *Abaqus 6.11 Benchmarks Manual*. Dassault Systèmes Simulia Corp. Providence, RI, USA, 2011.

[2] F. Alonso-Marroquín and H. J. Herrmann. Ratcheting of Granular Materials. *Phys. Rev. Lett.* **92** (2004), 054301.

[3] D. Ambrosi and F. Guana. Stress-Modulated Growth. *Math. Mech. Solids* **12** (2007), 319–342.

[4] J. Argyris. An excursion into large rotations. *Comput. Meth. Appl. Mech. Eng.* **32** (1982), 85–155.

[5] J. Arsuaga, R. K.-Z. Tan, M. Vazquez, D. W. Sumners, and S. C. Harvey. Investigation of viral DNA packaging using molecular mechanics models. *Biophys. Chem.* **101–102** (2002), 475–484.

[6] B. Audoly and A. Boudaoud. Self-Similar Structures near Boundaries in Strained Systems. *Phys. Rev. Lett.* **91** (2003), 086105.

[7] B. Audoly. The self-similar rippling of leaf edges and torn plastic sheets. *Europhys. News* **35** (2004), 145–148.

[8] Y. Başar and W. B. Krätzig. *Mechanik der Flächentragwerke: Theorie, Berechnungsmethoden, Anwendungsbeispiele*. Braunschweig: Vieweg, 1985.

[9] K. J. Bathe and S. Bolourchi. Large displacement analysis of three-dimensional beam structures. *Int. J. Numer. Meth. Eng.* **14** (1979), 961–986.

[10] K. J. Bathe, A. Iosilevich, and D. Chapelle. An evaluation of the MITC shell elements. *Comput. Struct.* **75** (2000), 1–30.

[11] E. Bayart, S. Deboeuf, F. Corson, A. Boudaoud, and M. Adda-Bedia. Measuring order in the isotropic packing of elastic rods. *Europhys. Lett.* **95** (2011), 34002.

[12] G. P. Bazeley, K. Cheung, B. Irons, and O. C. Zienkiewicz. Triangular elements in plate bending—conforming and non-conforming solutions. In: *Air Force Flight Dynamics Laboratory Technical Report: AFFDL-TR-66-80*. Duyton, Ohio, 1966, 547–576.

[13] T. Belytschko and B. J. Hsieh. Non-linear transient finite element analysis with convected co-ordinates. *Int. J. Numer. Meth. Eng.* **7** (1973), 255–271.

[14] T. Belytschko, H. Stolarski, W. K. Liu, N. Carpenter, and J. S. J. Ong. Stress projection for membrane and shear locking in shell finite elements. *Comput. Meth. Appl. Mech. Eng.* **51** (1985), 221–258.

[15] M. Ben Amar and Y. Pomeau. Crumpled paper. *Proc. R. Soc. A* **453** (1997), 729–755.

[16] H. Biermann, A. Levin, and D. Zorin. Piecewise smooth subdivision surfaces with normal control. *SIGGRAPH 'oo* (2000), 113–120.

[17] D. L. Blair and A. Kudrolli. Geometry of crumpled paper. *Phys. Rev. Lett.* **94** (2005), 166107.

[18] L. Boué, M. Adda-Bedia, A. Boudaoud, D. Cassani, Y. Couder, A. Eddi, and M. Trejo. Spiral patterns in the packing of flexible structures. *Phys. Rev. Lett.* **97** (2006), 166104.

[19] B. Brank, F. B. Damjanić, and D. Perić. On implementation of a nonlinear four node shell finite element for thin multilayered elastic shells. *Comput. Mech.* **16** (1995), 341–359.

[20] R. Bridson, R. Fedkiw, and J. Anderson. Robust treatment of collisions, contact and friction for cloth animation. *Trans. Graph.* **21** (2002), 594–603.

[21] G. Buck and J. Simon. The spectrum of filament entanglement complexity and an entanglement phase transition. *Proc. R. Soc. A* **468** (2012), 4024–4040.

[22] G. R. Buck and J. K. Simon. Total curvature and packing of knots. *Topol. Appl.* **154** (2007), 192–204.

[23] C. J. Burgoyne and M. G. Brennan. Exact Ilyushin yield surface. *Int. J. Solids Struct.* **30** (1993), 1113–1131.

[24] R. Carbó, L. Leyda, and M. Arnau. How similar is a molecule to another? An electron density measure of similarity between two molecular structures. *Int. J. Quantum Chem.* **17** (1980), 1185–1189.

[25] A. Cardona and M. Geradin. A beam finite element non-linear theory with finite rotations. *Int. J. Numer. Meth. Eng.* **26** (1988), 2403–2438.

[26] E. Catmull and J. Clark. Recursively generated B-spline surfaces on arbitrary topological meshes. *Comput. Aided Des.* **10** (1978), 350–355.

[27] E. Cerda, K. Ravi-Chandar, and L. Mahadevan. Thin films: Wrinkling of an elastic sheet under tension. *Nature* **419** (2002), 579–580.

[28] M. E. Cerritelli, N. Cheng, A. H. Rosenberg, C. E. McPherson, F. P. Booy, and A. C. Steven. Encapsidated conformation of bacteriophage T7 DNA. *Cell* **91** (1997), 271–280.

[29] S. Chandrasekhar. *Liquid crystals*. 2nd ed. Cambridge: Cambridge University Press, 1992.

[30] D. Chapelle and K. J. Bathe. Fundamental considerations for the finite element analysis of shell structures. *Comput. Struct.* **66** (1998), 19–36.

[31] D. Chapelle and K. J. Bathe. *The Finite Element Analysis of Shells: Fundamentals*. 2nd ed. Berlin: Springer, 2011.

[32] L. Chen, H. Wang, J. Xu, X. Shen, L. Yao, L. Zhu, Z. Zeng, H. Zhang, and H. Chen. Controlling reversible elastic deformation of carbon nanotube rings. *J. Am. Chem. Soc.* **133** (2011), 9654–9657.

[33] L. Chen, S. Yu, H. Wang, J. Xu, C. Liu, W. H. Chong, and H. Chen. General methodology of using oil-in-water and water-in-oil emulsions for coiling nanofilaments. *J. Am. Chem. Soc.* **135** (2013), 835–843.

[34] P. G. Ciarlet. Un modèle bi-dimensionnel non linéaire de coque analogue à celui de W.T. Koiter. *C. R. Acad. Sci. I* **331** (2000), 405–410.

[35] F. Cirak and Q. Long. Subdivision shells with exact boundary control and non-manifold geometry. *Int. J. Numer. Meth. Eng.* **88** (2011), 897–923.

[36] F. Cirak and M. Ortiz. Fully C^1-conforming subdivision elements for finite deformation thin-shell analysis. *Int. J. Numer. Meth. Eng.* **51** (2001), 813–833.

[37] F. Cirak, M. Ortiz, and A. Pandolfi. A cohesive approach to thin-shell fracture and fragmentation. *Comput. Meth. Appl. Mech. Eng.* **194** (2005), 2604–2618.

[38] F. Cirak, M. Ortiz, and P. Schröder. Subdivision surfaces: a new paradigm for thin-shell finite-element analysis. *Int. J. Numer. Meth. Eng.* **47** (2000), 2039–2072.

[39] W. D. Cohen, Y. Sorokina, and I. Sanchez. Elliptical versus circular erythrocyte marginal bands: Isolation, shape conversion, and mechanical properties. *Cell. Motil. Cytoskel.* **40** (1998), 238–248.

[40] E. Cosserat and F. Cosserat. *Théorie des corps déformables*. Paris: A. Hermann et Fils, 1909.

[41] M. A. Crisfield. A consistent co-rotational formulation for non-linear, three-dimensional, beam-elements. *Comput. Meth. Appl. Mech. Eng.* **81** (1990), 131–150.

[42] M. A. Crisfield. *Non-linear Finite Element Analysis of Solids and Structures: Vol. 2: Advanced Topics*. Chichester: John Wiley & Sons, 1997. Chap. 16–17.

[43] J. Dervaux and M. Ben Amar. Morphogenesis of Growing Soft Tissues. *Phys. Rev. Lett.* **101** (2008), 068101.

[44] J. Dervaux, P. Ciarletta, and M. B. Amar. Morphogenesis of thin hyperelastic plates: A constitutive theory of biological growth in the Föppl–von Kármán limit. *J. Mech. Phys. Solids* **57** (2009), 458–471.

[45] A. DiCarlo and S. Quiligotti. Growth and balance. *Mech. Res. Commun.* **29** (2002), 449–456.

[46] E. H. Dill. Kirchhoff's theory of rods. *Arch. Hist. Exact Sci.* **44** (1992), 1–23.

[47] C. C. Donato and M. A. F. Gomes. Condensation of elastic energy in two-dimensional packing of wires. *Phys. Rev. E* **75** (2007), 066113.

[48] C. C. Donato, M. A. F. Gomes, and R. E. de Souza. Crumpled wires in two dimensions. *Phys. Rev. E* **66** (2002), 015102.

[49] C. C. Donato, M. A. F. Gomes, and R. E. de Souza. Scaling properties in the packing of crumpled wires. *Phys. Rev. E* **67** (2003), 026110.

[50] C. C. Donato, F. A. Oliveira, and M. A. F. Gomes. Anomalous diffusion on crumpled wires in two dimensions. *Physica A* **368** (2006), 1–6.

[51] D.-Z. Du and X.-S. Zhang. Global convergence of Rosen's gradient projection method. *Math. Program.* **44** (1989), 357–366.

[52] J. Dujc and B. Brank. Stress resultant plasticity for shells revisited. *Comput. Meth. Appl. Mech. Eng.* **247–248** (2012), 146–165.

[53] W. C. Earnshaw and S. C. Harrison. DNA arrangement in isometric phage heads. *Nature* **268** (1977), 598–602.

[54] D. Eberly. *Distance Between Two Line Segments in 3D*. 1999. URL: `http://www.geometrictools.com/Documentation/DistanceLine3Line3.pdf` (visited on 2012-03-15).

[55] D. Eberly. *3D Game Engine Design: A Practical Approach to Real-Time Computer Graphics*. San Francisco: Morgan Kaufmann, 2000, pp. 43–49.

[56] E. Efrati, E. Sharon, and R. Kupferman. Elastic theory of unconstrained non-Euclidean plates. *J. Mech. Phys. Solids* **57** (2009), 762–775.

[57] M. Elbaum, D. Kuchnir Fygenson, and A. Libchaber. Buckling microtubules in vesicles. *Phys. Rev. Lett.* **76** (1996), 4078–4081.

[58] C. Ericson. *Real-Time Collision Detection*. San Francisco: Morgan Kaufmann, 2005, pp. 136–142.

[59] C. Ernst and A. Por. Average crossing number, total curvature and rope-length of thick knots. *J. Knot. Theor. Ramif.* **21** (2012), 1250028.

[60] C. A. Felippa. *Advanced Finite Element Methods*. Lecture delivered at the University of Colorado at Boulder. 2013. URL: `http://www.colorado.edu/engineering/CAS/courses.d/AFEM.d/AFEM.Ch15.d/AFEM.Ch15.pdf` (visited on 2014-07-30).

[61] B. Fernholm. Thread Cells from the Slime Glands of Hagfish (Myxinidae). *Acta Zool.* **62** (1981), 137–145.

[62] R. P. Feynman, R. P. Leighton, and M. Sands. *The Feynman lectures on physics: Vol I: Mainly mechanics, radiation and heat*. Reading: Addison-Wesley, 1964.

[63] P. J. Flory. The Configuration of Real Polymer Chains. *J. Chem. Phys.* **17** (1949), 303–310.

[64] S. R. Forrest and T. A. Witten. Long-range correlations in smoke-particle aggregates. *J. Phys. A: Math. Gen.* **12** (1979), L109.

[65] M. Forsting and I. Wanke. Tiefe Einsichten und schonende Eingriffe. In: *Neurowissenschaften: Wir und unser Gehirn*. Ed. by D. Stolke. Vol. 22. UNIKATE. Essen: Universität Duisburg-Essen / Wissenschaftsverlag, 2003, 42–49.

[66] M. Fošnarič, A. Iglič, D. M. Kroll, and S. May. Monte Carlo simulations of a polymer confined within a fluid vesicle. *Soft Matter* **9** (2013), 3976–3984.

[67] M. H. Freedman and Z.-X. He. Divergence-free fields: Energy and asymptotic crossing number. *Ann. Math.* **134** (1991), 189–229.

[68] J. C. F. Gauss. *Werke*. Vol. 5. Göttingen: Dieterich, 1867, p. 605.

[69] S. Ghosal. Capstan friction model for DNA ejection from bacteriophages. *Phys. Rev. Lett.* **109** (2012), 248105.

[70] G. Gilat. Chiral coefficient—a measure of the amount of structural chirality. *J. Phys. A* **22** (1989), L545–L550.

[71] L. Giomi and L. Mahadevan. Minimal surfaces bounded by elastic lines. *Proc. R. Soc. A* **468** (2012), 1851–1864.

[72] M. A. F. Gomes, V. P. Brito, and M. S. Araújo. Geometric properties of crumpled wires and the condensed non-solid packing state of very long molecular chains. *J. Braz. Chem. Soc.* **19** (2008), 293–298.

[73] M. A. F. Gomes, V. P. Brito, A. S. O. Coelho, and C. C. Donato. Plastic deformation of 2D crumpled wires. *J. Phys. D: Appl. Phys.* **41** (2008), 235408.

[74] A. Goriely and M. Tabor. Spontaneous Helix Hand Reversal and Tendril Perversion in Climbing Plants. *Phys. Rev. Lett.* **80** (1998), 1564–1567.

[75] P. Grayson and I. J. Molineux. Is phage DNA 'injected' into cell—biologists and physicists can agree. *Curr. Opin. Microbiol.* **10** (2007), 401–409.

[76] A. E. Green and R. T. Shield. Finite Elastic Deformation of Incompressible Isotropic Bodies. *Proc. R. Soc. Lond. A* **202** (1950), 407–419.

[77] S. Green. *Multilevel, Subdivision-Based, Thin Shell Finite Elements: Development and an Application to Red Blood Cell Modelings*. PhD thesis. Seattle: University of Washington, 2003.

[78] S. Green and G. Turkiyyah. Second-order accurate constraint formulation for subdivision finite element simulation of thin shells. *Int. J. Numer. Meth. Eng.* **61** (2004), 380–405.

[79] E. Grinspun. *The basis refinement method*. PhD thesis. Pasadena: California Institute of Technology, 2003.

[80] E. Grinspun, P. Krysl, and P. Schröder. CHARMS: a simple framework for adaptive simulation. *Trans. Graph.* **21** (2002), 281–290.

[81] E. Grinspun, F. Cirak, P. Schröder, and M. Ortiz. *Non-Linear Mechanics and Collisions for Subdivision Surfaces*. Technical report. Pasadena: California Institute of Technology, 1999.

[82] A. Y. Grosberg, S. Nechaev, and E. Shakhnovich. The role of topological constraints in the kinetics of collapse of macromolecules. *J. Phys. France* **49** (1988), 2095–2100.

[83] F. Gruttmann, E. Stein, and P. Wriggers. Theory and numerics of thin elastic shells with finite rotations. *Arch. Appl. Mech.* **59** (1989), 54–67.

[84] G. Guglielmi, F. Viñuela, I. Sepetka, and V. Macellari. Electrothrombosis of saccular aneurysms via endovascular approach. Part 1: Electrochemical basis, technique, and experimental results. *J. Neurosurg.* **75** (1991), 1–7.

[85] G. Guglielmi, F. Viñuela, J. Dion, and G. Duckwiler. Electrothrombosis of saccular aneurysms via endovascular approach. Part 2: Preliminary clinical experience. *J. Neurosurg.* **75** (1991), 8–14.

[86] J. Guven, M. M. Müller, and P. Vázquez-Montejo. Conical instabilities on paper. *J. Phys. A* **45** (2012), 015203.

[87] J. Guven and P. Vázquez-Montejo. Confinement of semiflexible polymers. *Phys. Rev. E* **85** (2012), 026603.

[88] J. C. Hart. Distance to an Ellipsoid. In: *Graphics Gems IV*. Ed. by P. S. Heckbert. AP Professional, 1994, 113–119.

[89] H. Hertz. Ueber die Berührung fester elastischer Körper. *J. reine angew. Math.* **92** (1882), 156–171.

[90] A. Hoger. On the determination of residual stress in an elastic body. *J. Elasticity* **16** (1986), 303–324.

[91] M. Honda, K. Takiguchi, S. Ishikawa, and H. Hotani. Morphogenesis of liposomes encapsulating actin depends on the type of actin-crosslinking. *J. Mol. Biol.* **287** (1999), 293–300.

[92] F.-H. Hsu. The influences of mechanical loads on the form of a growing elastic body. *J. Biomech.* **1** (1968), 303–311.

[93] T. J. R. Hughes, J. A. Cottrell, and Y. Bazilevs. Isogeometric analysis: CAD, finite elements, NURBS, exact geometry and mesh refinement. *Comput. Meth. Appl. Mech. Eng.* **194** (2005), 4135–4195.

[94] T. J. R. Hughes. *The finite element method: linear static and dynamic finite element analysis*. Englewood Cliffs: Prentice-Hall, 1987.

[95] B. M. Irons, O. C. Zienkiewicz, and E. R. De Arantes E Olivera. Comments on the paper: Theoretical foundations of the finite element method. *Int. J. Solids Struct.* **6** (1970), 695–697.

[96] A. Iwase et al. The AP2/ERF Transcription Factor WIND1 Controls Cell Dedifferentiation in Arabidopsis. *Curr. Biol.* **21** (2011), 508–514.

[97] L. Jia, A. Cao, D. Lévy, B. Xu, P.-A. Albouy, X. Xing, M. J. Bowick, and M.-H. Li. Smectic polymer vesicles. *Soft Matter* **5** (2009), 3446–3451.

[98] W. Jiang, J. Chang, J. Jakana, P. Weigele, J. King, and W. Chiu. Structure of epsilon15 bacteriophage reveals genome organization and DNA packaging/injection apparatus. *Nature* **439** (2006), 612–616.

[99] K. L. Johnson. *Contact Mechanics*. Cambridge: Cambridge University Press, 1985. Chap. 4.

[100] E. Katzav, M. Adda-Bedia, and A. Boudaoud. A statistical approach to close packing of elastic rods and to DNA packaging in viral capsids. *Proc. Natl. Acad. Sci. USA* **103** (2006), 18900–18904.

[101] J. Kiendl, K.-U. Bletzinger, J. Linhard, and R. Wüchner. Isogeometric shell analysis with Kirchhoff–Love elements. *Computer Methods in Applied Mechanics and Engineering* **198** (2009), 3902–3914.

[102] J. Kim, J. A. Hanna, M. Byun, C. D. Santangelo, and R. C. Hayward. Designing Responsive Buckled Surfaces by Halftone Gel Lithography. *Science* **335** (2012), 1201–1205.

[103] J. Kim, J. A. Hanna, R. C. Hayward, and C. D. Santangelo. Thermally responsive rolling of thin gel strips with discrete variations in swelling. *Soft Matter* **8** (2012), 2375–2381.

[104] J. Kindt, S. Tzlil, A. Ben-Shaul, and W. M. Gelbart. DNA packaging and ejection forces in bacteriophage. *Proc. Natl. Acad. Sci. USA* **98** (2001), 13671–13674.

[105] G. Kirchhoff. Ueber des Gleichgewicht und die Bewegung eines unendlich dünnen elastischen Stabes. *J. reine angew. Math.* **56** (1859), 285–313.

[106] G. R. Kirchhoff. *Vorlesungen über mathematische Physik: Mechanik*. Leipzig: B. G. Teubner, 1876.

[107] B. S. Kirk, J. W. Peterson, R. H. Stogner, and G. F. Carey. libMesh: a C++ library for parallel adaptive mesh refinement/coarsening simulations. *Eng. Comput.* **22** (2006), 237–254.

[108] Y. Klein, E. Efrati, and E. Sharon. Shaping of Elastic Sheets by Prescription of Non-Euclidean Metrics. *Science* **315** (2007), 1116–1120.

[109] W. T. Koiter. On the nonlinear theory of thin elastic shells. *Proc. Kon. Ned. Akad. Wetensch. Ser. B* **69** (1966), 1–54.

[110] D. A. Koster, V. Croquette, C. Dekker, S. Shuman, and N. H. Dekker. Friction and torque govern the relaxation of DNA supercoils by eukaryotic topoisomerase IB. *Nature* **434** (2005), 671–674.

[111] S. M. Kostic, F. C. Filippou, and C.-L. Lee. An Efficient Beam-Column Element for Inelastic 3D Frame Analysis. In: *Computational Methods in Earthquake Engineering*. Ed. by M. Papadrakakis, M. Fragiadakis, and V. Plevris. Vol. 30. Dordrecht: Springer, 2013, 49–67.

[112] E. M. Kramer and T. A. Witten. Stress Condensation in Crushed Elastic Manifolds. *Phys. Rev. Lett.* **78** (1997), 1303–1306.

[113] P. Krysl, A. Trivedi, and B. Zhu. Object-oriented hierarchical mesh refinement with CHARMS. *Int. J. Numer. Meth. Eng.* **60** (2004), 1401–1424.

[114] D. Kuchnir Fygenson, J. F. Marko, and A. Libchaber. Mechanics of Microtubule-Based Membrane Extension. *Phys. Rev. Lett.* **79** (1997), 4497–4500.

[115] P. Langston, A. R. Kennedy, and H. Constantin. Discrete element modelling of flexible fibre packing. *Computational Materials Science* **96, Part A** (2015), 108–116.

[116] E. H. Lee. Elastic-Plastic Deformation at Finite Strains. *J. Appl. Mech.* **36** (1969), 1–6.

[117] A. Y. T. Leung and C. K. Wong. Symmetry Reduction of Structures for Large Rotations. *Adv. Steel Struct.* **3** (2000), 81–102.

[118] Z. X. Li. A co-rotational formulation for 3D beam element using vectorial rotational variables. *Comput. Mech.* **39** (2007), 309–322.

[119] J. Lidmar, L. Mirny, and D. R. Nelson. Virus shapes and buckling transitions in spherical shells. *Phys. Rev. E* **68** (2003), 051910.

[120] E. Lieberman-Aiden et al. Comprehensive Mapping of Long-Range Interactions Reveals Folding Principles of the Human Genome. *Science* **326** (2009), 289–293.

[121] V. Lienhard. *Improvement of Contact-Evaluation in Thin-Shell Finite Element Analysis*. Semester Thesis. ETH Zürich, 2010.

[122] V. Lienhard. *Influence of Kinetic Friction on a Spherically Confined Shell*. Master's Thesis. ETH Zürich, 2010.

[123] L. Limozin and E. Sackmann. Polymorphism of Cross-Linked Actin Networks in Giant Vesicles. *Phys. Rev. Lett.* **89** (2002), 168103.

[124] S.-F. Liou, C.-C. Lo, M.-H. Chou, P.-Y. Hsiao, and T.-M. Hong. Effect of ridge-ridge interactions in crumpled thin sheets. *Phys. Rev. E* **89** (2014), 022404.

[125] A. P. Liu, D. L. Richmond, L. Maibaum, S. Pronk, P. L. Geissler, and D. A. Fletcher. Membrane-induced bundling of actin filaments. *Nat. Phys.* **4** (2008), 789–793.

[126] S. H. Lo. Geometrically nonlinear formulation of 3D finite strain beam element with large rotations. *Comput. Struct.* **44** (1992), 147–157.

[127] A. Lobkovsky, S. Gentges, H. Li, D. Morse, and T. A. Witten. Scaling properties of stretching ridges in a crumpled elastic sheet. *Science* **270** (1995), 1482–1485.

[128] A. E. Lobkovsky. Boundary layer analysis of the ridge singularity in a thin plate. *Phys. Rev. E* **53** (1996), 3750–3759.

[129] Q. Long, P. B. Bornemann, and F. Cirak. Shear-flexible subdivision shells. *Int. J. Numer. Meth. Eng.* **90** (2012), 1549–1577.

[130] C. T. Loop. *Smooth Subdivision Surfaces Based on Triangles*. Master's Thesis. Salt Lake City: University of Utah, 1987.

[131] A. E. H. Love. The Small Free Vibrations and Deformation of a Thin Elastic Shell. *Phil. Trans. R. Soc. Lond. A* **179** (1888), 491–546.

[132] A. E. H. Love. *A Treatise on the Mathematical Theory of Elasticity*. 2nd ed. Cambridge: Cambridge University Press, 1906.

[133] V. A. Lubarda and A. Hoger. On the mechanics of solids with a growing mass. *Int. J. Solids Struct.* **39** (2002), 4627–4664.

[134] B. Mandelbrot. How Long Is the Coast of Britain? Statistical Self-Similarity and Fractional Dimension. *Science* **156** (1967), 636–638.

[135] B. B. Mandelbrot. *The fractal geometry of nature*. W. H. Freeman, 1982.

[136] M. Marder, E. Sharon, S. Smith, and B. Roman. Theory of edges of leaves. *Europhys. Lett.* **62** (2003), 498.

[137] M. Marder. The Shape of the Edge of a Leaf. *Found. Phys.* **33** (2003), 1743–1768.

[138] M. Marder, R. D. Deegan, and E. Sharon. Crumpling, Buckling, and Crackling: Elasticity of Thin Sheets. *Phys. Today* **60** (2007), 33–38.

[139] D. Marenduzzo and E. Orlandini. Dynamics of fibers growing inside soft vesicles. *Europhys. Lett.* **80** (2007), 48004.

[140] D. Margolis. Fixed causality slip-stick friction models for use in simulation of non-linear systems. *Proc. Inst. Mech. Eng. I* **219** (2005), 199–206.

[141] S. Martin, P. Kaufmann, M. Botsch, E. Grinspun, and M. Gross. Unified Simulation of Elastic Rods, Shells, and Solids. *Trans. Graph.* **29** (2010), 39.

[142] K. Mattiasson, A. Bengtsson, and A. Samuelsson. On the accuracy and efficiency of numerical algorithms for geometrically nonlinear structural analysis. In: *Finite element methods for nonlinear problems*. Ed. by P. G. Bergan, K. J. Bathe, and W. Wunderlich. Berlin: Springer, 1986, 3–23.

[143] T. McMillen and A. Goriely. Tendril Perversion in Intrinsically Curved Rods. *J. Nonlinear Sci.* **12** (2002), 241–281.

[144] A. Y. Meyer and W. G. Richards. Similarity of molecular shape. *J. Comput.-Aided Mol. Des.* **5** (1991), 427–439.

[145] R. D. Mindlin. Influence of rotatory inertia and shear on flexural motions of isotropic elastic plates. *J. Appl. Mech.* **18** (1951), 31–38.

[146] L. A. Mirny. The fractal globule as a model of chromatin architecture in the cell. *Chromosome Res.* **19** (2011), 37–51.

[147] A. Mogilner and B. Rubinstein. The physics of filopodial protrusion. *Biophys. J.* **89** (2005), 782–795.

[148] A. Monnerot-Dumaine. *The Fibonacci Word Fractal*. 2009. URL: `http://hal.archives-ouvertes.fr/hal-00367972`.

[149] D. Moulton and A. Goriely. Anticavitation and Differential Growth in Elastic Shells. *J. Elasticity* **102** (2011), 117–132.

[150] P.-O. Mouthuy, M. Coulombier, T. Pardoen, J.-P. Raskin, and A. M. Jonas. Overcurvature describes the buckling and folding of rings from curved origami to foldable tents. *Nat. Commun.* **3** (2012), 1290.

[151] M. M. Müller, M. Ben Amar, and J. Guven. Conical Defects in Growing Sheets. *Phys. Rev. Lett.* **101** (2008), 156104.

[152] J. Najafi, N. Stoop, F. Wittel, and M. Habibi. Ordered packing of elastic wires in a sphere. *Phys. Rev. E* **85** (2012), 061108.

[153] A. Needleman. Inflation of spherical rubber balloons. *Int. J. Solids Struct.* **13** (1977), 409–421.

[154] M. Negahban, A. Goel, P. Marchon, and A. Azizinamini. Geometrically Exact Nonlinear Extended-Reissner/Mindlin Shells: Fundamentals, Finite Element Formulation, Elasticity. *Int. J. Comput. Meth. Eng. Sci. Mech.* **10** (2009), 430–449.

[155] I. Nemhauser, J. Joseph-Silverstein, and W. D. Cohen. Centriole as microtubule-organizing centers for marginal bands of molluscan erythrocytes. *J. Cell. Biol.* **96** (1983), 979–989.

[156] A. G. Neto, P. M. Pimenta, and P. Wriggers. Contact between rolling beams and flat surfaces. *Int. J. Numer. Meth. Eng.* **97** (2014), 683–706.

[157] N. M. Newmark. A Method of Computation for Structural Dynamics. *J. Eng. Mech. Div.* **85** (1959), 67–94.

[158] J. Nocedal and S. J. Wright. *Numerical optimization*. New York: Springer, 1999.

[159] T. Odijk. Statics and dynamics of condensed DNA within phages and globules. *Phil. Trans. R. Soc. Lond. A* **362** (2004), 1497–1517.

[160] N. H. Olson, M. Gingery, F. A. Eiserling, and T. S. Baker. The structure of isometric capsids of bacteriophage T4. *Virology* **279** (2001), 385–391.

[161] *OpenMP Application Program Interface Version 3.0*. OpenMP Architecture Review Board. 2008.

[162] C. Oran. Tangent Stiffness in Plane Frames. *J. Struct. Div.* **99** (1973), 973–985.

[163] C. Oran. Tangent Stiffness in Space Frames. *J. Struct. Div.* **99** (1973), 987–1001.

[164] O. Otto, S. Sturm, N. Laohakunakorn, U. F. Keyser, and K. Kroy. Rapid internal contraction boosts DNA friction. *Nat. Commun.* **4** (2013), 1780.

[165] H. Parisch. A continuum-based shell theory for non-linear applications. *Int. J. Numer. Meth. Eng.* **38** (1995), 1855–1883.

[166] A. S. Petrov and S. C. Harvey. Packaging Double-Helical DNA into Viral Capsids: Structures, Forces, and Energetics. *Biophys. J.* **95** (2008), 497–502.

[167] A. P. Philipse. The Random Contact Equation and Its Implications for (Colloidal) Rods in Packings, Suspensions, and Anisotropic Powders. *Langmuir* **12** (1996), 1127–1133.

[168] M. Pinot, F. Chesnel, J. Kubiak, I. Arnal, F. Nedelec, and Z. Gueroui. Effects of Confinement on the Self-Organization of Microtubules and Motors. *Curr. Biol.* **19** (2009), 954–960.

[169] J. Pitkäranta, Y. Leino, O. Ovaskainen, and J. Piila. Shell deformation states and the finite element method: A benchmark study of cylindrical shells. *Comput. Meth. Appl. Mech. Eng.* **128** (1995), 81–121.

[170] G. H. Powell and P. F.-S. Chen. 3D Beam-Column Element with Generalized Plastic Hinges. *J. Eng. Mech.* **112** (1986), 627–641.

[171] G. Prathap and G. R. Bhashyam. Reduced integration and the shear-flexible beam element. *Int. J. Numer. Meth. Eng.* **18** (1982), 195–210.

[172] P. K. Purohit, J. Kondev, and R. Phillips. Mechanics of DNA packaging in viruses. *Proc. Natl. Acad. Sci.* **100** (2003), 3173–3178.

[173] B. Quentrec and C. Brot. New Method for Searching for Neighbors in Molecular Dynamics Computations. *J. Comput. Phys.* **13** (1973), 430–432.

[174] R Radloff, W Bauer, and J Vinograd. A dye-buoyant-density method for the detection and isolation of closed circular duplex DNA: the closed circular DNA in HeLa cells. *P. Natl. Acad. Sci. USA* **57** (1967), 1514–1521.

[175] C. C. Rankin and F. A. Brogan. An Element Independent Corotational Procedure for the Treatment of Large Rotations. *J. Press. Vessel Technol.* **108** (1986), 165–174.

[176] D. M. Raymer and D. E. Smith. Spontaneous knotting of an agitated string. *P. Natl. Acad. Sci. USA* **104** (2007), 16432–16437.

[177] J. N. Reddy. *An introduction to the finite element method*. 2nd ed. New York: McGraw-Hill, 1993, pp. 292–295.

[178] J. N. Reddy. On locking-free shear deformable beam finite elements. *Comput. Meth. Appl. Mech. Eng.* **149** (1997), 113–132.

[179] J. N. Reddy. *An Introduction to Nonlinear Finite Element Analysis*. Oxford: Oxford University Press, 2004, pp. 292–295.

[180] J. N. Reddy, C. M. Wang, and K. Y. Lam. Unified finite elements based on the classical and shear deformation theories of beams and axisymmetric circular plates. *Commun. Numer. Meth. Eng.* **13** (1997), 495–510.

[181] E. Reissner. The effect of transverse shear deformation on the bending of elastic plates. *J. Appl. Mech.* **12** (1945), A68–77.

[182] J. Rhim and S. W. Lee. A vectorial approach to computational modelling of beams undergoing finite rotations. *Int. J. Numer. Meth. Eng.* **41** (1998), 527–540.

[183] M. Robinson. A comparison of yield surfaces for thin shells. *Int. J. Mech. Sci.* **13** (1971), 345–354.

[184] E. K. Rodriguez, A. Hoger, and A. D. McCulloch. Stress-dependent finite growth in soft elastic tissues. *J. Biomech.* **27** (1994), 455–467.

[185] W. J. van Rooij and M. Sluzewski. Packing performance of GDC 360° coils in intracranial aneurysms: a comparison with complex orbit coils and helical GDC 10 coils. *Am. J. Neuroradiol.* **28** (2007), 368–370.

[186] W. Roos, I. Ivanovska, A. Evilevitch, and G. Wuite. Viral capsids: Mechanical characteristics, genome packaging and delivery mechanisms. *Cell. Mol. Life Sci.* **64** (2007), 1484–1497.

[187] J. B. Rosen. The Gradient Projection Method for Nonlinear Programming. Part I. Linear Constraints. *J. Soc. Indust. Appl. Math.* **8** (1960), 181–217.

[188] A. Rosenfeld and J. S. Weszka. Picture Recognition. In: *Digital Pattern Recognition*. Ed. by K. S. Fu. Vol. 10. Berlin: Springer, 1976, 135–166.

[189] J. Salençon. *Calcul à la rupture et analyse limite*. Paris: Presses de l'école nationale des ponts et chaussée, 1983.

[190] T. Sanchez, D. T. N. Chen, S. J. DeCamp, M. Heymann, and Z. Dogic. Spontaneous motion in hierarchically assembled active matter. *Nature* **491** (2012), 431–434.

[191] J. S. Sandhu, K. A. Stevens, and G. Davies. A 3-D, co-rotational, curved and twisted beam element. *Comput. Struct.* **35** (1990), 69–79.

[192] C. Sansour and H. Bufler. An exact finite rotation shell theory, its mixed variational formulation and its finite element implementation. *Int. J. Numer. Meth. Eng.* **34** (1992), 73–115.

[193] T. Savin, N. A. Kurpios, A. E. Shyer, P. Florescu, H. Liang, L. Mahadevan, and C. J. Tabin. On the growth and form of the gut. *Nature* **476** (2011), 57–62.

[194] J. E. Schweitzer. *Analysis and Application of Subdivision Surfaces*. PhD thesis. Seattle: University of Washington, 1996.

[195] A. A. Shabana. *Computational Continuum Mechanics*. Cambridge: Cambridge University Press, 2008, pp. 118–120.

[196] E. Sharon, M. Marder, and H. L. Swinney. Leaves, Flowers and Garbage Bags: Making Waves. *Am. Sci.* **93** (2004), 254–261.

[197] E. Sharon, B. Roman, and H. L. Swinney. Geometrically driven wrinkling observed in free plastic sheets and leaves. *Phys. Rev. E* **75** (2007), 046211.

[198] E. Sharon, B. Roman, M. Marder, G.-S. Shin, and H. L. Swinney. Buckling cascades in free sheets. *Nature* **419** (2002), 579.

[199] J. C. Simo and D. D. Fox. On a stress resultant geometrically exact shell model. Part I: Formulation and optimal parametrization. *Comput. Meth. Appl. Mech. Eng.* **72** (1989), 267–304.

[200] J. C. Simo, D. D. Fox, and M. S. Rifai. On a stress resultant geometrically exact shell model. Part II: The linear theory; Computational aspects. *Comput. Meth. Appl. Mech. Eng.* **73** (1989), 53–92.

[201] J. C. Simo, D. D. Fox, and M. S. Rifai. On a stress resultant geometrically exact shell model. Part III: Computational aspects of the nonlinear theory. *Comput. Meth. Appl. Mech. Eng.* **79** (1990), 21–70.

[202] J. C. Simo and T. J. R. Hughes. *Computational Inelasticity*. New York: Springer, 1998.

[203] J. C. Simo and L. Vu-Quoc. A three-dimensional finite-strain rod model. Part II: Computational aspects. *Comput. Meth. Appl. Mech. Eng.* **58** (1986), 79–116.

[204] R. Skalak, S. Zargaryan, R. K. Jain, P. A. Netti, and A. Hoger. Compatibility and the genesis of residual stress by volumetric growth. *J. Math. Biol.* **34** (1996), 889–914.

[205] D. E. Smith, S. J. Tans, S. B. Smith, S. Grimes, D. L. Anderson, and C. Bustamante. The bacteriophage ϕ29 portal motor can package DNA against a large internal force. *Nature* **413** (2001), 748–752.

[206] A. J. Spakowitz and Z.-G. Wang. DNA Packaging in Bacteriophage: Is Twist Important? *Biophys. J.* **88** (), 3912–3923.

[207] R. A. Spurrier. Comment on "Singularity-Free Extraction of a Quaternion from a Direction-Cosine Matrix". *J. Spacecraft Rockets* **15** (1978), 255.

[208] J. Stam. Evaluation of Loop Subdivision Surfaces. In: *SIGGRAPH '99 course notes*. 1999.

[209] H. J. Steiger, R. Aaslid, S. Keller, and H.-J. Reulen. Strength, elasticity and viscoelastic properties of cerebral aneurysms. *Heart Vessels* **5** (1989), 41–46.

[210] R. H. Stogner and G. F. Carey. C^1 macroelements in adaptive finite element methods. *Int. J. Numer. Meth. Eng.* **70** (2007), 1076–1095.

[211] H. Stolarski and T. Belytschko. Membrane Locking and Reduced Integration for Curved Elements. *J. Appl. Mech.* **49** (1982), 172–176.

[212] H. Stolarski and T. Belytschko. Shear and membrane locking in curved {C0} elements. *Comp. Meth. Appl. Mech. Eng.* **41** (1983), 279–296.

[213] N. Stoop, F. K. Wittel, and H. J. Herrmann. Morphological Phases of Crumpled Wire. *Phys. Rev. Lett.* **101** (2008), 094101.

[214] N. Stoop, J. Najafi, F. K. Wittel, M. Habibi, and H. J. Herrmann. Packing of Elastic Wires in Spherical Cavities. *Phys. Rev. Lett.* **106** (2011), 214102.

[215] N. B. Stoop. *Morphogenesis in Constrained Spaces*. PhD thesis. Zürich: Swiss Federal Institute of Technology, 2011.

[216] N. Stoop, F. K. Wittel, M. Ben Amar, M. M. Müller, and H. J. Herrmann. Self-Contact and Instabilities in the Anisotropic Growth of Elastic Membranes. *Phys. Rev. Lett.* **105** (2010), 068101.

[217] A. H. Stroud. *Approximate Calculation of Multiple Integrals*. Englewood Cliffs: Prentice–Hall, 1971.

[218] D. Sunday. *Distance between Lines and Segments with their Closest Point of Approach*. 2001. URL: `http://www.softsurfer.com/Archive/algorithm_0106/algorithm_0106.htm` (visited on 2012-03-15).

[219] T. M. Svitkina, E. A. Bulanova, O. Y. Chaga, D. M. Vignjevic, S.-i. Kojima, J. M. Vasiliev, and G. G. Borisy. Mechanism of filopodia initiation by reorganization of a dendritic network. *J. Cell. Biol.* **160** (2003), 409–421.

[220] K. Y. Sze, X. H. Liu, and S. H. Lo. Popular benchmark problems for geometric nonlinear analysis of shells. *Finite Elem. Anal. Des.* **40** (2004), 1551–1569.

[221] L. A. Taber. Biomechanics of Growth, Remodeling, and Morphogenesis. *Appl. Mech. Rev.* **48** (1995), 487–545.

[222] T. Tallinen, J. A. Åström, and J. Timonen. Deterministic Folding in Stiff Elastic Membranes. *Phys. Rev. Lett.* **101** (2008), 106101.

[223] T. Tallinen, J. A. Åström, and J. Timonen. The effect of plasticity in crumpling of thin sheets. *Nat. Mater.* **8** (2009), 25–29.

[224] S. Tamatani, Y. Ito, H. Abe, T. Koike, S. Takeuchi, and R. Tanaka. Evaluation of the Stability of Aneurysms after Embolization Using Detachable Coils: Correlation between Stability of Aneurysms and Embolized Volume of Aneurysms. *Am. J. Neuroradiol.* **23** (2002), 762–767.

[225] L. H. Teh and M. J. Clarke. Co-rotational and Lagrangian formulations for elastic three-dimensional beam finite elements. *J. Construct. Steel Res.* **48** (1998), 123–144.

[226] A. Tessler and S. B. Dong. On a hierarchy of conforming Timoshenko beam elements. *Comput. Struct.* **14** (1981), 335–344.

[227] D. W. Thompson. *On Growth and Form*. Cambridge: Cambridge University Press, 1917.

[228] S. P. Timoshenko. On the correction for shear of the differential equation for transverse vibrations of prismatic bars. *Philos. Mag.* **41** (1921), 744–746.

[229] S. P. Timoshenko. On the transverse vibrations of bars of uniform cross-section. *Philos. Mag.* **43** (1922), 125–131.

[230] S. P. Timoshenko. *Theory of elastic stability*. New York: McGraw-Hill, 1936.

[231] P. Tong, T. H. H. Pian, and L. L. Bucciarblli. Mode shapes and frequencies by finite element method using consistent and lumped masses. *Comput. Struct.* **1** (1971), 623–638.

[232] C. Truesdell and W. Noll. *The non-linear field theories of mechanics*. Berlin: Springer, 1965.

[233] Y. Urthaler and J. N. Reddy. A corotational finite element formulation for the analysis of planar beams. *Commun. Numer. Methods Eng.* **21** (2005), 553–570.

[234] R. Vetter. *Packing of Elastic Wires in Three-Dimensional Cavities*. Master's Thesis. ETH Zürich, 2011.

[235] G. A. Vliegenthart and G. Gompper. Forced crumpling of self-avoiding elastic sheets. *Nat. Mater.* **5** (2006), 216–221.

[236] G. A. Vliegenthart and G. Gompper. Compression, crumpling and collapse of spherical shells and capsules. *New J. Phys.* **13** (2011), 045020.

[237] S. Wang, L. Furchtgott, K. C. Huang, and J. W. Shaevitz. Helical insertion of peptidoglycan produces chiral ordering of the bacterial cell wall. *Proc. Natl. Acad. Sci. USA* **109** (2012), E595–E604.

[238] G. Wempner. Finite elements, finite rotations and small strains of flexible shells. *Int. J. Solids Struct.* **5** (1969), 117–153.

[239] T. Winegard et al. Coiling and maturation of a high-performance fibre in hagfish slime gland thread cells. *Nat. Commun.* **5** (2014), 3534.

[240] K. Wiśniewski. *Finite Rotation Shells: Basic Equations and Finite Elements for Reissner Kinematics*. Barcelona: Springer, 2010.

[241] F. Wittel, F. Kun, H. J. Herrmann, and B. H. Kröplin. Fragmentation of Shells. *Phys. Rev. Lett.* **93** (2004), 035504.

[242] J. Xu, H. Wang, C. Liu, Y. Yang, T. Chen, Y. Wang, F. Wang, X. Liu, B. Xing, and H. Chen. Mechanical nanosprings: Induced coiling and uncoiling of ultrathin Au nanowires. *J. Am. Chem. Soc.* **132** (2010), 11920–11922.

[243] G. Zavarise and P. Wriggers. Contact with friction between beams in 3-D space. *Int. J. Numer. Meth. Eng.* **49** (2000), 977–1006.

[244] L. F. Zeng, N.-E. Wiberg, X. D. Li, and Y. M. Xie. A posteriori local error estimation and adaptive time-stepping for Newmark integration in dynamic analysis. *Earthq. Eng. Struct. Dyn.* **21** (1992), 555–571.

[245] O. C. Zienkiewicz and R. L. Taylor. *The Finite Element Method for Solid and Structural Dynamics*. 6th ed. Amsterdam: Elsevier Butterworth–Heinemann, 2005.

[246] O. C. Zienkiewicz, R. L. Taylor, and J. M. Too. Reduced integration technique in general analysis of plates and shells. *Int. J. Numer. Meth. Eng.* **3** (1971), 275–290.

[247] O. C. Zienkiewicz and Y. M. Xie. A simple error estimator and adaptive time stepping procedure for dynamic analysis. *Earthq. Eng. Struct. Dyn.* **20** (1991), 871–887.